The Modern Rotor Aerodynamic Limits Survey: A Report and Data Survey

J. Cross, J. Brilla, R. Kufeld, and D. Balough
Ames Research Center, Moffett Field, California

OCTOBER 1993

CONTENTS

NOMENCLATURE

a_r	blade-root acceleration
a_t	blade-tip acceleration
c	blade chord
C	airspeed position error
C_T/σ	thrust coefficient over sigma
e	blade-hinge offset
H_d	density altitude
H_p	pressure altitude
K_{1-10}	blade-motion correction coefficients
KCAS	calibrated airspeed, knots
KIAS	indicated airspeed, knots
KTAS	true airspeed, knots
Nr	rotor speed, % of nominal
p	roll rate
p_0	atmospheric pressure, sea level standard day
q	pitch rate
r	yaw rate
r_r	radial location of blade-root accelerometer
r_t	radial location of blade-tip accelerometer
R	rotor radius
T_0	atmospheric temperature, sea level standard
V_h	maximum achievable velocity in level flight

V_{ne}	never-to-exceed forward velocity
W	aircraft gross weight
β	corrected blade flapping
β_1	measured blade flapping
β''	blade-flapping acceleration
ς	rotor rotational speed
θ	pitch attitude
θ_t	temperature ratio
λ	corrected blade lead-lag angle
λ_1	measured blade lead-lag angle
μ	advance ratio
υ	corrected blade-feathering angle
υ_1	measured blade-feathering angle
ζ	damping ratio
ρ	local atmospheric density
ρ_0	atmospheric density, sea level standard
σ	rotor solidity
σ_d	density ratio
ϕ	roll attitude
Φ	equations of motion roots
χ	yaw attitude
ψ	heading angle
Ω	main-rotor speed
ω_n	undamped natural frequency

SUMMARY

The first phase of the Modern Technology Rotor program, the Modern Rotor Aerodynamic Limits Survey, was a flight test conducted by the United States Army Aviation Engineering Flight Activity for NASA Ames Research Center. The test was performed using a United States Army UH-60A Black Hawk aircraft and the United States Air Force HH-60A Night Hawk instrumented main-rotor blade. The primary purpose of this test was to gather high-speed, steady-state, and maneuvering data suitable for correlation purposes with analytical prediction tools. All aspects of the data base, flight-test instrumentation, and test procedures are presented and analyzed. Because of the high volume of data, only select data points are presented here. However, access to the entire data set is available upon request.

1. INTRODUCTION

This report describes a flight test conducted in 1987 by the United States Army Aviation Engineering Flight Activity (AEFA) at Edwards Air Force Base, California, for the NASA Ames Research Center. The Modern Rotor Aerodynamic Limits Survey (MRALS), conducted on a UH-60A Black Hawk, was divided into four sections: high-speed limits; maneuver limits; stability and control; and acoustics. The sensors included in the test are categorized as follows: rotor parameters, fuselage vibration, aircraft state, and engine parameters. The data accumulated from this first phase of the Modern Technology Rotor Program reside at Ames Research Center and are accessible through two data-analysis/management computer programs, the Tilt Rotor ENgineering Database System (TRENDS) and the Data from Aeromechanics Test and Analytics-Management and Analysis Program (DATAMAP).

A data survey is presented here covering a sample of each of the sensor types included in this test. The survey includes both statistical and time-history data plots and summary tables. Data accuracy and data-base limitations are discussed. A data analysis section is included which addresses many of the phenomena found in the data. Appendixes provide reference information on the following: UH-60A aircraft physical characteristics (appendix A); flight cards (appendix B); Information File for DATAMAP (appendix C); sign conventions (appendix D); and sensor calibration information (appendix E).

The numbered tables and figures cited throughout the text appear after the main text, appendixes, and refer-ences. An exception is the sensor calibration plots (appendix E), which are unnumbered and are arranged in alphabetical order by mnemonic name within appendix E.

2. INSTRUMENTATION AND EQUIPMENT

MRALS involved the use of two aircraft, a UH-60A and a YO-3A, the AEFA ground station, and special instrumentation. The primary data were recorded on board the UH-60A test aircraft; the NASA YO-3A Acoustic Research Aircraft was used to obtain the in-flight acoustics data. The ground station was used to monitor flight loads, maintain test conditions, and provide preliminary postflight data processing. The special instrumentation on the UH-60A consisted of sensors measuring blade motion, rotor loads and vibration, control loads, and fuselage vibration.

UH-60A Black Hawk

The UH-60A Black Hawk used in this test, tail number 23748, is shown in figure 1. The physical characteristics of the UH-60A are presented in appendix A. This discussion of the aircraft will cover the basic production qualities and the special instrumentation installed for this test. The test equipment included for this test can be divided into the following categories: fuselage, rotor system, and data system.

The aircraft was manned by a pilot, co-pilot, and flight-test engineer. During MRALS, the flight engineer controlled and verified the operation of the tape recorder, maintained the desired aircraft longitudinal center of gravity (c.g.) trim using the ballast cart, monitored the status of the test condition, and maintained the flight notes on the flight cards.

The UH-60A flight-control system includes five major automatic subsystems: the stability augmentation system (SAS); flight-path-stabilization system (FPS); trim system; stabilator control system; and pitch bias actuator (PBA). The SAS subsystem is a dual subsystem consisting of a digital (SAS1) and an analog (SAS2) control. The SAS is designed to provide three-axis rate-damping, partial attitude retention, and limited turn coordination. The FPS is designed to provide three-axis attitude-hold, airspeed-hold, and principal turn coordination. The trim system is designed to provide stick-position-hold and force-feel. The stabilator control system positions the stabilator as a function of airspeed and collective positions, and is designed to control the aircraft pitch attitude as a function of airspeed. The PBA was designed to insure positive static and dynamic longitudinal stability. It was found to be of little benefit, however, and was disabled for

this test. More detailed descriptions of these control systems are provided in reference 1.

The UH-60A was equipped with a ballast cart, shown in figure 2, that travels longitudinally to compensate for fuel burn-off, thus maintaining a constant aircraft longitudinal c.g. Additional ballast weight was added at three locations to achieve the desired thrust coefficients. Figure 3 shows one of the two locations over the fuel tanks behind the aft cabin bulkhead. The third site was on the cabin floor to either side of the engineers seat. During the acoustics test a transmitter, shown in figure 4, was installed in the nose of the aircraft to send the once-per-main-rotor-revolution (1/rev) contactor signal to the YO-3A aircraft.

Instrumentation system– A pulse code modulation (PCM) data-acquisition system, known as the high-capacity, or Hi-Cap, system was used during this flight test. The system was set up for this test with 58 words in the mainframe, with two subframes. The first subframe was 4 levels deep, and the second was 16 levels deep. This provided data sampling at nominal rates of 517, 129.25, and 32.3 samples/sec. The PCM map used for the test is presented in table 1, which details the locations of all sensors, as well as their sample rates. Filtering of the data was provided as a part of the signal conditioning.

Each test point was identified by a unique label called a counter. The counter is a numerical series that has the flight number in the hundreds place and begins at zero for each flight. An example of this scheme would be counter 2208 which is the eighth test point obtained on flight 22.

This was the first field test of the Hi-Cap system, shown in figure 5; all things considered, it worked very well. The data were recorded by using an on-board, 14-track, wideband FM tape recorder; the data were also telemetered to the ground station where a ground tape was recorded as backup. The ground tape was used to provide data for the second half of flight 20, counters 2015 through 2021, after the on-board recorder ran out of tape.

All instrumentation on board the aircraft was given two separate identification labels—mnemonics and item codes. Both labels are alphanumeric; the mnemonics contain up to eight characters, whereas the item code contains precisely four characters. Both types of identification labels were required since AEFA uses mnemonics, the data analysis program TRENDS uses either, and the program DATAMAP uses only the item code. The two analysis programs are discussed in section 5.

The mnemonics generally are abbreviations of the sensor name. Examples of mnemonics are PITCHATT, pitch attitude; STABLR, horizontal stabilizer position; and AZPS, vertical acceleration at the pilots station. Not all mnemonics abbreviations are so obvious, however, as illustrated by PAICB, which is the boom system static pressure.

Item codes fall into one of the following four sets: one letter and three digits; two letters and two digits; three letters and one digit; and four letters. All four-letter item codes are derived parameters (i.e., calculated, not measured) with the following three exceptions: BFAT, BFAR, and CART, which stand for blade tip and root flapwise accelerometers, and ballast cart position, respectively. The item codes use letters to denote sensor type or aircraft component or both, and numbers to denote exact physical location or sensor orientation. Examples of the first-letter notations are the following: "A" denotes an accelerometer; "B" denotes a sensor related to the instrumented blade; "D" denotes a sensor that measures an aircraft state; "E" denotes an engine-related parameter; "H" denotes an altitude measurement; "M" denotes a sensor related to the rotor; "R" is a miscellaneous grouping; "T" denotes a temperature reading; and "V" denotes a velocity sensor. The second and third letters provide further identification of the sensor type. Examples of the use of numbers are BN50, which denotes the blade-normal stress at 50% radius, and ET01, which denotes the engine turbine temperature of engine No. 1. All aircraft-state parameters, such as control positions, body attitudes, rates, and accelerations, use the numeric code of zero for longitudinal, 1 for lateral, 2 for yaw, and 3 for horizontal orientations. Table 2 summarizes the item-code structure.

Fuselage– The fuselage instrumentation includes what are collectively known as aircraft-state parameters and airframe vibration measurements. The aircraft-state parameters include fuselage attitudes, rates, and angular and linear accelerations. These are housed on a pallet on the aft cabin bulkhead, as shown in figure 5. Control-stick positions, engine data, main-rotor speed, and both main- and tail-rotor contactors are also included in the aircraft-state measurement list. The aircraft is equipped with an instrumentation boom that monitors static and dynamic pressure, outside air temperature, and angles of attack and side slip. A low-airspeed sensor was installed (fig. 6) in order to obtain accurate velocity measurements where the pitot static system did not function. Many of the aircraft control-system components were instrumented for this test, including the output motion of the three primary servos (fig. 7), along with SAS outputs and control mixer input signals. The tail rotor had only minimal instrumentation, which included tail-rotor shaft torque, by means of slip rings at the intermediate gear box (fig. 8) and a tail-rotor once-per-rev contactor (fig. 9). The aircraft-state parameters comprise three categories: aircraft parameters (table 3), test condition (table 4), and engine parameters (table 5).

Table 6 presents the mnemonics, item codes, and orientations of the fuselage vibration sensors. The locations of the accelerometers were selected to match those used on an airframe shake test conducted by Sikorsky

Aircraft, in support of the NASA Langley Design Analysis Methods for Vibrations (DAMVIBS) program (ref. 2). The precise physical locations of the fuselage accelerometers are given in table 7. The accelerometers were sampled so as to provide data up to 20 harmonics, although the processed data are filtered such that only the first 10 harmonics are included in the data base.

Rotor system– The rotor-system instrumentation is divided into blade loads, control loads, and hub measurements. The blade was instrumented with strain gauges to measure normal, edgewise, and total stresses, as well as blade-root and tip normal accelerations. Included with the blade-load measurement is the pitch-link load. The control loads primarily include nonrotating hardware, whereas the hub sensors consist of orthogonal accelerations, blade motions, and shaft parameters. Table 8 presents a complete sensor list of the rotor-system parameters.

The instrumented blade used for the MRALS was obtained from the USAAF Night Hawk program. The blade is only slightly modified from the production blade by the addition of instrumentation wiring laid down in the troughs cut into the skin of both the top and bottom surfaces. The aerodynamic contour of the blade is interrupted to some extent, because the room-temperature vulcanizing (RTV) compound used to cover the wires did not harden to a uniform surface. The instrumentation embedded in the Night Hawk blade included four normal, three edgewise, three total, and two tip-cap strain gauges.

The two tip gauges were disconnected, for MRALS, and were replaced by two accelerometers, one normal and one edgewise (fig. 10). The tip-normal accelerometer was matched with a root accelerometer mounted on the outboard section of the hub arm (fig. 11).

The tip-normal accelerometer failed early in the test; because it was the more important of the two tip sensors, the edgewise tip accelerometer was used to replace it. This quick fix initially caused havoc with postflight data processing, which was not flexible enough to handle sensor swapping. However, after modification this too was remedied.

The pitch link that connects the instrumented blade to the swash plate was instrumented with strain gauges to measure the axial control loads. The stationary rotor control links were instrumented with strain gauges to measure axial loads. These values were monitored during flight.

The hub instrumentation group consists of accelerometers, strain gauges, and motion pots. The hub was instrumented with three orthogonal accelerometers (fig. 12). The blade-motion hardware (fig. 13) was developed for the Rotorcraft Systems Integration Simulator (RSIS) flight test, conducted by AEFA in 1981-1982 (ref. 3). The special hardware was required because of the unusual hinge arrangement of the hub. The blade-motion in flap, feather, and lead-lag is allowed by an elastomeric

bearing in each arm of the hub. Proper measurement with this hardware requires a complex and meticulous calibration, the theory of which is outlined in appendix F. The shaft strain gauges are shown in figure 14.

Derived parameters– A group of derived parameters has been included, along with the measured parameters, in the stored data base. Table 9 presents the mnemonics, item codes, units, and descriptions of these derived parameters. The exact equations used to compute the derived parameters are available as a part of the data base.

YO-3A Acoustic Research Aircraft

Acoustic data of the UH-60 were taken during MRALS by the YO-3A Acoustic Research Aircraft (fig. 15). The Acoustic Research Aircraft is a specially instrumented version of the low-speed observation aircraft manufactured for the military by the Lockheed Aircraft Corporation, which is used as a flying microphone platform for the study of rotorcraft noise. The YO-3A Acoustic Research Aircraft is equipped with a special instrumentation package which includes three 0.5-in. microphones, one on each wing tip and one atop the vertical tail; gain-adjustable microphone power supplies; an instrumentation boom; a radio link with the test helicopter, which carries the main-rotor contactor signal; an IRIG-B time-code receiver; and a 14-track FM tape recorder.

The YO-3A is powered by a highly modified Continental engine (210 hp), which is equipped with a three-bladed, wide-chord wooden propeller. The engine is equipped with a very effective muffler which, combined with the low-tip-speed propeller, results in a very quiet aircraft. A thorough discussion of this aircraft is presented in reference 4.

3. TEST DESCRIPTION

The conduct of the test is divided into four general categories: performance limits, maneuver limits, dynamic stability, and acoustics. All test points were partially defined by the nondimensional value of thrust coefficient over sigma (C_T/σ), and the referred rotor speed ($Nr/\sqrt{\theta_t}$). The remainder of the test-point definitions were set by the requirements unique to each of the four categories. Detailed descriptions of the required piloting techniques used to acquire the various test-point types are presented in reference 1.

The ground station was used during each of the four test categories testings to establish the required test altitude and rotor speed. In the event of telemetry (TM) failure (which did occur) or extended site testing (which also occurred), the on-board flight-test engineer used a

hand-held, portable calculator to make the necessary calculations.

Two separate support tests were conducted in support of MRALS: a dynamic shake test of the instrumented Night Hawk blade, conducted before the flight test; and a fuselage shake test which was conducted concurrently with the flight test.

Performance Limits

The objective of the performance-limits test element was to measure the increase in rotor loads and fuselage vibration as a function of airspeed and correlate that with analytical predictions and ground test. This portion of the test matrix was designed to obtain performance data from all sensors from hover to V_{ne} at C_T/σ values of 0.08, 0.09, and 0.10. Table 10 presents the test points obtained during this portion of the test.

The data from hover to V_h were obtained in level flight at approximately 5,000 ft pressure altitude. The speeds from V_h out to V_{ne} were achieved while in a powered descent. Additional test points were obtained at several speeds below V_h while at maximum power. The low-airspeed sensor was used to establish airspeed below 25 KIAS; above this speed the ships system was used. The SAS systems were disengaged for these test points, except at the high-speed end, where they were required.

Maneuver Limits

The test objective for the maneuver-limits element of the program was to obtain high-g data in a constant steady maneuver; that is to say that airspeed, pitch attitude, roll attitude, pitch rate, pitch angular acceleration, and g loading, were to be held constant. All other means of achieving high-g loads require that some of these be continually varying. It is felt that constant maneuvers simplify the correlation effort with many of the comprehensive rotorcraft codes.

This portion of the test matrix obtained vibration and blade-loads data encountered in high-speed wind-up turns at two gross weight conditions. Table 11 presents the test points obtained during this portion of the test. The maneuver limits data was originally to be obtained at the same altitude as the performance data; however, because of temporary altitude restrictions placed on the aircraft during the time of testing, the target altitude was raised to 9,000 ft. This made it impossible to obtain data at $C_T/\sigma = 0.08$. The maneuver limits tests provide aircraft response data at high-load and high-speed conditions which can then be compared with level and descending flight results.

These points were obtained by flying to an initial altitude of over 11,000 ft, establishing airspeed, nosing

the aircraft over and beginning the wind-up turn. The bank angle was varied to 37°, 48°, 55°, 60°, and 65° and held for 5 sec of steady data. Several bank angles were usually attained during each descent through the target altitude, while the tape ran continuously. Telemetry was monitored to assess the quality of each bank-angle condition and to monitor load buildup. Rotor and control endurance limits were exceeded at many of the higher speed points.

Dynamic Stability

The objective of the dynamic stability test was to quantitatively measure the UH-60's unaugmented, rigid-body dynamic response to various discrete control inputs. Dynamic stability, a secondary goal of MRALS, was included primarily to provide some data with which to evaluate the capabilities of comprehensive analysis computer codes in modeling dynamic stability. An additional interest in obtaining these data was the individual blade control (IBC) concept, which is discussed in detail in section 7. The control inputs consisted of doublets and sinusoidal control sweeps The dynamic stability tests were performed from trim conditions at two airspeeds: 60 and 140 knots calibrated, and the sinosoidal sweeps were conducted at hover and 108 KIAS (table 12). The control inputs consisted of longitudinal, lateral, directional, and collective doublets of approximately ±1 in. from the trim positions. The doublet inputs were designed to have a total duration of 1.0 sec, 0.5 sec/pulse, before returning to trim. The control was then held for approximately 7 sec, or until corrective control action was required. To ensure that only the unaugmented aircraft response was measured, both stability augmentation systems and the flight-path stabilization system were disengaged.

Acoustics

The acoustic data from MRALS was gathered to serve as a baseline for the more encompassing tests to be conducted during the second phase of the Modern Technology Rotor program. The test matrix that was flown during phase 1, as shown in table 13, was therefore relatively modest. The air-to-air acoustics data were obtained with the YO-3A Acoustic Research Aircraft flying formation with the UH-60A, as depicted in figure 16. Three formations, trail, left, and right (fig. 17), were flown during this portion of the flight-test program. The trail formation consists of the UH-60 flying 1.5 rotor diameters behind the YO-3A with its rotor hub in the horizontal plane of the tail-mounted microphone. The left and right formations are mirror images of each other, with the UH-60 at 30° elevation above and behind the

4

respective wing-tip-mounted microphone at a distance of 1.5 rotor diameters. The proper aircraft separation was obtained by using an optical range finder, which was operated by one of the pilots. While in the trail formation, both UH-60 pilots had an unobstructed view of the YO-3A, thus ensuring that separation was consistent. However, during the other formations only the crew member actually flying the helicopter had an unobstructed view of the YO-3A. It was therefore not possible to use the range finder throughout the maneuver; instead, the formation was held by using visual references.

Support Tests

Two support tests were conducted as an integral part of MRALS, a blade-shake test, and a fuselage-shake test. The blade-shake test was conducted using the instrumented Night Hawk blade prior to commencement of flight testing. The test involved applying forces to the root end of the blade with a shaker, while the blade was suspended with bungee cords in a vertical orientation. The tests produced data on mode shapes and natural frequencies, which are discussed in more detail in section 6 of this report and in reference 5.

The fuselage-shake test was conducted by Sikorsky under a modification to the NASA Langley DAMVIBS program. This test involved loading the test fuselage to model the flight aircraft including ballast, fuel, instrumentation, and crew. It should be noted that the test fuselage was not that of the flight-test vehicle. Final test results and correlation with NASTRAN predictions are presented in references 2 and 6.

4. DATA PROCESSING AND ACCESS

The goal of processing the flight data was to produce a data base in the proper format for use with the two data analysis programs, TRENDS (Tilt Rotor Engineering Database System) and DATAMAP (Data from Aeromechanics Test and Analytics-Management and Analysis Package) (refs. 7-9). The data are stored in what has become known as the TRENDS format. This actually consists of several different formats, depending on the types of data. Data are referenced to a specific sensor (referred to as a mnemonic or item code) and test point (referred to as a counter).

Data-Base Contents

The data base for the UH-60 consists of time-histories, statistical summaries, harmonics, loads, and narratives. Each of these is discussed below.

Blade and control loads time-histories are stored at the full rate provided by the on-board instrumentation system, but vibration and aircraft-state sensors have been filtered and decimated. The fuselage accelerometers were filtered at 60 Hz, with every other data point eliminated from the stored data base. The aircraft-state time-histories were filtered at 5 Hz, with every other data point eliminated. Time-histories of the engine parameters and many of the derived parameters were not processed in order to minimize data storage requirements.

The statistical data base consists of standard and per-rev calculations. The standard package includes the mean, maximum, minimum, and standard deviation of each sensor for each counter. The per-rev package includes the average vibratory, average steady, 95th-percentile vibratory, maximum vibratory, and steady value at maximum vibratory. The standard package applies the statistical equations to all of the data for each sensor and to each counter. The per-rev package, however, first performs the statistics on the data from each revolution of each sensor in a counter, then averages those results to produce the values for that counter. Detailed definitions of these statistical data are discussed in reference 10.

The first 15 harmonics are computed and stored for a select list of parameters and are then included in the data base, accessible for analysis. The maximum, minimum, and mean for each revolution, computed in the per-rev statistics package, are added to the data base for selected sensors. This information is presented for each counter as a histogram and a revolution history (as opposed to a time-history) plot. The narrative data documents the flights, as to time, place, events, personnel, and test points, and are an integral part of the TRENDS data base.

Data Processing

The data from MRALS followed a circuitous route (fig. 18) from the flight tape to the data base. The first step in the process converted the data from the flight tape into the standard AEFA compressor format. These formatted data were then reprocessed into the TRENDS data format as statistics and time-histories. The on-site engineering evaluation team reviewed all data by using TRENDS, critiquing for data quality and consistency. Assuming that the quality checks demonstrated good data, each test point was evaluated for its premier data. The premier data were defined to be that section of stable data that best matched the desired test condition. This section of the data was called the "time slice." Backup tapes of the statistical files were made for transfer of the data to Ames. The time-history slices were then copied to tape from the AEFA formatted data, for transfer to Ames by using the CUTNSAVE routine.

At Ames, the data-transfer tapes were reprocessed using the FILLER routine to produce TRENDS formatted data for permanent storage. The processing with FILLER at Ames produced statistical files and time-histories from the time-sliced data. Statistical data of the full test points, from the backup tapes produced at AEFA, were included in the data base at Ames also.

A part of the data processing was the manual entry into the data base, through use of the BASKER routine, of the related narrative summaries. The narrative summaries document the flight log, flight descriptions, and maneuver descriptions.

Data Reviews

The data were processed during the conduct of the test so that they could be reviewed for data quality and consistency in near-real time. This included looking for spikes, band edge, time errors, dead transducers, and misscalings. Two special programs were used in evaluating the data processing quality, in addition to TRENDS. To ensure parity, a program called MERGER was used to compare the statistical data in the AEFA format with that in TRENDS. A routine called HAZEL was used to compare the statistical data from the baseline and current flights housekeeping points. The results, although not perfect, are much improved over what they would have been without this effort.

The data review was followed by the selection of the prime data, or time-slice, with reprocessing of those data from the AEFA to TRENDS format for inclusion in the permanent data base at Ames. Each test point consisted of more data than were required for storage in the data base. The purpose of the time-slice was to store only those data that were closest to the desired test condition.

The process of selecting the time-slice involved a routine in TRENDS called Normalize. Select parameter time-histories were plotted which were first subtracted by the statistical average and then divided by a predetermined allowable deviation value. An example is shown in figure 19. The 5 sec of data that appeared to be the steadiest, and within the allowable band of ±1 was selected for inclusion in the final data base. This technique was not used for transient maneuvers, for these test points were self-defining and the data were selected accordingly. The statistical files in the final data base contain two subsets, the full test-point data and the selected prime-data-time-slice statistics. When accessing data in TRENDS, the prime data statistics are the default values.

Data Access

The MRALS data base is resident at the Ames Research Center's computing facility where it is stored on an optical-disk data retrieval system. Access to the data from MRALS is obtained in one of two ways using the two data access programs TRENDS and DATAMAP. The program TRENDS provides access of time-history data to DATAMAP from inside of TRENDS, or the data files can be accessed directly from DATAMAP. The TRENDS program provides access to all of these various data types, whereas DATAMAP only provides access to the time-history data base.

5. DATA SURVEY

This section presents samples of every major instrumentation category for a select subset of test points. The data are presented as statistical plots versus advance ratio, and also as time-history and azimuthal plots. The entire data base resides on the Ames Research Center computing facility. Statistical data sets of select sensors and derived parameters are presented for the level-flight speed sweeps, and for the high-g and dynamic stability maneuvers. Selected time-histories are presented to highlight the specific changes shown in the statistical plots. The cycle-averaged time-history data presented in this report have been averaged over several consecutive rotor revolutions. The consecutive cycles used were those whose control inputs and aircraft states were the closest to steady state of the available time-histories. The data presented in the Speed Sweep subsection have been averaged over 15 consecutive cycles; the data presented in the high-g maneuver section have been averaged over 8 revolutions.

Data Anomalies

In the process of reviewing the data obtained from the Phase 1 flight test, several observations were made regarding data anomalies. All of these anomalies have been removed from the user accessible data base. The anomalies are of the following varieties: excessive spiking; band edge; incorrect scaling bias and scaling factor; pot slippage; static drift; cross-labeling of several parameters; and excessive noise.

Where possible, the encountered spikes have been removed from the data base, using a routine in the TRENDS data maintenance program. The routine takes the two end points that bound the spike and replace the spike with their average.

The data found to contain band-edge have been flagged and removed from the available data base. As a result, for a given flight, certain sensors may not be available for all counters.

During postflight processing, the conversion from PCM counts to engineering units was occasionally

6

assigned the wrong slope or offset. This has been rectified by adjusting the stored bias or scaling factor resident in the data base. The procedure for this is to adjust the bias by the offset found with the R-Cal value for the affected flight, or to adjust the scaling factor by the offset found in the average oscillatory values for the affected flight compared with a comparable test point on one or more unaffected flights. These corrections have been quite rare, occurring only on sensors BE01, BE50, and BN70.

Slippage of the motion pots used on the blade-motion hardware caused errors in the flap, feather, and lead-lag measurements. At present, these have not been corrected, but they have been removed from the accessible data base.

Two aircraft-state variables, roll rate and yaw rate, were found to be cross-labeled, and that problem has been rectified. Aircraft angular accelerometer measurements were excessively noisy during much of the flight program and have been removed from much of the data base. All data that have been found to be excessively noisy have been filtered, where possible, and removed, where filtering was not possible.

The aircraft was instrumented with two tail-rotor torque gauges, for historically this has been a troublesome parameter to maintain, principally because of the high wear rate of the tail-rotor slip rings. On most of the flights, this parameter gave incorrect results. A correlation of these data with previous test data has been performed. Figure 20 presents the composite curve that gives the best estimate of what tail-rotor torque should be for a speed sweep.

Sensor Limitations

Each of the sensors included in MRALS have capability limitations that restrict their application. The more subtle of these will be discussed here. Applicable dimensions are provided in appendix A.

The LASSIE low-airspeed data system (VX03, VY03, VZ03) measures the longitudinal, lateral, and vertical velocity of the air mass under the rotor. It was calibrated in the low-speed flight regime only, out to 50 knots. Any attempt to use this sensor in any other flight regime will yield incorrect results. In addition, the data stored in the data base are the raw values, not the calibrated values. The calibrations were used in the computation of the true airspeed (VTRU) only.

The aircraft-state measurements relative to the center of gravity (c.g.) were, of necessity, not measured at the c.g. Their exact locations are given in appendix A. These measurements must be adjusted when used in analysis, in order to compensate for the physical offset.

The aircraft angle of attack and sideslip vanes measure the local angles, not the angles at the c.g. Hence, they include moment-arm components that arise as a result of

pitch and yaw rates. The physical dimensions of the instrumentation boom sensors are given in appendix A. These measurements must be adjusted when used in analysis to compensate for the unwanted additional components.

Speed Sweep

Figures 21 through 28 present the statistical mean values of control positions, main-rotor torque, coefficients of thrust and power, and advancing-tip Mach number for all test points of the speed-sweep subset, at all three aircraft gross weight configurations. These plots present the effects of the gross weight change and the consistency of the test points. Figures 29 through 38 present aircraft-state data taken at $C_T/\sigma = 0.09$ only. Figures 39 through 47 present blade, control, and pitch-link loads. They each consist of two plots: the top one presents the mean value and the bottom one presents the average oscillatory values. The figures presenting statistical values are followed by figures of time-history data. Figures 48 through 51 present normal blade bending at 50, 60, and 70% radius, and push-rod load versus rotor azimuth, respectively. A list of advance ratio, angle of attack, angle of side slip, and engine torque for these counters is presented in table 14. Figures 52 through 55 present the average oscillatory values of the vertical accelerometers at the pilots seat, main-rotor hub, vertical tail, and right aft cabin, locations. Figures 56 and 57 present the vertical and lateral accelerometer average oscillatory data for the right forward cabin station.

High-g Turn

Maneuver data were recorded with the aircraft ballasted for $C_T/\sigma = 0.09$ and 0.10 in level flight at the test pressure altitude of 9,000 ft. This section presents data of selected sensors from the 0.09 C_T/σ configured aircraft. Figures 58 through 60 present summary plots of advance ratio versus aircraft normal loading, pitch attitude versus bank angle, and aircraft normal loading versus bank angle, respectively. Figures 61 through 80 present plots of statistical mean and vibratory versus advance ratio of the high-speed maneuver points. Each plot contains the relevant level flight loads and loads obtained in both left and right turns at the indicated g loading. The values presented here are not the statistical values resident on the data base at Ames. The exact test condition of interest lasted only several seconds; however, the stored statistics in the data base are for the entire stored time-slice of up to 10 sec. The events preceding and following the desired condition have been retained in the stored time-histories, in order to give the researcher the best understanding of the exact state of the aircraft during the

maneuver. The statistics presented here have been computed from the stored time-histories and represent that 2-sec-time period when the aircraft was nearest the specified condition and was steady. The time-intervals used are included in table 15. Time-history plots of selected sensors are presented in figures 81 through 85. The time-histories are plotted versus rotor azimuth as discussed above.

Doublet

For this report, two examples of the aircraft's response to doublet inputs are presented: a 60-knot (calibrated) longitudinal doublet and a 140-knot (calibrated) directional doublet. The trim conditions for each of the doublet maneuvers are shown in table 16. Time-histories of the aircraft's control positions, attitudes, rates, and accelerations are shown in figures 86 through 90 for the longitudinal doublet and in figures 91 through 95 for the directional doublet.

6. INVESTIGATIONS

This section discusses various phenomena observed in the data survey just presented. A summary discussion of a gust-alleviation study known as individual blade control (IBC) is also presented. The following discussions will often refer to the figures presented in the preceding section.

Performance and High-Speed Limits

One of the principal interests in conducting this test was that of the power train and structural limits encountered in high-speed flight. The particular structural limits of interest are the rotor-control and blade loads. The data presented in figures 24, 25, 28, 37, and 38, in section 5, show the increase in the power train loads as speed is increased. The component limit is defined for this test as that speed at which the slope of the curve increases. The particular curve of interest, that is, average or oscillatory, depends on the sensor. The oscillatory curve is used to define the limit for structural hardware, such as rotor-control loads. The average curve is used for power train components. This definition of the term "limit" does not involve component life, as is usually the case.

The data presented in section 5 (figs. 39 through 47) show the increase in these loads as speed is increased, for $C_T/\sigma = 0.09$. Figure 39 shows pitch-link load, both average and oscillatory, versus advance ratio (μ). The mean loading is bell-shaped, with the peak occurring around $\mu = 0.18$. The high-speed end, 0.35 and greater, is

relatively flat and, not coincidentally, that portion of the speed sweep conducted in a powered descent. The V_h for this data set resulted in an advance ratio of 0.38.

The plot of average oscillatory load is characterized by a slight positive slope out to $\mu = 0.3$ where the curve slope increases sharply. The curve flattens out slightly just past the point of maximum level flight, where the aircraft began its powered descent. The curve then increases in slope to a value greater than that before the aircraft began its powered descent.

The corresponding time-history plots for pitch-link load are presented in figure 51. The plots are presented with rotor azimuth on the abscissa and with a conventional orientation of zero over the tail boom. Each plot can be divided into the following four quadrants: first, 0° - 90°; second, 90° - 180°; third, 180° - 270°; fourth, 270° - 360°. The statistical summary data for the counters present in these time-history plots are listed in table 14.

The loads approach zero at 60° and 150° azimuth, and reach a maximum negative value at 215° and 300° azimuth at an advance ratio of 0.096 (counter 1708). The negative peak is in the fourth quadrant and just exceeds 1,000 ft·lb. The smallest values at this speed are approximately one tenth the peak value.

As the speed increases to an advance ratio of 0.197 (counter 1704), the zero approach in the first quadrant has become a slightly positive peak and has moved from 60° to 45°. The zero approach at 150° has disappeared altogether. The negative peak at 215° has increased in value and shifted to 200°. The second negative peak has decreased in magnitude but has not shifted azimuthally.

At an advance ratio of 0.314 (counter 1717), the first quadrant positive peak has moved from 45° to 35° with no increase in value, and the negative peak at 200° has moved to 160° with a nearly 50% increase in value. The negative peak in the fourth quadrant has shifted to the third quadrant, to 255°, and has increased to more than its original value at the slowest speed presented.

At an advance ratio of 0.395 (counter 3016), the amplitudes have continued to increase and the peaks have continued to shift. The positive peak in the first azimuthal quadrant has continued its shift to 20°. The large negative peak in the second quadrant has continued to grow in magnitude and has rotated to 150°. The negative peak in the third quadrant has narrowed, but otherwise remains much the same. A new positive peak is now present at 300° in the azimuthal location of the largest negative peak at 0.096μ.

The highest speed presented here, 0.460μ (counter 3011), has several new peaks that were not previously apparent, most notably at 90° and 240°. The first is a negative peak, and the second is a positive peak. Of the peaks that carry over from the lower airspeeds, only the ones in the second and fourth quadrants have

significantly changed. The second-quadrant peak has increased by about 30% and has reversed its trend in azimuthal shift from 150° to 175°. The fourth-quadrant peak is now the largest positive peak, 800 ft·lb, with minimal azimuthal shift encountered.

The counter listed in table 14 are shown in the frequency domain rather than in the time domain in figures 96 through 100. The results show that only for the low-speed and the very-high-speed cases is there a large 4/rev content to the signal. The other flight conditions result in the 4/rev content being the third most prominent component, always slightly greater than the 3/rev.

The phase relationship of the frequency content of the 4/rev is shown in figure 101, as phase angle versus advance ratio. The phase angle is defined here as the azimuthal delta between pitch-link load peak values found from using a bandpass filter to isolate the 4/rev content of the data in figure 51. The symbols denote the load peak of azimuthal quadrant pairs, for example, the difference between the load peak in the first and second quadrants. It can be seen that the phases of just over half of the quadrant pairs are nominally 90°, the rest being nearly 10° either side of 90°.

The phase relationships of the 4/rev to the 1/rev component as functions of airspeed are presented in table 17. The information presented here has been nondimentionalized to a percentage of a complete cycle where a 1/rev cycle is referenced to 4.300 Hz, and a 4/rev cycle is referenced to 17.200 Hz. The columns are the difference, in percent of a cycle, that exists between the slowest-speed counter and the four higher-speed counters. The 1/rev is relative to the negative peak at 260°, and the 4/rev is relative to the negative peak at 208°. The results show that the speed increase results in an increase in phase shift of both the 1/rev and 4/rev signals. The negative sign indicates that the pulses are occurring earlier in the cycle as the speed increases. The amount of phase increase of the 4/rev over the 1/rev is significant.

The most obvious source of the 4/rev loading is the swash plate transmitting load from the other three blades to the pitch link of the fourth blade. If this were the source of the 4/rev loading, the phase angle at all airspeeds would be expected to be 90°, because the swash-plate-to-blade physical relationship is fixed. However, as figure 101 shows, the phase angle is near 90° in only half of the incidences, and the remaining are nearly 10° out of phase. It would be assumed that the phase shift due to airspeed is constant between blades. Therefore, the summed loads from the four blades that are seen by the pitch link, should shift in phase like those of the single blade. However, as seen in table 17, this is not so. There is no obvious correlation between the 4/rev and 1/rev components of the pitch-link load.

The non-orthogonal alignment of phase angles between the 4/rev peaks, as well as the inconsistent phase shift with airspeed between the 1/rev and 4/rev signal components, casts doubt on the other blades as the source of the higher harmonic loading. This leaves aerodynamic loading as the next logical candidate. However, this requires a more detailed analysis than can be presented here, and is left for a separate in-depth study.

Maneuvering Limits

Figure 59 shows that the aircraft pitch attitude required to perform the turns to the right was consistently more nose-down than for the turns to the left. With the exceptions discussed below, there is no conclusive indication that the direction of the turn results in higher or lower structural loads. The effect of building load factor by performing wind-up turns to the left versus to the right can be observed in figures 61 through 80. The following sensors do show indications of higher loads: blade normal bending at 0.70 r/R (BN70) vibratory; pitch-link load (BP00) average; and forward stationary control load (MR00) average. The increase in loads occurs at 1.9 g for all sensors, except MR00, where it occurs at all but 1.3 g. It is not certain how much of the load increase is due to the direction of the turn and how much to the increased nose-down pitch attitude.

The data from the maneuvering flights presented in section 5 is reformatted in figures 102 through 106. Each figure consists of both averaged value and vibratory, plotted against advance ratio. Each plot contains families of curves grouped by load factor. Each family is denoted by a symbol and a curve. The curves have no rigorous mathematical basis; rather they are only an aid in visualizing the trends present in the data. The symbol labels represent the approximate mean load factor, and are rounded off, more to ensure an even increment than to accurately depict the load-factor distribution. There is much data scatter in this data set, a result in part to the complexity of achieving the test points, and in part to the categorization of the data points for presentation purposes.

The effect of increasing load factor on the averaged normal blade bending (BN70) is greater than the effect of increasing advance ratio, as shown in figure 102. The same is not the case for the vibratory normal blade bending, however, since the response to both load factor and speed is relatively linear. The result is that the vibratory response of the rotor in level flight at an advance ratio of 0.45 is equivalent to sustaining 1.9 g at an advance ratio at 0.375, whereas the steady response at these two flight conditions results in an increase of 200 ft·lb.

The effect of load factor versus speed on the averaged and vibratory pitch-link load (BP00) is that the load factor is an order of magnitude more sensitive (fig. 103). The

vibratory response to airspeed increase appears to be reasonably linear, whereas the average value seems to reach a maximum and then decrease as speed increases. There is little effect on the vibratory response between level flight and 1.3 g until speed increases past an advance ratio of 0.4. The average value response to load-factor increase from 1 to 1.3 g is significantly less sensitive than the corresponding increase from 1.3 to 1.5 g. There is a significant increase in load at both 1.5 and 1.7 g at an advance ratio of 0.375, which effects both the average and the vibratory. This effect is prominent in all sensors presented, with the exception of the normal blade load at 70% radius. The ramifications of this observation are not yet fully understood.

The main-rotor stationary forward control load (MR00) is, like the pitch-link load, more sensitive to load factor than to airspeed in both its average and vibratory (fig. 104). The average value increases in sensitivity to load factor with increased airspeed, and the sensitivity to load factor decreases with airspeed for the vibratory. This component, as with the pitch-link load, is not sensitive to load factor from 1.0 to 1.3 g. Sensitivity increases markedly as the g-level increases past 1.3.

The main-rotor stationary lateral control load (MR01) is more sensitive to load factor than to airspeed in both vibratory and average value (fig. 105). The average decreases as the load factor increases, changing to a positive value at 1.9 g. The sensitivity of vibratory levels to load factor decreases with speed increase.

The main-rotor stationary aft control load (MR03) is more sensitive to load factor than to airspeed only for the average value, as shown by figure 106. The vibratory level is more balanced between load factor and speed. The response to the high-g condition, with the exception of $\mu = 0.42$, is insensitive to speed. The effect of load factor is minimal from 1 to 1.3 g for the vibratory, although this is not so for the average value.

The vibratory curve of MR01 in level flight is flat out to $\mu = 0.4$, where the slope increases markedly. The load-limit slope change for MR03 also occurs near $\mu = 0.4$, whereas the limit for MR00 appears to be delayed until near $\mu = 0.42$. The remaining sensors presented display no such apparent slope change.

Vibration

The sample of data presented in figures 52 through 57 contains average vibratory levels for pilot floor, right-forward and aft-cabin floor, vertical tail and main-rotor hub vertical sensors, and the right-forward cabin lateral sensor. The data include steady-state dives and climbs at constant power, and show several trends that are of interest. The first is as expected; vibratory load increases exponentially with airspeed. These loads are thought to be

caused by the rotor high-speed phenomena of compressibility and dynamic stall. The increase in vibratory load at the transitional advance ratios of 0.05 to 0.15 are also seen in the data. This is caused by rotor-wake interference. The data from the climbs and dives generally fall on top of the level-flight data. This indicates that the angle of attack of the aircraft has a small influence on vibration levels. Finally, near hover the data show a fair amount of scatter. The reason for this phenomenon, discussed further later in this section, is unknown at this time.

A harmonic analysis was also performed and saved in the data base for the 18 accelerometers. Harmonic data are useful in helping to identify sources of vibratory excitation. Figures 107 through 114 show a few examples of this type of data. The data include the 4th, 8th, and 12th harmonics plotted versus advance ratio for the pilot floor, vertical tail, right-forward cabin floor, and the vertical hub accelerometers. The three fuselage accelerometer plots show increasing vibratory levels for all harmonics with increasing advance ratio. However, the 4/rev harmonic of the main-rotor hub is at a minimum at these advance ratios. This points to a different source of vibratory excitation for the 4/rev component of the main-rotor hub than for the fuselage. It is also interesting to note that the two vibratory levels at the low advance ratios (near hover) mentioned above, are also visible in the 4/rev harmonic content of all the accelerometers presented here. These data suggest that the different vibratory levels at the low advance ratios are related to a 4/rev phenomenon.

Dynamic Stability

The dynamic stability tests were conducted to obtain high-quality flight-test data that could be used for simulation validation, preliminary control-system design, and parameter identification of six-degree-of-freedom (DOF) rigid-body dynamics. The input profile selected for these tests was the doublet, as described in section 3. The doublet profile was chosen to excite the high-frequency (short-period) dynamics of the helicopter, while maintaining a reasonable range of aircraft body attitudes. Limiting the aircraft excursions from trim allows the use of linear analysis techniques with reasonable confidence. It also reduced the risk of an unscheduled "E-Ticket" ride.

As seen in figures 88(a) and 88(b) the helicopter change in attitude caused by the 60-knot longitudinal doublet was less than ±2° in all axes, followed by divergence. The divergence initially began in pitch and was followed immediately by roll and yaw axes divergence. This divergence was undoubtedly caused by the phugoid mode, which is unstable at these flight conditions for the unaugmented UH-60 helicopter.

For the 140-knot pedal doublet, the deviations from trim attitude caused by the input were less than ±10° in all

axes, as shown in figures 93(a) and 93(b). Although there were initially much greater forces and displacements at 140 knots than at 60 knots, the aircraft diverged more slowly because the phugoid mode is much less unstable at the higher airspeed.

Another rigid-body mode is readily observed in the yaw-rate response to the pedal doublet shown in figure 94(b). The mode evident is clearly the Dutch roll mode and is stable. Analysis of the yaw-rate response provides a rough estimate of the Dutch roll mode characteristics. The mode is described approximately by the roots $\Phi = -0.20$ sec $\pm$ 1.63i rad/sec ($\omega_n = 1.64$ rad/sec, $\zeta = 0.122$). A perturbation analysis was performed, prior to the flight testing, using the Gen Hel Simulation program (ref. 11), for purposes of comparison. This lateral decoupled solution predicted a Dutch roll root of $\Phi = -0.22$ sec $\pm$ 1.47i rad/sec ($\omega_n = 1.49$ rad/sec, $\zeta = 0.148$), which agrees very well with that estimated from the flight-test data.

To investigate the consistency of the flight-test data, comparisons were made of attitudes and rates. The two types of comparisons that were made are shown in figure 115 for the 60-knot longitudinal doublet and in figure 116 for the 140-knot pedal doublet. Figure 115(a) shows the time-derivative of the measured pitch attitude ($d\theta/dt$) compared with the estimated $d\theta/dt$ based on other flight-test measurements and calculated from the Euler rate equation:

$$d\theta/dt = q \cos \phi - r \sin \phi$$

where q and r are the angular body rates in pitch and yaw, respectively, and ϕ is the instantaneous aircraft roll attitude. The two curves show excellent agreement, with a very slight amount of bias evident between the two curves.

The comparison of "measured" and estimated $d\phi/dt$ is shown in figure 115(b), with the estimated value calculated from

$$d\phi/dt = p + \tan \theta(r \cos \phi + q \sin \phi)$$

where p is the roll rate. The two curves are virtually identical, with no apparent phase or magnitude shift. Figure 116(b) shows the same comparison for the pedal input, and a similar correlation is evident.

Figure 116(a) shows the comparison of measured and estimated $d\psi/dt$ with the estimated value calculated from

$$d\psi/dt = \sec \theta(r \cos \phi + q \sin \phi)$$

where ψ is the aircraft heading angle. Again, it is seen that the two responses exhibit nearly identical behavior.

Although these curves demonstrate that the aircraft attitudes and body rates are all consistent, they do not form the basis of an exhaustive effort to determine all scale and bias errors present in the flight-test data. It is recommended that these data be more closely examined

using state-estimation techniques, or other kinematic analysis tools prior to detailed dynamic investigations.

Individual Blade Control

The individual blade control (IBC) investigation was conducted as part of a cooperative agreement with the Massachusetts Institute of Technology. This section will give a basic description of the IBC concept and sample results obtained from this flight test. A more complete analysis and description of this investigation may be found in reference 12.

In a true IBC scheme, each blade would be controlled independently through use of individual, high-bandwidth actuators located in the rotating system. The controller would consist of several subsystems and be designed in a modal fashion where each subsystem would be fine-tuned to a particular frequency application. The controller would use feedback signals from sensors mounted on each blade to determine the required control inputs. The true IBC system is therefore very flexible, and allows the control of dynamic phenomena that occur at any frequency, regardless of the rotor rotational speed.

However, it is also possible to use a conventional swashplate to control certain multiples of the rotor frequency. In a four-bladed rotor system, for example, the 0P to 1P and 3P to 5P harmonics can be controlled using a swashplate, thus allowing a type of "pseudo" individual blade control. This pseudo IBC can then be used to control many of the undesirable dynamic effects inherent to a four-bladed helicopter, since they occur at the rotor harmonics listed above. Examples of these undesirable effects include gust response (0P to 1P) and vibration (1P and 4P). The IBC investigation is presently focused on the low-frequency gust alleviation system. This system would require feedback of the 1P blade flapping acceleration, rate, and displacement, and a controller optimized for the 0P to 1P range.

The purpose of this flight test was simply to demonstrate that blade-mounted sensors (accelerometers) could potentially provide accurate feedback signals to a controller. This flight test was entirely an open-loop experiment, with no controller or control-system interface installed on the aircraft.

Two miniature accelerometers were placed on the instrumented Night Hawk rotor blade as shown in figure 117. The design range of the root accelerometer was ± 5 g and the range of the tip accelerometer was ± 250 g. The accelerometers were mounted along the blade feathering axis, with their sensitive axis approximately parallel to the main-rotor shaft. To account for blade-pitch changes, the accelerometers were mounted on the blade at an angle that would represent an average collective position in flight.

11

Figures 118 and 119 show the time-history and frequency response of the root and tip accelerometers at 80 knots. The root accelerometer displays more high-frequency content than the tip accelerometer. This is likely a result of the combination of a more sensitive instrument (15 mV/g at the root vs 1 mV/g at the tip), and much lower overall acceleration levels at the root.

In order to use these accelerations as feedback signals to a gust-alleviation controller, the flapping position and acceleration (β and β'') must be determined. The most elementary model of blade motion assumes a totally rigid blade. Only steady and 1P rigid-flapping motion remain in this simple approach; β'' and β may then be easily calculated using the blade accelerometer information by

$$\beta'' = [r_r a_t - a_r r_t] / [e(r_t - r_r)]$$

$$\beta = [(e - r_r)a_t - (e - r_t)a_r] / (\Omega^2 e(r_t - r_r))$$

where

a_r root acceleration

a_t tip acceleration

r_r radial location of root accelerometer

r_t radial location of tip accelerometer

e blade-hinge offset

The blade accelerations must be filtered to the frequency range of interest, which in this case is approximately 1P (4.3 Hz) before they can be used. Figure 120 shows the relative root- and tip-accelerometer response at 80 knots for an average of four rotor revolutions. These data were processed with a 5-Hz convolution filter. Comparison of the accelerometer responses reveals that there is a significant phase difference between the root and the tip signals. The tip response apparently leads the root response by approximately 42° of rotor azimuth at the 80-knot flight condition. Analysis of other flight conditions shows that various degrees of phase shift exist at all airspeeds and rotor loadings. Figure 121 shows the blade flapping based on the accelerometer measurements, including the phase shift.

The existence of the phase difference between the root and tip accelerations is not completely unexpected when one considers that the blade is not rigid and that it behaves elastically in flight. However, this phase difference does cause a problem when computing β and β'' from the simple equations above, which do not consider any elastic motion. The two accelerometer signals would have to be phase-aligned in order to correctly calculate β and β'' for the rigid-flapping case. However, shifting the phase of the signals will complicate any controller design. Since the phase differences are not constant with airspeed, additional inputs to the controller are required, and gains must be scheduled for airspeed.

A possible alternative to the current root-tip sensor locations, which may help reduce the phase-shift problem caused by blade bending, would be to move the tip accelerometer inboard. By placing the two accelerometers close together and near the root of the blade, bending effects would be greatly reduced, and the subsequent phase problem would be eliminated. However, this arrangement would only work for rigid-flapping estimates used in gust alleviation or handling-qualities-type improvements. Any consideration of vibration reduction would require a minimum of four sensors at various radial locations in order to estimate the first flatwise bending mode.

Another major problem is the rigid-blade model itself. A completely rigid-blade model is far too restricting, and does not physically represent the blade dynamics in flight. It is, therefore, recommended that to more accurately model the flapping motion, at least the first elastic bending mode be considered in the blade dynamics.

Blade-Shake Test

A part of the UH-60 phase 1 test documentation includes a modal analysis shake test, preformed during the summer of 1986, of the Night Hawk instrumented blade. The shake test was conducted to accurately document the dynamic characteristics of the instrumented blade. The results have been compared with the blade as modeled for the prediction codes that are used in correlation studies with the flight-test data. The blade-shake test was conducted to simulate a free-free boundary condition. This was accomplished by suspending the blade vertically from the root end by means of bungee chords. A shaker attached to the blade by a thin stinger at the blade root was anchored to the support structure.

The results of the test are reported in reference 5; they include the frequencies, damping, and mode shapes of the first five flapping modes, two chordwise modes, and two torsion modes. Table 18 shows the frequencies and damping measured during the test. Figure 122 presents the first and second flapwise mode shapes obtained from the test.

Low-Speed Data Scatter

A recurrent feature found in nearly all of the speed sweep plots, figures 21 through 47, is a split in the data at the low-speed end. This split is present in all three C_T/σ data sets and has been a subject of much study during the data evaluation phase of this program. Figure 123 presents pitch-link load time-history data plotted versus main-rotor azimuth, with data from both sides of the data split. It is readily seen that the wave forms of the two subsets are

distinctly different, the frequency content is different, and there appears to be a phase shift as well. Select statistical aircraft-state values for these counters are presented in table 19. There has been no acceptable physical explanation for this occurrence, and no evidence has been found to indicate a malfunction of the instrumentation system. Because the data cannot be discounted, they have been retained in the data base, and provide an interesting area for further study.

7. PREDICTIONS

One of the primary purposes of MRALS was to obtain quality data for use in correlating with predictions from several comprehensive analytical computer codes, notably the Comprehensive Analytical Modeling of Rotorcraft Aerodynamics and Dynamics (CAMRAD) (refs. 13 and 14) and C-81 (refs. 15 and 16). NASA also has a modified analysis code originally developed by Sikorsky Aircraft called Gen Hel (ref. 11), for which a Black Hawk model is available.

A workshop with industry participation was conducted for the purpose of introducing the MRALS data base. As a part of the workshop, manufacturers were contracted to predict pitch-link loads using prediction tools of their choice for comparison with the high-speed test points. Predictions were also made by NASA using CAMRAD. The results of the prediction efforts are presented in figure 124. With the exception of company No. 2, the results were not especially accurate. It should be noted that the test points being modeled are high speed, and were obtained in a dive. This introduces many variables, which, if improperly accounted for, could adversely affect the correlation.

An inhouse correlation study of CAMRAD and the MRALS data has been undertaken (ref. 17). The effort focuses on structural blade loads; an example of the results is presented in figure 125.

8. CONCLUDING REMARKS

It is the intent of this report that it serve not only as a data survey, but also as the reference source for all matters relating to the Modern Rotor Aerodynamic Limits Survey (MRALS). As such, in addition to the presentation of sample data, this report contains detailed descriptions of the instrumentation, test hardware, and test procedures used during the test, as well as brief descriptions of the pertinent data formats and data analysis tools. Six

appendixes have been included in the report so as to complete the documentation on the first test phase.

The sample data presented here include examples of all the various sensor types for a speed-sweep from hover to V_{ne} at a C_T/σ of 0.09. The data are presented as plots of statistical averages versus advance ratio, and azimuthal and time-history plots. The data base has been rigorously reviewed for errors, and all detected errors have been removed. The data have been reviewed from the perspective of various technical disciplines, including dynamic stability, vibration, and maneuver and high-speed loads. The more prominent aerodynamic and dynamic phenomena found in the data have been discussed. In addition, a gust-alleviation concept, individual blade control, was reviewed, and the details of a blade-shake test are summarized.

The data base currently resides on the Ames Research Center computer complex. Access to the data can be obtained in many ways. Among them are interactive use of either TRENDS or DATAMAP on the host computer through a remote modem, transfer of selected data subsets in the TRENDS format via digital tape, or transfer of digital tapes containing harmonic tables stored in a NASA-specified format.

The data obtained from MRALS are currently being used in correlation studies with several comprehensive rotorcraft codes, including CAMRAD, C-81, Gen Hel, and CAMRAD/JA. An industry/academia/government workshop was held in June 1988 to introduce the data base to potential users. The workshop involved hands-on sessions with TRENDS and DATAMAP, a review of industry predictions of pitch-link loads, and a review of the flight-test program.

This first phase is the beginning of a comprehensive program to document the physical, aerodynamic, and dynamic characteristics of the UH-60. It is to be followed by a second phase which includes extensive airloads, much more thorough blade loads, blade vibration, hub impedance, control loads, and a more thorough fuselage vibration survey. A third phase is planned for an entry into the National Fullscale Aerodynamic Complex (NFAC), that will complement the flight data with tunnel testing. A rigorous fuselage-shake test of the flight vehicle is planned to follow the specific in-flight vibration test matrix. The goal of the program is to provide a single complete, accurate, documented data base for use in understanding basic helicopter phenomena, and for correlation efforts with advanced predictive codes.

APPENDIX A. UH-60A AIRCRAFT DESCRIPTION

The dimensions and pertinent characteristics of the Black Hawk test aircraft are presented here. The information is organized by airframe, vehicle weight, main rotor, tail rotor, rotor speeds, gear ratios, and engine data. In addition, the rigging information for both the main and tail rotors, and rotor azimuth references are presented. The aircraft stations, waterlines, and butt lines are presented, as are the main and tail rotor azimuthal orientations relative to the position sensors.

Airframe

Length
    Maximum (rotor blades turning)   64 ft, 10 in.
    Fuselage (nose to vertical tail)   50 ft, 0.75 in.
    Main-rotor to tail-rotor clearance   2.8 in.

Width
    Main-rotor blades turning   53 ft, 8 in.
    Main landing gear   9 ft, 8 in.

Height
    Maximum (tail-rotor blades turning)   16 ft, 10 in.
    Main-rotor ground clearance (rotor stopped)   7 ft, 14 in.

Approximate moments of inertia
    $I_{xx} = 4659$ slug·ft^2
    $I_{yy} = 38,512$ slug·ft^2
    $I_{zz} = 36,796$ slug·ft^2
    $I_{xz} = 1882$ slug·ft^2

Horizontal stabilator
    Span   172.6 in.
    Root chord   44.0 in.
    Tip chord   30.5 in.
    Aspect ratio   4.6
    Airfoil section   NACA 0014
    Sweep at quarter chord   0°
    Dihedral   0°
    Incidence travel (relative to WL) $-38° \pm 4°$ to $8° \pm 2°$
    Taper ratio   1.87
    Area (total)   45.0 ft^2

Vertical tail
    Span   8 ft, 2 in.
    Aspect ratio   1.92
    Taper ratio   1.623
    Sweep at quarter chord   41°
    Airfoil section   NACA 0021 to 65% span, 7° trailing edge camber on lower section
    Incidence angle (relative to BL)   0°
    Area (total)   32.3 ft^2

Gross weight	
Maximum alternate	20,250 lb
Empty weight	10,750 lb
Primary mission	16,455 lb
Fuel capacity	364 gal
Control stick ranges	
Longitudinal	0 - 10.0 in.
Lateral	0 - 10.0 in.
Collective	0 - 10.0 in.
Pedal	0 - 4.92 in.

Rotors

Main rotor	
Number of blades	4
Diameter	53 ft, 8 in.
Main-rotor location	341.2 FS 0.0 BL 315.0 WL, in.
Blade chord	1.73 ft/1.75 ft
Blade twist (equivalent linear)	$-18°$
Blade-tip sweep	20°
Tip sweep point	0.9286r/R
Blade area (one blade)	46.7 ft^2
Geometric disk area (total)	2262 ft^2
Geometric solidity ratio	0.0826
Airfoil section distribution (SC1095)	0.1304r/R–0.4658r/R
Airfoil section distribution (SC1095R8)	0.4969r/R–0.8230r/R
Airfoil section distribution (SC1095)	0.8540r/R–1.0000r/R
Thickness	9.5 %
Main-rotor mast tilt (forward)	3°
Blade aspect ratio	15.4
Flapping range	$-6°$ to 25°
Blade static droop stop	$-0.5°$
Blade flight droop stop	$-6°$
Hub precone	8°
Hub prelag	7°
Tail rotor	
Number of blades	4
Diameter	11 ft
Tail-rotor location	732.0 in. FS, 14.0 in. BL, 324.0 in. WL
Blade chord	0.81 ft
Blade twist (equivalent linear)	$-18°$
Blade area (one blade)	4.46 ft^2
Geometric disk area (total)	95 ft^2
Geometric solidity ratio	0.1875
Airfoil section	SC1095
Thickness	9.5 %
Aspect ratio	6.79
Cant angle (from vertical)	20°

Rotors (continued)

Rotor speeds

Main rotor rpm	Power on	Power off
Minimum	234.7	232.1
Normal	245.0 to 260.5	232.1 to 270.8
Maximum	275.9	283.7
Design	257.8	—

Tail rotor rpm	Power on	Power off
Minimum	1082.7	1070.8
Normal	1130.3 to 1201.7	1070.8 to 1249.3
Maximum	1273.1	1308.8
Design	1189.8	—

Gear ratios	Input rpm	I/O ratio
Main transmission		
Input bevel	29,900.0	3.6364
Main bevel	5747.5	4.7647
Planetary	1206.3	4.6774
Tail takeoff	1206.3	0.2931
Generator acces.	5747.5	0.4868
Hydraulics acces.	11,805.7	1.6429
Intermediate gearbox	4115.5	1.2400
Tail gearbox	3318.9	2.7895
Engine to MR	20,900.0	81.0419
Engine to TR	20,900.0	17.5658
TR to MR	1189.8	4.6136

Rotational speeds at 100%	rpm
Main rotor (NR)	257.89
Power Turbine (NP)	20,900
Gas Producer (NG)	44,700

Engine description

Model	T700-GE-700
Rated power	1553 shp sls at 100%
Compressor	5 axial stages, 1 centrifugal
Combustion chamber	Single annular chamber, axial flow
Gas generator stages	2
Power turbine stages	2
Weight (dry)	415 lb
Length	47 in.
Maximum diameter	25 in.
Engine rotation	Clockwise (aft looking fwd)
Fuel	JP-4 or 5

Instrumentation locations

Sensor	FS, inches	BL, inches	WL, inches
Alpha vane	116.5	19.7	208.0
Beta vane	112.0	25.7	214.0
LASSIE	248.0	73.0	270.0
Boom airspeed	97.0	25.7	208.0
Pitch attitude	389.25	219.45	-3.69
Roll attitude	389.25	219.45	-3.69
Heading	388.0	222.58	+4.0
Pitch accelerometer	390.25	215.7	+8.75
Roll accelerometer	396.0	224.83	+5.5
Yaw accelerometer	393.69	218.45	0.0
Pitch rate	393.38	218.45	+6.0
Roll rate	393.38	218.45	+6.0
Yaw rate	393.38	218.45	+6.0
CG vertical accelerometer	396.12	231.45	+6.88
CG longitudinal accelerometer	396.12	233.2	+5.25
CG lateral accelerometer	395.62	231.45	+5.0
A/C CG	361.0	251.0	0.0

Main-rotor rigging

Flight control position				Swashplate tilt		Collective blade pitch at root
Coll	Long	Lat	Pedal	Long	Lat	
Low	*	*	*	-8.7	-2.1	9.6
High	*	*	*	-4.2	-3.3	24.3
Low	Aft	Lt	*	-9.4	-7.4	8.8
High	Aft	Lt	*	-9.2	-7.6	24.0
Low	Fwd	Rt	*	11.0	7.2	9.3
High	Fwd	Rt	*	17.3	6.5	23.4
High	Aft	Lt	Lt	-11.3	-7.7	23.6
Mid	Aft	Lt	*	-11.7	-7.5	16.6
Mid	Fwd	Rt	*	15.6	6.2	15.5
Mid	*	*	*	-7.4	-2.6	17.0

Notes: *Indicates the control was pinned at a rigged position. The blade collective position was the average of all four blades. All numbers in degrees.

Tail-rotor rigging

Flight control position		Tail-rotor collective blade
Collective	Pedal	Pitch at the root
Mid	Lt	−23.3
Mid	Rt	7.5
Mid	Mid	−7.7
Low	Mid	−0.1
High	Mid	−16.2
High	Lt	−23.8
High	Rt	−1.8
Low	Rt	6.3
Low	Lt	−15.7
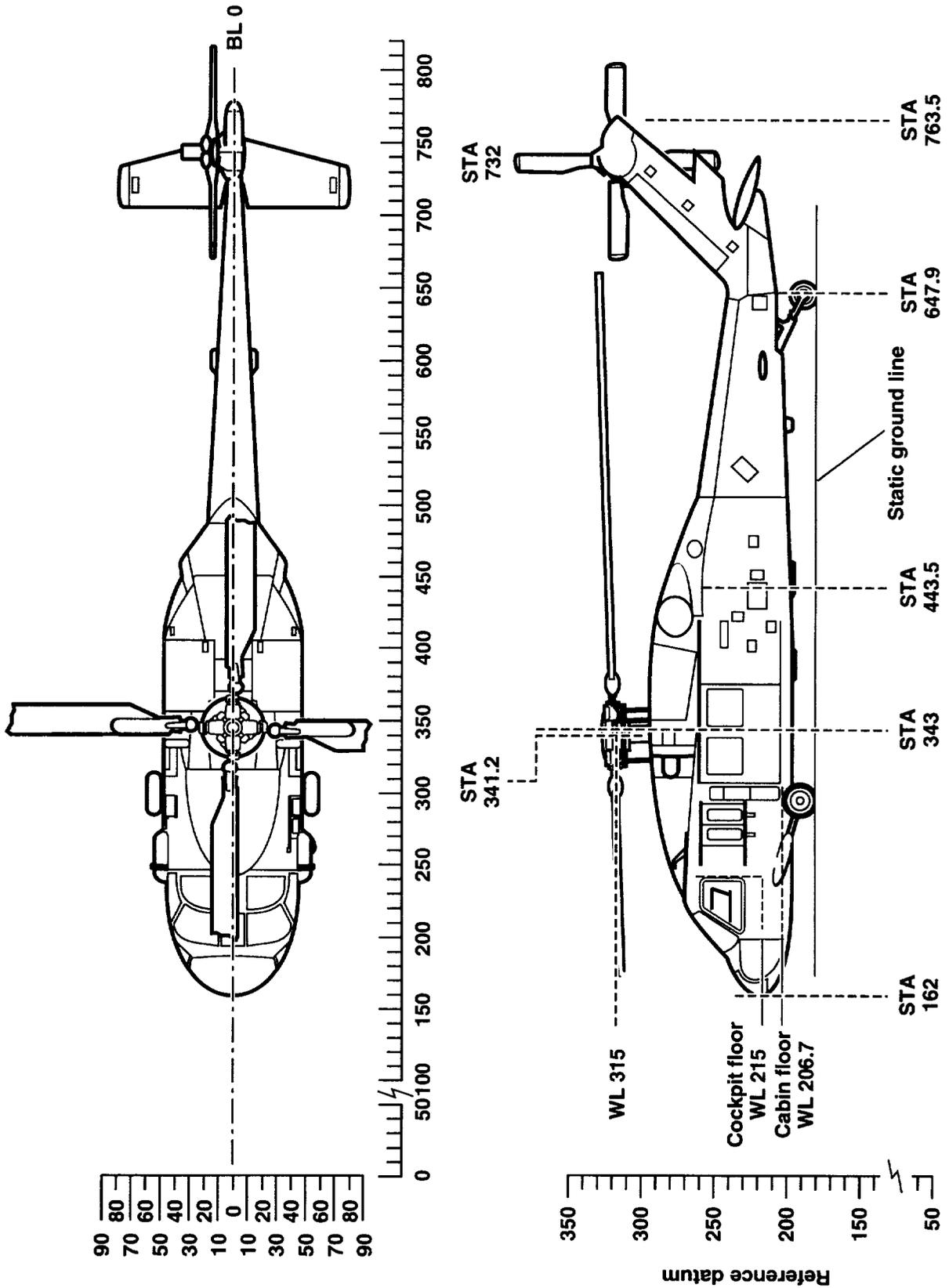
Figure A1. UH-60A aircraft stations (STA), waterlines (WL), and butt line (BL).

20

RED

180°

BLU

BLK

YEL

**Direction of
rotation**

**Rigging mark on
stationary swashplate**

7° 22'

**Direction of
rotation**

YEL   BLU

5° 4"

BLK   RED

**Level with respect
to main transmission**
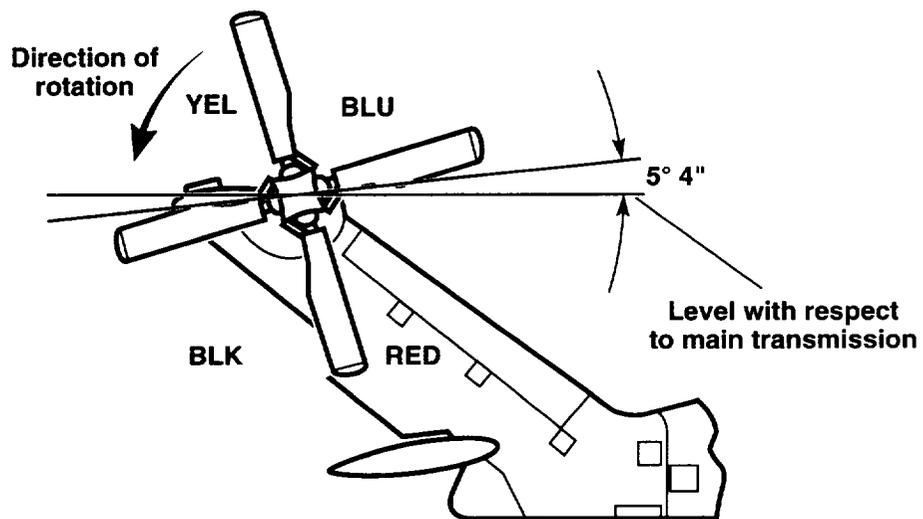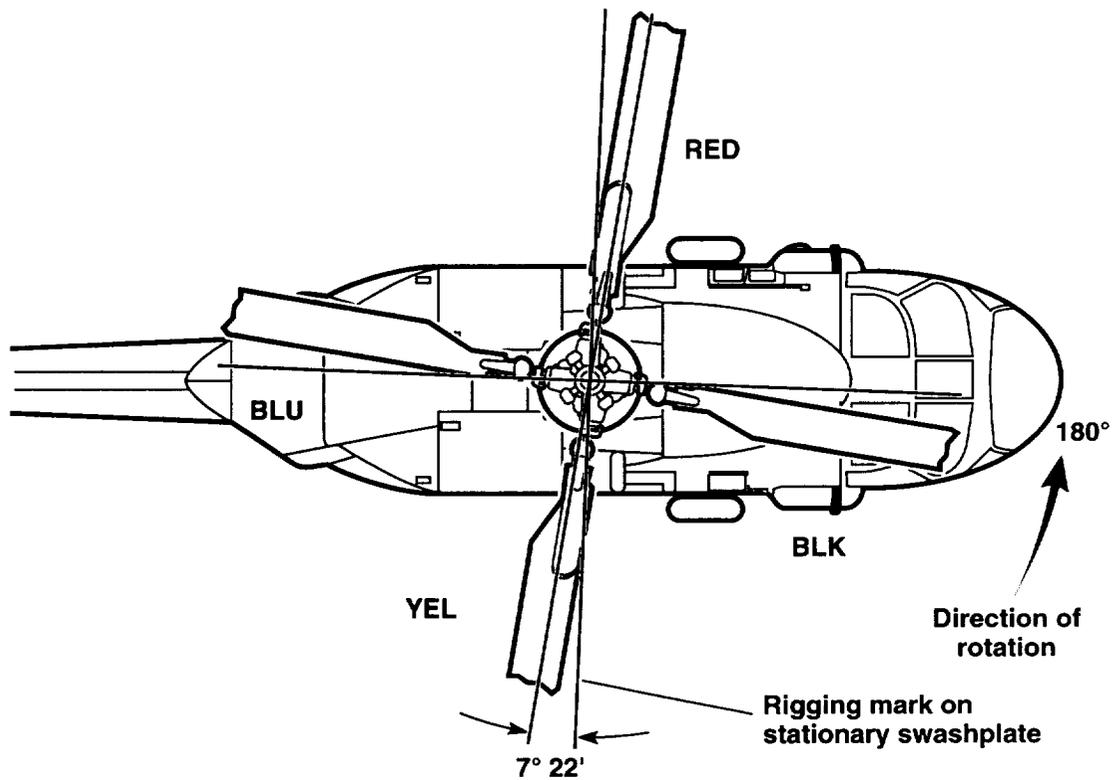
Figure A-2. Main and tail rotor azimuthal orientations.

APPENDIX B. FLIGHT CARDS

The flight cards present a synopsis of each test flight, including a counter-by-counter description. Each flight card contains a short summary of the flight, including flight number, flight date, test director, pilots, flight time, and counter range. This is followed by a list of the run numbers (or counter numbers), the coded description of each test point, the duration of data for each test point, the start time of each maneuver, and the data types available.

Each counter is labeled with a code that identifies the test condition. The code is designed to make maximum use of a feature in TRENDS which allows searches of the counter labels. The result of such a search is a collection of test points that have in common the element searched for (e.g., hover points, or RCALS, or housekeeping points). The code makes use of the following key terms:

KIASB	Boom indicated airspeed, knots
KIASS	Ship indicated airspeed, knots
CTS	Thrust coefficient over sigma
LEVEL	Level flight test point
SWEEP	Part of a speed-sweep from 0 to V_{ne}
R/C	Nominal rate of climb during test point
R/S	Nominal rate of sink during test point
R AOB	Angle of bank to the right
L AOB	Angle of bank to the left
MVR	Maneuvering test point
CALS	Calibration point
STATIC	Cal point, sensors at nominal value
RCAL	Cal point, sensors at resistance value
LEAD-LAG	Cal point, blade lag motion input
FULL THROWS	Cal Point, stick stir

Examples of counter descriptions are presented below:

60 KIASB,.08CTS,LEVEL SWEEP: This test point was a part of a speed sweep conducted in level flight. The airspeed was 60 knots indicated on the instrumentation boom, and the thrust coefficient was 0.08.

142 KIASB,.09CTS,400R/S,SWEEP: This test point was a part of a speed sweep conducted in a powered descent. The airspeed was 142 knots indicated on the instrumentation boom, the thrust coefficient was 0.09, and the rate of sink was targeted at 400 ft/min.

110 KIASB,.10CTS,55R AOB,MVR: This test point was a part of the maneuver test matrix. The airspeed was 110 knots indicated of the instrumentation boom, the thrust coefficient was 0.10, and the angle of bank was 55° to the right.

LEAD-LAG CALS, FULL THROW: This counter was a cyclic calibration of control-stick travel and blade lead-lag travel. All sensors not associated with this were at static calibration value.

HOUSEKEEPING POINT,80 KIASB: This counter was a housekeeping point used to verify the repeatability of all aircraft sensors. The point was taken at 80 knots indicated boom, and at 2,800 ft pressure altitude.

Flight descriptions

Flight	Date	Description	T/O gross weight, lb	c.g., in. FS
9	3-17	Level flight performance at 0.08	16200	361.7
10	3-26	Level flight performance at 0.08	16219	361.5
11	3-27	Level flight performance at 0.08	16260	361.7
12	4-2	Power descent at .08	16245	361.4
13	4-2	Level flight performance at 0.09	16245	361.4
17	4-14	Level flight performance at 0.09	18166	361.5
18	4-14	Level flight performance at 0.09	17212	358.2
19	4-15	Level flight performance at 0.09	17201	358.2
20	4-15	Dynamic stability	16430	360.7
22	4-27	Level flight performance at 0.10	20200	361.3
23	4-28	Level flight performance at 0.10	20220	361.1
25	5-16	Level flight performance at 0.10	19018	361.3
26	5-17	Level flight performance at 0.08	16224	361.6
27	5-17	Level, descent performance at 0.08	16200	363.2
28	5-21	Maneuvering limits at 0.10	18131	361.3
29	5-21	Maneuvering limits at 0.10	18218	361.5
30	5-22	Power descent at 0.09	18193	361.5
31	5-22	Control frequency SWEEPs	18193	363.8
32	5-28	Power descent at 0.10	20198	361.4
33	5-29	Maneuvering limits at 0.09	16217	361.9
35	5-30	Maneuvering limits at 0.09	16197	361.8
36	5-30	Maneuvering limits at 0.09	16172	361.7
37	6-1	Maneuvering limits at 0.10	18197	361.7
39	6-2	Acoustics at 0.08	16186	361.6

Counter descriptions: Flight 9

CTR	901	Preflight static CALS
CTR	902	Preflight RCALS
CTR	903	LEAD-LAG CALS, FULL THROW
CTR	904	HOUSEKEEPING POINT, 80 KIASB
CTR	905	80 KIASB,.08CTS,LEVEL SWEEP
CTR	906	80 KIASB,.08CTS,LEVEL SWEEP
CTR	907	90 KIASB,.08CTS,LEVEL SWEEP
CTR	908	100 KIASB,.08CTS,LEVEL SWEEP
CTR	909	110 KIASB,.08CTS,LEVEL SWEEP
CTR	910	120 KIASB,.08CTS,LEVEL SWEEP
CTR	911	130 KIASB,.08CTS,LEVEL SWEEP
CTR	912	70 KIASB,.08CTS,LEVEL SWEEP
CTR	913	50 KIASB,.08CTS,LEVEL SWEEP
CTR	914	40 KIASB,.08CTS,LEVEL SWEEP
CTR	915	30 KIASB,.08CTS,LEVEL SWEEP

Counter descriptions: Flight 10

CTR	1001	Preflight static CALS
CTR	1002	Preflight RCALS
CTR	1003	LEAD-LAG CALS, FULL THROWS
CTR	1004	HOUSEKEEPING POINT, 80KIASB
CTR	1005	130 KIASB,.08CTS,LEVEL SWEEP
CTR	1006	60 KIASB,.08CTS,LEVEL SWEEP
CTR	1007	22 KIASB,.08CTS,LEVEL SWEEP
CTR	1008	22 KIASB,.08CTS,LEVEL SWEEP
CTR	1009	140 KIASB,.08CTS,LEVEL SWEEP

Counter descriptions: Flight 11

CTR	1101	Preflight static CALS
CTR	1102	Preflight RCALS
CTR	1103	LEAD-LAG, FULL THROWS
CTR	1104	HOUSEKEEPING, 80 KIASB
CTR	1105	17 KIASB,.08CTS,LEVEL SWEEP
CTR	1106	9 KIASB,.08CTS,LEVEL SWEEP
CTR	1107	HOVER,.08CTS,LEVEL SWEEP
CTR	1108	HOVER,.08CTS,LEVEL SWEEP
CTR	1109	5 KIASB,.08CTS,LEVEL SWEEP

Counter descriptions: Flight 12

CTR	1201	Preflight static CALS
CTR	1202	Preflight RCALS
CTR	1203	FULL THROWS, LEAD-LAG CALS
CTR	1204	HOUSEKEEPING POINT, 80 KIASB
CTR	1205	140 KIASB,.08CTS,LEVEL, SWEEP
CTR	1206	148 KIASB,.08CTS,500R/S,SWEEP
CTR	1207	137 KIASB,.08CTS,climb,SWEEP
CTR	1208	158 KIASB.08CTS,1600R/S,SWEEP
CTR	1209	128 KIASB,.08CTS,800R/C,SWEEP
CTR	1210	128 KIASB,.08CTS,600R/C,SWEEP
CTR	1211	156 KIASB,.08CTS,R/S,SWEEP

Counter descriptions: Flight 13

CTR	1301	Preflight static CALS
CTR	1302	Preflight RCALS
CTR	1303	FULL THROWS, LEAD-LAG CALS
CTR	1304	HOUSEKEEPING POINT, 80KIASB
CTR	1305	90 KIASB,.08CTS, LEVEL SWEEP
CTR	1306	91 KIASB,.08CTS, LEVEL SWEEP
CTR	1307	30 KIASB,.08CTS, LEVEL SWEEP
CTR	1308	19 KIASB,.08CTS, LEVEL SWEEP
CTR	1309	15 KIASB,.08CTS, LEVEL SWEEP
CTR	1310	15 KIASB,.08CTS, LEVEL SWEEP
CTR	1311	10 KIASB,.08CTS, LEVEL SWEEP

Counter descriptions: Flight 17

CTR	1701	Preflight static CALS
CTR	1702	FULL THROWS, LEAD-LAG CALS
CTR	1703	HOUSEKEEPING POINT, 80 KIASB
CTR	1704	70 KIASB,.09CTS, LEVEL SWEEP
CTR	1705	60 KIASB,.09CTS, LEVEL SWEEP
CTR	1706	50 KIASB,.09CTS, LEVEL SWEEP
CTR	1707	40 KIASB,.09CTS, LEVEL SWEEP
CTR	1708	30 KIASB,.09CTS, LEVEL SWEEP
CTR	1709	22 KIASB,.09CTS, LEVEL SWEEP
CTR	1710	18 KIAS,.09CTS, LEVEL SWEEP
CTR	1711	10 KIAS,.09CTS, LEVEL SWEEP
CTR	1712	10 KIAS,.09CTS,SAS on,LEVEL
CTR	1713	80 KIASB,.09CTS, LEVEL SWEEP
CTR	1714	80 KIASB,.09CTS, LEVEL SWEEP
CTR	1715	90 KIASB,.09CTS, LEVEL SWEEP
CTR	1716	100 KIASB,.09CTS, LEVEL SWEEP
CTR	1717	110 KIASB,.09CTS, LEVEL SWEEP
CTR	1718	120 KIASB,.09CTS, LEVEL SWEEP
CTR	1719	130 KIASB,.09CTS, LEVEL SWEEP

Counter descriptions: Flight 18

CTR	1801	Preflight RCAL
CTR	1802	FULL THROWS, LEAD-LAG CALS
CTR	1803	HOUSEKEEPING POINT
CTR	1804	137 KIASB,.09CTS, LEVEL SWEEP
CTR	1805	25 KIASB,.09CTS, LEVEL SWEEP
CTR	1806	115 KIASB,.09CTS, LEVEL SWEEP
CTR	1807	HOVER,.09CTS, LEVEL SWEEP
CTR	1808	HOVER,.09CTS, LEVEL SWEEP

Counter descriptions: Flight 19

CTR	1901	Preflight static CALS
CTR	1902	Preflight RCALS
CTR	1903	FULL THROWS, LEAD-LAG CALS
CTR	1904	HOUSEKEEPING POINT
CTR	1905	3 KIAS,.09CTS,LEVEL SWEEP
CTR	1906	3 KIAS,.09CTS,LEVEL SWEEP
CTR	1907	5 KIAS,.09CTS,LEVEL SWEEP
CTR	1908	15 KIAS,.09CTS,LEVEL SWEEP
CTR	1909	15 KIAS,.09CTS,LEVEL SWEEP
CTR	1910	25 KIASB,.09CTS,LEVEL SWEEP
CTR	1911	35 KIASB,.09CTS,LEVEL SWEEP
CTR	1912	45 KIASB,.09CTS,LEVEL SWEEP

Counter descriptions: Flight 20

CTR	2001	Preflight static CALS
CTR	2002	Preflight RCALS
CTR	2003	FULL THROWS, LEAD-LAG CALS
CTR	2004	57 KIASB,1"fwd long,doublet
CTR	2005	57 KIASB,1"fwd long,doublet
CTR	2006	57 KIASB,1"aft long,doublet
CTR	2007	57 KIASB,1"lt lat,doublet
CTR	2008	59 KIASB,1"lt lat,doublet
CTR	2009	57 KIASB,1"rt lat,doublet
CTR	2010	58 KIASB,1"lt ped,doublet
CTR	2011	57 KIASB,1"rt ped,doublet
CTR	2012	57 KIASB,1"up col,doublet
CTR	2013	127 KIASB,1"fwd long,doublet
CTR	2014	127 KIASB,1"aft long,doublet
CTR	2015	127 KIASB,1"lt lat,doublet
CTR	2016	127 KIASB,1"rt lat,doublet
CTR	2017	127 KIASB,1"lt ped,doublet
CTR	2018	127 KIASB,1"rt ped,doublet
CTR	2019	129 KIASB,1"rt ped,doublet
CTR	2020	127 KIASB,1"up col,doublet
CTR	2021	127 KIASB,1"dn col,doublet

Counter descriptions: Flight 22

CTR	2201	1 Preflight static and RCALS
CTR	2202	Preflight static CALS
CTR	2203	Preflight RCALS
CTR	2204	FULL THROW CALS
CTR	2205	HOUSEKEEPING POINT, 80KIASS
CTR	2206	70 KIASB,.10CTS,LEVEL SWEEP
CTR	2207	60 KIASB,.10CTS,LEVEL SWEEP
CTR	2208	60 KIASB,.10CTS,LEVEL SWEEP
CTR	2209	50 KIASB,.10CTS,LEVEL SWEEP
CTR	2210	40 KIASB,.10CTS,LEVEL SWEEP
CTR	2211	40 KIASB,.10CTS,LEVEL SWEEP
CTR	2212	30 KIASB,.10CTS,LEVEL SWEEP
CTR	2213	30 KIASB,.10CTS,LEVEL SWEEP
CTR	2214	22 KIASB,.10CTS,LEVEL SWEEP
CTR	2215	18 KIAS,.10CTS,LEVEL SWEEP
CTR	2216	10 KIAS,.10CTS,LEVEL SWEEP
CTR	2217	80 KIASB,.10CTS,LEVEL SWEEP
CTR	2218	90 KIASB,.10CTS,LEVEL SWEEP
CTR	2219	100 KIASB,.10CTS,LEVEL SWEEP
CTR	2220	110 KIASB,.10CTS,LEVEL SWEEP
CTR	2221	120 KIASB,.10CTS,LEVEL SWEEP
CTR	2222	130 KIASB,.10CTS,LEVEL SWEEP
CTR	2223	137 KIASB,.10CTS,LEVEL SWEEP

Counter descriptions: Flight 23

CTR	2301	Preflight static CALS
CTR	2302	Preflight RCALS
CTR	2303	Preflight static CALS
CTR	2304	Preflight RCALS
CTR	2305	FULL THROW CALS
CTR	2306	Hover, IGE
CTR	2307	HOUSEKEEPING POINT,80 KIASS
CTR	2308	25 KIASB,.10CTS,LEVEL SWEEP
CTR	2309	35 KIASB,.10CTS,LEVEL SWEEP
CTR	2310	45 KIASB,.10CTS,LEVEL SWEEP
CTR	2311	18 KIAS,.10CTS,LEVEL SWEEP
CTR	2312	18 KIAS,.10CTS,LEVEL SWEEP
CTR	2313	18 KIAS,.10CTS,LEVEL SWEEP
CTR	2314	15 KIAS,.10CTS,LEVEL SWEEP
CTR	2315	133 KIASB,.10CTS,LEVEL SWEEP
CTR	2316	128 KIASB,.10CTS,LEVEL SWEEP
CTR	2317	118 KIASB,.10CTS,LEVEL SWEEP
CTR	2318	HOVER,.10CTS,LEVEL SWEEP
CTR	2319	Postflight static CALS
CTR	2320	Postflight RCALS

28

Counter descriptions: Flight 25

CTR	2501	Preflight static CALS
CTR	2502	Preflight RCALS
CTR	2503	FULL THROW CALS
CTR	2504	HOUSEKEEPING POINT, 80 KIASB
CTR	2505	28 KIAS,.10CTS,LEVEL SWEEP
CTR	2506	23 KIAS,.10CTS,LEVEL SWEEP
CTR	2509	5 KIAS,.10CTS,LEVEL SWEEP
CTR	2510	10 KIAS,.10CTS,LEVEL SWEEP
CTR	2511	23 KIAS,.10CTS,LEVEL SWEEP
CTR	2512	28 KIAS,.10CTS,LEVEL SWEEP
CTR	2513	24 KIASB,.10CTS,LEVEL SWEEP
CTR	2514	20 KIASB,.10CTS,LEVEL SWEEP
CTR	2515	20 KIASB,.10CTS,LEVEL SWEEP

Counter descriptions: Flight 26

CTR	2601	Preflight static CALS
CTR	2602	Preflight RCALS
CTR	2603	FULL THROW CALS
CTR	2604	3 KIAS,.08CTS,LEVEL SWEEP
CTR	2605	3 KIAS,.08CTS,LEVEL SWEEP
CTR	2606	10 KIAS,.08CTS,LEVEL SWEEP
CTR	2607	28 KIAS,.08CTS,LEVEL SWEEP
CTR	2608	24 KIASB,.08CTS,LEVEL SWEEP,NG
CTR	2609	24 KIASB,.08CTS,LEVEL SWEEP
CTR	2610	Settling with power,NG
CTR	2611	10 KIAS,.08CTS,LEVEL SWEEP

Counter descriptions: Flight 27

CTR	2701	Preflight static CALS
CTR	2702	Preflight RCALS
CTR	2703	FULL THROW CALS
CTR	2704	HOUSEKEEPING POINT, 80 KIASS
CTR	2705	166 KIASB,.08CTS,R/S,SWEEP
CTR	2706	170 KIASB,.08CTS,R/S,SWEEP
CTR	2707	175 KIASB,.08CTS,R/S,SWEEP
CTR	2708	3 KIAS,.08CTS,LEVEL SWEEP
CTR	2711	3 KIAS,.08CTS,LEVEL SWEEP
CTR	2712	10 KIAS,.08CTS,LEVEL SWEEP
CTR	2713	28 KIAS,.08CTS,LEVEL SWEEP
CTR	2714	25 KIASB,.08CTS,LEVEL SWEEP
CTR	2715	24 KIASB,.08CTS,LEVEL SWEEP
CTR	2716	132 KIASB,.08CTS,LEVEL SWEEP

Counter descriptions: Flight 28

CTR 2801	Preflight static CALS
CTR 2802	Preflight RCALS
CTR 2803	FULL THROW CALS
CTR 2804	LEAD-LAG CALS
CTR 2805	110 KIASB,.10CTS,0 AOB,MVR
CTR 2806	110 KIASB,.10CTS,37L AOB,MVR
CTR 2807	110 KIASB,.10CTS,48L AOB,MVR
CTR 2808	110 KIASB,.10CTS,55L AOB,MVR
CTR 2809	110 KIASB,.10CTS,60L AOB,MVR
CTR 2810	129 KIASB,.10CTS,0 AOB,MVR
CTR 2811	129 KIASB,.10CTS,37L AOB,MVR
CTR 2812	129 KIASB,.10CTS,48L AOB,MVR
CTR 2813	129 KIASB,.10CTS,50L AOB,MVR
CTR 2814	129 KIASB,.10CTS,60L AOB,MVR
CTR 2815	138 KIASB,.10CTS,0 AOB,MVR
CTR 2816	138 KIASB,.10CTS,37L AOB,MVR
CTR 2817	138 KIASB,.10CTS,48L AOB,MVR
CTR 2818	138 KIASB,.10CTS,60L AOB,MVR
CTR 2819	138 KIAS3,.10CTS,60L AOB,MVR
CTR 2820	138 KIASB,.10CTS,55L AOB,MVR
CTR 2821	138 KIASB,.10CTS,55L AOB,MVR
CTR 2822	148 KIASB,.10CTS,0 AOB,MVR
CTR 2823	148 KIASB,.10CTS,37L AOB,MVR
CTR 2824	148 KIASB,.10CTS,48L AOB,MVR
CTR 2825	148 KIASB,.10CTS,55L AOB,MVR
CTR 2826	148 KIASB,.10CTS,60L AOB,MVR

Counter descriptions: Flight 29

CTR	2901	Preflight static CALS
CTR	2902	Preflight RCALS
CTR	2903	FULL THROWS, LEAD-LAG CALS
CTR	2904	HOUSEKEEPING POINT, 80KIASS
CTR	2905	158 KIASB,.10CTS,0 AOB,MVR
CTR	2906	158 KIASB,.10CTS,37L AOB,MVR
CTR	2907	158 KIASB,.10CTS,48L AOB,MVR
CTR	2908	158 KIASB,.10CTS,37R AOB,MVR
CTR	2909	129 KIASB,.10CTS,0 AOB,MVR
CTR	2910	129 KIASB,.10CTS,37R AOB,MVR
CTR	2911	129 KIASB,.10CTS,55R AOB,MVR
CTR	2912	129 KIASB,.10CTS,60R AOB,MVR
CTR	2913	129 KIASB,.10CTS,55L AOB,MVR
CTR	2914	138 KIASB,.10CTS,0 AOB,MVR
CTR	2915	138 KIASB,.10CTS,37R AOB,MVR
CTR	2916	138 KIASB,.10CTS,48R AOB,MVR
CTR	2917	138 KIASB,.10CTS,55R AOB,MVR
CTR	2918	138 KIASB,.10CTS,60R AOB,MVR
CTR	2919	138 KIASB,.10CTS,55L AOB,MVR
CTR	2920	138 KIASB,.10CTS,37R AOB,MVR
CTR	2921	138 KIASB,.10CTS,37R AOB,MVR
CTR	2922	148 KIASB,.10CTS,0 AOB,MVR
CTR	2923	148 KIASB,.10CTS,60L AOB,MVR
CTR	2924	148 KIASB,.10CTS,60L AOB,MVR

Counter descriptions: Flight 30

CTR	3001	Preflight static CAL
CTR	3002	Preflight RCALS
CTR	3003	FULL THROWS, LEAD-LAG CALS
CTR	3004	HOUSEKEEPING POINT
CTR	3005	137 KIASB,.09CTS,LEVEL SWEEP
CTR	3006	137 KIASB,.09CTS,LEVEL SWEEP
CTR	3007	148 KIASB,.09CTS,800R/S,SWEEP
CTR	3008	128 KIASB,.09CTS,690R/C,SWEEP
CTR	3009	158 KIASB.09CTS,1800R/S,SWEEP
CTR	3010	119 KIASB.09CTS,1100R/C,SWEEP
CTR	3011	169 KIASB.09CTS,3200R/S,SWEEP
CTR	3012	23 KIASB.09CTS,800R/C,SWEEP
CTR	3013	162 KIASB.09CTS,2300R/S,SWEEP
CTR	3014	132 KIASB.09CTS,100R/C,SWEEP
CTR	3015	152 KIASB.09CTS,1100R/S,SWEEP
CTR	3016	142 KIASB.09CTS,400R/S,SWEEP
CTR	3017	169 KIASB.09CTS,3100R/S,SWEEP
CTR	3018	137 KIASB,.09CTS,LEVEL SWEEP

Counter descriptions: Flight 31

CTR	3101	Preflight static CALS
CTR	3102	Preflight RCALS
CTR	3103	FULL THROW CALS
CTR	3104	Hover,long stick sine sweeps
CTR	3105	Hover,long stick sine sweeps
CTR	3106	Hover,long stick sine sweeps
CTR	3107	Hover,lat stick sine sweeps
CTR	3108	Hover,lat stick sine sweeps
CTR	3109	Hover,pedal sine sweeps
CTR	3110	Hover,col stick sine sweeps
CTR	3111	Hover,col stick sine sweeps
CTR	3112	108 KIASB,long stick sweeps
CTR	3113	108 KIASB,lat stick sweeps
CTR	3114	108 KIASB,pedal sweeps
CTR	3115	108 KIASB,coll stick sweeps
CTR	3116	108 KIASB,long stick sweeps
CTR	3117	108 KIASB,long stick sweeps
CTR	3118	Postflight static CALS
CTR	3119	Postflight RCALS (if present)

Counter descriptions: Flight 32

CTR	3201	Preflight static CAL
CTR	3202	Preflight RCAL
CTR	3203	FULL THROWS, LEAD-LAG CALS
CTR	3204	Preflight RCAL
CTR	3205	HOUSEKEEPING POINT, 80 KIASS
CTR	3206	133 KIASB,.10CTS,LEVEL SWEEP
CTR	3207	138 KIASB,.10CTS,500R/S,SWEEP
CTR	3208	Bad data—no record
CTR	3209	119 KIASB,.10CTS,500R/C,SWEEP
CTR	3210	149 KIASB.10CTS,1100R/S,SWEEP
CTR	3211	123 KIASB,.10CTS,400R/C,SWEEP
CTR	3212	140 KIASB,.10CTS,500R/S,SWEEP
CTR	3213	138 KIASB,.10CTS,500R/S,SWEEP
CTR	3214	126 KIASB,.10CTS,200R/C,SWEEP
CTR	3215	144 KIASB,.10CTS,700R/S,SWEEP
CTR	3216	3 KIAS,.10CTS,LEVEL SWEEP
CTR	3217	Hover,.10CTS,LEVEL SWEEP
CTR	3218	Hover,.10CTS,LEVEL SWEEP

Counter descriptions: Flight 33

CTR	3301	Preflight static CALS
CTR	3302	Preflight RCALS
CTR	3303	FULL THROWS, LEAD-LAG CALS
CTR	3304	HOUSEKEEPING POINT, 80 KIASS
CTR	3305	110 KIASB,.09CTS,0 AOB,MVR
CTR	3306	110 KIASB,.09CTS,37L AOB,MVR
CTR	3307	110 KIASB,.09CTS,48L AOB,MVR
CTR	3308	110 KIASB,.09CTS,55L AOB,MVR
CTR	3309	110 KIASB,.09CTS,60L AOB,MVR
CTR	3310	129 KIASB,.09CTS,0 AOB,MVR
CTR	3311	129 KIASB,.09CTS,37L AOB,MVR
CTR	3312	129 KIASB,.09CTS,48L AOB,MVR
CTR	3313	129 KIASB,.09CTS,55L AOB,MVR
CTR	3314	129 KIASB,.09CTS,60L AOB,MVR
CTR	3315	138 KIASB,.09CTS,0 AOB,MVR
CTR	3316	138 KIASB,.09CTS,37L AOB,MVR
CTR	3317	138 KIASB,.09CTS,37L AOB,MVR
CTR	3318	138 KIASB,.09CTS,37L AOB,MVR
CTR	3319	138 KIASB,.09CTS,48L AOB,MVR
CTR	3320	138 KIASB,.09CTS,60L AOB,MVR

Counter descriptions: Flight 35

CTR	3501	Preflight static CALS
CTR	3502	Preflight RCALS
CTR	3503	FULL THROW CALS
CTR	3504	HOUSEKEEPING POINT, 80KIASS
CTR	3505	148 KIASB,.09CTS,0 AOB,MVR
CTR	3506	148 KIASB,.09CTS,37L AOB,MVR
CTR	3507	148 KIASB,.09CTS,48L AOB,MVR
CTR	3508	148 KIASB,.09CTS,55L AOB,MVR
CTR	3509	148 KIASB,.09CTS,60L AOB,MVR
CTR	3510	158 KIASB,.09CTS,0 AOB,MVR
CTR	3511	158 KIASB,.09CTS,37L AOB,MVR
CTR	3512	158 KIASB,.09CTS,48L AOB,MVR
CTR	3513	158 KIASB,.09CTS,55L AOB,MVR
CTR	3514	158 KIASB,.09CTS,60L AOB,MVR
CTR	3515	163 KIASB,.09CTS,37L AOB,MVR
CTR	3516	163 KIASB,.09CTS,60L AOB,MVR
CTR	3517	163 KIASB,.09CTS,55L AOB,MVR

Counter descriptions: Flight 36

CTR	3601	Preflight static CAL
CTR	3602	Preflight RCAL
CTR	3603	FULL THROW CALS
CTR	3604	HOUSEKEEPING POINT, 80KIASS
CTR	3605	129 KIASB,.09CTS,0 AOB,MVR
CTR	3606	129 KIASB,.09CTS,37R AOB,MVR
CTR	3607	129 KIASB,.09CTS,37R AOB,MVR
CTR	3608	129 KIASB,.09CTS,48R AOB,MVR
CTR	3609	129 KIASB,.09CTS,60R AOB,MVR
CTR	3610	138 KIASB,.09CTS,0 AOB,MVR
CTR	3611	138 KIASB,.09CTS,37R AOB,MVR
CTR	3612	138 KIASB,.09CTS,48R AOB,MVR
CTR	3613	138 KIASB,.09CTS,55R AOB,MVR
CTR	3614	138 KIASB,.09CTS,60R AOB,MVR
CTR	3615	158 KIASB,.09CTS,0 AOB,MVR
CTR	3616	158 KIASB,.09CTS,37R AOB,MVR
CTR	3617	158 KIASB,.09CTS,60R AOB,MVR
CTR	3618	158 KIASB,.09CTS,55R AOB,MVR
CTR	3619	163 KIASB,.09CTS,0 AOB,MVR
CTR	3620	163 KIASB,.09CTS,37R AOB,MVR
CTR	3621	163 KIASB,.09CTS,60R AOB,MVR

Counter descriptions: Flight 37

CTR	3701	Preflight static CAL
CTR	3702	Preflight RCAL
CTR	3703	FULL THROW CALS
CTR	3704	HOUSEKEEPING POINT, 80KIASS
CTR	3705	110 KIASB,.10CTS,0 AOB,MVR
CTR	3706	110 KIASB,.10CTS,37R AOB,MVR
CTR	3707	110 KIASB,.10CTS,37R AOB,MVR
CTR	3708	110 KIASB,.10CTS,55R AOB,MVR
CTR	3709	110 KIASB,.10CTS,55R AOB,MVR
CTR	3710	148 KIASB,.10CTS,0 AOB,MVR
CTR	3711	148 KIASB,.10CTS,37R AOB,MVR
CTR	3712	148 KIASB,.10CTS,48R AOB,MVR
CTR	3713	148 KIASB,.10CTS,60R AOB,MVR
CTR	3714	148 KIASB,.10CTS,55R AOB,MVR
CTR	3715	148 KIASB,.10CTS,55R AOB,MVR
CTR	3716	158 KIASB,.10CTS,0 AOB,MVR
CTR	3717	158 KIASB,.10CTS,0 AOB,MVR
CTR	3718	158 KIASB,.10CTS,60R AOB,MVR
CTR	3719	158 KIASB,.10CTS,55R AOB,MVR
CTR	3720	158 KIASB,.10CTS,55L AOB,MVR
CTR	3721	158 KIASB,.10CTS,60L AOB,MVR

Counter descriptions: Flight 39

CTR	3901	Preflight static CALS
CTR	3902	Preflight RCALS
CTR	3903	LEAD-LAG CALS
CTR	3904	HOUSEKEEPING POINT, 80KIASS
CTR	3905	77 KIAS,LEVEL,trail,acoustic
CTR	3906	77 KIAS,LEVEL,left,acoustic
CTR	3907	77 KIAS,LEVEL,right,acoustic
CTR	3908	77 KIAS,400R/S,right,acoustic
CTR	3909	Bad point
CTR	3910	77 KIAS,400R/S,left,acoustic
CTR	3911	77 KIAS,800R/S,left,acoustic
CTR	3912	60 KIAS,LEVEL,trail,acoustic
CTR	3913	60 KIAS,LEVEL,left,acoustic
CTR	3914	60 KIAS,400R/S,left,acoustic
CTR	3915	60 KIAS,800R/S,left,acoustic
CTR	3916	60 KIAS,800R/S,left,acoustic
CTR	3917	124 KIAS,400R/S,trail,acoustic
CTR	3918	124 KIAS,800R/S,trail,acoustic
CTR	3919	100 KIAS,LEVEL,trail,acoustic
CTR	3920	100 KIAS,LEVEL,left,acoustic
CTR	3921	100 KIAS,400R/S,trail,acoustic
CTR	3922	60 KIAS,LEVEL,right,acoustic
CTR	3923	60 KIAS,400R/S,right,acoustic
CTR	3924	60 KIAS,400R/S,trail,acoustic
CTR	3925	Bad point

APPENDIX C. MRALS INFORMATION FILE FOR DATAMAP

The data analysis computer program DATAMAP uses information that is stored in the information file to facilitate computation and display of related data sets. The file contains related sets of sensor item codes that are organized by their physical location, and that are given four-character group names. Each group can be a one-, two-, or three-dimensional array. The third dimension is limited to only two values.

The information file is divided into two sets of information. The first sets equivalences that relate item codes with codes used in DATAMAP for derivation equations. The first line, for example, equates the item code MRZ1 with the internal code MRAZ, and sets 82.63° as the location of the instrumented blade when the MRZ1 blipper is triggered. All azimuthal plots generated need this information to properly phase the rotating parameters. The word end is used to terminate this set. The second set follows immediately after the first. It contains groups of sensors that are physically related. A group has a four-character name and includes item codes, labels, and physical location information.

Each group name is followed by a narrative description of that sensor set. This description is included on any plot produced using this group name. The next line identifies the azimuthal offset of that sensor group with the main-rotor once-per-rev contactor. The next two lines are the labels applied to the first two dimensions of the array. These are followed by the physical locations of the sensors and the orientation of the first entrant, for the first-array dimension. If this is a two- or three-dimensional array, the information for the second-array dimension follows. Next is a four-character code unique to the type of sensors included in the group. If the group is a three-dimensional array, these codes are followed by the orientation of the third dimension.

In the information file, the item codes are presented last and in the reverse of the order just discussed; that is, the third dimension is varied first, then after a slash the second dimension is incremented and the third dimension is again varied. When the second dimension has been completely varied, a double slash denotes that the first dimension is incremented. The other two dimensions are then varied as before. Each group information section is terminated with the word END. A more thorough explanation of the structure of the information file can be found in reference 7.

MRAZ MRZ1 82.63/
TRAZ MRZ2/
TASK VTRU/
OATM T100/
STAT H001/
MTOR RQ10/
MFLP BH01 82.63/
MFTH BH02 82.63/
END
NBRB BLADE REAR BENDING, UH-60/1
FRACTN OF RADIUS
R/RADIUS
BLADE ROOT
0.50, 0.60, 0.70//
BLBB//
BR50/BR60/BR70//
END
NBEB BLADE EDGEWISE BENDING, UH-60/1
FRACTN OF RADIUS
R/RADIUS
BLADE ROOT
0.10, 0.50, 0.70//
BLBB//
BE01/BE50/BE70//
END
NBNB BLADE NORMAL BENDING, UH-60/1

FRACTN OF RADIUS
R/RADIUS
BLADE ROOT
0.10, 0.50, 0.60, 0.70//
BLBB//
BN01/BN50/BN60/BN70//
END
S2VZ VERTICAL FUSELAGE VIBRATION, UH-60/1
BUTT LINE
INCHES
CENTER LINE
−35.5, −31.0, 0.0, 31.0, 35.5//
FUSELAGE STATION
INCHES
FORWARD
253.0, 295.0, 702.2//
FSZV//
NULL/AF04/NULL/AF02/NULL//
AF07/NULL/NULL/NULL/AF06//
AF10/NULL/NULL/NULL/AF09//
NULL/NULL/AF12/NULL/NULL//
END
S2VY LATERAL FUSELAGE VIBRATION, UH-60/1
FUSELAGE STATION
INCHES
FORWARD

253.0, 295.0, 398.0, 702.2//
BUTT LINE
INCHES
CENTER LINE
–31.0, 0.0, 31.0, 35.5//
FSYV//
AF03/NULL/AF01/NULL//
NULL/NULL/NULL/AF05//
NULL/NULL/NULL/AF08//
NULL/AF11/NULL/NULL//
END
S2VX LONGITUDINAL FUSELAGE VIBRATION,
UH-60/1

BUTT LINE
INCHES
CENTER LINE
–83.5, 31.0, 83.5//
FUSELAGE STATION
INCHES
FORWARD
253.0, 732.0//
FSXV//
NULL/AF00/NULL//
AF14/NULL/AF13//
END

APPENDIX D. INSTRUMENTATION SIGN CONVENTION

Stick position	Positive direction or motion
Longitudinal cyclic	Stick motion aft from full fwd
Lateral cyclic	Stick motion to right of full left
Pedal	Right pedal forward
Collective	Stick motion up from full down

Aircraft state	
Angle of attack	Nose-up from wind axis
Side slip	Nose left from wind axis
Pitch attitude	Nose above horizon
Roll attitude	Starboard wing down
Heading	Clockwise
Pitch rate	Nose-up angular velocity
Roll rate	Starboard wing down angular velocity
Yaw rate	Nose right angular velocity
Pitch acceleration	Nose-up angular acceleration
Roll acceleration	Starboard wing down angular acceleration
Yaw acceleration	Nose right angular acceleration

Control linkages	
Longitudinal SAS output	Corresponding to aft long. stick
Lateral SAS output	Corresponding to right lat. stick
Directional SAS output	Corresponding to right pedal
Forward stationary link load	Link in tension
Lateral stationary link load	Link in tension
Aft stationary link load	Link in tension
Longitudinal mixer input	Corresponding to aft long. stick
Lateral mixer input	Corresponding to right lat. stick
Directional mixer input	Corresponding to right pedal

Rotor components	
Mast bending	Top of mast toward instrumented blade
Mast torque	Counterclockwise loading at mast bottom
Pitch-link load	Link in tension
Blade flapping	Instrumented blade moves upward
Blade feathering	Blade moves nose-up
Blade lead-lag	Blade moves aft of zero
Blade normal bending	Lower surface in tension
Blade edgewise bending	Leading edge in tension
Blade rear bending	Lead and lower surface in tension

Accelerometers	
X hub	Toward the hub center
Y hub	Toward the blade trailing edge
Z hub	Upward out of rotor plane
Fuselage vertical	Upward
Fuselage longitudinal	Forward
Fuselage lateral	Out starboard side
Blade vertical	Up out of rotor plane

Note: Hub accel package was 335° lead from the instrumented blade.

APPENDIX E. SENSOR CALIBRATION

Plots of pulse-code modulation counts to engineering unit conversion curves and the resultant polynomial coefficients for each sensor used in the test are presented here. The calibration plots are unnumbered and are arranged in alphabetical order by mnemonic name. The mnemonic names are listed and described in tables 3-6, 8, and 9.

Each plot is labeled with the mnemonic and the calibration date. Most coefficients are only first-order, although some are presented as higher-order, sometimes needlessly, for the functions are nearly linear. A case in point is yaw rate, given as a third-order polynomial when a linear fit is all that is needed. The linear fit is what was used in processing the data whenever possible.

Mnemonic name   ALPHA
Calibration date   9 Apr 87

Polynomial coefficients
B0   -.3462790E+03
B1   0.1712208E+00

deg

PCM counts

Figure E1.   Sensor calibration plots.

Figure E1. Sensor calibration plots (continued).

Figure E1. Sensor calibration plots (continued).

Figure E1. Sensor calibration plots (continued).

Figure E1. Sensor calibration plots (continued).

46

Figure E1. Sensor calibration plots (continued).

Figure E1. Sensor calibration plots (continued).

Figure E1. Sensor calibration plots (continued).

Figure E1. Sensor calibration plots (continued).

Mnemonic name   AYRFC
Calibration date   12 Mar 87

Polynomial coefficients
B0   -.2314235E+01
B1   0.1125418E-02

Figure E1. Sensor calibration plots (continued).

Figure E1. Sensor calibration plots (continued).

Figure E1. Sensor calibration plots (continued).

Figure E1. Sensor calibration plots (continued).

Figure E1. Sensor calibration plots (continued).

Figure E1. Sensor calibration plots (continued).

Figure E1. Sensor calibration plots (continued).

Figure E1. Sensor calibration plots (continued).

Figure E1. Sensor calibration plots (continued).

Figure E1. Sensor calibration plots (continued).

60

Figure E1. Sensor calibration plots (continued).

Figure E1. Sensor calibration plots (continued).

Figure E1. Sensor calibration plots (continued).

Figure E1. Sensor calibration plots (continued).

Figure E1. *Sensor calibration plots (continued).*

Figure E1. Sensor calibration plots (continued).

66

Figure E1. Sensor calibration plots (continued).

Figure E1. *Sensor calibration plots (continued).*

68

Figure E1. Sensor calibration plots (continued).

Figure E1. Sensor calibration plots (continued).

Figure E1. Sensor calibration plots (continued).

Figure E1. Sensor calibration plots (continued).

Mnemonic name   LATSTK
Calibration date   21 Jan 87

Polynomial coefficients
B0   -.3836205E+03
B1   0.1014762E+01
B2   -.1036024E-02
B3   0.5108365E-06
B4   -.1221352E-09
B5   0.1142027E-13

Figure E1.   Sensor calibration plots (continued).

Figure E1. Sensor calibration plots (continued).

Figure E1. Sensor calibration plots (continued).

Figure E1. Sensor calibration plots (continued).

Mnemonic name   MRALSS
Calibration date   28 Jan 87

Polynomial coefficients
B0   0.8143852E+04
B1   -.3951408E+01

Figure E1. Sensor calibration plots (continued).

Figure E1. Sensor calibration plots (continued).

Figure E1. Sensor calibration plots (continued).

Figure E1. Sensor calibration plots (continued).

Figure E1. Sensor calibration plots (continued).

Mnemonic name   MRBR6
Calibration date   13 Apr 87

Polynomial coefficients
B0   -.2558523E+05
B1   0.8528409E+01

Figure E1. Sensor calibration plots (continued).

Figure E1. Sensor calibration plots (continued).

Figure E1. Sensor calibration plots (continued).

Mnemonic name MREB7
Calibration date 20 Apr 87

Polynomial coefficients
B0 0.1853645E+05
B1 -.7955556E+01

Figure E1. Sensor calibration plots (continued).

85

Figure E1. Sensor calibration plots (continued).

Figure E1. Sensor calibration plots (continued).

Figure E1. Sensor calibration plots (continued).

Figure E1. Sensor calibration plots (continued).

Figure E1. Sensor calibration plots (continued).

Mnemonic name   MRLSS
Calibration date   10 Mar 87

Polynomial coefficients
B0   -.9758932E+05
B1   0.5427659E+02

Figure E1.   Sensor calibration plots (continued).

Figure E1. *Sensor calibration plots (continued).*

Mnemonic name   MRNB6
Calibration date   19 May 87

Polynomial coefficients
B0   -.1136143E+04
B1   0.9428571E+00

Figure E1. Sensor calibration plots (continued).

Figure E1. Sensor calibration plots (continued).

Mnemonic name MRPITCH
Calibration date 25 Feb 87

Polynomial coefficients
B0   -.2552716E+02
B1   0.2716370E-01

Figure E1. Sensor calibration plots (continued).

Figure E1. Sensor calibration plots (continued).

Figure E1. Sensor calibration plots (continued).

C-2

Mnemonic name   MRSEBL
Calibration date   10 Mar 87

Polynomial coefficients
B0   0.1307158E+05
B1   -.6401361E+01

Figure E1.   Sensor calibration plots (continued).

Figure E1. Sensor calibration plots (continued).

Figure E1. Sensor calibration plots (continued).

Figure E1. Sensor calibration plots (continued).

Figure E1. Sensor calibration plots (continued).

Figure E1. Sensor calibration plots (continued).

Mnemonic name   PSFWD
Calibration date   20 Jan 87

Polynomial coefficients
B0   -.1228934E+03
B1   0.7457121E-01

Figure E1.   Sensor calibration plots (continued).

104

Mnemonic name   PSLAT
Calibration date   20 Jan 87

Polynomial coefficients
B0   0.2738120E+03
B1   -.1011122E+00

Figure E1. Sensor calibration plots (continued).

Figure E1. Sensor calibration plots (continued).

Figure E1. Sensor calibration plots (continued).

Figure E1. Sensor calibration plots (continued).

Figure E1. Sensor calibration plots (continued).

Figure E1. Sensor calibration plots (continued).

Mnemonic name   QEIC2
Calibration date   9 Oct 86

Polynomial coefficients
B0   -.5124997E+03
B1   0.2499914E+00

Figure E1. Sensor calibration plots (continued).

Figure E1. Sensor calibration plots (continued).

Figure E1. Sensor calibration plots (continued).

Mnemonic name   QMR1
Calibration date   21 Jul 87

Polynomial coefficients
B0   0.3521715E+06
B1   -.1722110E+03

Figure E1. Sensor calibration plots (continued).

114

Figure E1. Sensor calibration plots (continued).

Mnemonic name   RADALT
Calibration date   8 Oct 86

Polynomial coefficients
B0   0.1447126E+04
B1   -.3571364E+00

ft

1600
1400
1200
1000
800
600
400
200

0   1000   2000   3000   4000   5000   6000   7000   8000

PCM counts

Figure E1. Sensor calibration plots (continued).

Figure E1. Sensor calibration plots (continued).

Figure E1. Sensor calibration plots (continued).

Figure E1. Sensor calibration plots (continued).

Figure E1. Sensor calibration plots (continued).

Mnemonic name SASA
Calibration date 21 Jan 87

Polynomial coefficients
B0 0.1765420E+03
B1 -.5055612E-01

Figure E1. Sensor calibration plots (continued).

Figure E1. Sensor calibration plots (continued).

Figure E1. Sensor calibration plots (continued).

Figure E1. *Sensor calibration plots (continued).*

Mnemonic name   STABLR
Calibration date   22 Jan 87

Polynomial coefficients
B0   0.1308648E+03
B1   -.1360467E+00
B2   0.1026003E-03
B3   -.5080118E-07
B4   0.1204147E-10
B5   -.1097587E-14

Figure E1. Sensor calibration plots (continued).

Figure E1. Sensor calibration plots (continued).

126

Figure E1. Sensor calibration plots (continued).

Figure E1. Sensor calibration plots (continued).

128

Figure E1. Sensor calibration plots (continued).

Mnemonic name   WFVOL2
Calibration date   19 Mar 87

Polynomial coefficients
B0   -.1805257E+03
B1   0.9028371E-01
B2   -.7687773E-06

Figure E1. Sensor calibration plots (continued).

Figure E1. Sensor calibration plots (continued).

Figure E1. Sensor calibration plots (continued).

132

Figure E1. Sensor calibration plots (concluded).

APPENDIX F. BLADE MOTION CORRECTION EQUATIONS

The blade-motion hardware developed for the Black Hawk aircraft has inherent interdependency of its measurement of blade flapping, feather, and lead-lag. The hardware produces three signal outputs that are cross-coupled, requiring a calibration to acquire the 10 coefficients of kinematic motion. The kinematic blade-motion equations are given in the following equations:

$$\text{Flapping} \quad \beta = (k_1\beta'^2 + k_2\beta' + k_3) + \frac{k_4(1 - \cos\theta')}{(1 + \sin\beta')}$$

$$\text{Feathering} \quad \theta = (k_5\theta'^2 + k_6\theta') \frac{(1 - k_7\tan\beta')}{(\cos\beta')^{0.5}}$$

$$+ k_{10}\left[\frac{\lambda' - 7 - k_8\theta'}{(1 + \sin\beta')^{k_9}}\right]$$

$$\text{Lead-lag} \quad \lambda = \lambda' - \frac{k_8\theta'}{(1 + \sin\beta')^{k_9}}$$

where

θ'	measured feathering
β'	measured flapping
λ'	measured lead-lag
k_{1-10}	blade-motion correction coefficients
θ	true feathering
β	true flapping
λ	true lead-lag

REFERENCES

1. Buckanin, R. M. et al.: Rotor System Evaluation, Phase 1, AEFA. AEFAPN 85-15, Edwards AFB, Calif., Mar. 1988.

2. Durne, J. A.; Howland, G. A.; and Twomey, W. J.: Comparison of Black Hawk Shake Test Results with NASTRAN Finite Element Analysis. 43rd Annual National Forum of the American Helicopter Society, May 1987.

3. Abbott, W. Y. et al.: Validation Flight Test of UH-60A for Rotorcraft Systems Integration Simulator. USAAEFA No. 79-24, Edwards AFB, Calif., Sept 1984.

4. Cross, J. L.: The YO-3A Acoustics Research Aircraft System Manual. NASA TM-85968, 1984.

5. Kufeld, R. M.; and Nguyen, D.: UH-60A Blade Shake Test. NASA TM-101005, 1989.

6. Goodman, R.: UH-60A NASA/AEFA Configuration Ground Vibration Test Results. SER-701619, Sikorsky Aircraft Co., Stratford, Conn., May 1990.

7. Philbrick, R. B.: The Data from Aeromechanics Test and Analytics–Management and Analysis Package, Vol. 1 Users Manual. USAAVRADCOM-TR-80-D-30A, Bell Helicopter Textron, Fortworth, Tex., Dec. 1980.

8. Philbrick, R. B.: The Data from Aeromechanics Test and Analytics—Management and Analysis Package. Vol. 2. System Manual. USAAVRADCOM-TR-80-D-30B, Bell Helicopter Textron, Fortworth, Tex., Dec. 1980.

9. Watts, M. E.; and Dejpour, S. R.: DATAMAP Upgrade Version 4.0. NASA TM-100993, 1989.

10. Bondi, M. J.; and Bjorkman, W. S.: TRENDS, the Aeronautical Post Test Data Base Management System. NASA TM-101025, 1990.

11. Ham, N. D.; Balough, D. L.; and Talbot, P. D.: The Measurement and Control of Helicopter Blade Modal Response Using Blade-Mounted Accelerometers. Paper No. 6-10, 13th European Rotorcraft Forum, Sept. 1987.

12. Johnson,W.: A Comprehensive Analytical Model of Rotorcraft Aerodynamics and Dynamics. Johnson Aeronautics Version. Vol. I Theory Manual. Johnson Aeronautics, Palo Alto, Calif., 1988.

13. Johnson,W.: A Comprehensive Analytical Model of Rotorcraft Aerodynamics and Dynamics. Johnson Aeronautics Version. Vol. II. Users Manual. Johnson Aeronautics, Palo Alto, Calif., 1988.

14. Van Gaasbeek, J. R.: Rotorcraft Flight Simulation Computer Program C81 with DATAMAP Interface. Vol. I. User's Manual. USAAVRADCOM-TR-80-D-38A, Oct. 1981.

15. Hsieh, P. Y.: Rotorcraft Flight Simulation Computer Program C81 with DATAMAP Interface. Vol. II. Programer's Manual. USAAVRADCOM-TR-80-D-38B, Oct. 1981.

16. Howlett, J. J.: UH-60A Black Hawk Engineering Simulation Program. NASA CR-166309, 1981.

17. Totah, J. J.: Correlation of UH-60A Phase I Flight Test Data with a Comprehensive Rotorcraft Model. To be published as NASA TM.

Table 1. PCM data system map

00 - SYNC1	01 - SYNC2	02 - TIME1	03 - TIME2	04 - TIME3	05 - SFID	06 - RECNO	07 - STATUS	08 - MRSEBL
09 - QMR	10 - QTR2	11 - MRNBX1	12 - MREBX1	13 - MRBR5	14 - MRBR6	15 - MRBR7	16 - MRNB5	17 - MRNB7
18 - MRNB6	19 - MREB5	20 - MREB7	21 - AZMRT	22 - AZMRR	23 - MRFLSS	24 - MRALSS	25 - MRLSS	26 - MRFLAP
27 - MRLAG	28 - MRPITCH	29 - AXMRT	30 - MRPR	31 - MR/TRAZI	32 - AXPS	33 - AYPS	34 - AZPS	35 - AYCS
36 - AZCS	37 - AYRFC	38 - AZRFC	39 - AZLFC	4O - AYRAC	41 - AZRAC	42 - AZLAC	43 - AYVT	44 - AZVT
45 - AZLST	46 - AZRST	47 - MRAXHUB	48 - MRAYHUB	49 - MRAZHUB				

50 - SPARE	51 - PTCHRATE	52 - AXCG	53 - QMR	54 - PITCHATT	55 - VOLTSTD1	56 - FCTS2	57 - DMIXE
- SPARE	- ROLLRATE	- AYCG	- PTCHACC	- ROLLATT	- VOLTSTD1	- FCTSAPU	- DMIXA
- QEIC1	- YAWRATE	- AZCG	- ROLLACC	- YAWATT	- VOLTSTD2	- WFVOL1	- DMIXR
- QEIC2	- SPARE	- AYCGSENS	- YAWACC	- QTR3	- VOLTSTD3	- WFVOL2	- SASE
					- VOLTSTD1	- COLLSTK	- SASA
					- VOLTSTD4	- LONGSTK	- SASR
					- MGT1	- LATSTK	- PSFWD
					- MGT2	- PEDAL	- PSAFT
					- FUELTMP1	- STABLR	- PSLAT
					- FUELTMP2	SPARE	- PBA
					- PAICS	- ALPHA	- LSSY
					- PAICB	- BETA	- LSSX
					- TTIC	SPARE	- LSSZ
					- RADALT	SPARE	- QCICB
					- RPMMR	SPARE	- QCICS
					- FCTS1	- TRIP	- BCART

PCM WORD LENGTH	12		
MSB LOG	FBT		
FRAME SYNC CODE	0101 0010 0000 0011 0101 0111		
BIT RATE	360 KBPS		
FRAME RATE	617 FPS		
FRAME TIME	1.93 MSEC		
WORD RATE	30K WPS		
WORD TIME	0.03 MSEC	TRACK 4	FM #1
FRAME LENGTH	58 WORDS	TRACK 5	IRIG TIME
CYCLE DEPTH	16 FRAMES	TRACK 6	MILLER
CYCLE TIME	30.95 MSEC	TRACK 7	BI-PHASE L
SFID WORD	WORD 5	TRACK 8	FM #2

Table 2. Item code key

A###	Accelerometer
F......	Fuselage
H......	Hub
nn	nn'th physical location
B###	Blade bending strain gauge
E......	Edgewise bending
N......	Normal bending
R......	Rear total bending
P......	Pushrod loading
nn	% radial location
D###	Misc. aircraft-state parameters
1.....	Control position
A.....	Aircraft attitude
AC..	Aircraft angular accelerometers
L.....	Aircraft linear accelerometers
M.....	Control mixer positions
P.....	Primary servo positions
R.....	Angular rates
S.....	SAS output positions
00	Longitudinal orientation
01	Lateral orientation
02	Yaw orientation
03	Vertical orientation
E###	Engine parameters
F.....	Fuel-related
Q.....	Torque related
T.....	Temperature-related
H###	Altitude parameters
MR##	Rotor control loads
nn	See DSnn Coding
R###	Rotor-related parameters
Q.....	Torque-related
O.....	Miscellaneous
V###	Velocity-related parameters

Note: All item codes consisting of four letters are derived parameters except BFAT and BFAR.

140

Table 3. Aircraft parameters

Mnemonic	Description	Units	Item code	Group
BCART	Ballast	in.	CART	AP
COLLSTK	Control position, collective	in.	D103	AP
DMIXA	Mixer input, lateral	%	DM01	AP
DMIXE	Mixer input position, long.	%	DM00	AP
DMIXR	Mixer input, directional	%	DM02	AP
LATSTK	Control position, lateral	in.	D101	AP
LONGSTK	Control position, longitudinal	in.	D100	AP
MRTRAZI	Main-rotor, tail-rotor azimuth	(Event)	MRZ1	AP
PBA	Pitch bias actuator position	%	R002	AP
PEDAL	Control position, directional	in.	D102	AP
PSAFT	Primary servo position, aft	%	DP03	AP
PSFWD	Primary servo position, forwd	%	DP00	AP
PSLAT	Primary servo position, lat.	%	DP01	AP
QMR	Main-rotor torque	ft·lb	RQ10	AP
QTR2	Tail-rotor shaft torque	ft·lb	RQ20	AP
QTR3	Tail-rotor shaft torque	ft·lb	RQ21	AP
RPMMR	Rotor speed	rpm	VR04	AP
SASA	SAS output position, lateral	%	DS01	AP
SASE	SAS output position, long.	%	DS00	AP
SASR	SAS output position, dir.	%	DS02	AP
STABLR	Stabilator position	deg	R003	AP
TRIP	Tail-rotor imprest pitch	deg	R021	AP

Table 4. Test condition parameters

Mnemonic	Description	Units	Item code	Group
ALPHA	Angle of attack	deg	DAA0	TC
AXCG	Linear acceleration c.g., longitudinal	g	DL00	TC
AYCG	Linear acceleration c.g., lateral	g	DL01	TC
AYCGSENS	Sensitive lateral acceleration	g	AF90	TC
AZCG	Linear acceleration c.g., normal	g	DL02	TC
BETA	Angle of sideslip	deg	DSS0	TC
HEADIN	Aircraft heading at 25 sps[a]	deg	DA12	TC
HEADING	Aircraft heading	deg	DA02	TC
LSSX	Raw airspeed (LASSIE) long	knots	VX03	TC
LSSY	Raw airspeed (LASSIE) lateral	knots	VY03	TC
LSSZ	Raw airspeed (LASSIE) vertical	ft/min	VZ03	TC
PAICB	Boom altitude	inHg	H001	TC
PAICS	Ship's altitude	inHg	H002	TC
PITCHAT	Pitch attitude at 25 sps	deg	DA10	TC
PITCHATT	Attitude, pitch angle	deg	DA00	TC
PTCHACC	Pitch acceleration	deg/sec^2	DAC0	TC
PTCHRATE	Angular rate, pitch	deg/sec	DR00	TC
QCICB	Boom airspeed	inHg	V001	TC
QCICS	Ship's airspeed	inHg	V002	TC
RADALT	Altitude (radar range)	ft	H003	TC
ROLLACC	Roll acceleration	deg/sec^2	DAC1	TC
ROLLAT	Roll attitude at 25 sps	deg	DA11	TC
ROLLATT	Attitude, roll angle	deg	DA01	TC
ROLLRATE	Angular rate, roll	deg/sec	DR01	TC
TTIC	OAT (outside air temperature)	°C	T100	TC
YAWACC	Yaw acceleration	deg/sec^2	DAC2	TC
YAWATT	Alternate for heading	deg	DA22	TC
YAWRATE	Angular rate, yaw	deg/sec	DR02	TC

[a]Samples per second.

Table 5. Engine parameters

Mnemonic	Description	Units	Item code	Group
FCTS1	Engine 1 fuel total	0.1 gal	EF01	EP
FCTS2	Engine 2 fuel total	0.1 gal	EF02	EP
FCTSAPU	APU fuel totalizer	0.1 gal	EF03	EP
FUELTMP1	Engine fuel temp. no. 1	°C	EF07	EP
FUELTM2	Engine fuel temp. no. 2	°C	EF08	EP
MGT1	Turbine exhaust temp.	°C	ET01	EP
MGT2	Turbine 2 exhaust temp.	°C	ET02	EP
QEIC1	Engine 1 output shaft Q	ft·lb	EQ01	EP
QEIC2	Engine 2 output shaft Q	ft·lb	EQ02	EP
WFVOL1	Engine 1 fuel rate	gal/hr	EF05	EP
WFVOL2	Engine 2 fuel rate	gal/hr	EF06	EP

Table 6. Fuselage accelerometer table

Mnemonic	Description	Units	Item code	Group
AXPS	Pilot longitudinal accel.	g	AF00	VP
AYCS	Co-pilot lateral accel.	g	AF03	VP
AYPS	Pilot lateral accel.	g	AF01	VP
AYRAC	Aft cabin R lateral accel.	g	AF08	VP
AYRFC	Forward cabin R lateral accel.	g	AF05	VP
AYVT	Vertical tail lateral accel.	g	AF11	VP
AZCS	Co-pilot vertical accel.	g	AF04	VP
AZLAC	Aft cabin L vertical accel.	g	AF10	VP
AZLFC	Forward cabin L vertical accel.	g	AF07	VP
AZLST	Horiz. tip L long accel.	g	AF14	VP
AZPS	Pilot vertical accel.	g	AF02	VP
AZRAC	Aft cabin R vertical accel.	g	AF09	VP
AZRFC	Forward cabin R vertical accel.	g	AF06	VP
AZRST	Horiz tip R long accel.	g	AF13	VP
AZVT	Vertical tail vertical accel.	g	AF12	VP
MRAXHUB	Hub acceleration X	g	AH0X	VP
MRAYHUB	Hub acceleration Y	g	AH0Y	VP
MRAZHUB	Hub acceleration Z	g	AH0Z	VP

Table 7. Fuselage accelerometer locations

Sensor location	Longitudinal	Lateral	Vertical	FS	BL	WL
Pilots floor	X	X	X	253.0	31.0	206.7
Copilot floor		X	X	253.0	-31.0	206.7
Fwd. cabin floor right		X	X	295.0	35.5	206.7
Fwd. cabin floor left			X	295.0	-35.5	206.7
Aft cabin floor right		X	X	295.0	35.0	206.7
Aft cabin floor left			X	295.0	-35.0	206.7
Vertical tail		X	X	732.0	0.0	325.0
Horiz. tail tips (L&R)	X			702.0	±83.5	247.0

Table 8. Instrumented blade sensor list

Mnemonic	Description	Units	Item code	Group
AXMRT	Tip acceleration edgewise	g	BEAT	RP
AZMRR	Root acceleration flapping	g	BFAR	RP
AZMRT	Tip acceleration flapping	g	BFAT	RP
MRALSS	MR link load aft	lb	MR03	RP
MRBR5	MR rear bending 50% radius	$lb/in.^2$	BR50	RP
MRBR6	MR rear bending 60% radius	$lb/in.^2$	BR60	RP
MRBR7	MR rear bending 70% radius	$lb/in.^2$	BR70	RP
MREB5	MR edgewise bending 50% rad.	ft·lb	BE50	RP
MREB7	MR edgewise bending 70% rad.	ft·lb	BE70	RP
MREBX1	MR root edgewise bending	ft·lb	BE01	RP
MRFLAP	MR flapping	deg	BH01	RP
MRFLSS	MR link load forward	lb	MR00	RP
MRLAG	MR lead-lag	deg	BH00	RP
MRLSS	MR link load lateral	lb	MR01	RP
MRNB5	MR normal bending 50% radius	ft·lb	BN50	RP
MRNB6	MR normal bending 60% radius	ft·lb	BN60	RP
MRNB7	MR normal bending 70% radius	ft·lb	BN70	RP
MRNBX1	MR root normal bending	ft·lb	BN01	RP
MRPITCH	MR pitch	deg	BH02	RP
MRPR	MR pushrod load	lb	BP00	RP
MRSEBL	MR shaft bending	in.–lb	RQ11	RP

Table 9. Derived parameter list

Mnemonics	Description	Units	Item code	Group
AMU	Advance ratio, derived	—	VOMU	DP
CP	Power coef. (eng. q)	—	CPOO	DP
CPROTOR	MR power coef. (QMR), derived	—	CPMR	DP
CT	MR thrust coef., derived	—	CTOO	DP
FLAP	Corrected blade flapping	deg	FLAP	DP
FSCG	A/C longitudinal c.g., derived	in.	FSCG	DP
GW	A/C gross weight, derived	lb	FSGW	DP
HDB	Boom density altitude, derived	ft	HDBO	DP
HPB	Boom press. alt. corrected	ft	HPBC	DP
HPS	Ship press. alt. corrected	ft	HPSC	DP
LEADLAG	Corrected blade lead-lag	deg	LLAG	DP
MTIP	Advancing-tip Mach number	—	VTIP	DP
PITCHC	Corrected blade pitch	deg	PTCH	DP
REFRPM	Referred main-rotor speed	rpm	VRMR	DP
SHPT	Combined engine shaft hp	hp	ESHP	DP
VCALB	Boom calibrated airspeed	knots	VCAS	DP
VT	Corrected compiled TAS	knots	VTRU	DP
VTB	Boom true airspeed	knots	VTAS	DP

Table 10. Speed sweep test matrix

Condition	C_T/σ	Pressure altitude, ft	Calibrated airspeed
Level flight	0.08		0-40 in 5-knot increments 40-140 in 10-knot increments 140-V_h in 5-knot increments
	0.09	4,000 to 6,500	0-40 in 5-knot increments 40-140 in 10-knot increments 140-V_h in 5-knot increments
	0.10		0-40 in 5-knot increments 40-120 in 10-knot increments 120-V_h in 5-knot increments
Climb and powered descent	0.08		140-V_{ne} in 5-knot increments
	0.09		130-V_{ne} in 5-knot increments
	0.10		120-V_{ne} in 5-knot increments

Table 11. Maneuvering flight test matrix

Condition	C_T/σ	Pressure altitude, ft	Vertical g loading	Calibrated airspeed
Left and right turns	0.09	7,900 to 9,500	1.0 1.25 1.5 1.75 2.0	120 - V_{ne} in 20-knot increments
	0.10	7,900 to 9,500	1.0 1.25 1.5 1.75 2.0	120 - V_{ne} in 20-knot increments

Table 12. Dynamic stability test matrix

Condition	C_T/σ	Pressure altitude, ft	Calibrated airspeed	Axis
Doublet	0.08	4,000 to 6,500	65	Longitudinal, lateral directional, collective
	0.08	4,000 to 6,500	140	Longitudinal, lateral directional, collective
Sinusoidal	0.00	2,500	Hover	Longitudinal, lateral directional, collective
	0.08	4,000 to 6,500	140	Longitudinal, lateral directional, collective

Table 13. Acoustic test matrix

Calibrated airspeed, knots	Rate of descent, ft/min	C_T/σ	Altitude, ft	Positions relative to YO-3A
60	0	0.08		Left, right, trail
	400		4,000	Left, right, trail
	800			Left
80	0	0.08	to	Left, right, trail
	400			Left, right
	800		7,000	Left
100	0	0.08		Left, trail
	400			Trail
	800			Trail

Table 14. Aircraft-state statistical summaries for the speed-sweep time-history plots

Counter	μ	α	β	Engine-Q
1708	0.096	−1.1	−13.1	1398
1704	0.197	1.6	−7.4	1150
1717	0.314	−2.8	−4.1	1670
3016	0.395	−5.2	−1.3	2701
3011	0.460	−2.6	−2.5	2361

Table 15. Time intervals for maneuver data

Counter	Test point description	Start time, sec
3305	110 KIASB,.09CTS,0 AOB,MVR	2
3306	110 KIASB,.09CTS,37L AOB,MVR	7
3307	110 KIASB,.09CTS,48L AOB,MVR	4
3308	110 KIASB,.09CTS,55L AOB,MVR	4.5
3309	110 KIASB,.09CTS,60L AOB,MVR	4
3310	129 KIASB,.09CTS,0 AOB,MVR	6
3311	129 KIASB,.09CTS,37L AOB,MVR	7
3312	129 KIASB,.09CTS,48L AOB,MVR	2
3313	129 KIASB,.09CTS,55L AOB,MVR	3.5
3314	129 KIASB,.09CTS,60L AOB,MVR	5
3315	138 KIASB,.09CTS,0 AOB,MVR	2.5
3316	138 KIASB,.09CTS,37L AOB,MVR	3
3317	138 KIASB,.09CTS,37L AOB,MVR	2.5
3318	138 KIASB,.09CTS,48L AOB,MVR	6
3319	138 KIASB,.09CTS,48L AOB,MVR	5
3320	138 KIASB,.09CTS,60L AOB,MVR	4
3505	148 KIASB,.09CTS,0 AOB,MVR	6
3506	148 KIASB,.09CTS,37L AOB,MVR	4
3507	148 KIASB,.09CTS,48L AOB,MVR	4
3508	148 KIASB,.09CTS,55L AOB,MVR	5.2
3509	148 KIASB,.09CTS,60L AOB,MVR	4
3510	158 KIASB,.09CTS,0 AOB,MVR	7
3511	158 KIASB,.09CTS,37L AOB,MVR	6.5
3512	158 KIASB,.09CTS,48L AOB,MVR	5
3513	158 KIASB,.09CTS,55L AOB,MVR	3
3514	158 KIASB,.09CTS,60L AOB,MVR	3.5
3515	163 KIASB,.09CTS,37L AOB,MVR	1.4
3516	163 KIASB,.09CTS,60L AOB.MVR	0.25
3517	163 KIASB,.09CTS,55L AOB,MVR	4
3605	129 KIASB,.09CTS,0 AOB,MVR	2
3606	129 KIASB,.09CTS,37R AOB,MVR	8
3607	129 KIASB,.09CTS,37R AOB,MVR	2
3608	129 KIASB,.09CTS,48R AOB,MVR	4
3609	129 KIASB,.09CTS,60R AOB,MVR	4
3610	138 KIASB,.09CTS,0 AOB,MVR	8
3611	138 KIASB,.09CTS,37R AOB,MVR	5.6
3612	138 KIASB,.09CTS,48R AOB,MVR	2
3613	138 KIASB,.09CTS,55R AOB,MVR	6
3614	138 KIASB.,09CTS,60R AOB,MVR	8
3615	158 KIASB,.09CTS,0 AOB,MVR	2
3616	158 KIASB,.09CTS,37R AOB,MVR	7
3617	158 KIASB,.09CTS,60R AOB,MVR	8
3618	158 KIASB,.09CTS,55R AOB,MVR	8
3619	163 KIASB,.09CTS,0 AOB,MVR	8
3620	163 KIASB,.09CTS,37R AOB,MVR	5
3621	163 KIASB,.09CTS,60R AOB,MVR	7

Table 16. Trim conditions for doublet maneuvers

State or control	Longitudinal doublet	Pedal doublet
VCAS, knots	62	136
VTAS, knots	68	152
Longstk, in.	4.5	3.5
Latstk, in.	4.8	5.2
Pedal, in.	3.2	3.3
Collstk, in.	4.3	7.9
α, deg	0.8	-5.4
β, deg	-8.3	-1.1
θ, deg	1.5	-1.7
ϕ, deg	-1.4	-0.54
ψ, deg	13	34
ω, rpm	260	259
μ	0.156	0.352
M_{tip}	0.75	0.88
C_T/σ	0.08	0.08

Table 17. Nondimensionalized phase relationship of 4-1/rev frequency content

	1704 to 1708	1717 to 1708	3016 to 1708	3011 to 1708
1/rev	-11.1	-16.6	-23.6	-27.7
4/rev	-12.2	-36.7	-42.2	-36.7

Table 18. UH-60 blade modal frequencies and damping

Description	Frequency, Hz	% Critical damping
1st flapwise	4.34	0.27
2nd flapwise	12.55	0.09
3rd flapwise	24.99	0.12
4th flapwise	41.63	0.14
5th flapwise	63.71	0.16
1st torsional	44.55	0.10
2nd torsional	82.44	0.21
1st chordwise	25.40	0.24
2nd chordwise	67.38	0.14

148

Table 19. Statistical aircraft-state values for low-speed data split time-history plots

Counter	μ	PITCHATT	Collstk	Engine hp	C_T/σ
1710	0.034	4.9	5.5	1505	0.0904
1711	0.016	8.0	6.0	1760	0.0904
1712	0.029	7.8	6.0	1679	0.0912
1713	0.228	2.3	5.4	1145	0.0914
1807	−0.006	5.1	7.2	2133	0.0899
1808	−0.007	4.2	7.3	2203	0.0901
1905	0.022	6.8	7.2	2242	0.0907
1906	0.008	5.0	7.2	2185	0.0896
1907	0.020	4.3	7.1	2149	0.0895
1908	0.032	6.4	6.9	1969	0.0899
1909	0.034	5.9	7.0	2054	0.0906

PAGE 150 INTENTIONALLY BLANK
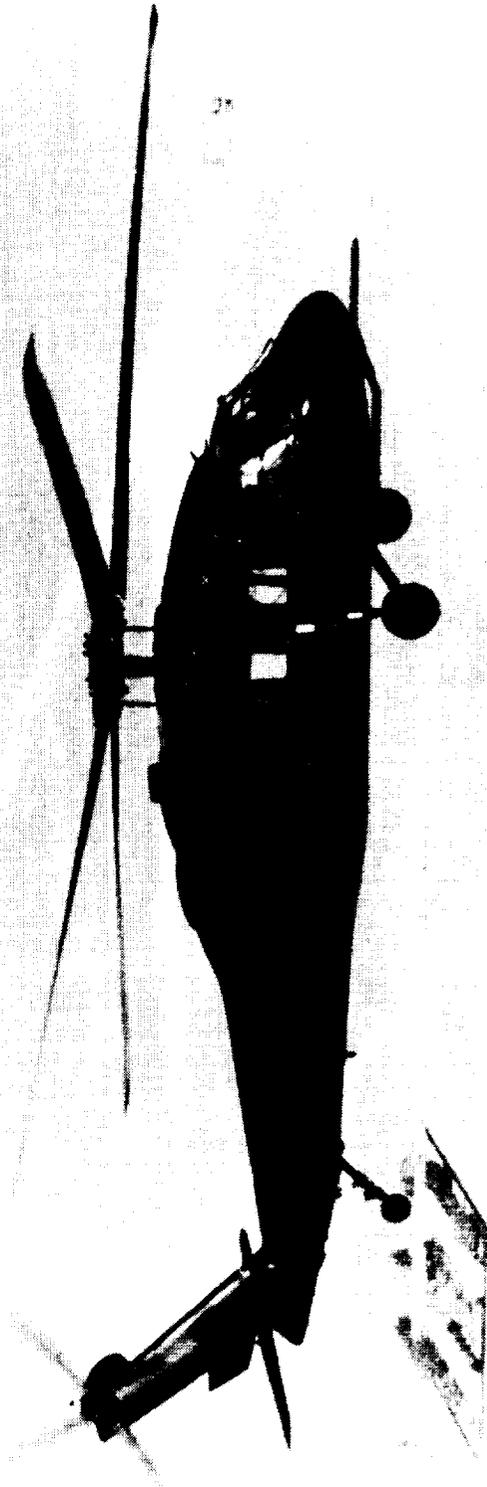
Figure 1. UH-60 Black Hawk.
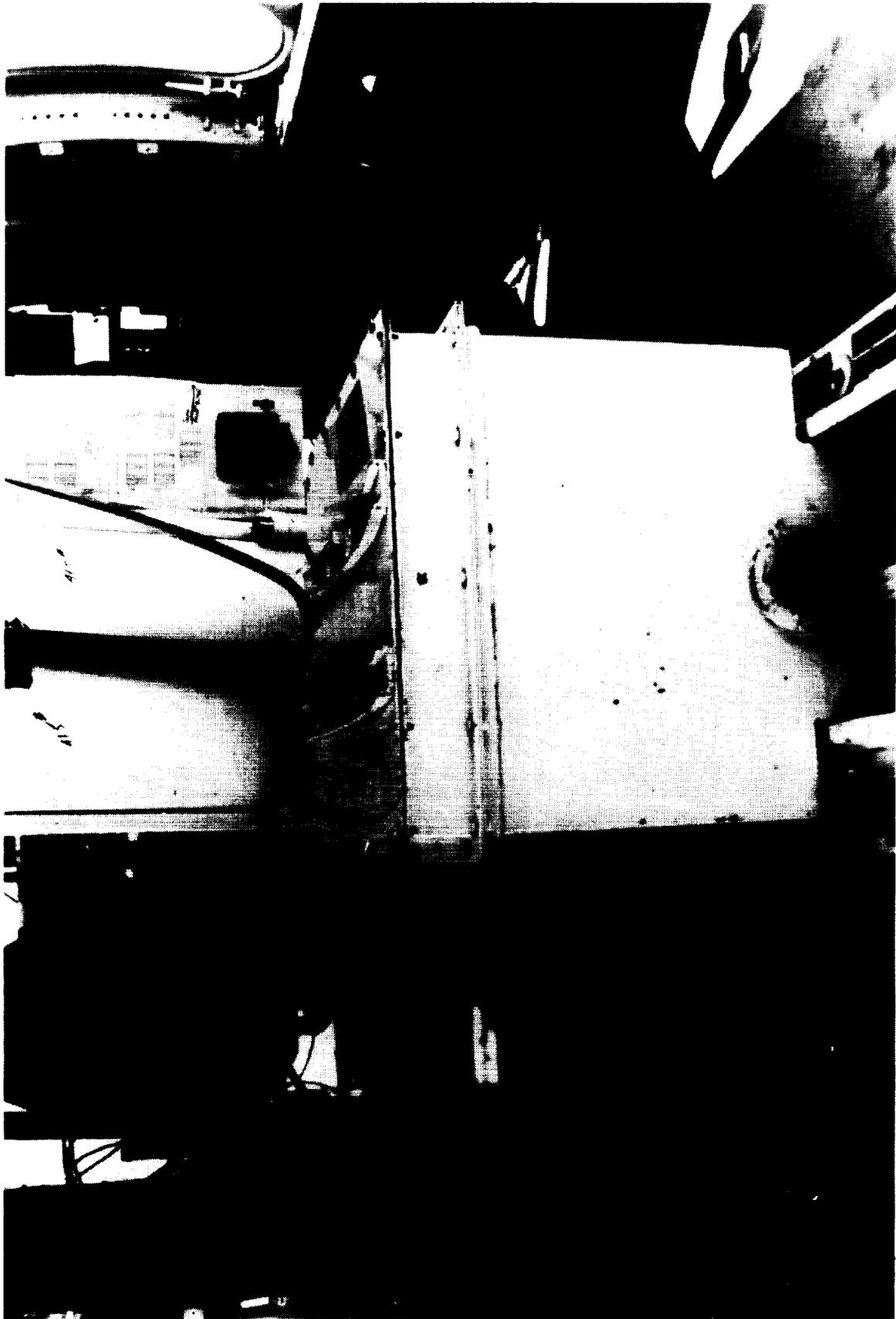
Figure 2. Ballast cart.
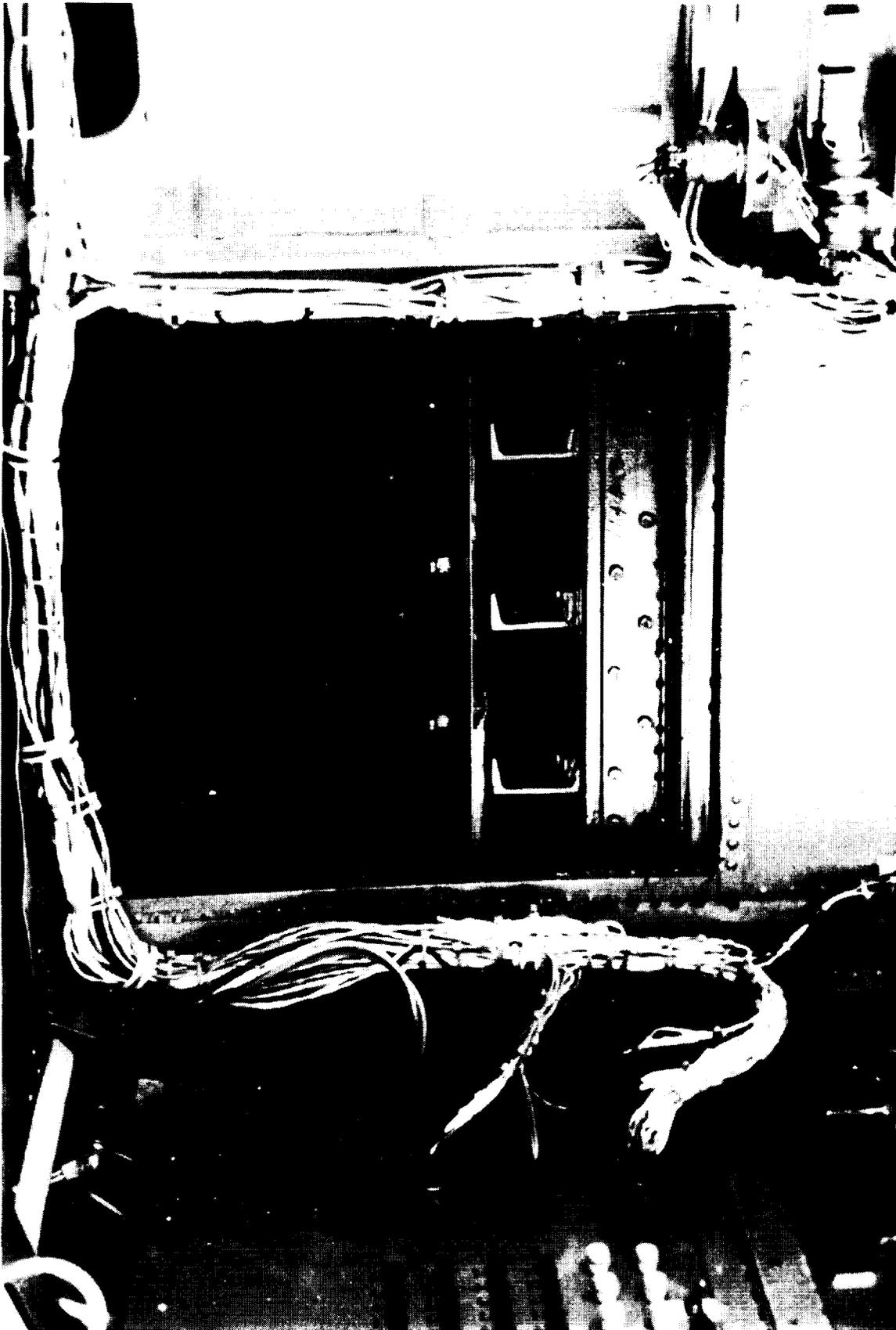
Figure 3. Fuel tank ballast weight.
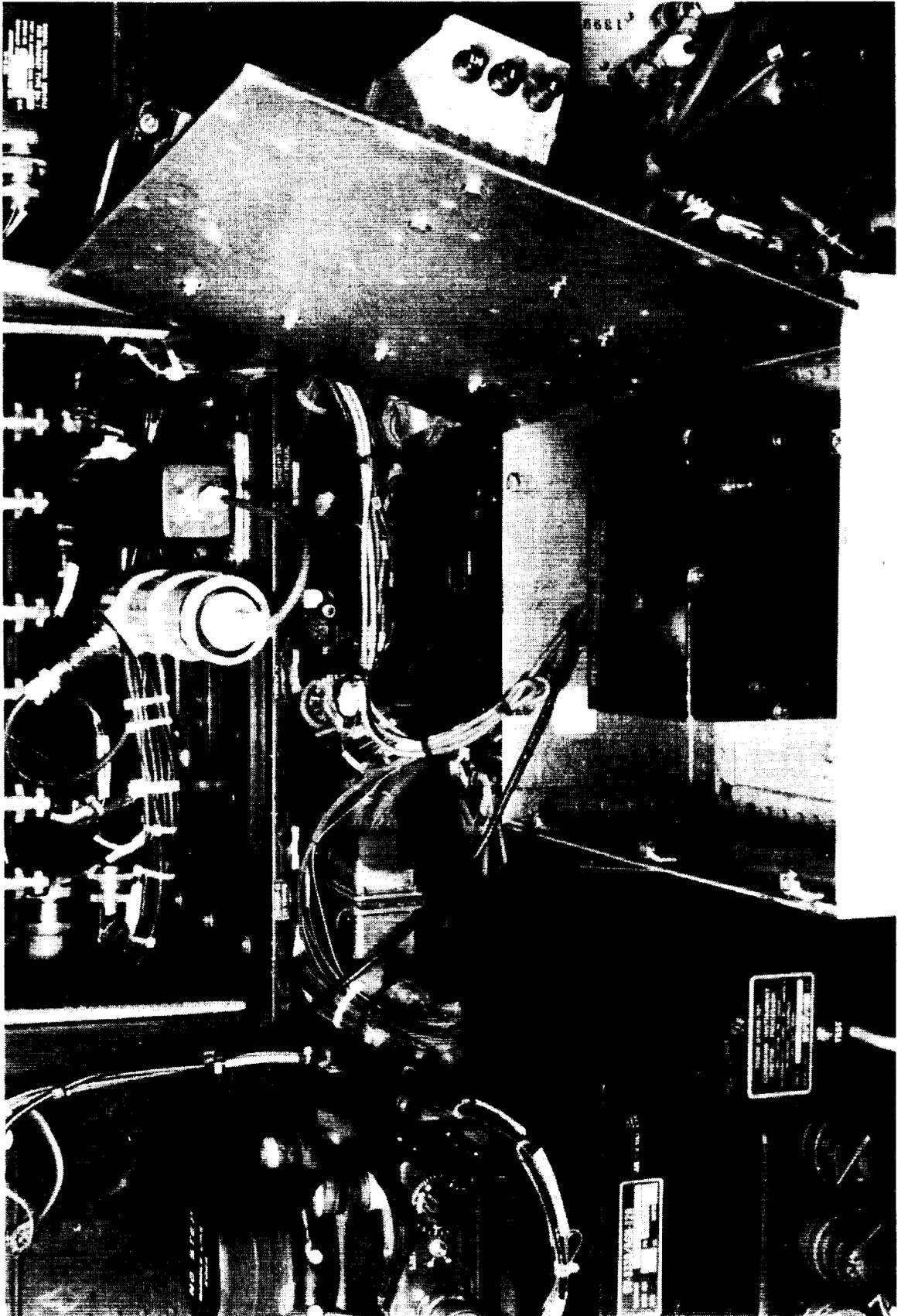
Figure 4. 1/rev transmitter site.

154
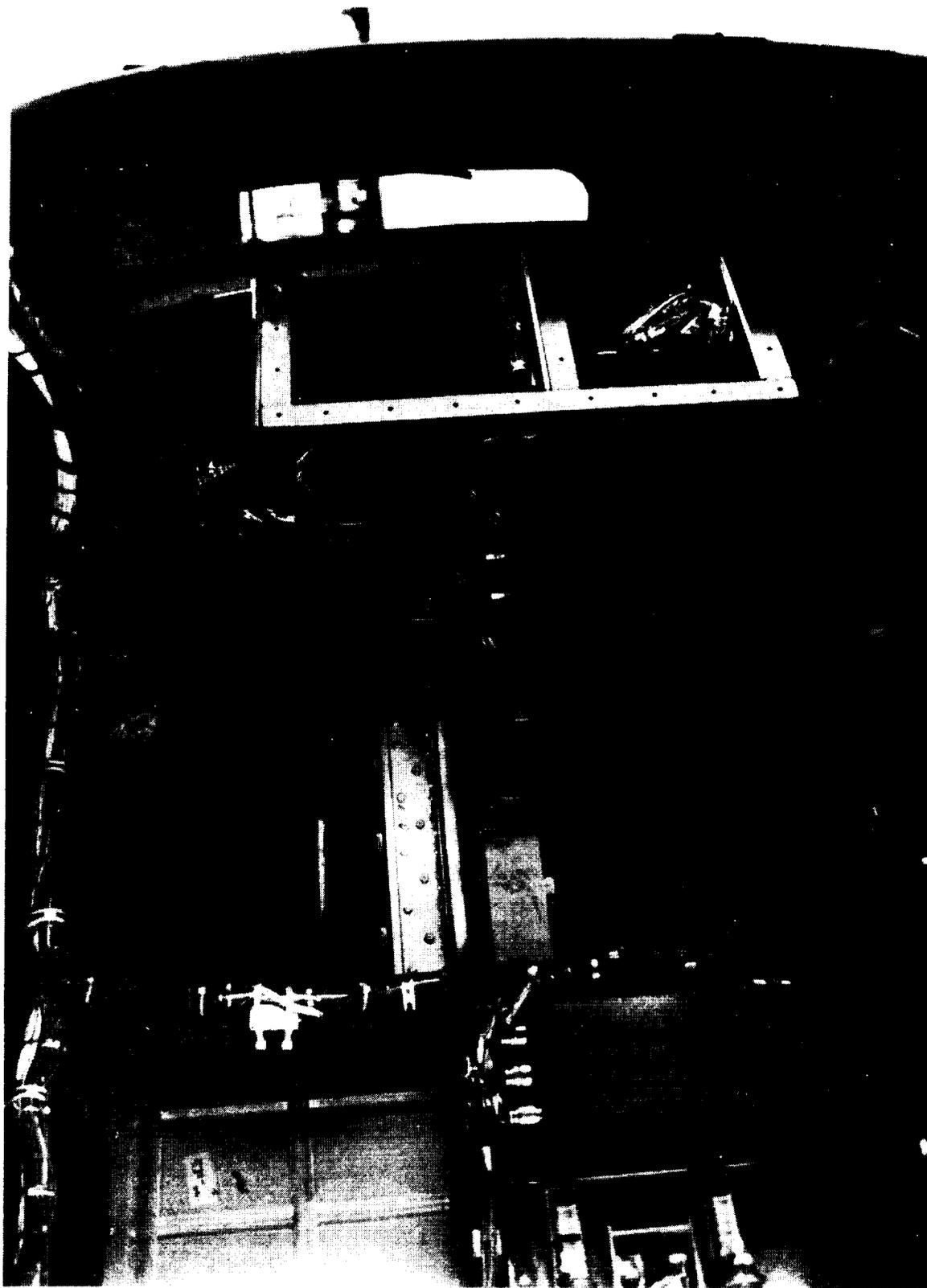
(a) Port rack.

Figure 5. Instrument pallet on aft bulkhead.
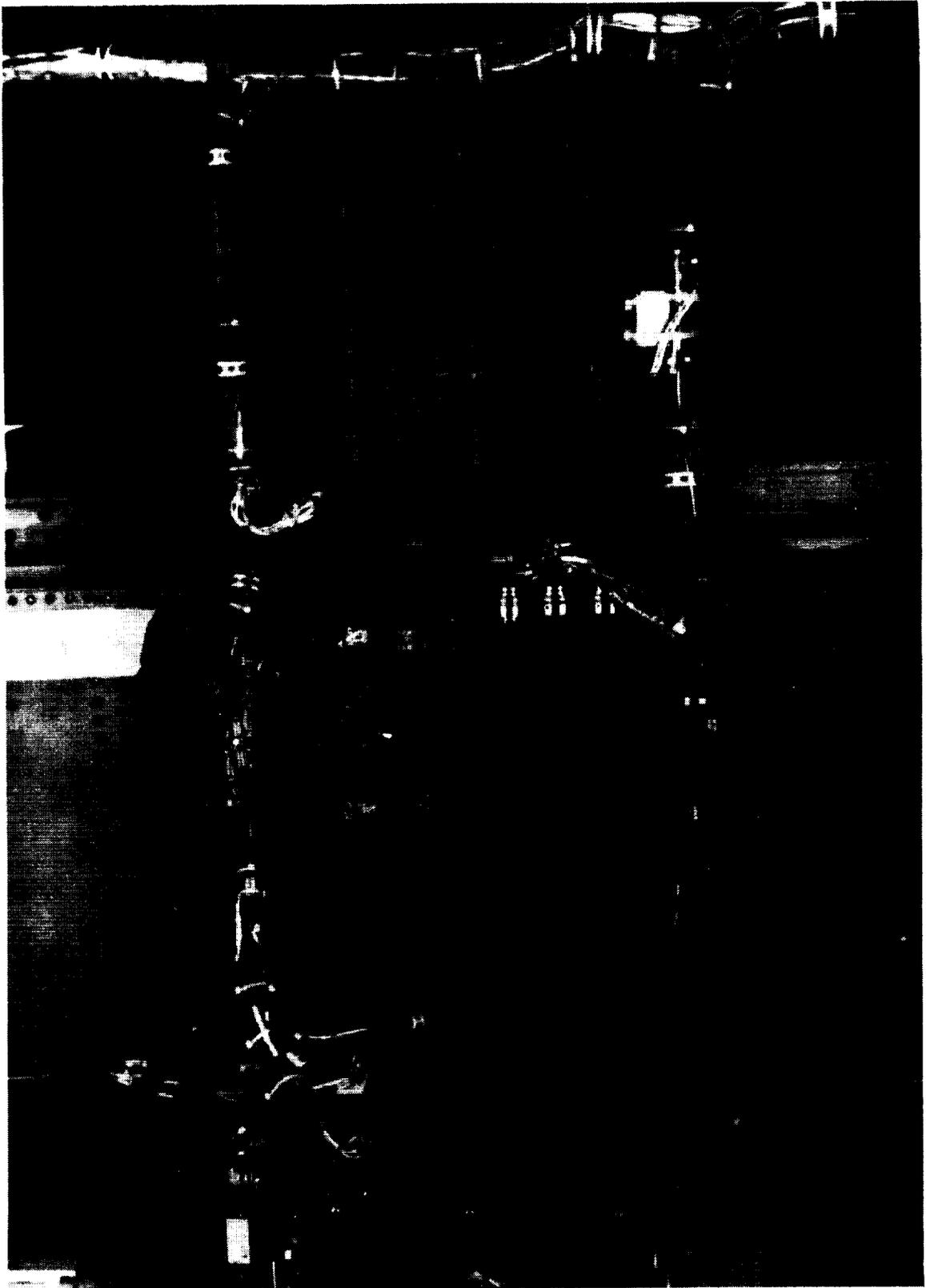
(b) Center rack.

Figure 5. Continued.

156

(c) Starboard rack.

Figure 5. Concluded.
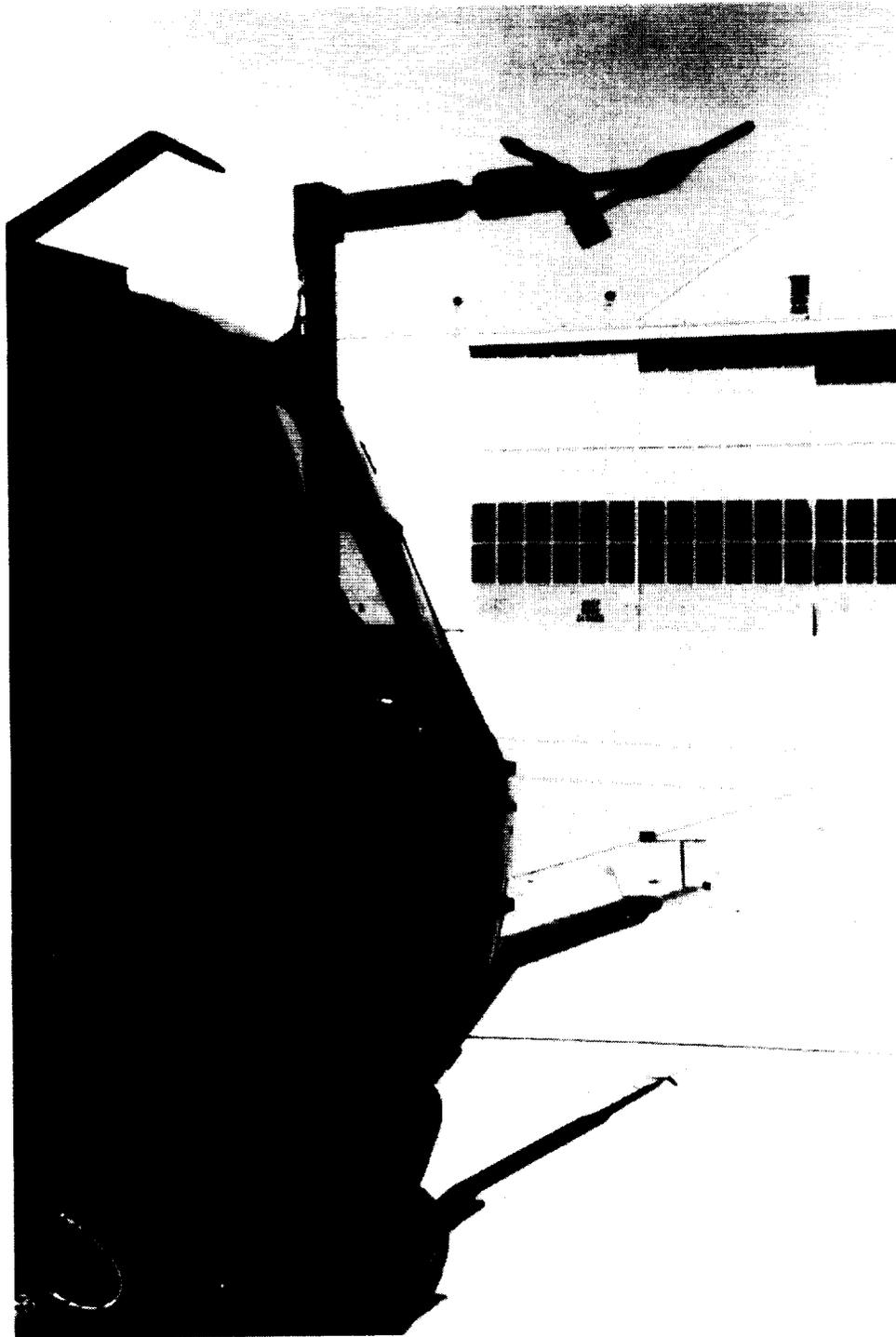
Figure 6. Low-airspeed sensor.
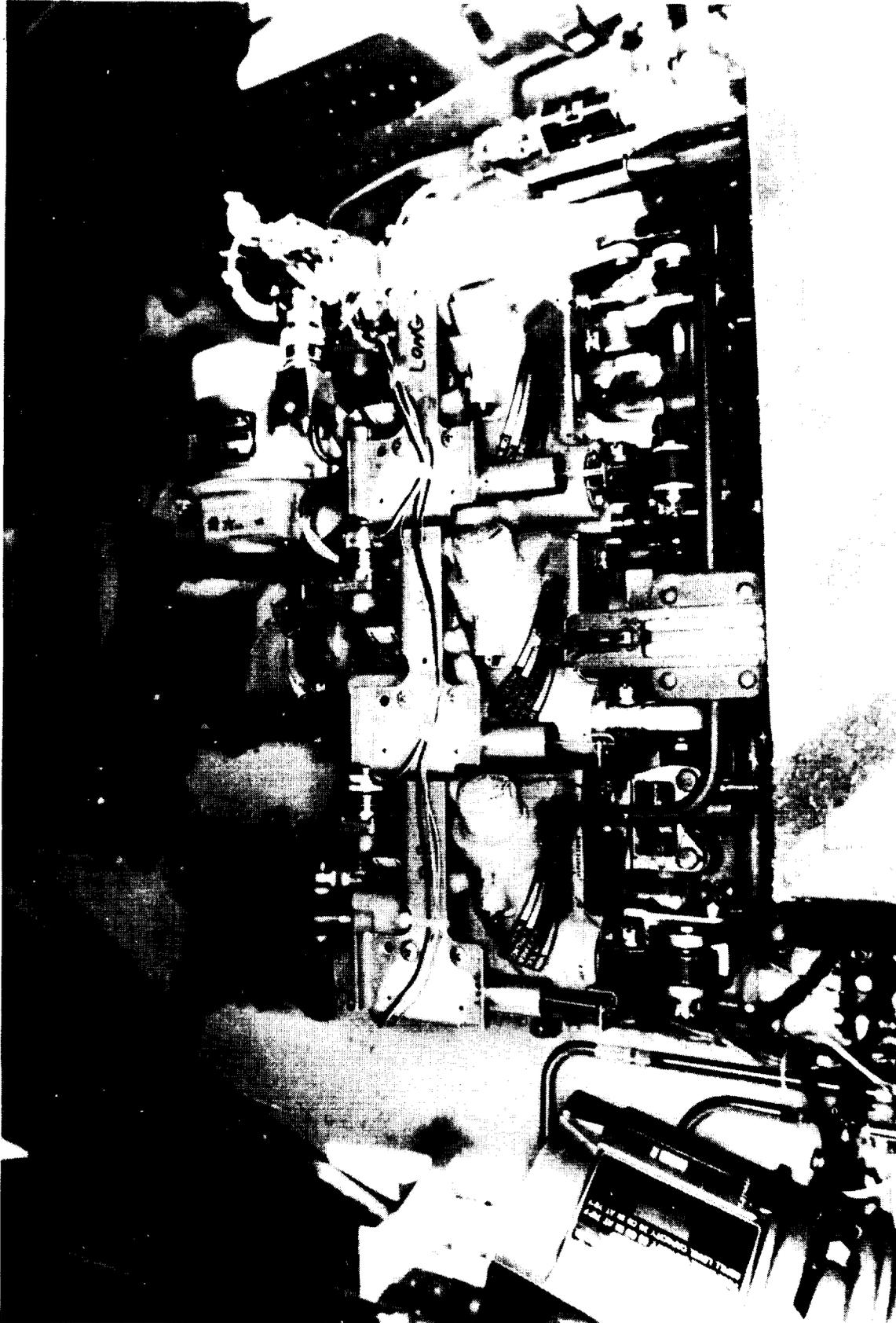
Figure 7. Primary servos.

Figure 8. Tail-rotor slip-ring housing.

160

Figure 9. Tail-rotor contactor.
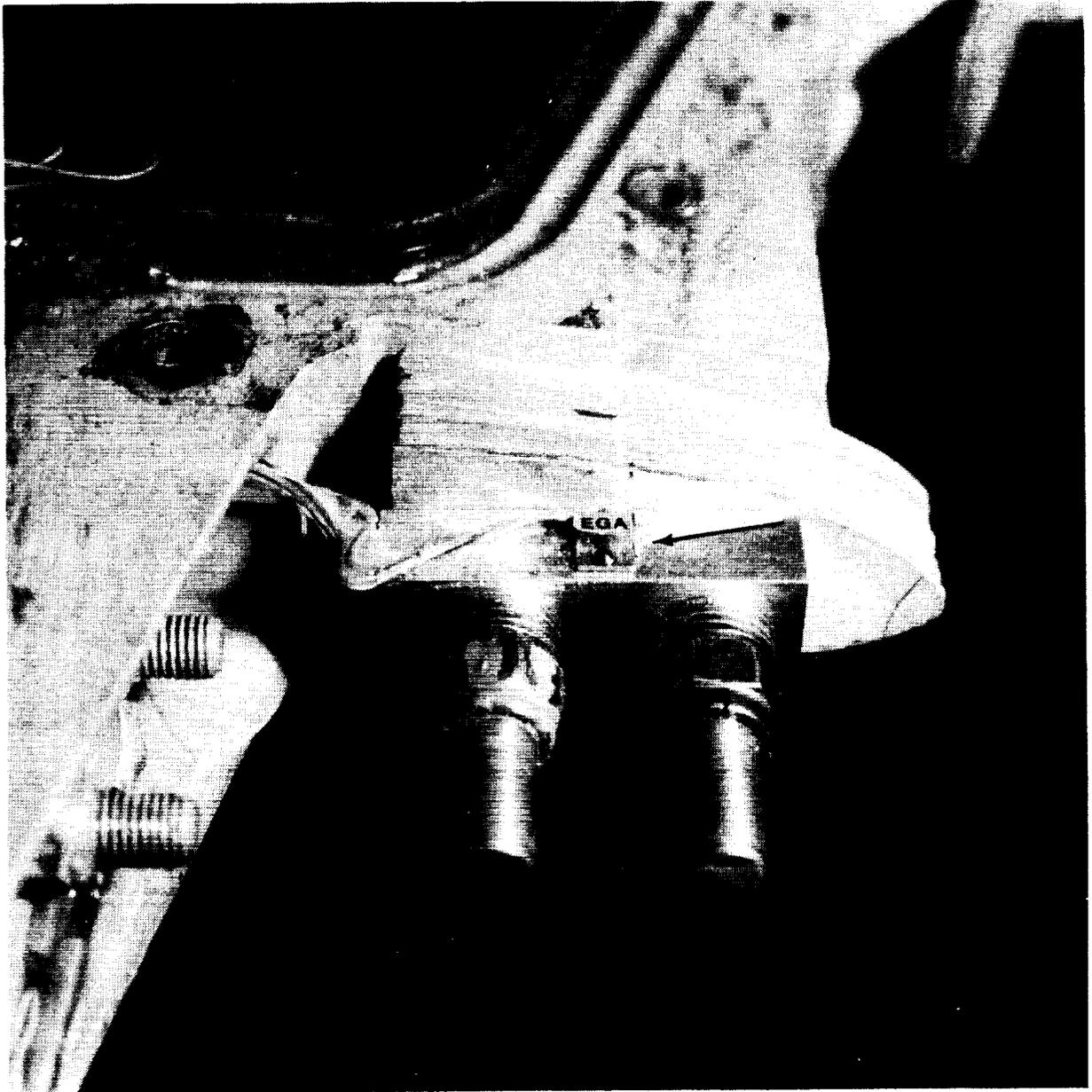
Figure 10. Tip accelerometer.

162
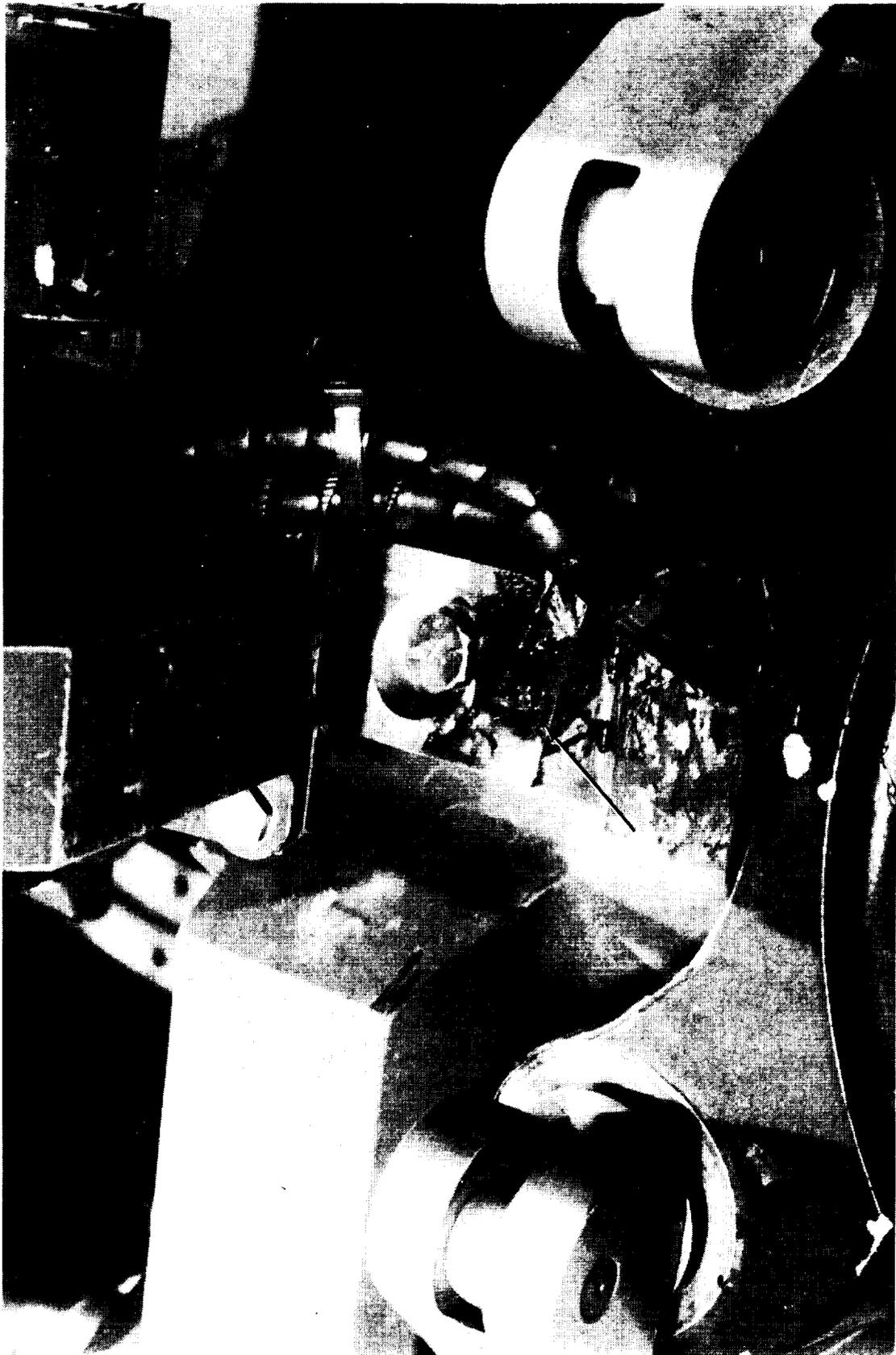
Figure 11. Root accelerometer.
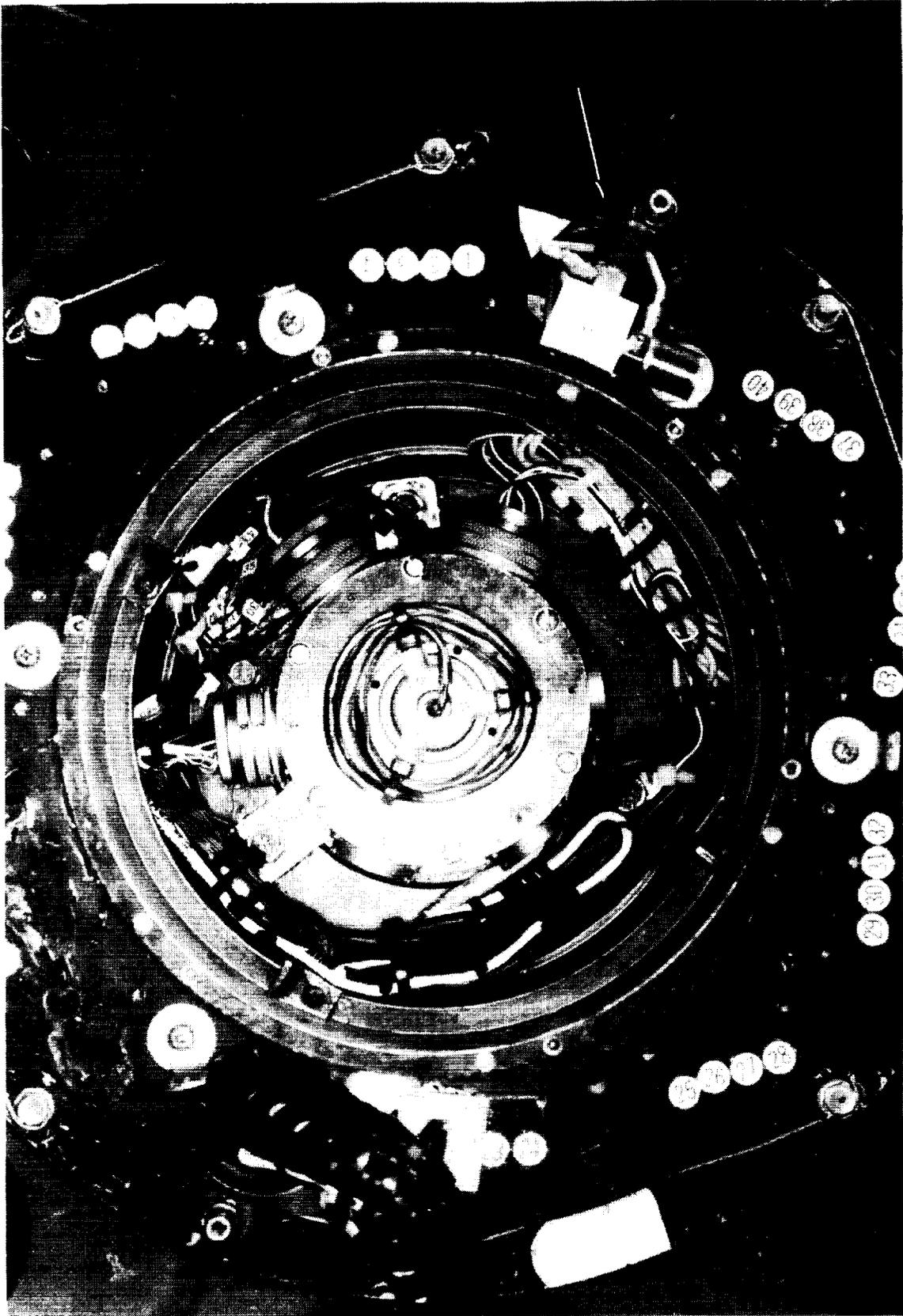
Figure 12. Orthogonal accelerometers

164
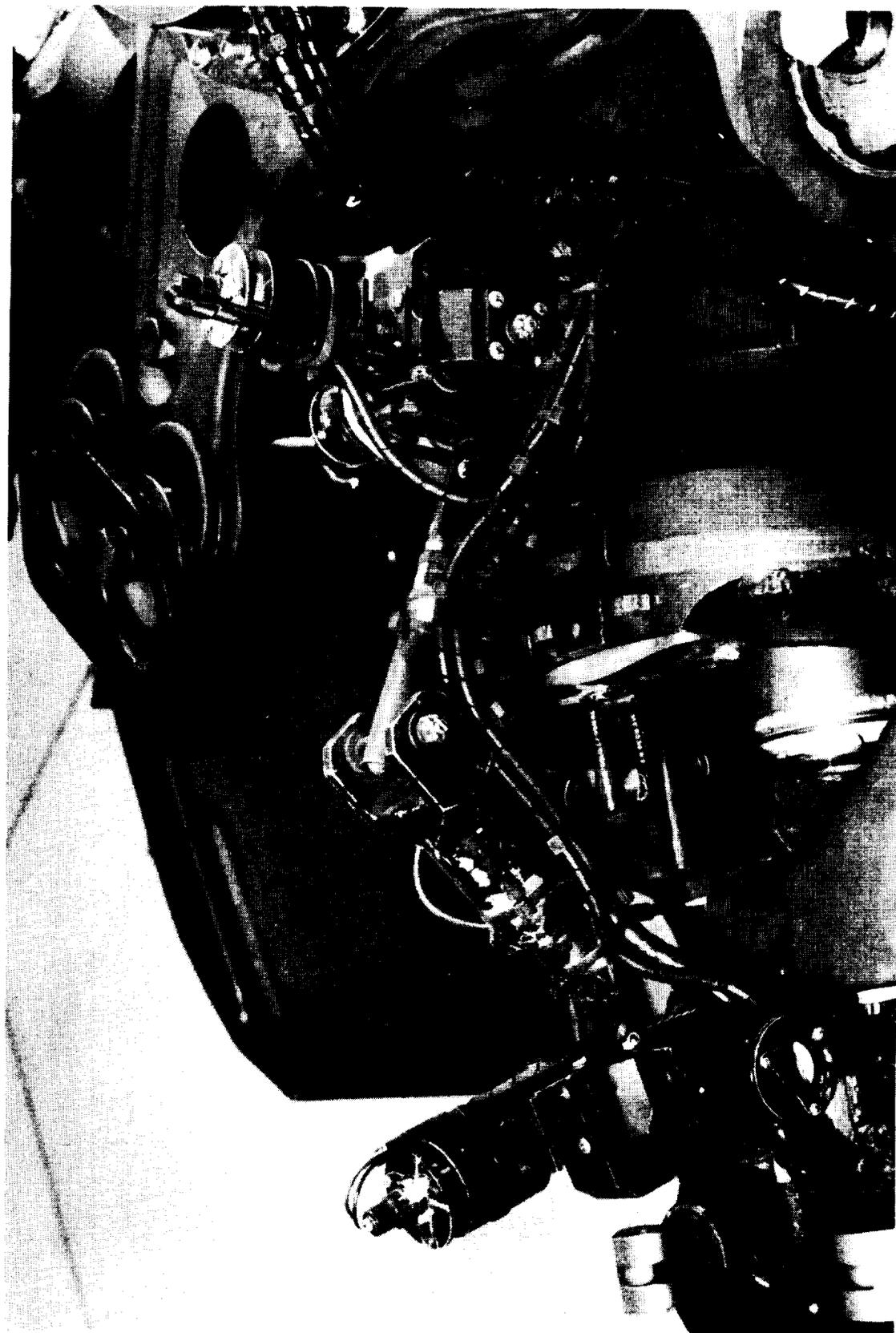
Figure 13. Blade-motion hardware.
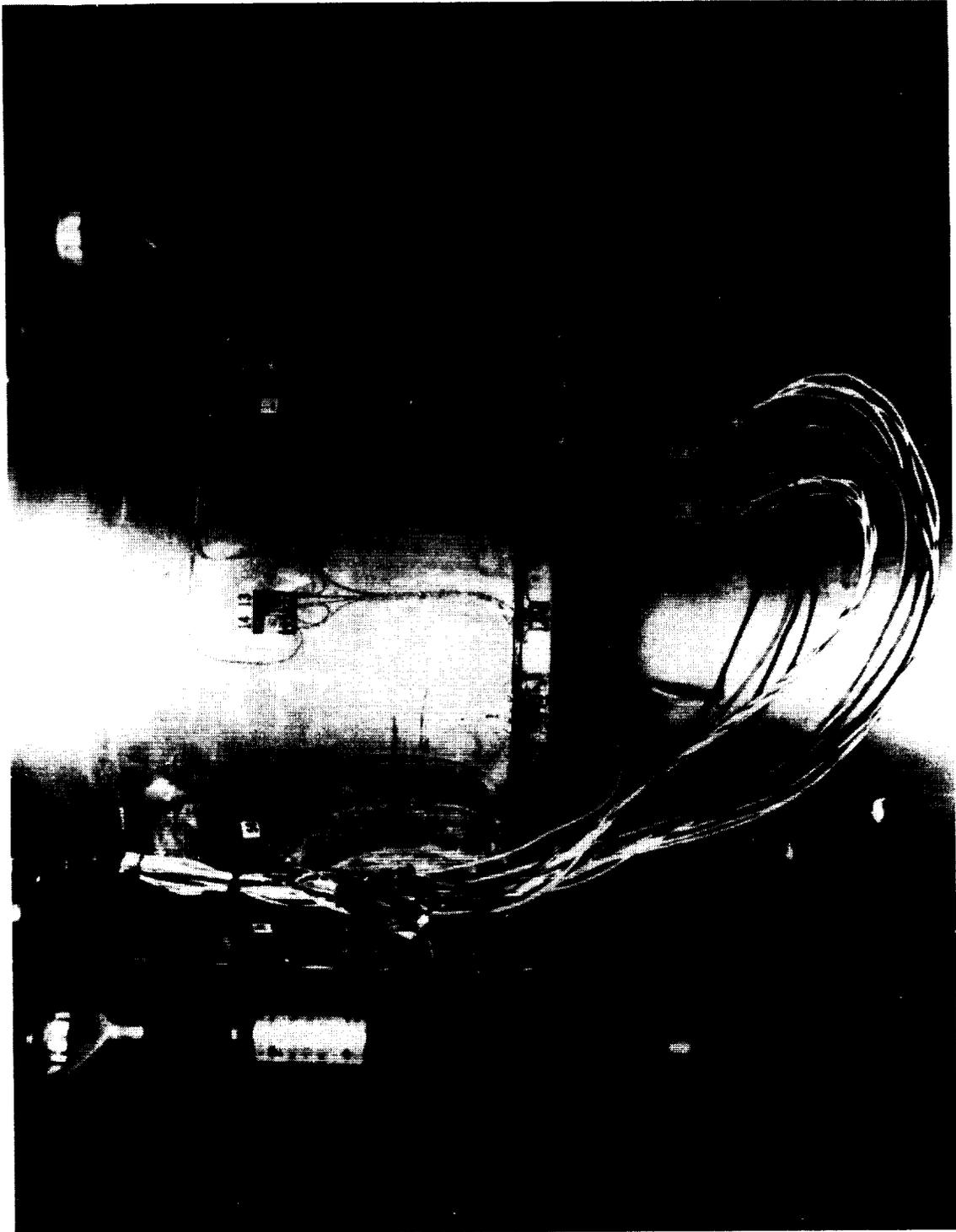
Figure 14. Shaft strain gauges.
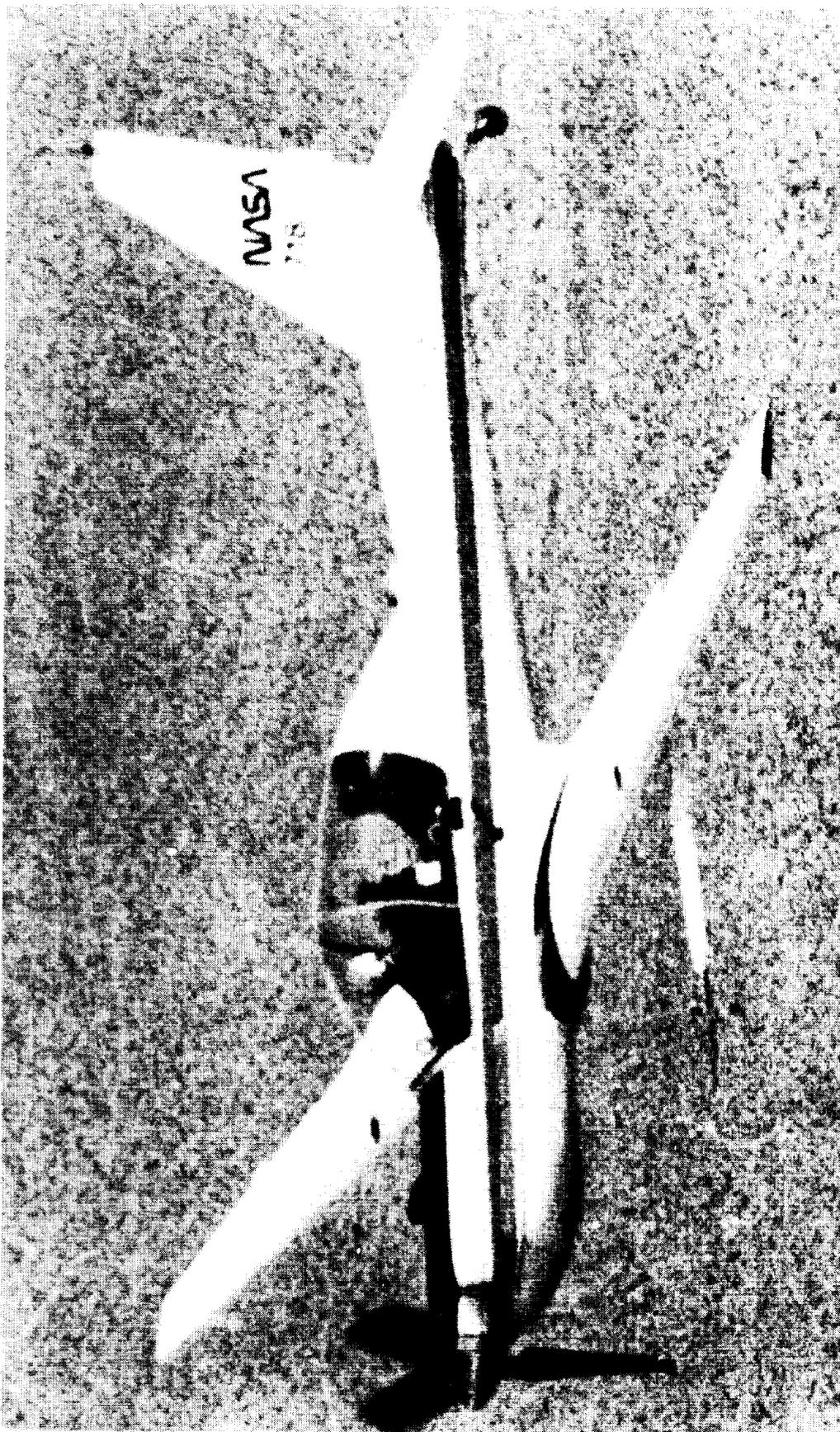
Figure 15. YO-3A aircraft.

Figure 16. *UH-60 and YO-3A information.*
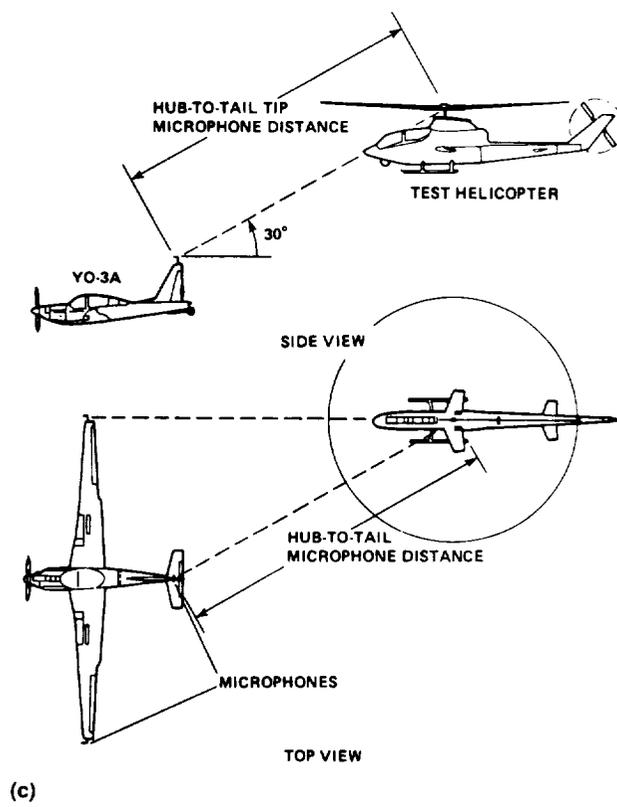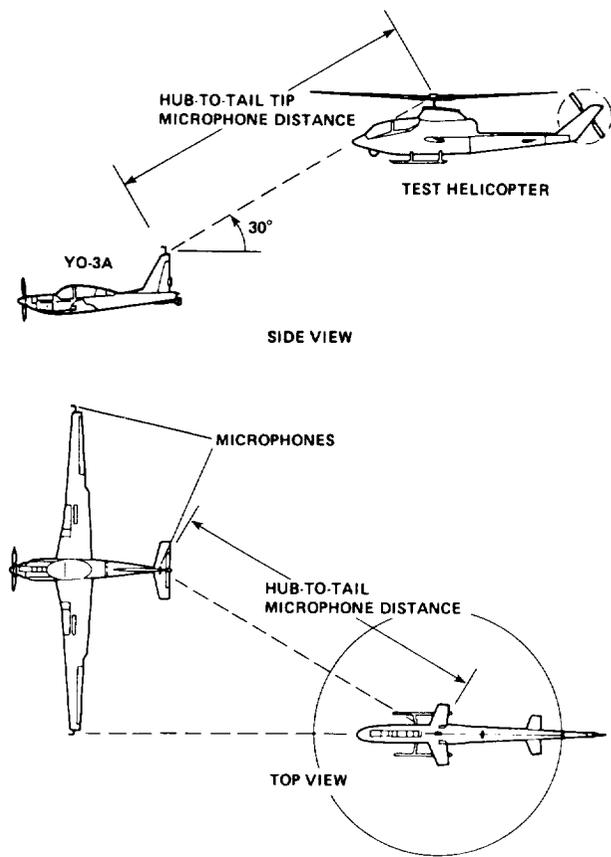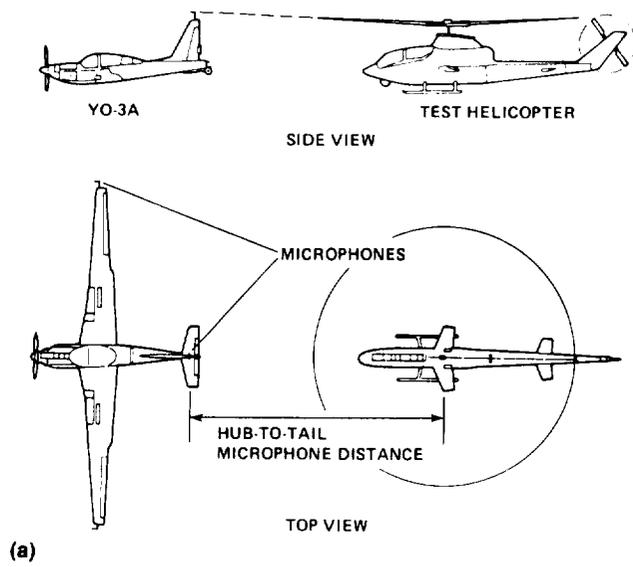
Figure 17. YO-3A/UH-60A formations. (a) Trail formation, (b) left position, (c) right position.

UH-60 BLACK HAWK PHASE I DATA PROCESSING
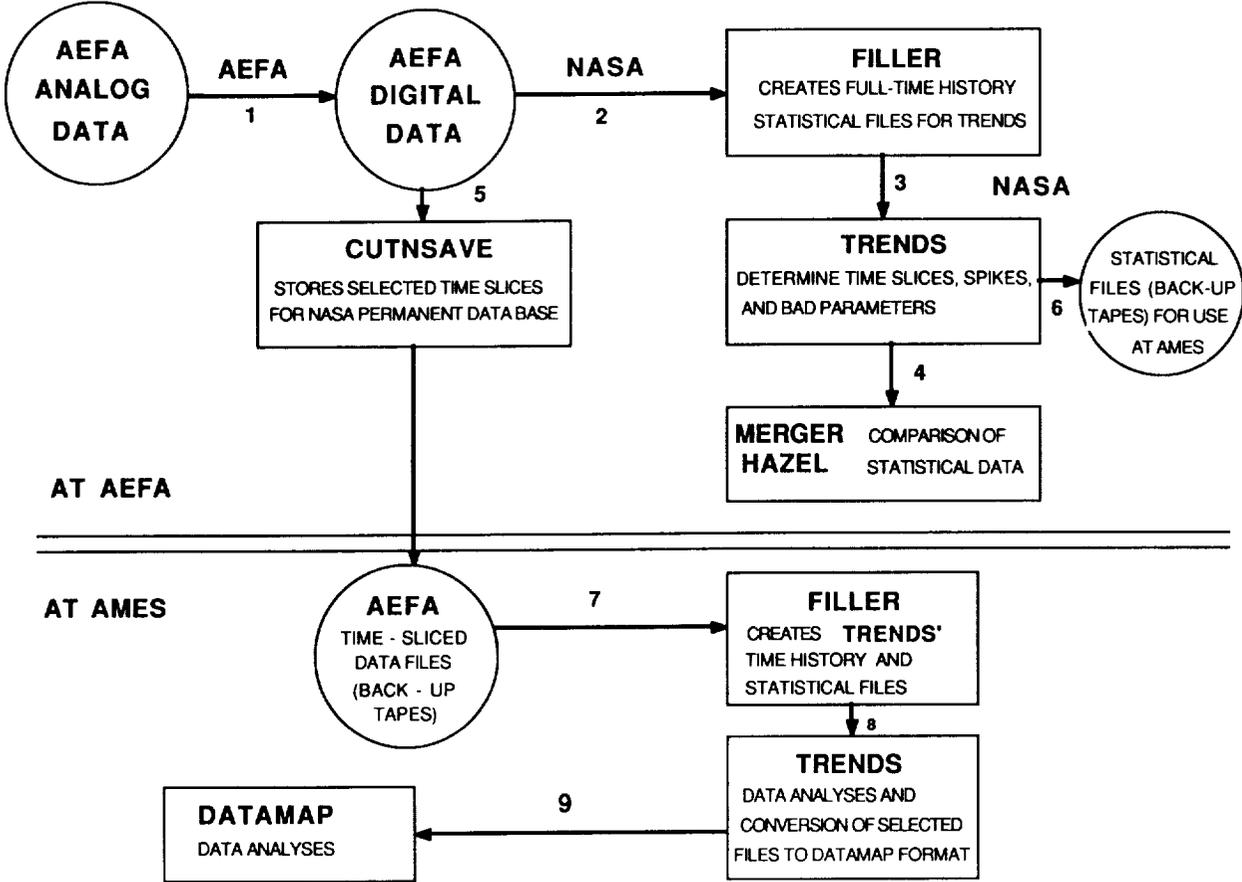
Figure 18. Data processing flowchart.
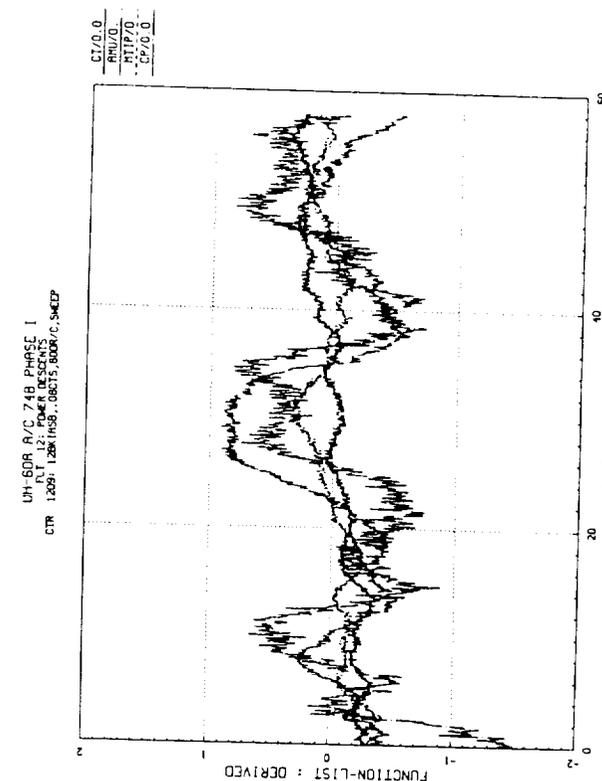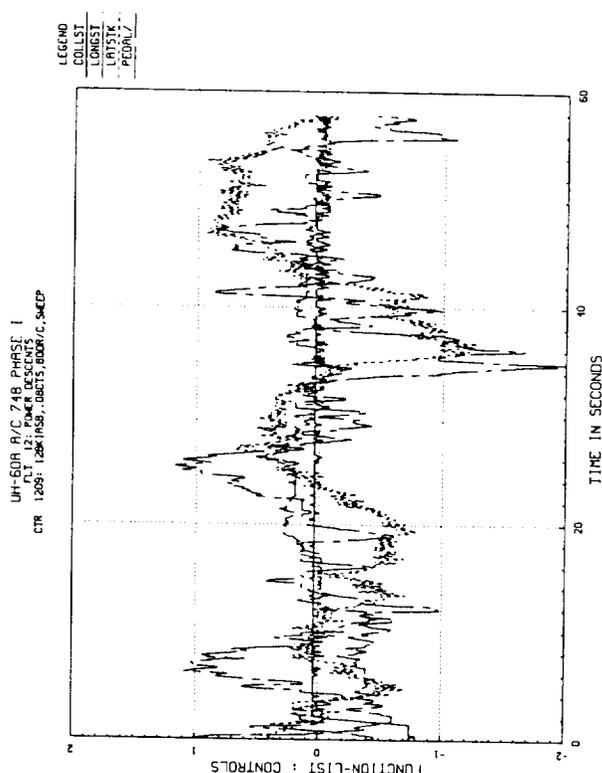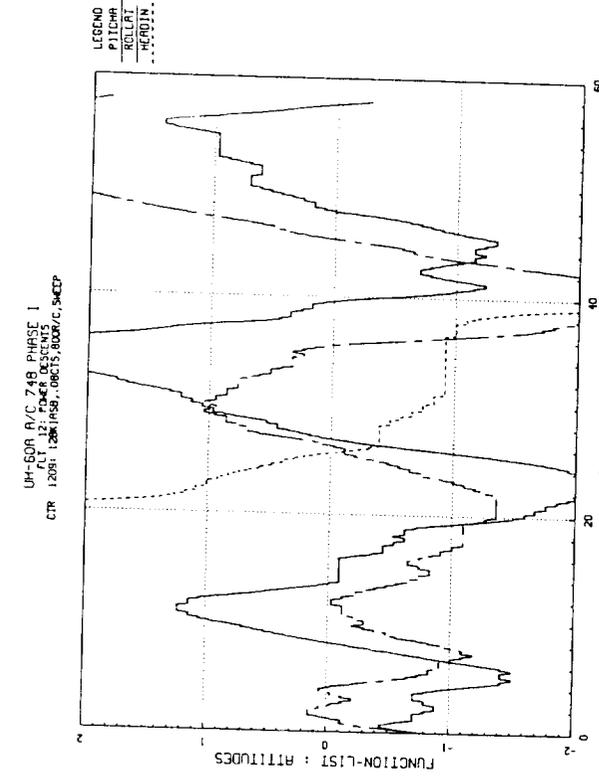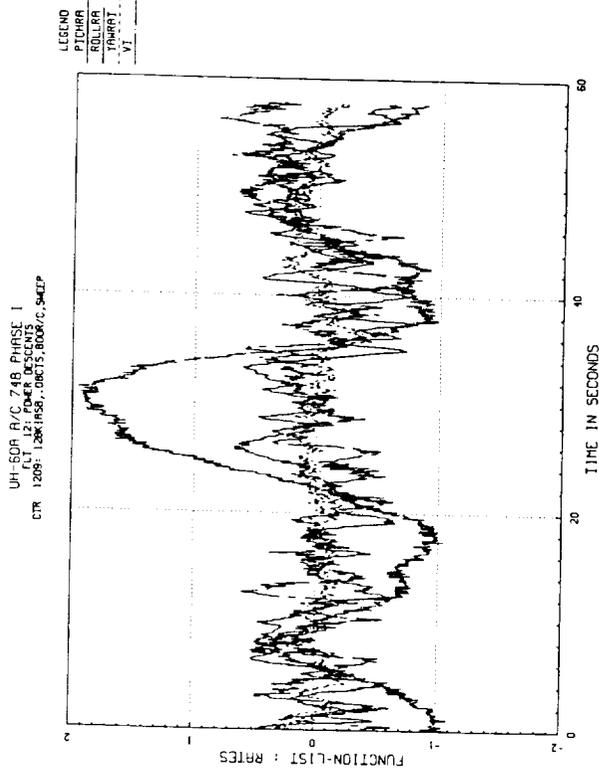
Figure 19. Sample normalized plots.
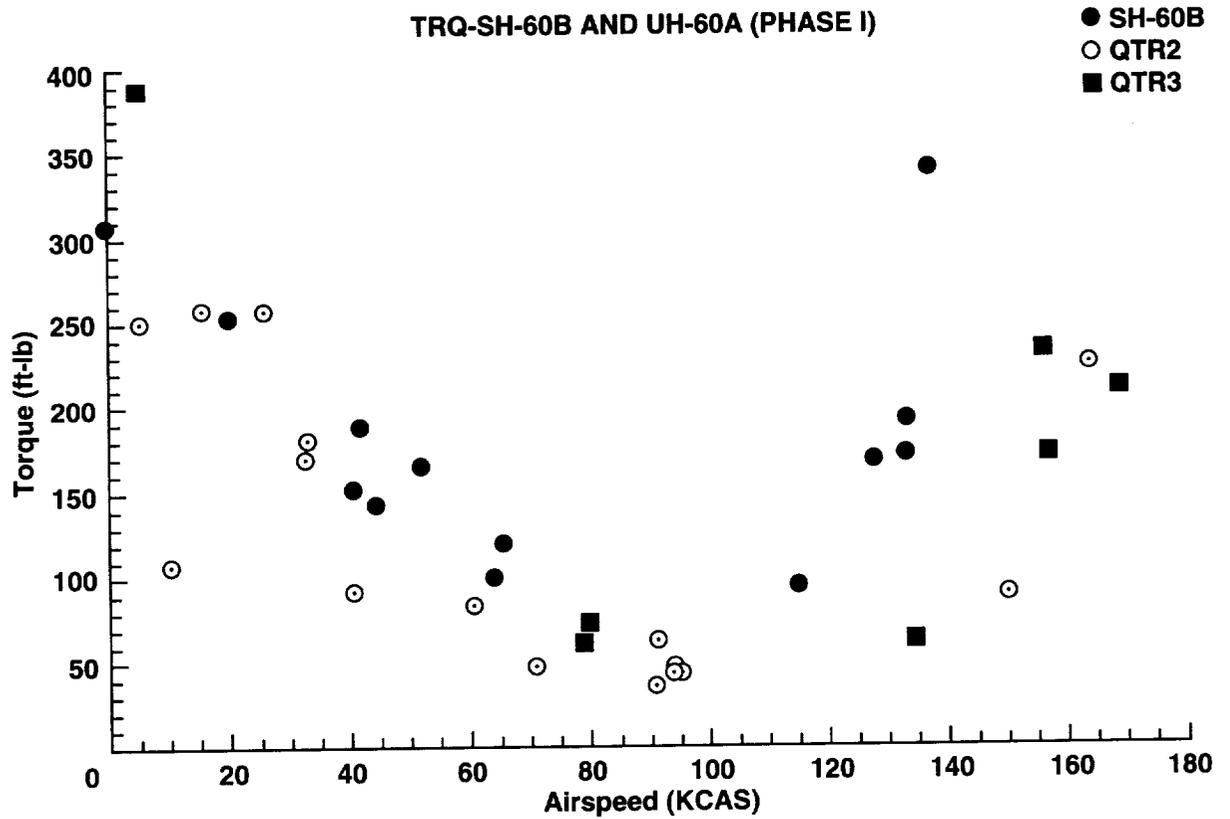
Figure 20. Composite tail-rotor torque vs advance ratio.
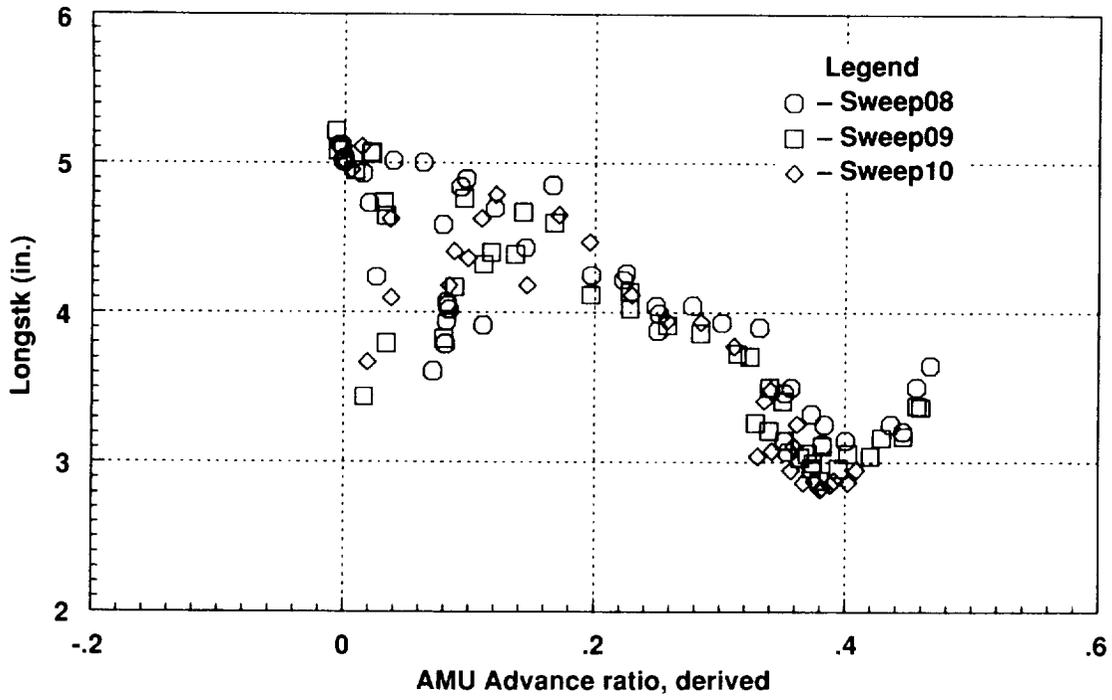
Figure 21. Statistical mean of longitudinal stick; all speed sweeps.
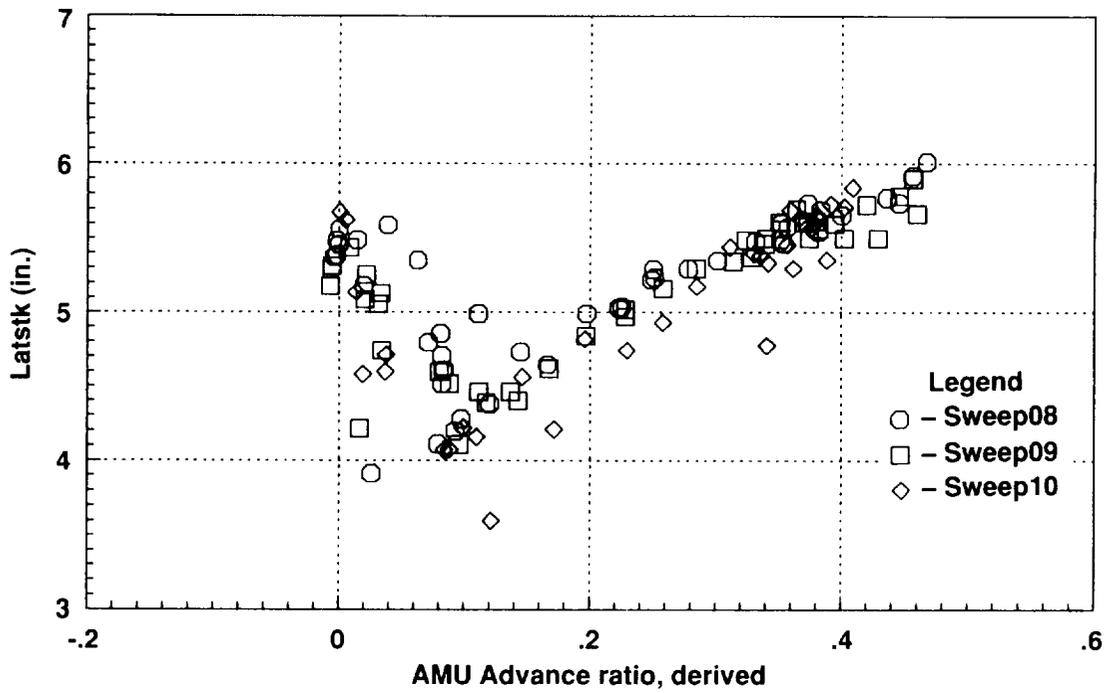
Figure 22. Statistical mean of lateral stick; all speed sweeps.
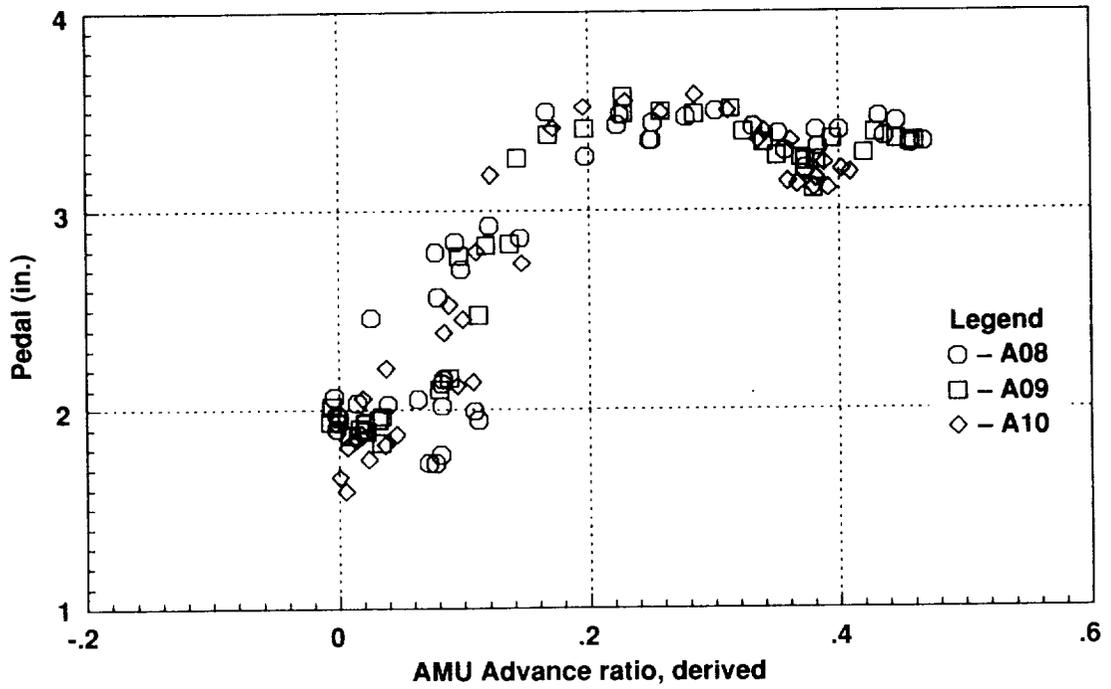
Figure 23. Statistical mean of pedal; all speed sweeps.
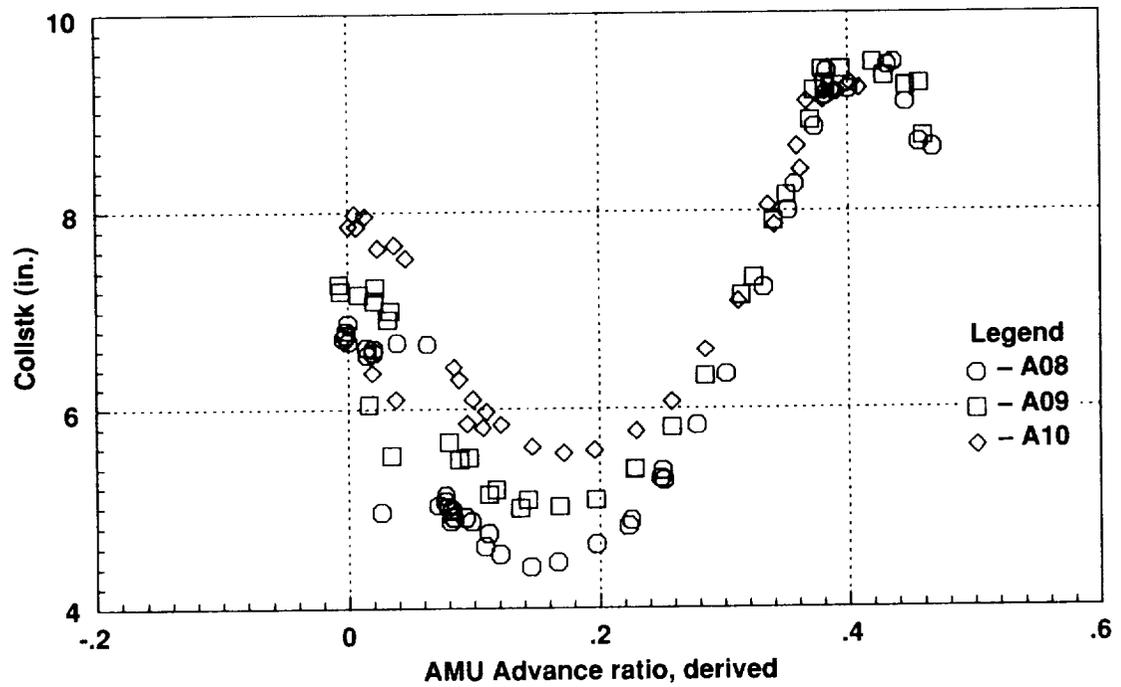
Figure 24. Statistical mean of collective stick; all speed sweeps.
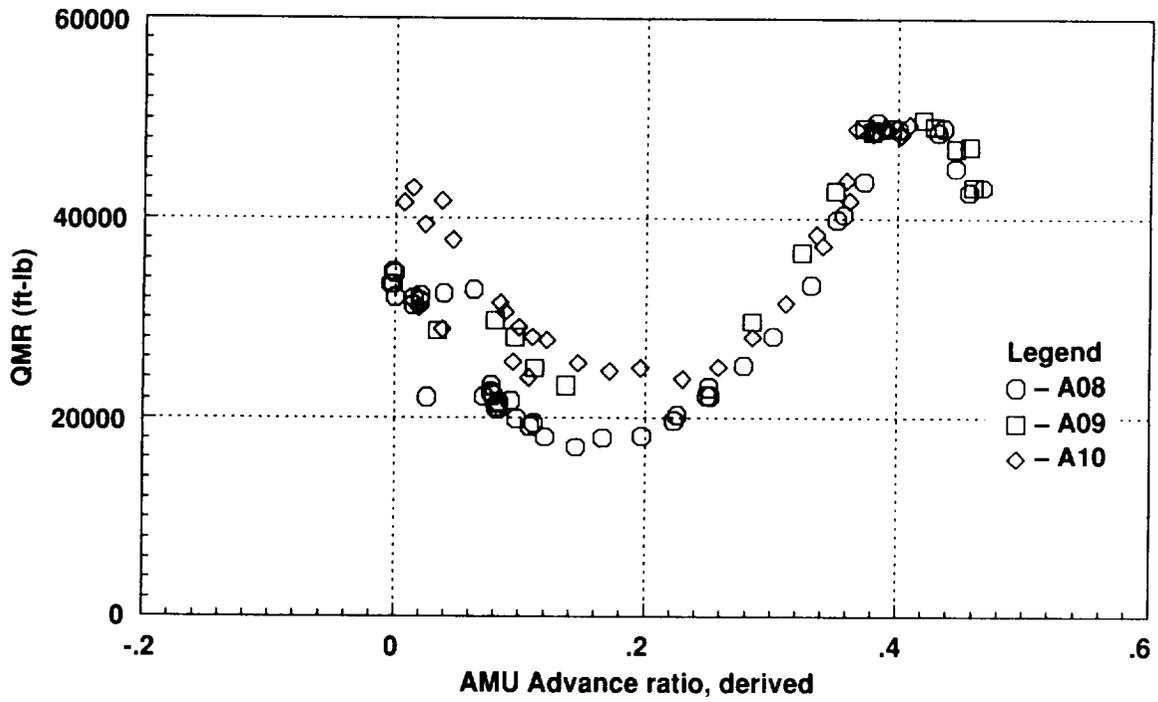
Figure 25. Statistical mean of main-rotor torque; all speed sweeps.
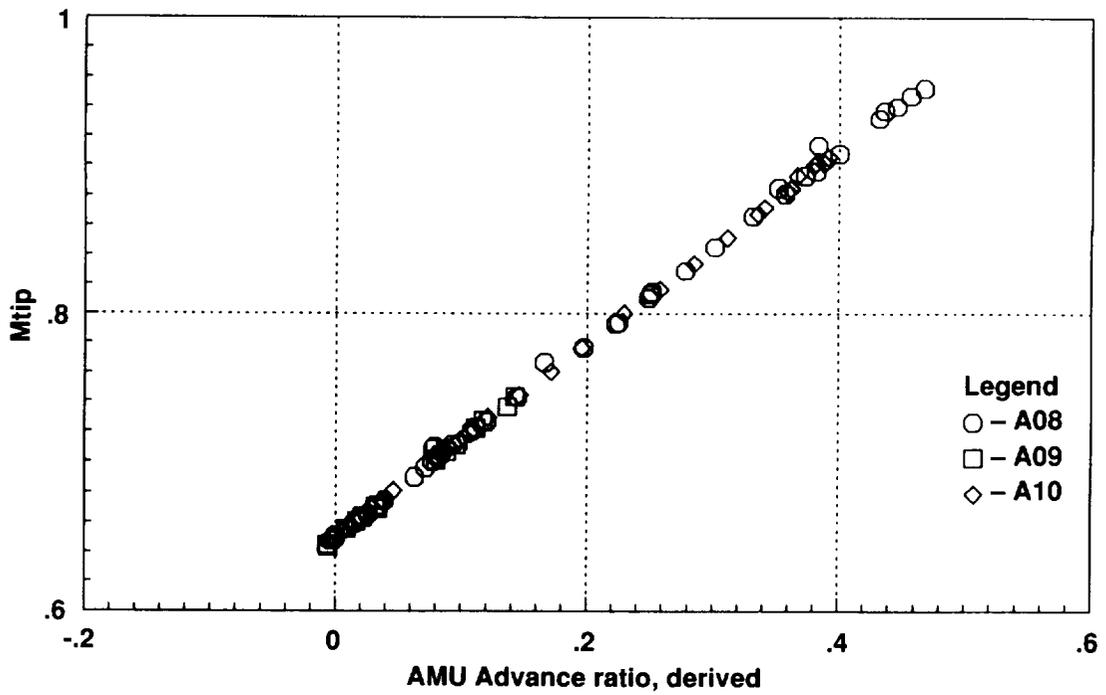
Figure 26. Statistical mean of tip Mach number, all speed sweeps.
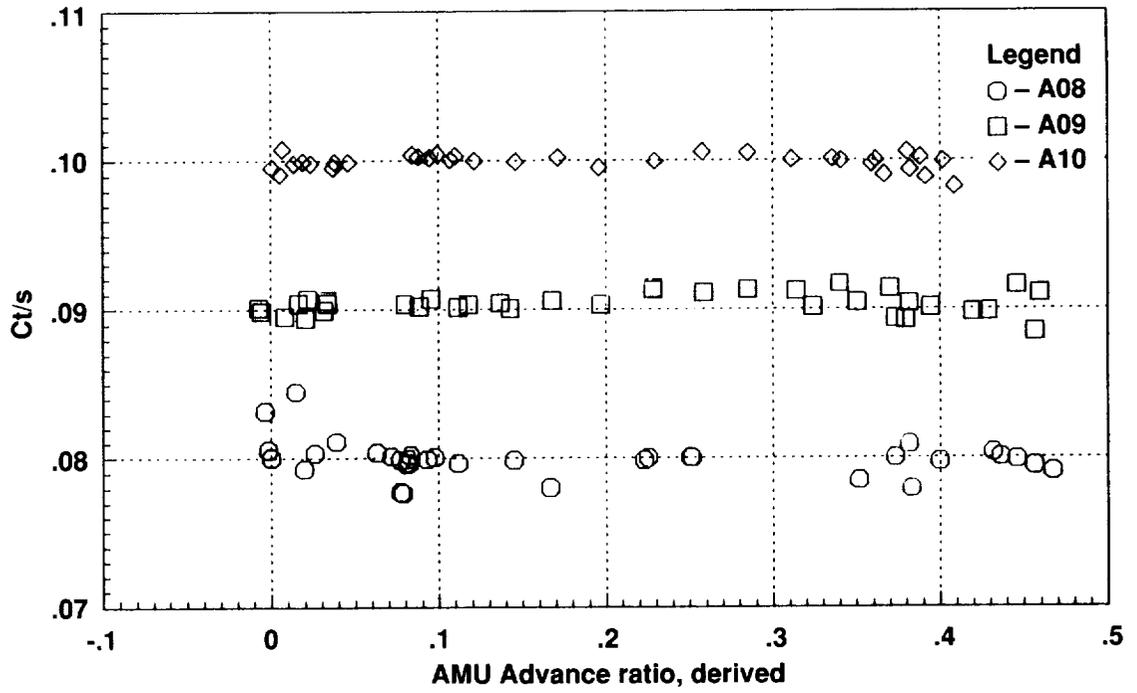
Figure 27. Statistical mean of C_T/σ, all speed sweeps.
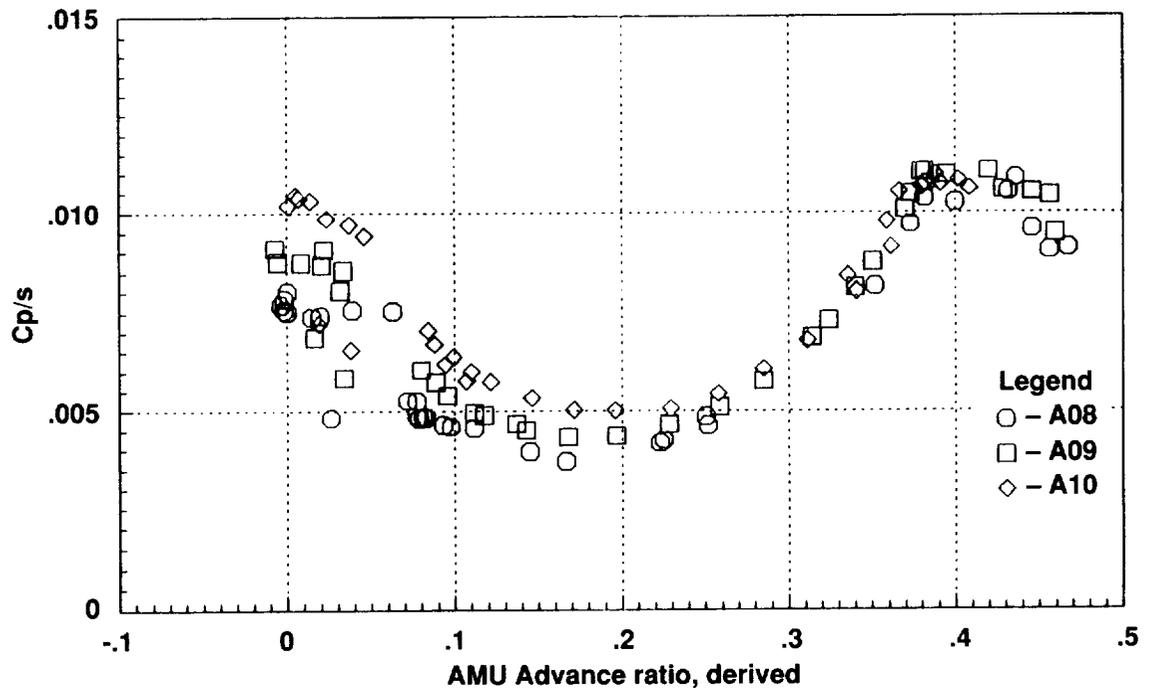
Figure 28. Statistical mean of C_P/σ, all speed sweeps.
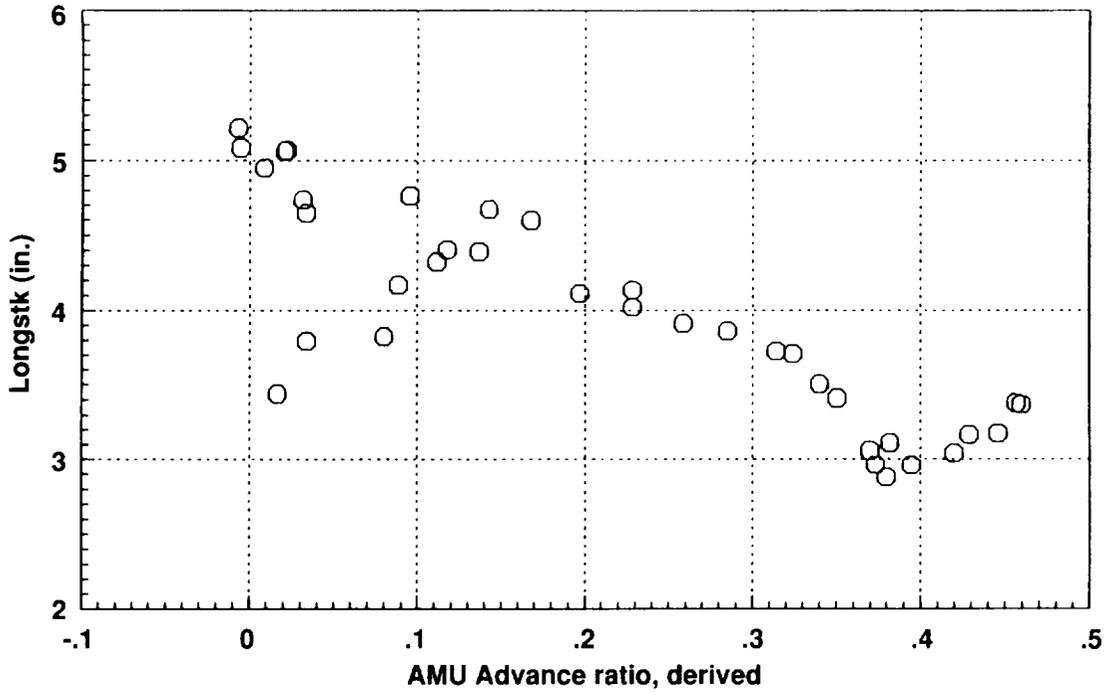
Figure 29. Statistical mean of longitudinal stick; $C_T/\sigma = 0.09$.
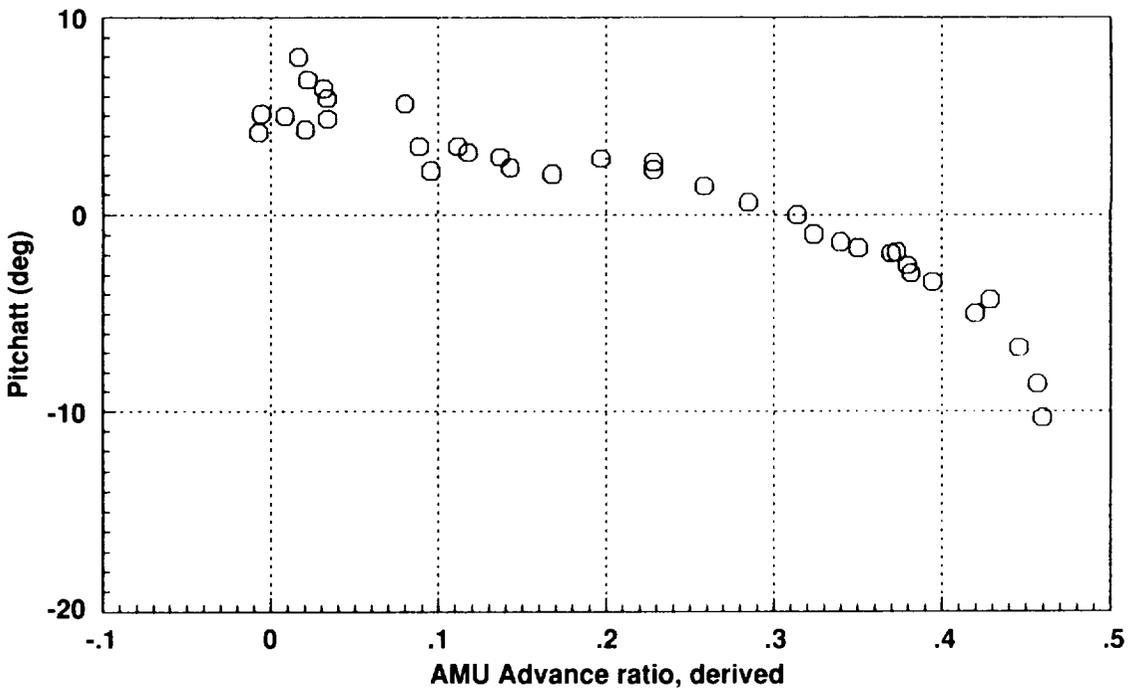
Figure 30. Statistical mean of pitch attitude; $C_T/\sigma = 0.09$.
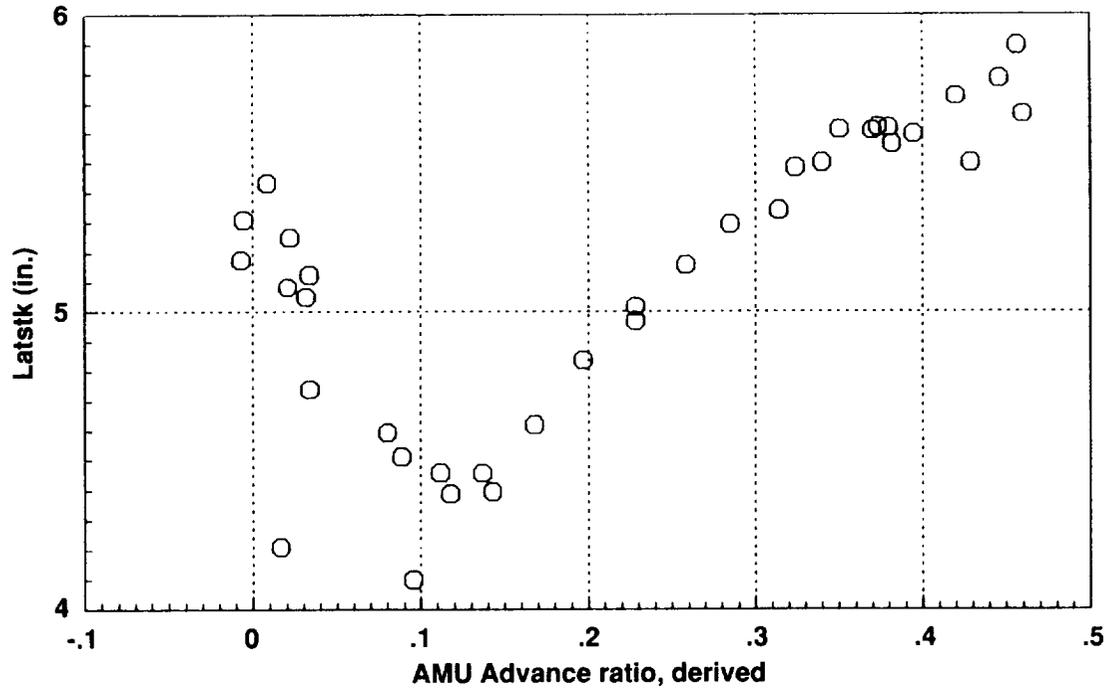
Figure 31. Statistical mean of lateral stick; $C_T/\sigma = 0.09$.
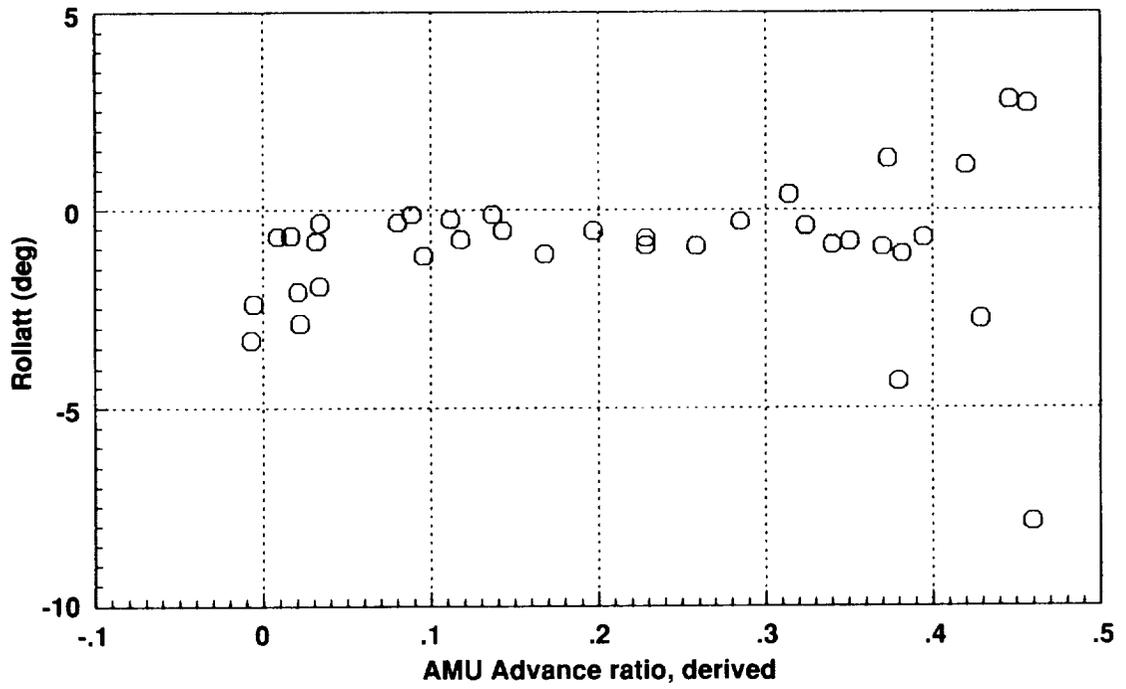
Figure 32. Statistical mean of roll attitude; $C_T/\sigma = 0.09$.

178
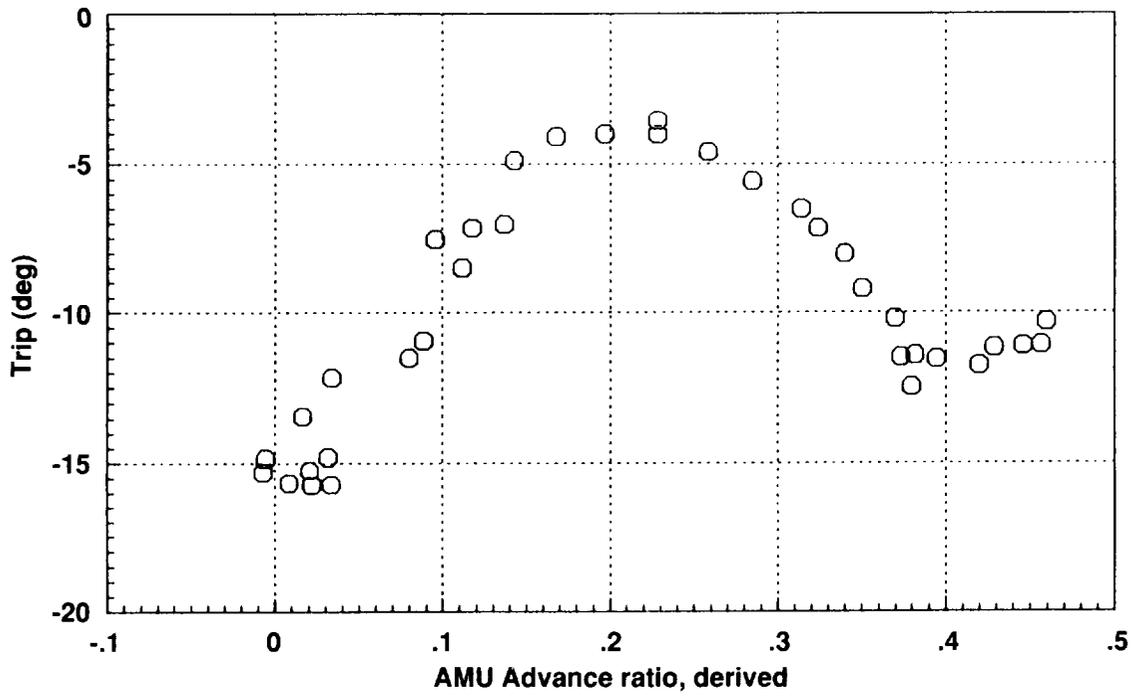
Figure 33. Statistical mean of tail-rotor pitch; $C_T/\sigma = 0.09$.

Figure 34. Statistical mean of stabilator angle; $C_T/\sigma = 0.09$.
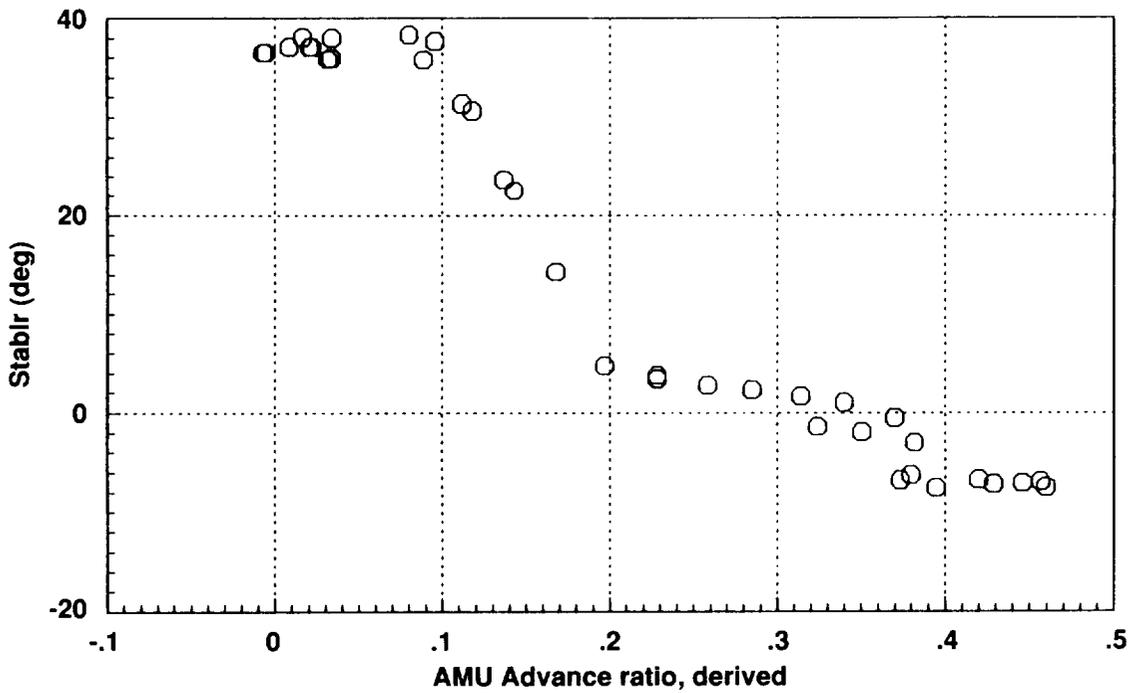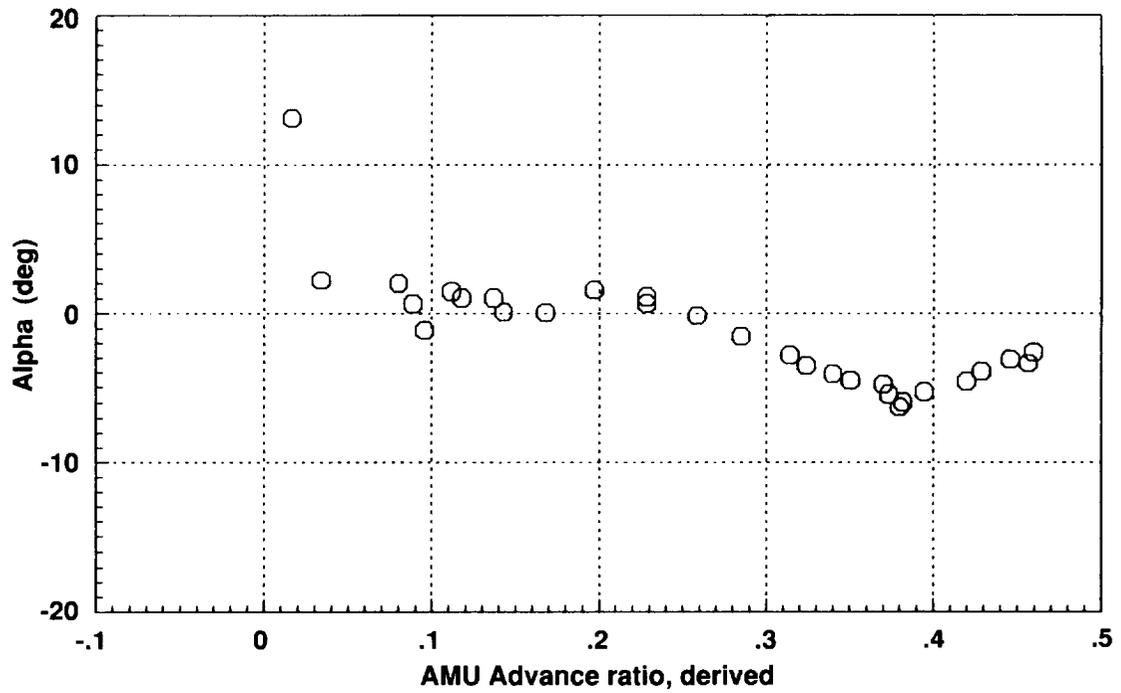
Figure 35. Statistical mean of angle of attack; $C_T/\sigma = 0.09$.
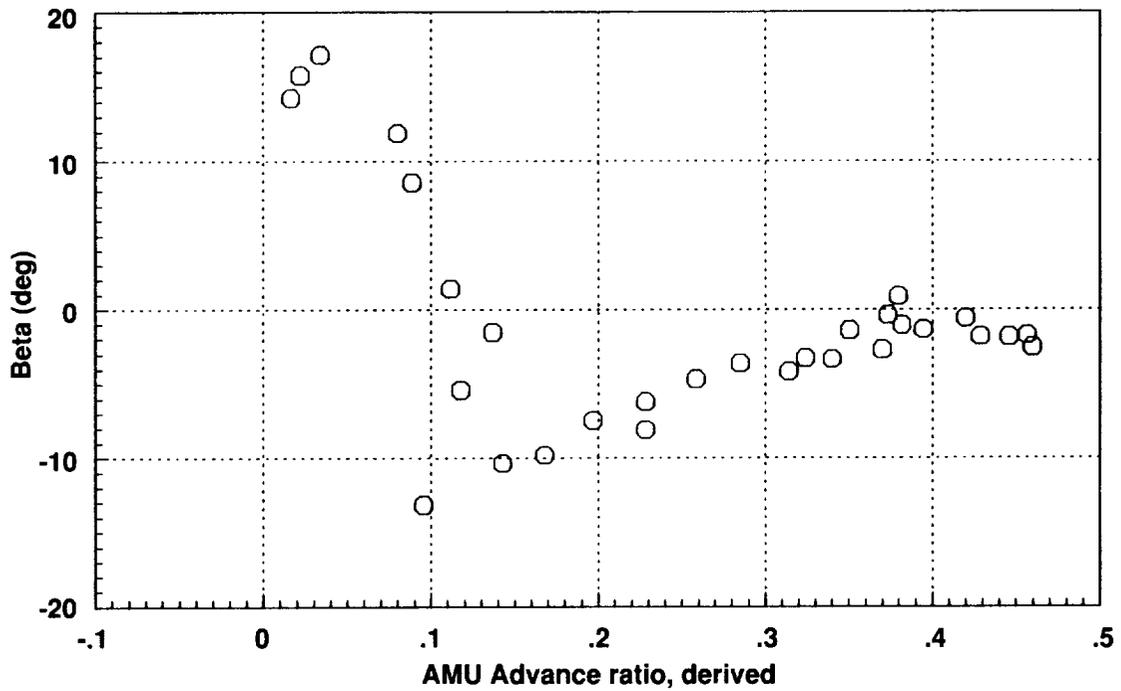
Figure 36. Statistical mean of side slip angle; $C_T/\sigma = 0.09$.
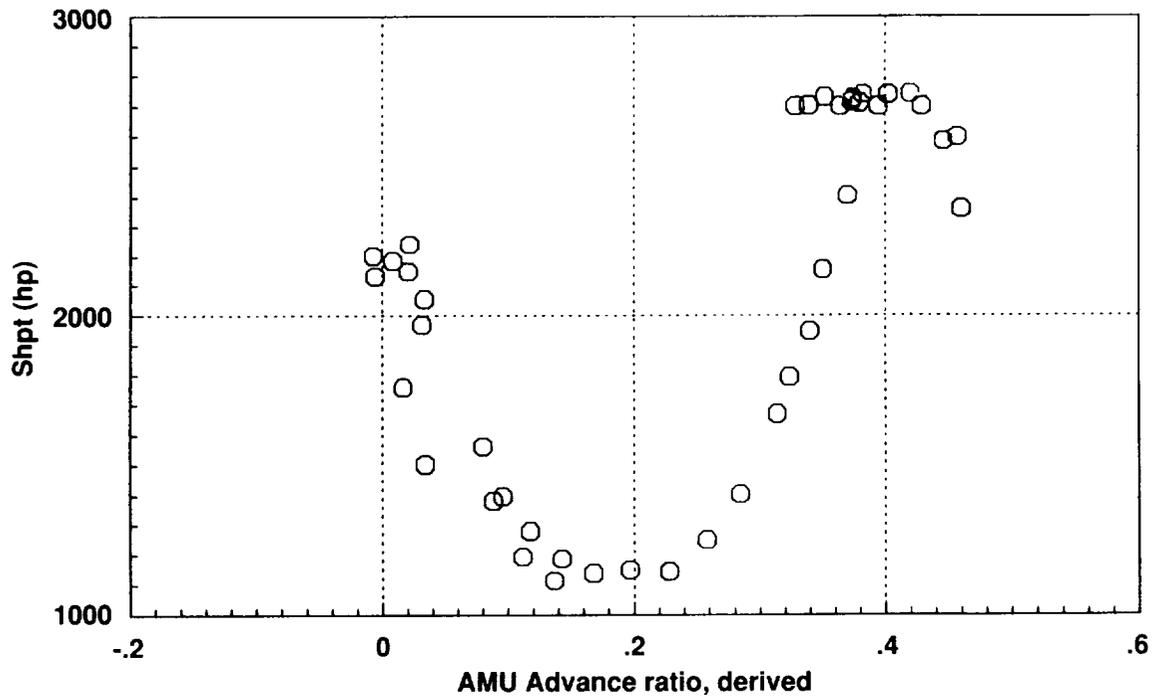
Figure 37. Statistical mean of shaft horsepower; $C_T/\sigma = 0.09$.
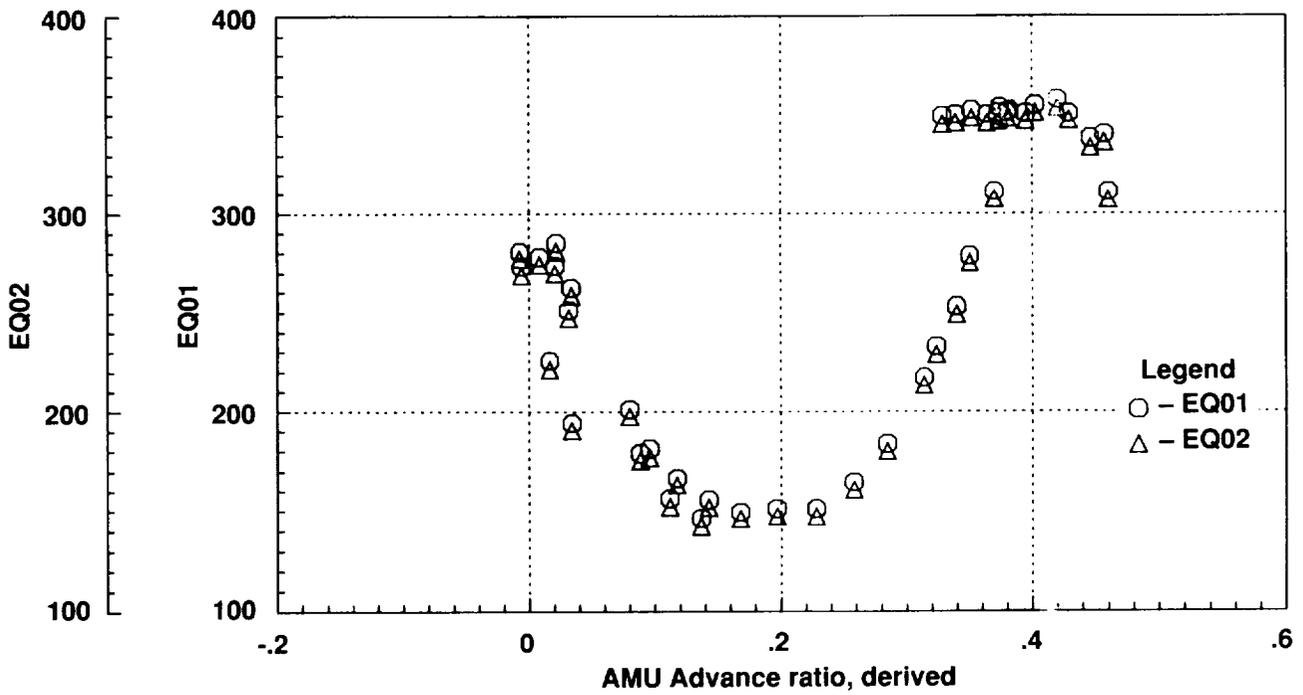
Figure 38. Statistical mean of engine torques; $C_T/\sigma = 0.09$.
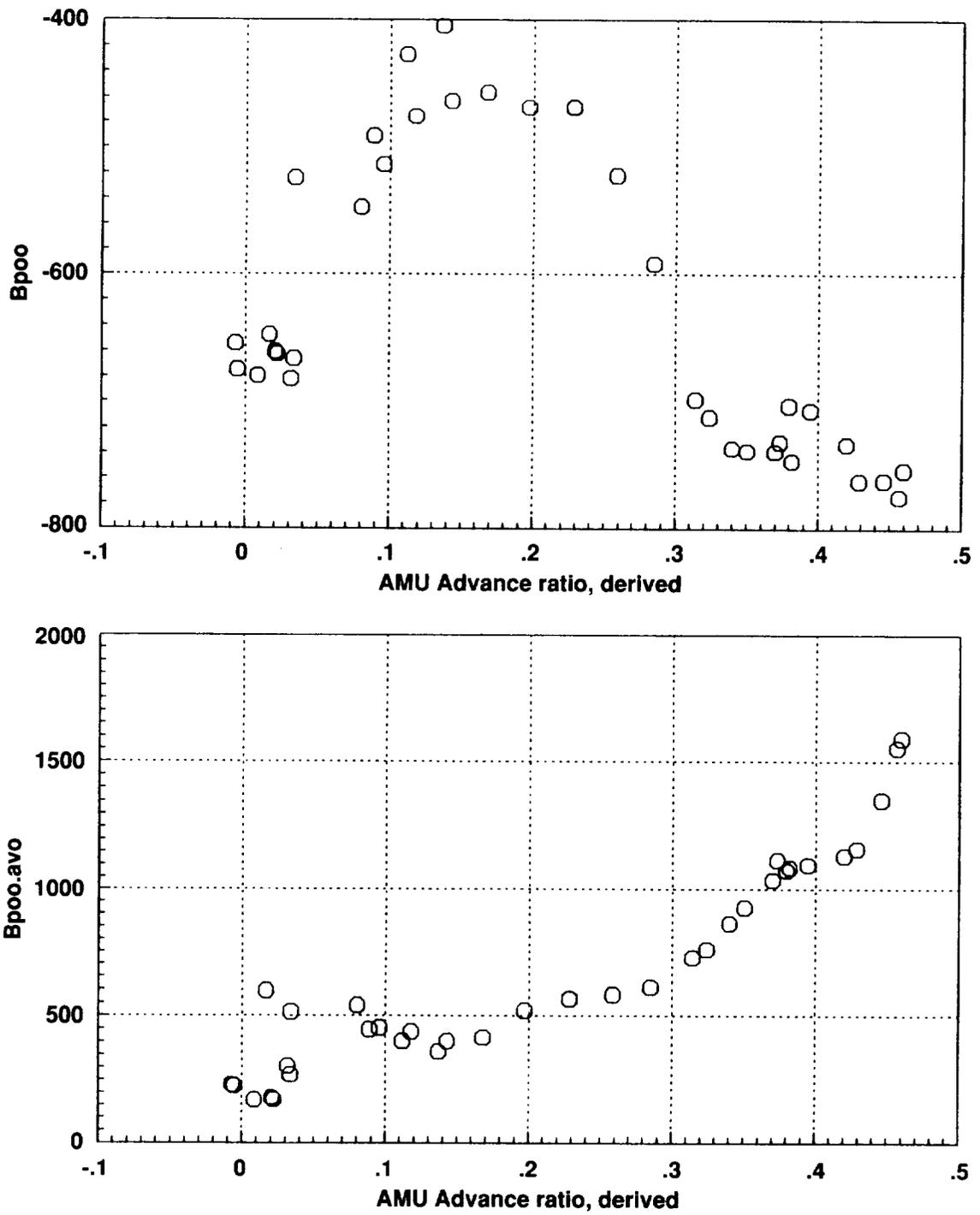
Figure 39. Average (top) and vibratory (bottom) pitch-link loads; $C_T/\sigma = 0.09$.

182
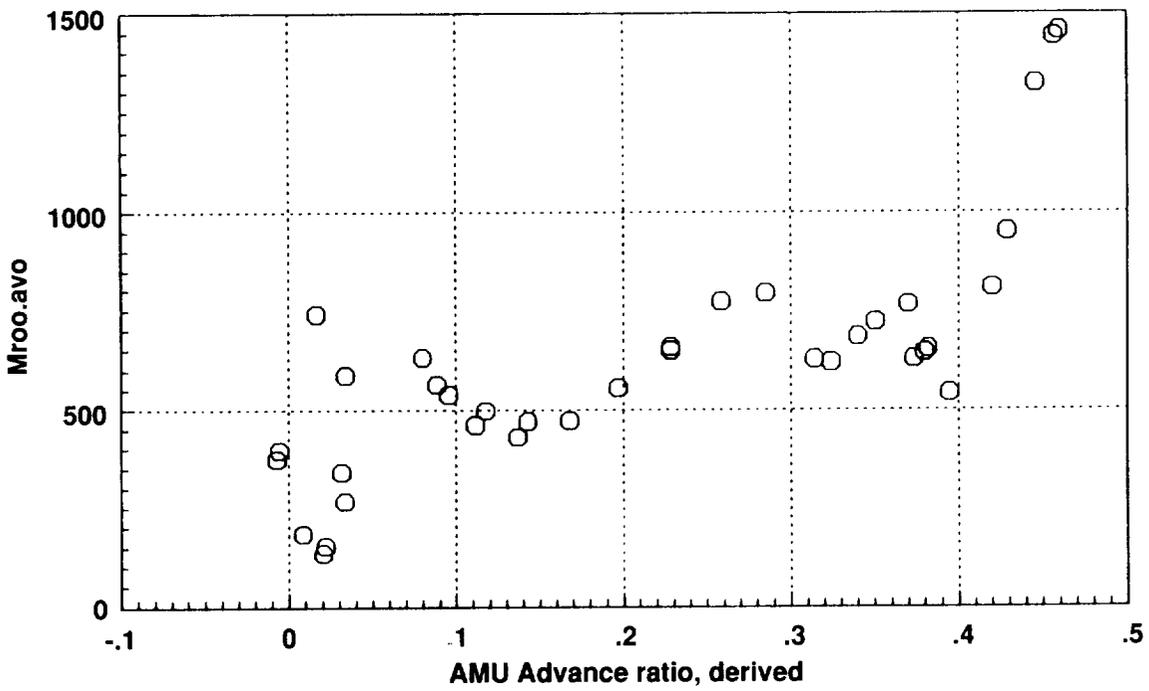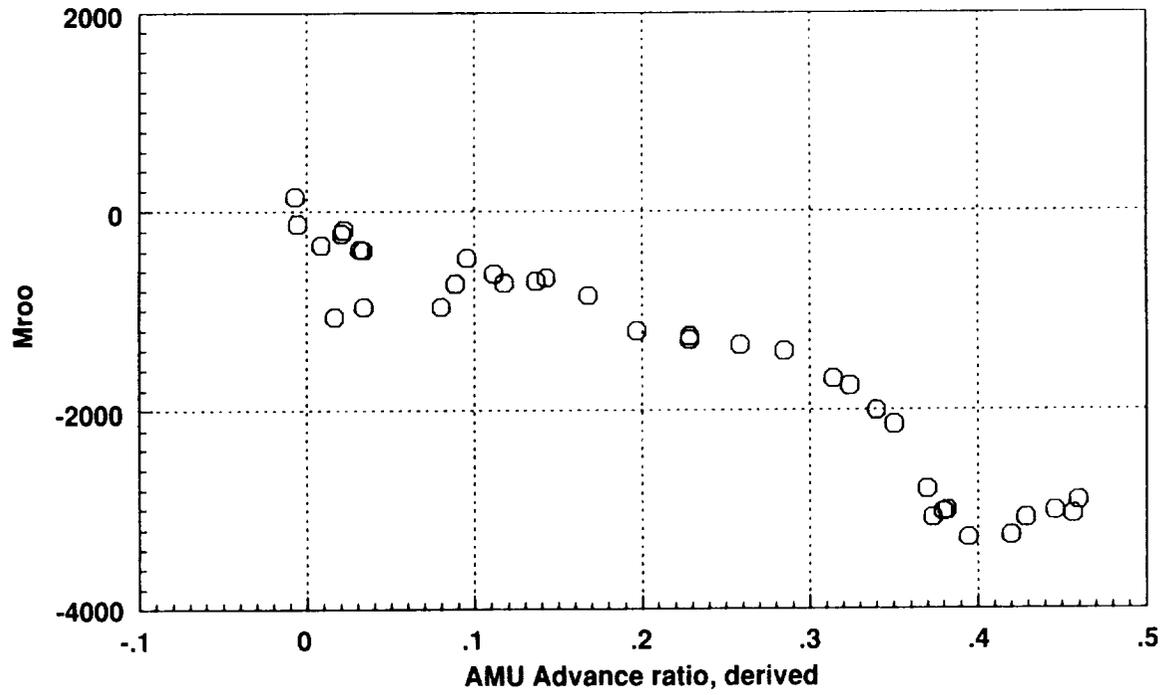
Figure 40. Average (top) and vibratory (bottom) forward link load; $C_T/\sigma = 0.09$.
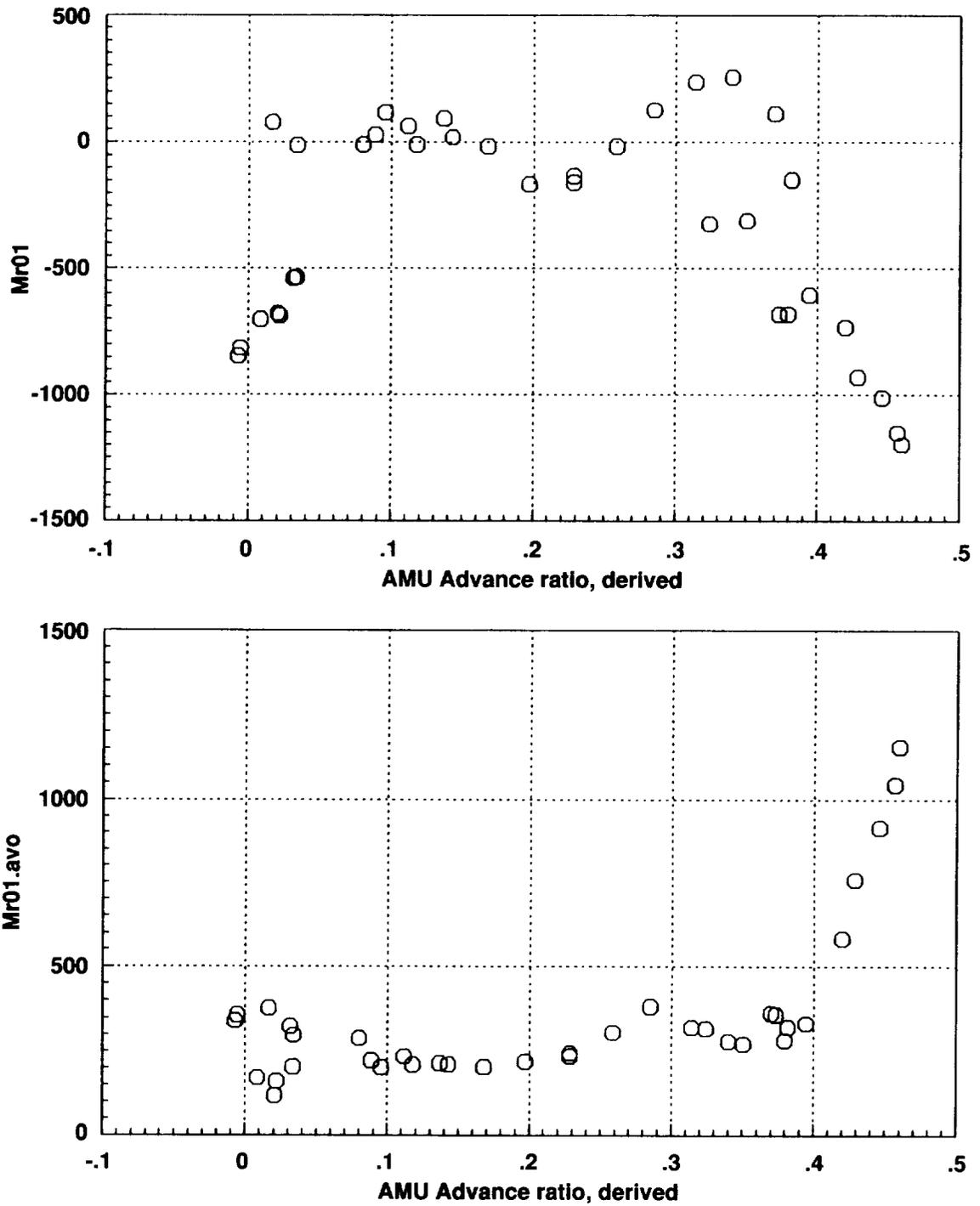
Figure 41. Average (top) and vibratory (bottom) lateral link load; $C_T/\sigma = 0.09$.
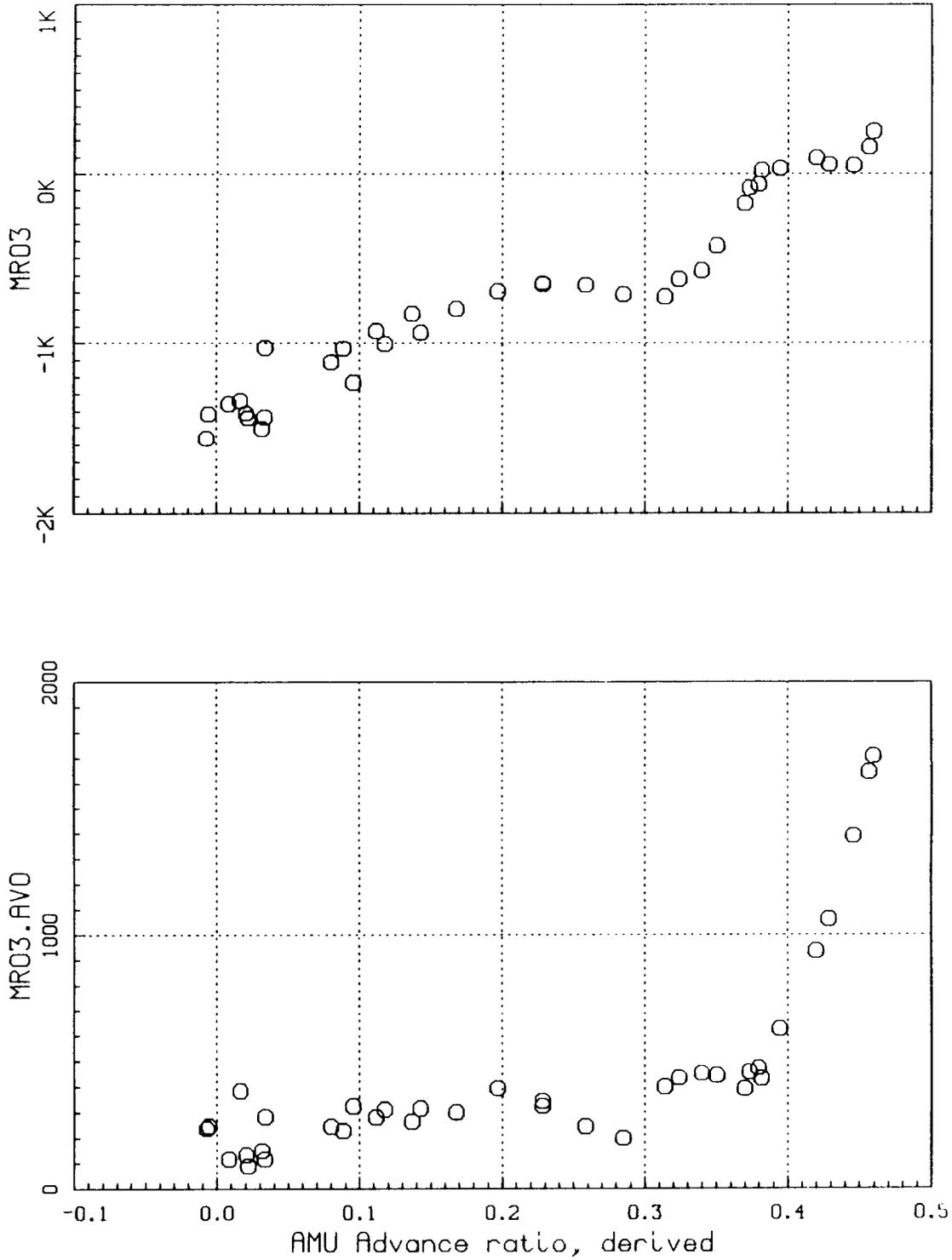
Figure 42. Average (top) and vibratory (bottom) aft link load; $C_T/\sigma = 0.09$.
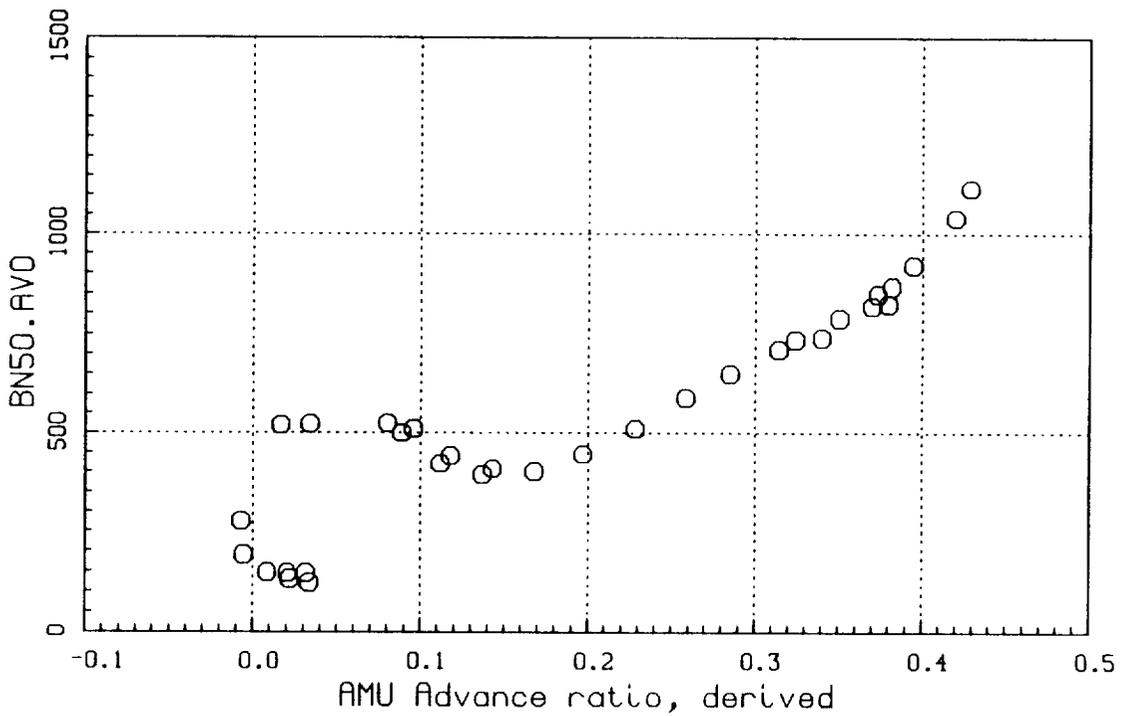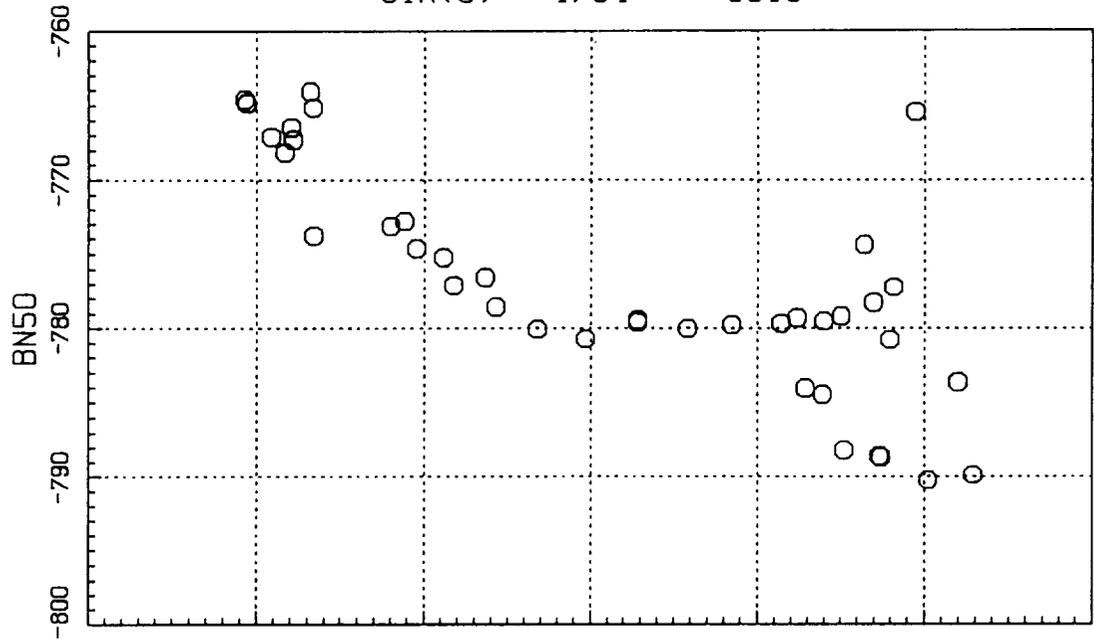
Figure 43. Average (top) and vibratory (bottom) blade normal bending, 50%: $C_T/\sigma = 0.09$.

UH-60A A/C 748 PHASE I TESTS
SPEED SWEEP AT .09 CT/S
CTR(S)   1704 -   3018
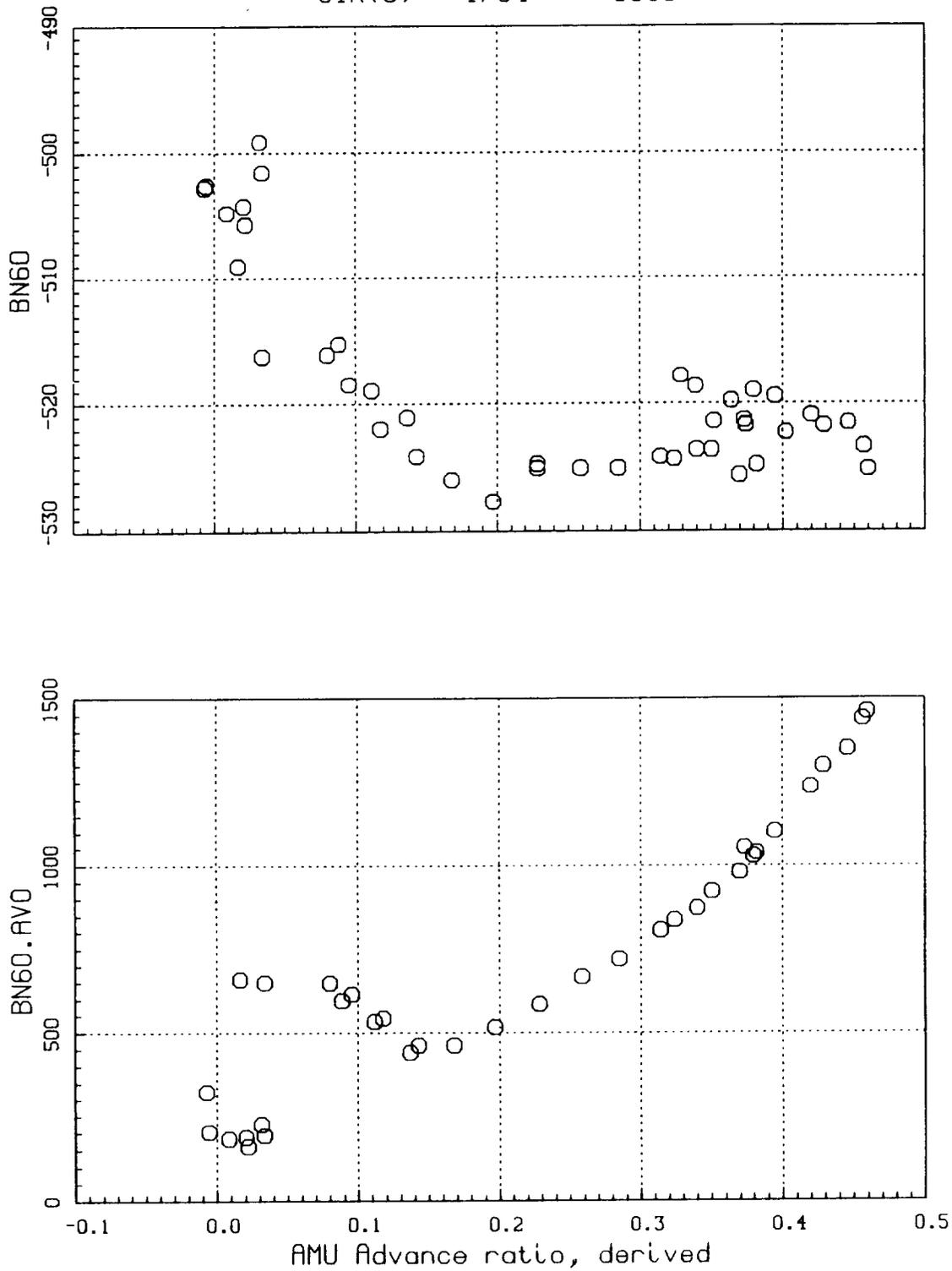
Figure 44. Average (top) and vibratory (bottom) blade normal bending, 60%: $C_T/\sigma = 0.09$.
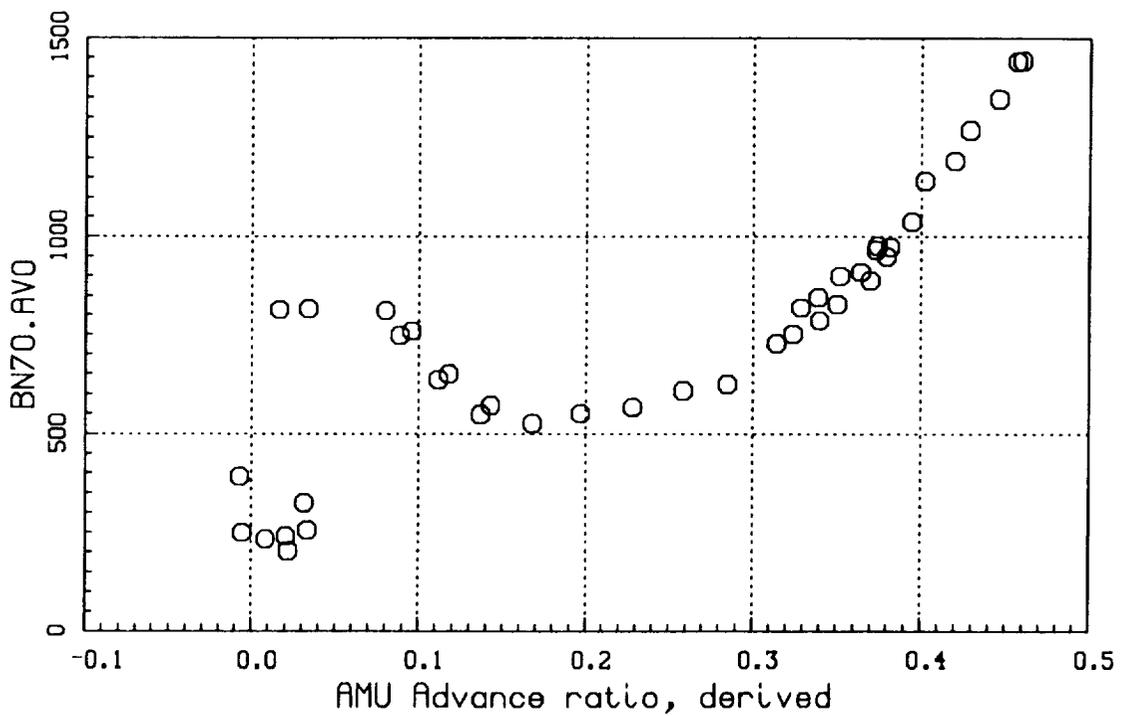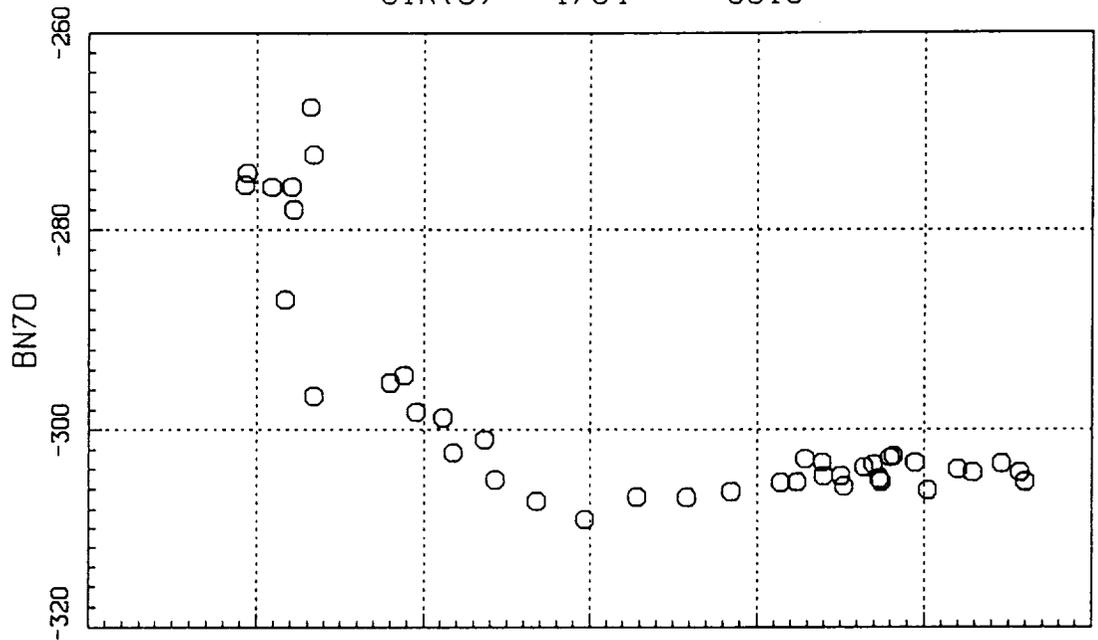
Figure 45. Average (top) and vibratory (bottom) blade normal bending, 70%: $C_T/\sigma = 0.09$.

UH-60A A/C 748 PHASE I TESTS
SPEED SWEEP AT .09 CT/S
CTR(S)   1704 -   3018

Figure 46. Average (top) and vibratory (bottom) blade normal bending root; $C_T/\sigma = 0.09$.

Figure 47. Average (top) and vibratory (bottom) edgewise bending root; $C_T/\sigma = 0.09$.

190

Figure 48. Normal bending 50% R vs azimuth at four speeds; $C_T/\sigma = 0.09$.

Figure 49. Normal bending 60% R vs azimuth at five speeds; $C_T/\sigma = 0.09$.

Figure 50. Normal bending 70% R vs azimuth at five speeds; $C_T/\sigma = 0.09$.

Figure 51. Pitch-link load vs azimuth at five speeds; $C_T/\sigma = 0.09$.

Figure 52. Vibratory vertical pilot station vs advance ratio; $C_T/\sigma = 0.09$.
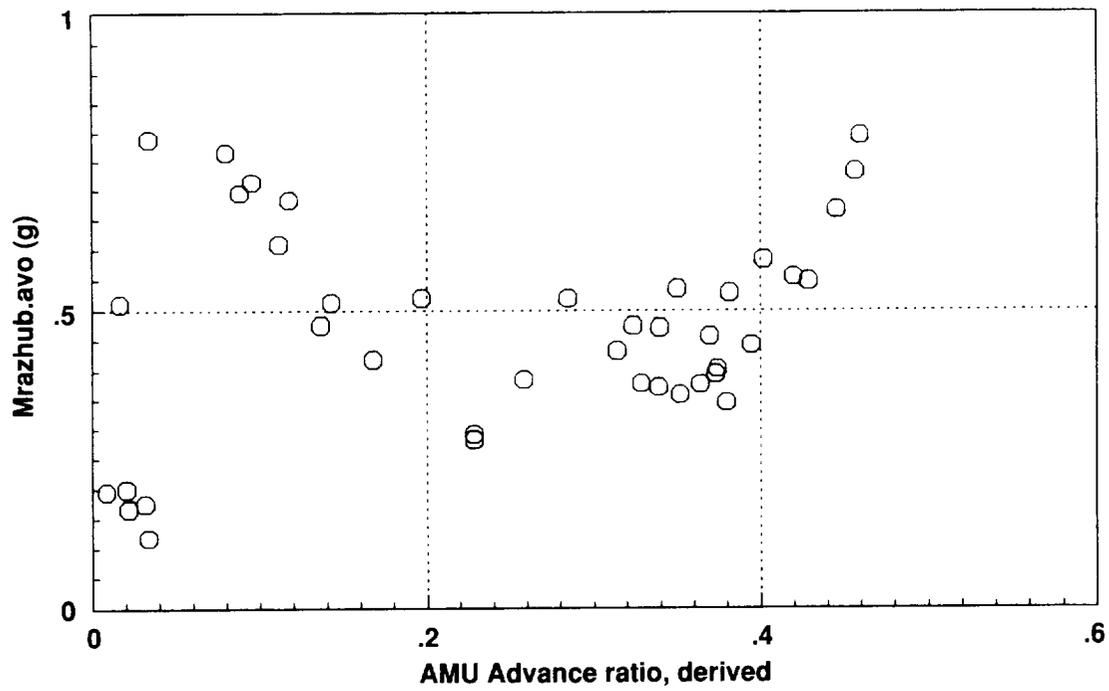
Figure 53. Vibratory vertical hub vs advance ratio; $C_T/\sigma = 0.09$.
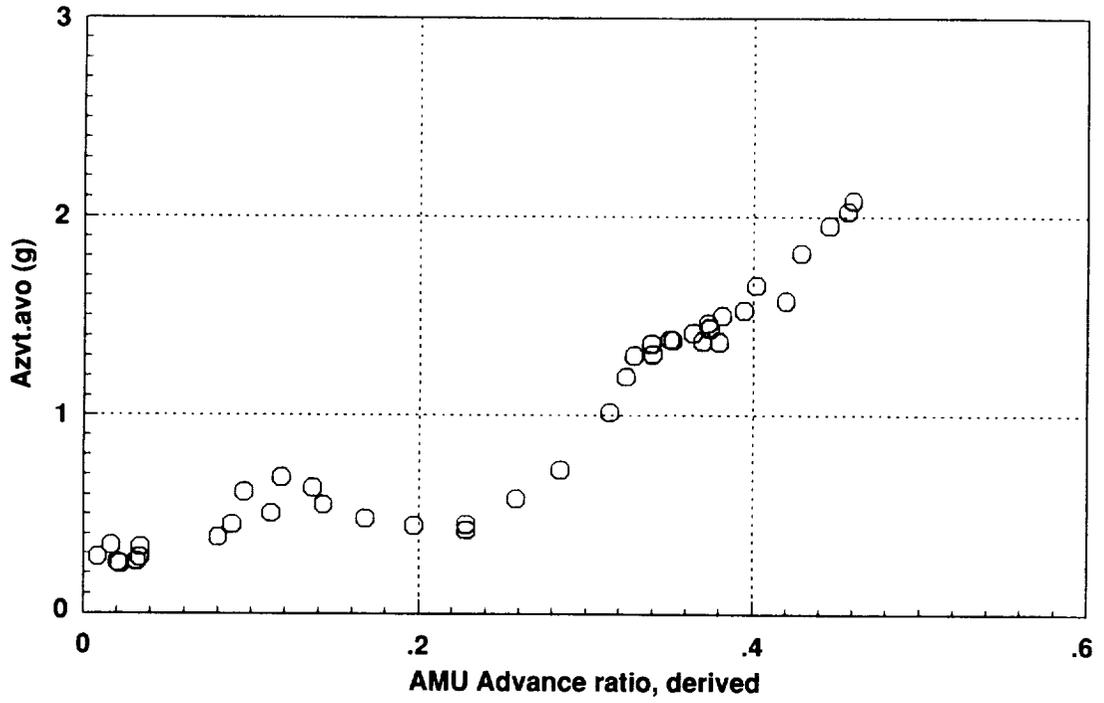
Figure 54. Vibratory vertical tail vs advance ratio; $C_T/\sigma = 0.09$.
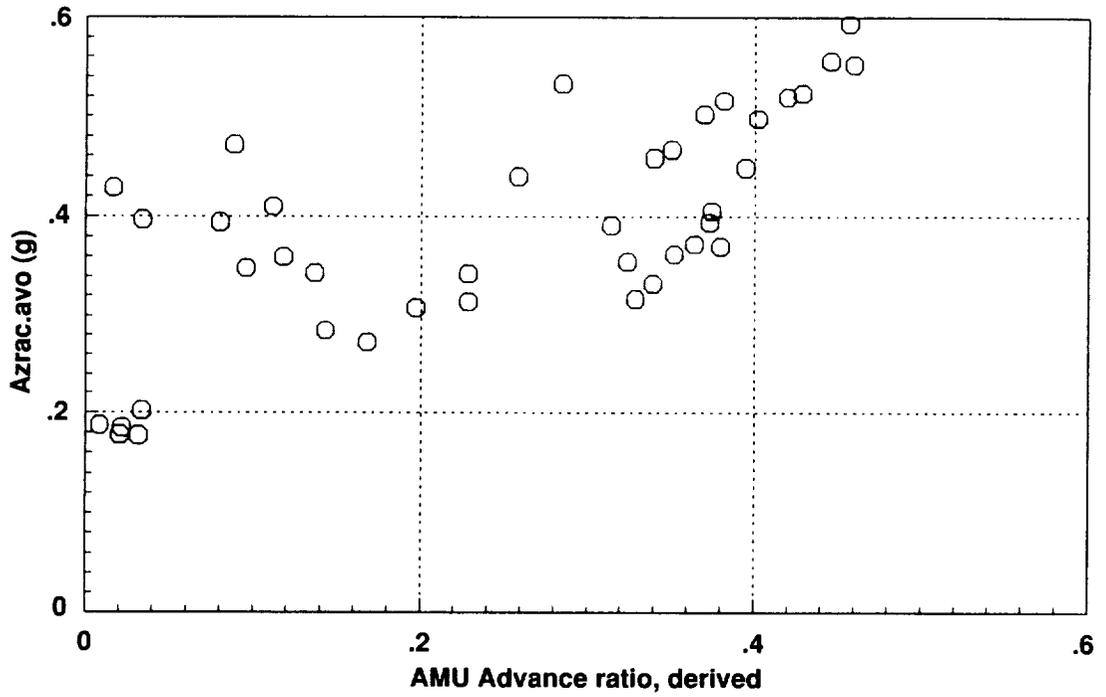
Figure 55. Vibratory vertical tail vs advance ratio; $C_T/\sigma = 0.09$.
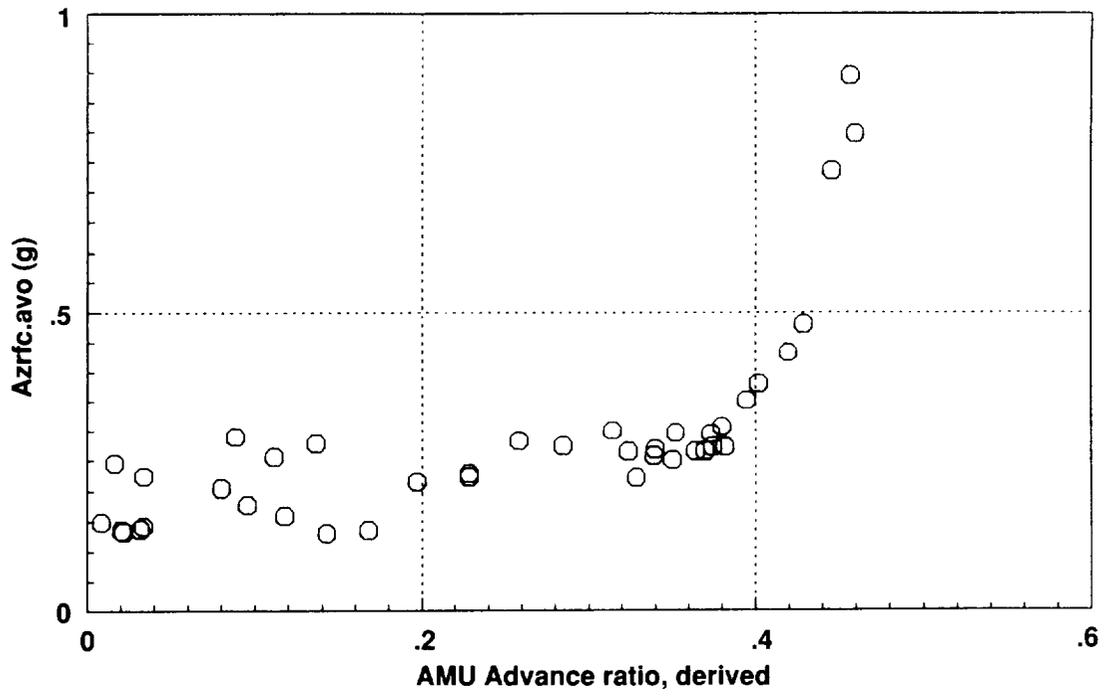
Figure 56. Vibratory vertical right forward cabin; $C_T/\sigma = 0.09$.
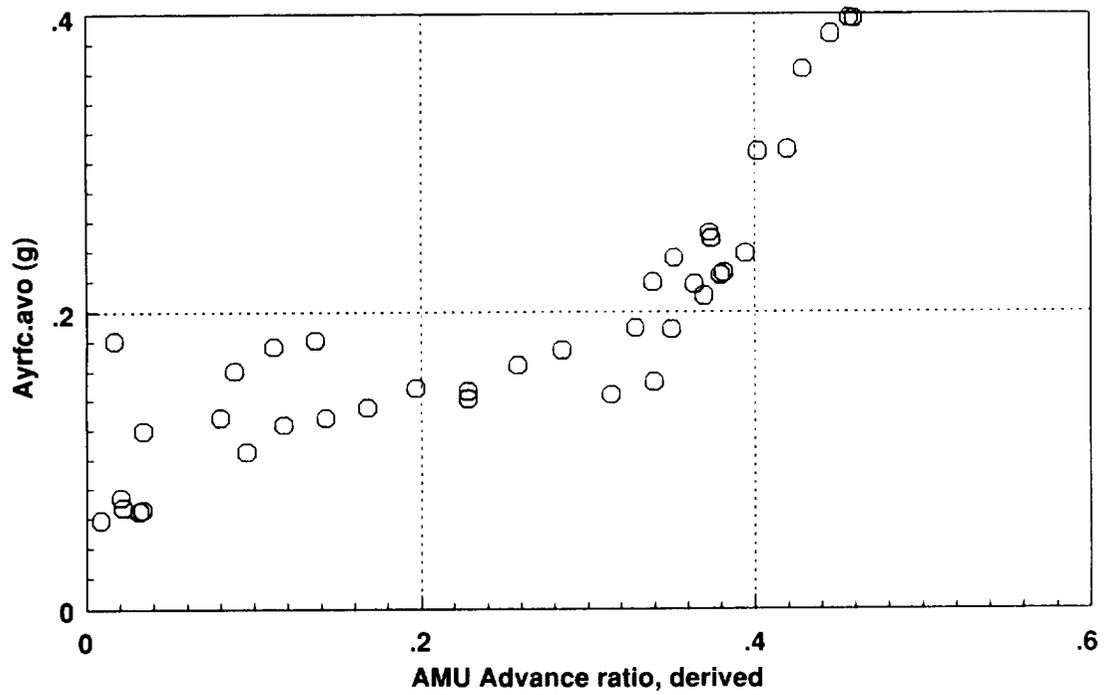
Figure 57. Vibratory lateral right forward cabin; $C_T/\sigma = 0.09$.
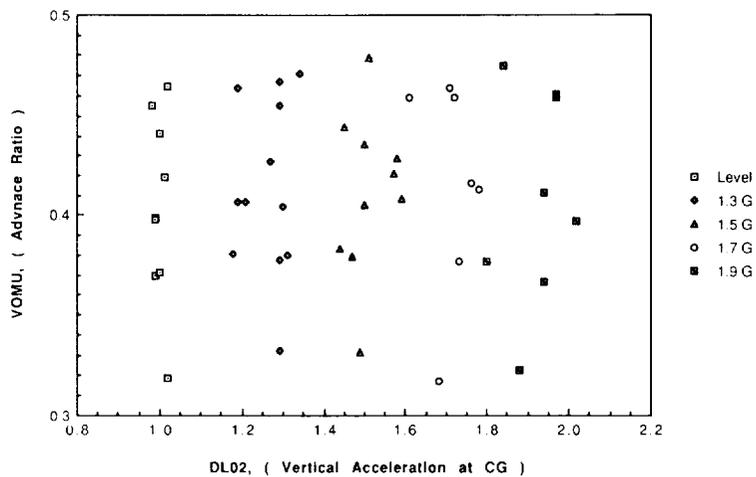
Figure 58. Advance ratio vs vertical g loading maneuvers; C_T/σ = 0.09.
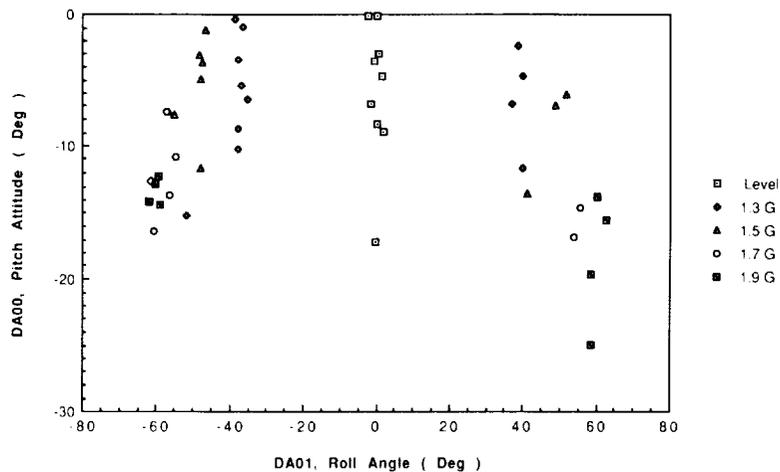
Figure 59. Pitch attitude vs roll angle for maneuvers; C_T/σ = 0.09.
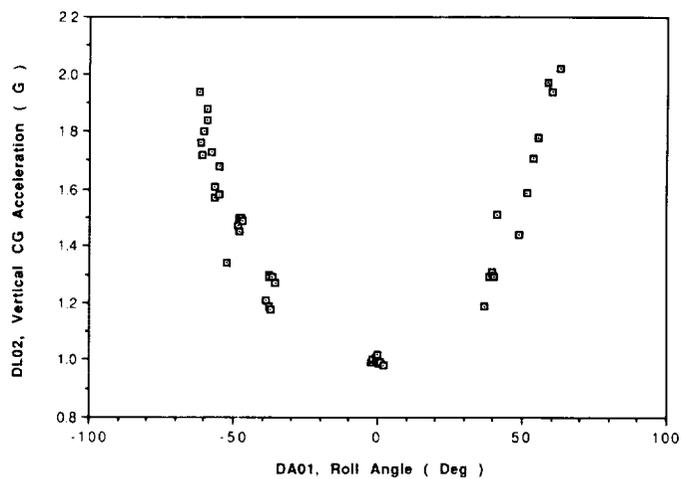
Figure 60. Vertical g loading vs roll angle for maneuvers; C_T/σ = 0.09.

C-3
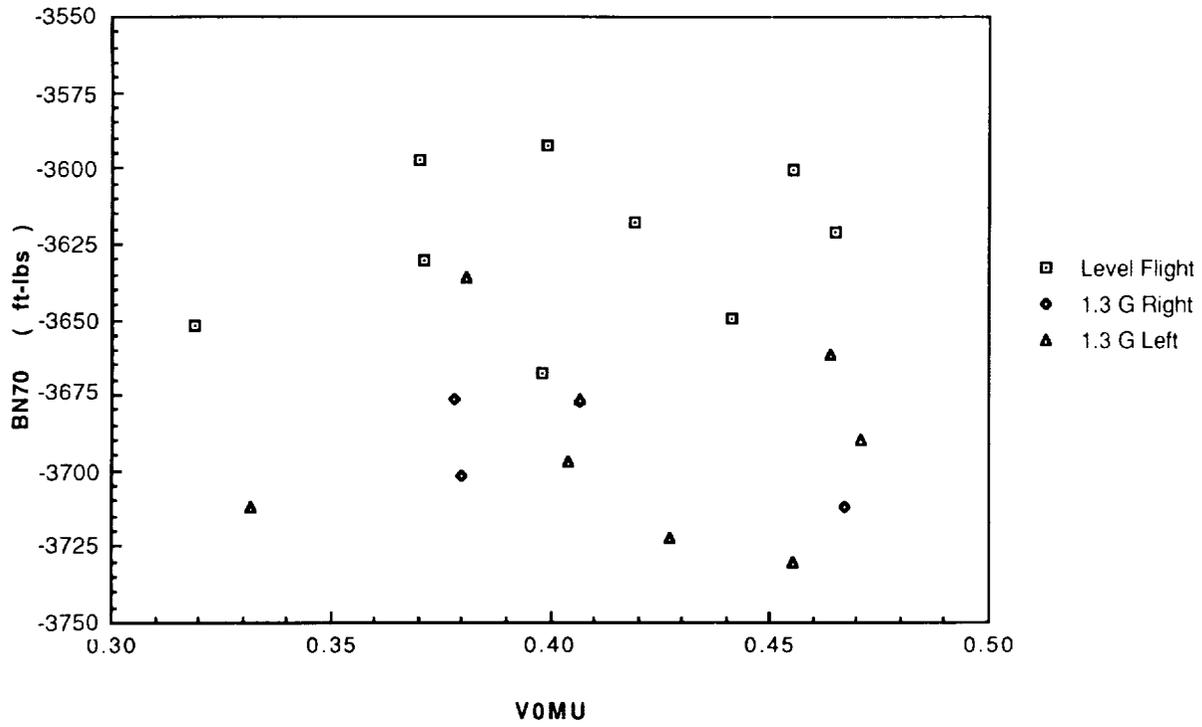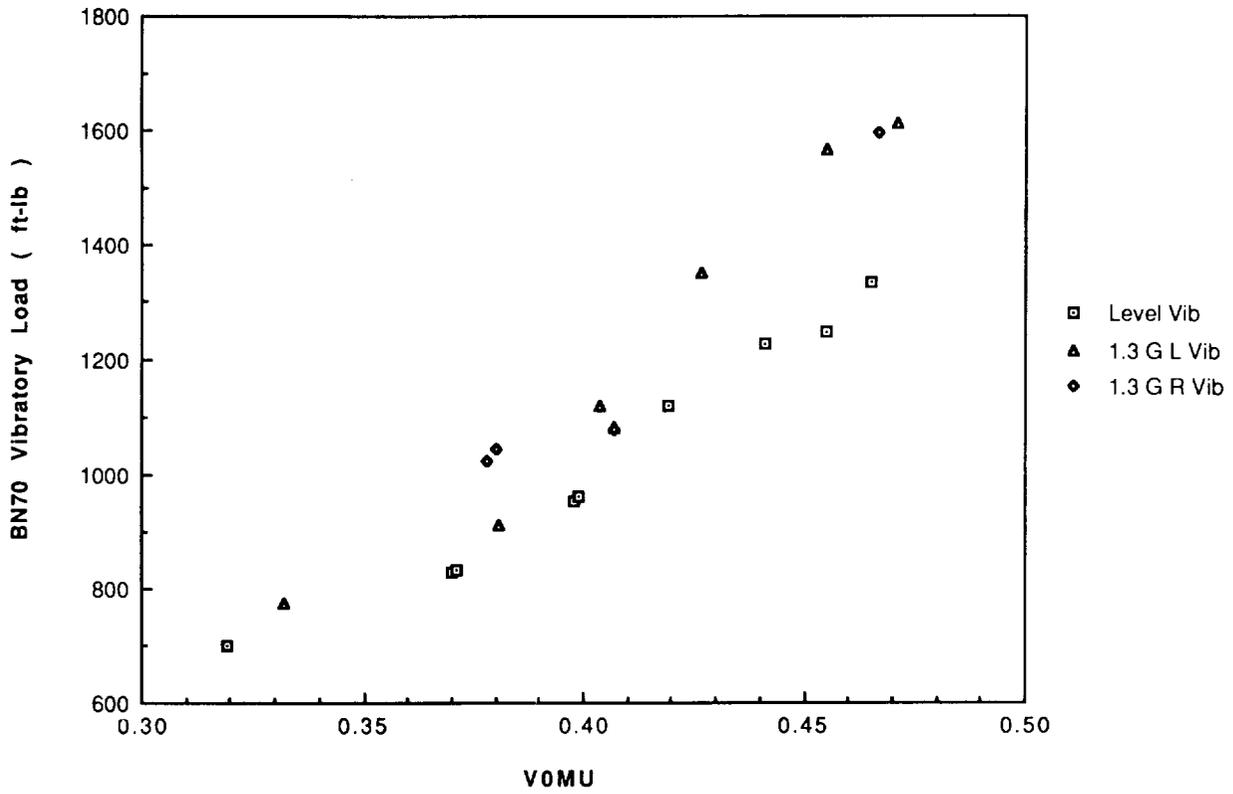
(a) Average.

(b) Vibratory.

Figure 61. Normal bending 70% R vs μ, left and right banks, 1.3 g.
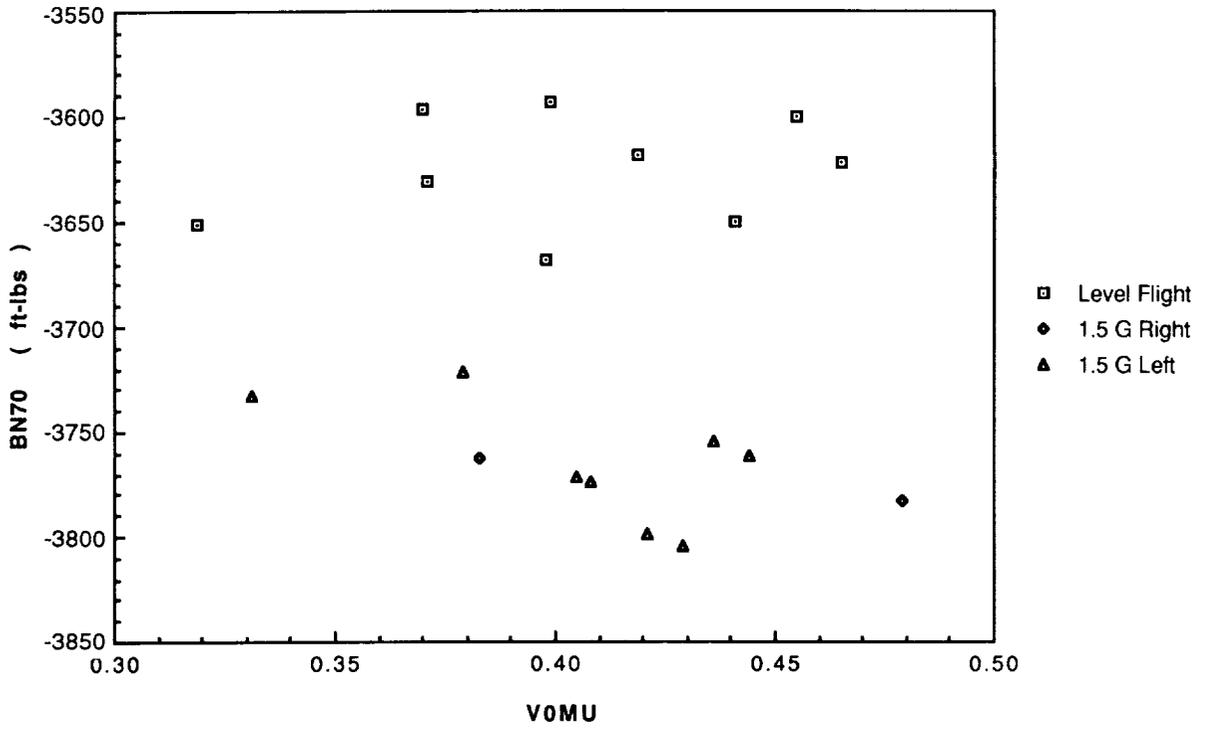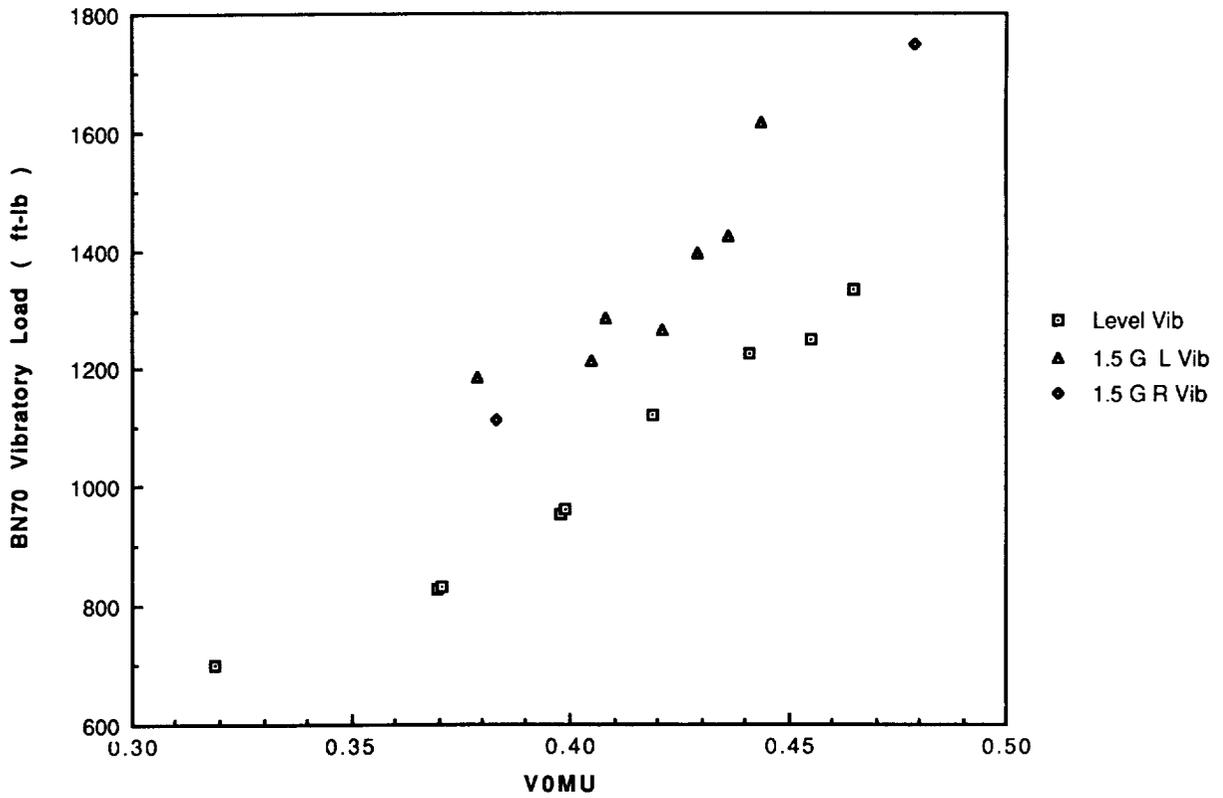
(a) Average.

(b) Vibratory.

Figure 62. Normal bending 70% R vs μ, left and right banks, 1.5 g.
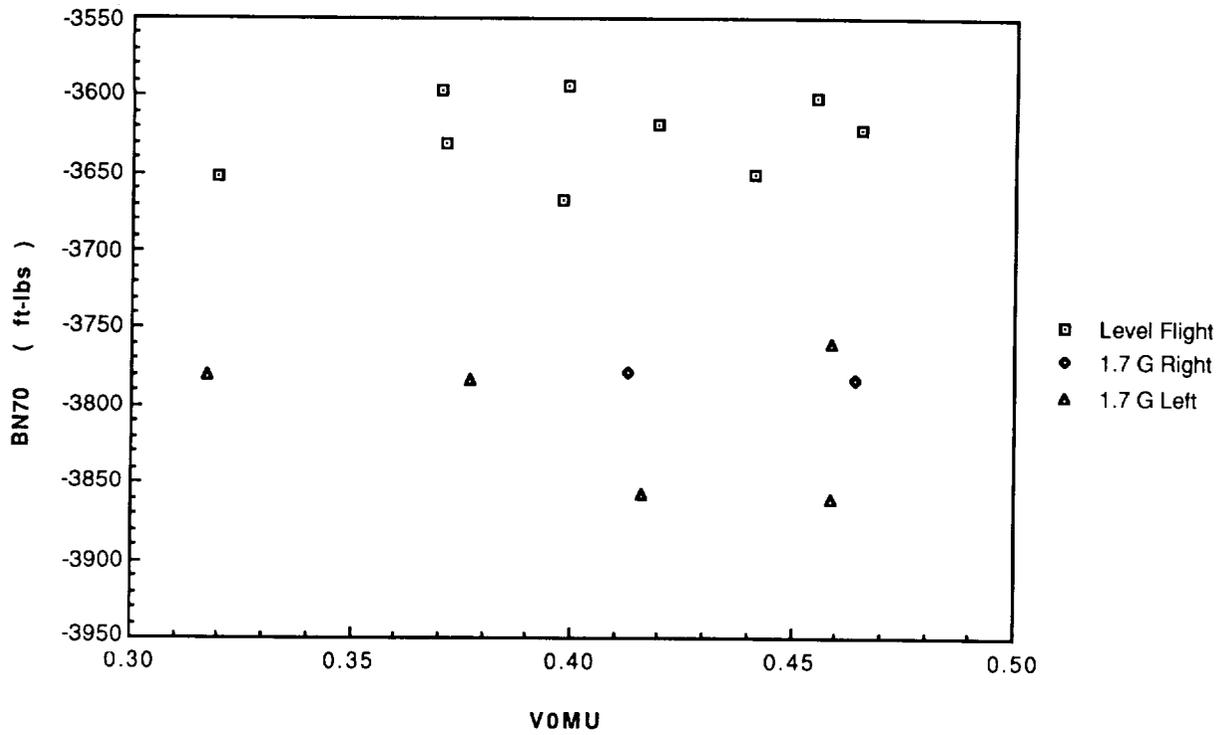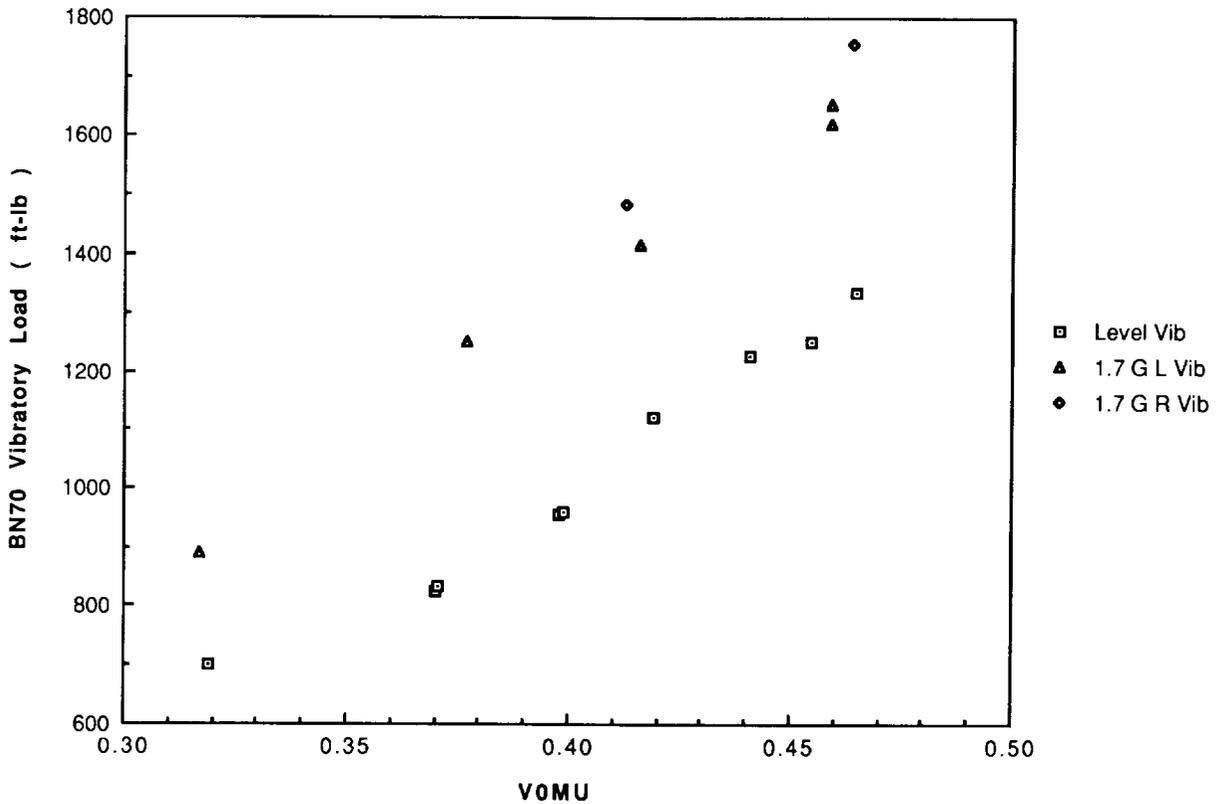
(a) Average.

(b) Vibratory.

Figure 63. Normal bending 70% R vs μ, left and right banks, 1.7 g.
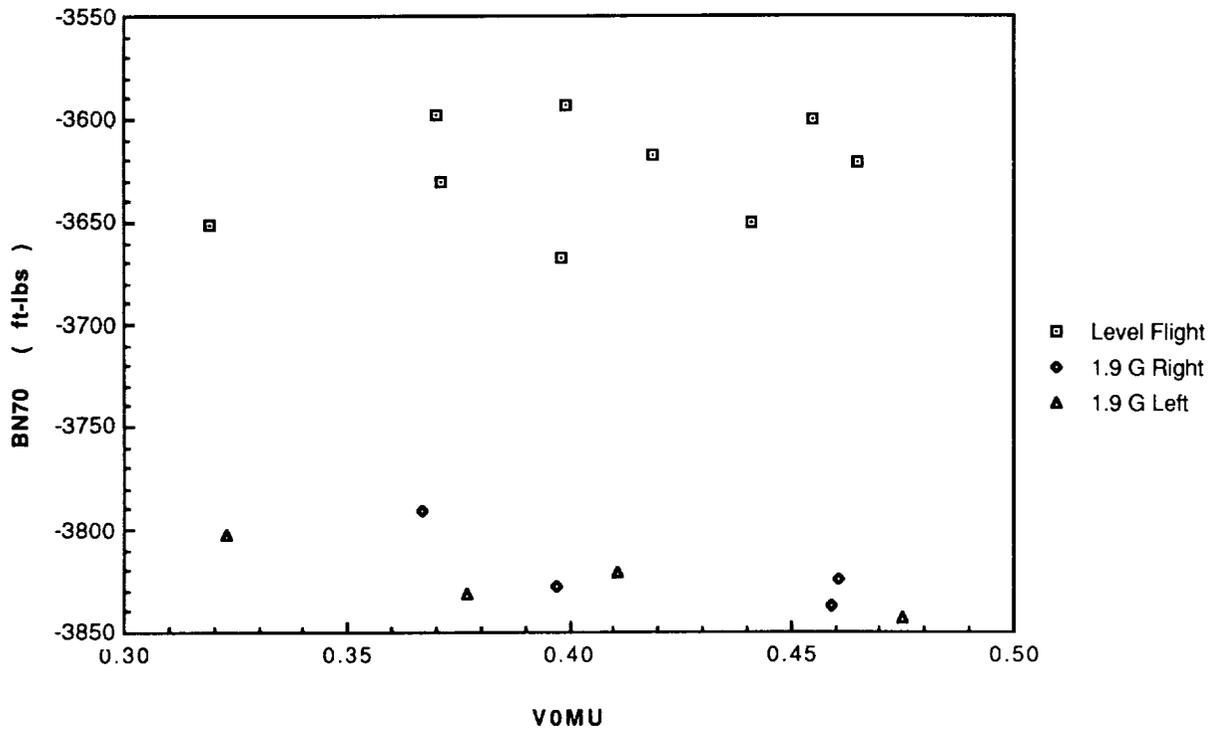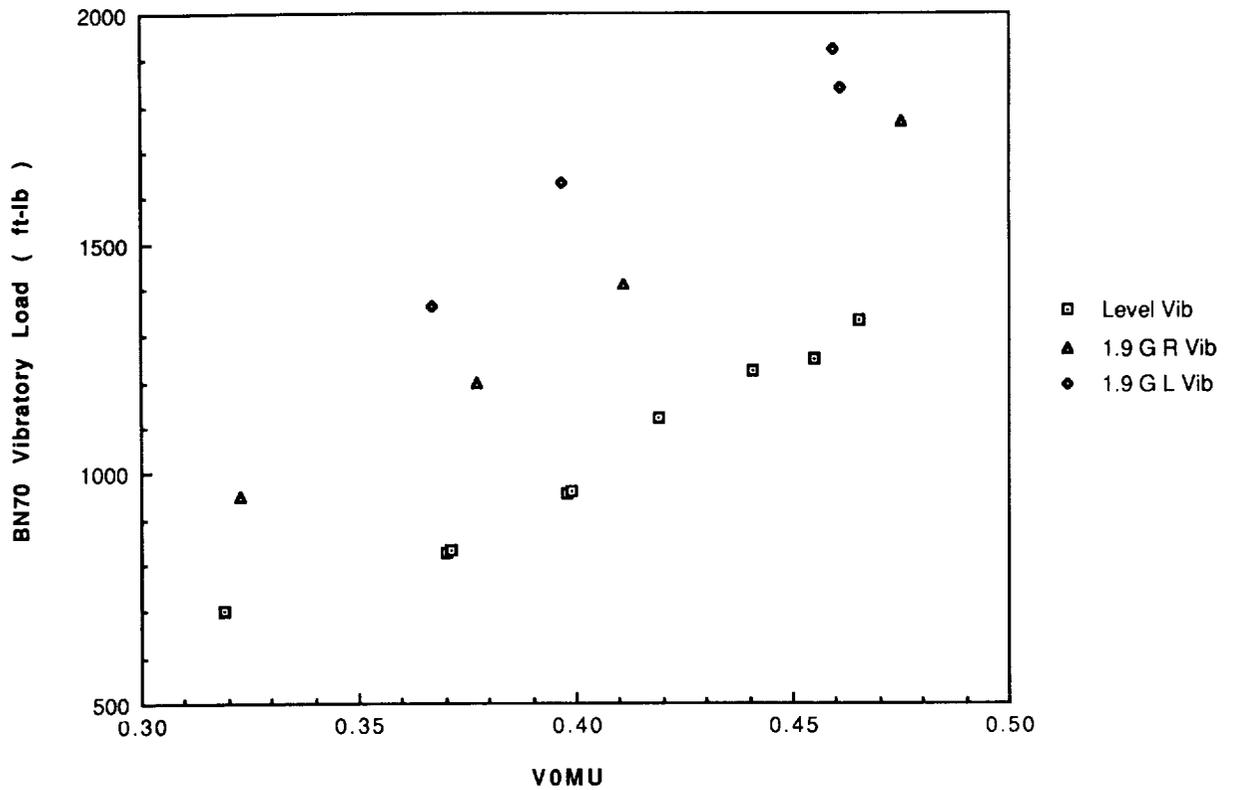
(a) Average.

(b) Vibratory.

Figure 64. Normal bending 70% R vs μ, left and right banks, 1.9 g.
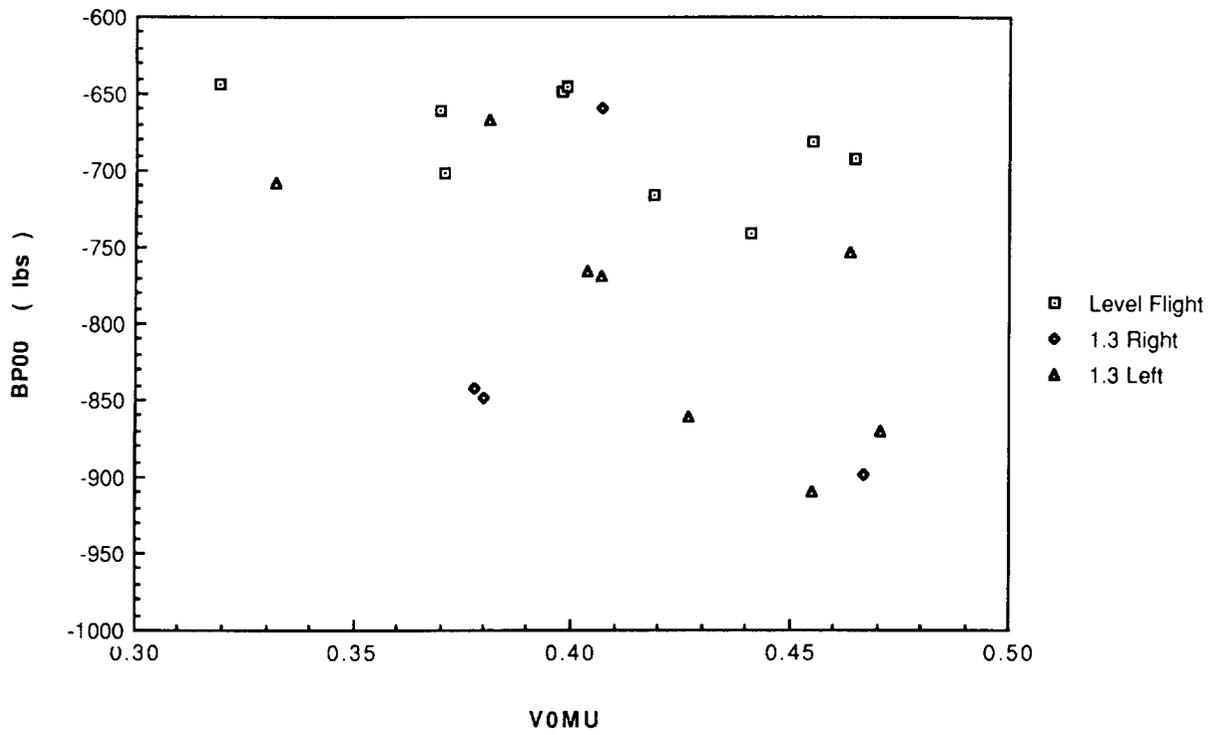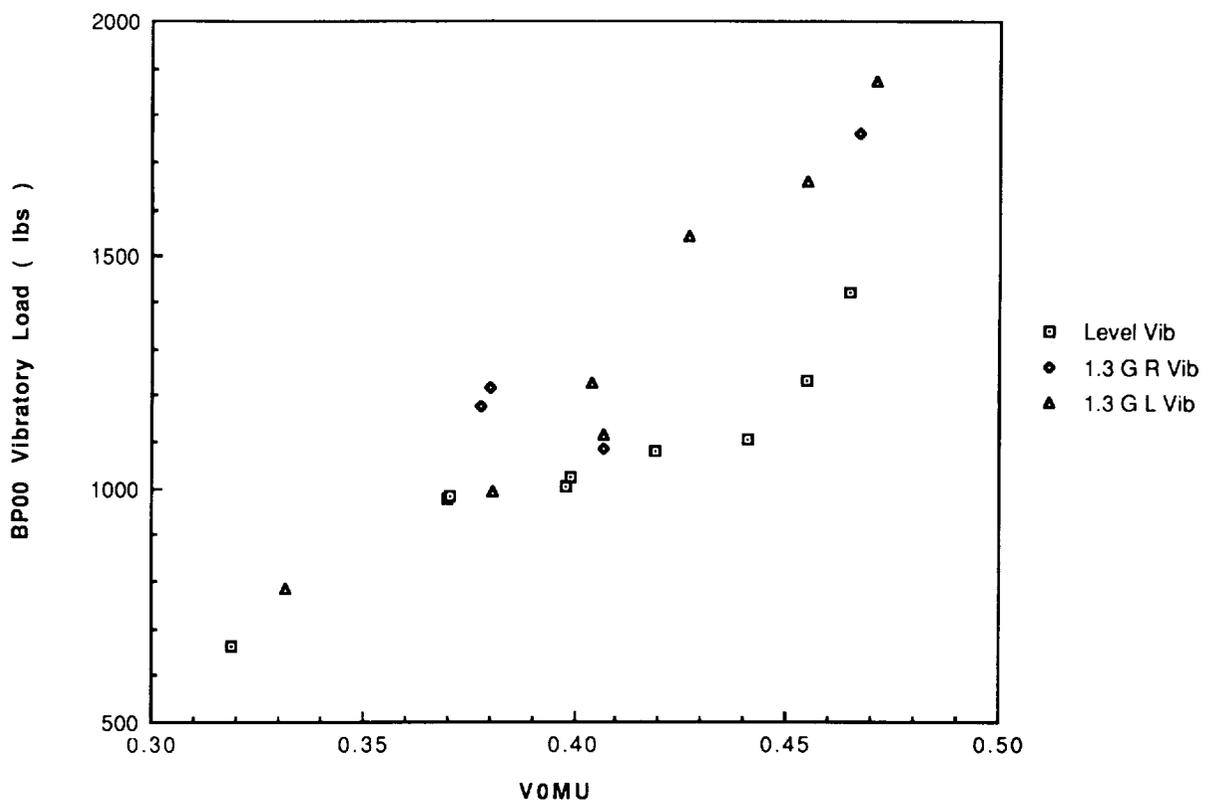
(a) Average.

(b) Vibratory.

Figure 65. Pitch-link load vs μ, left and right banks, 1.3 g.
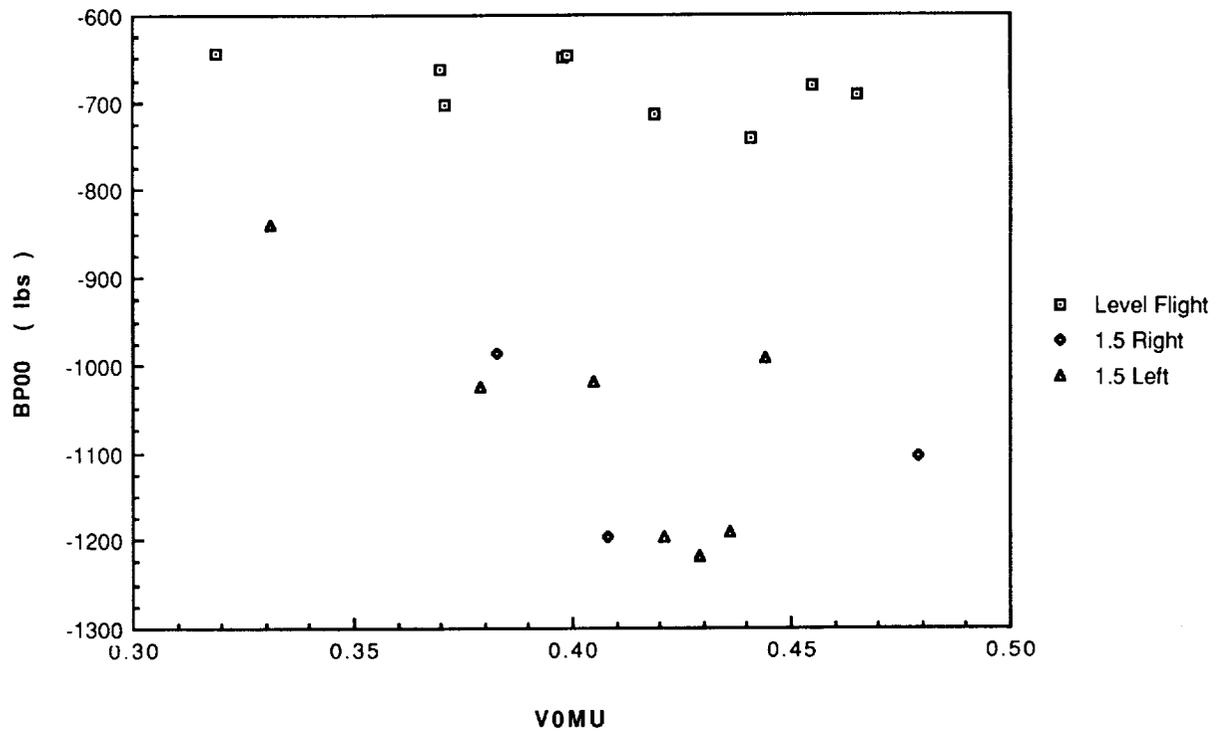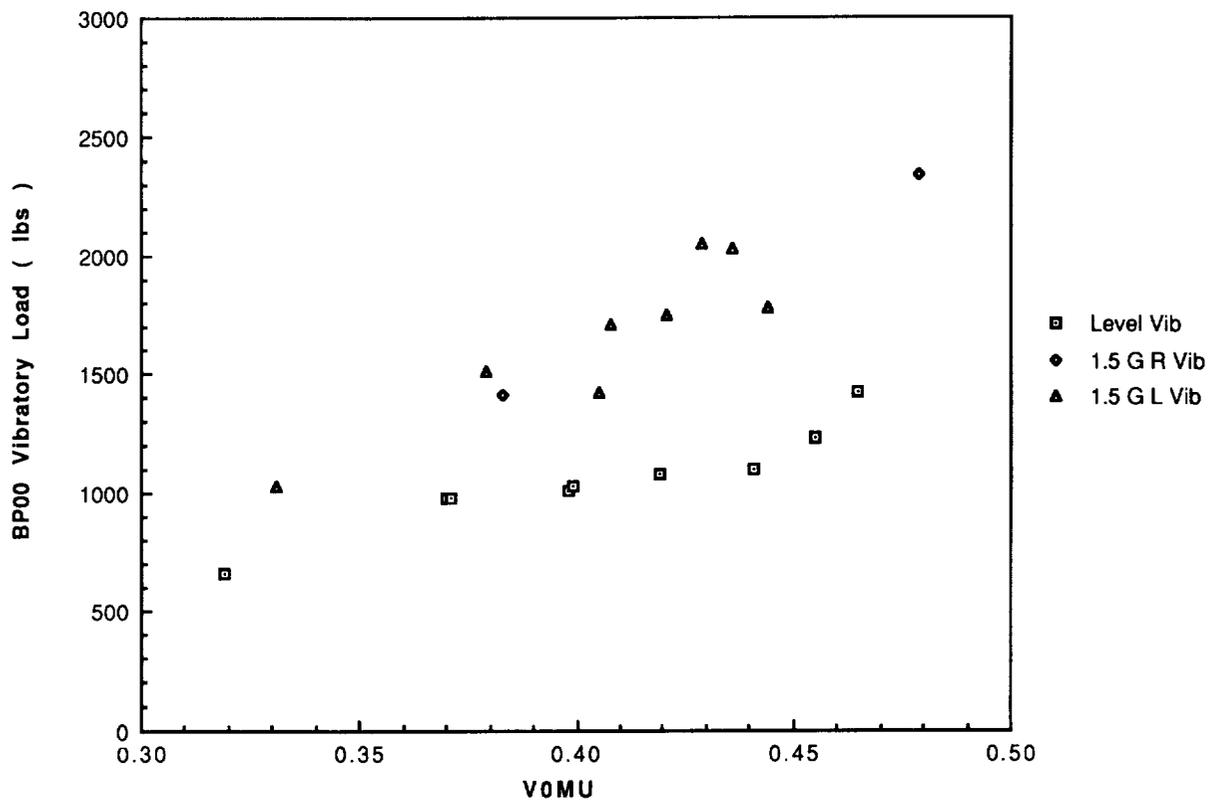
(a) Average.

(b) Vibratory.

Figure 66. Pitch-link load vs μ, left and right banks, 1.5 g.
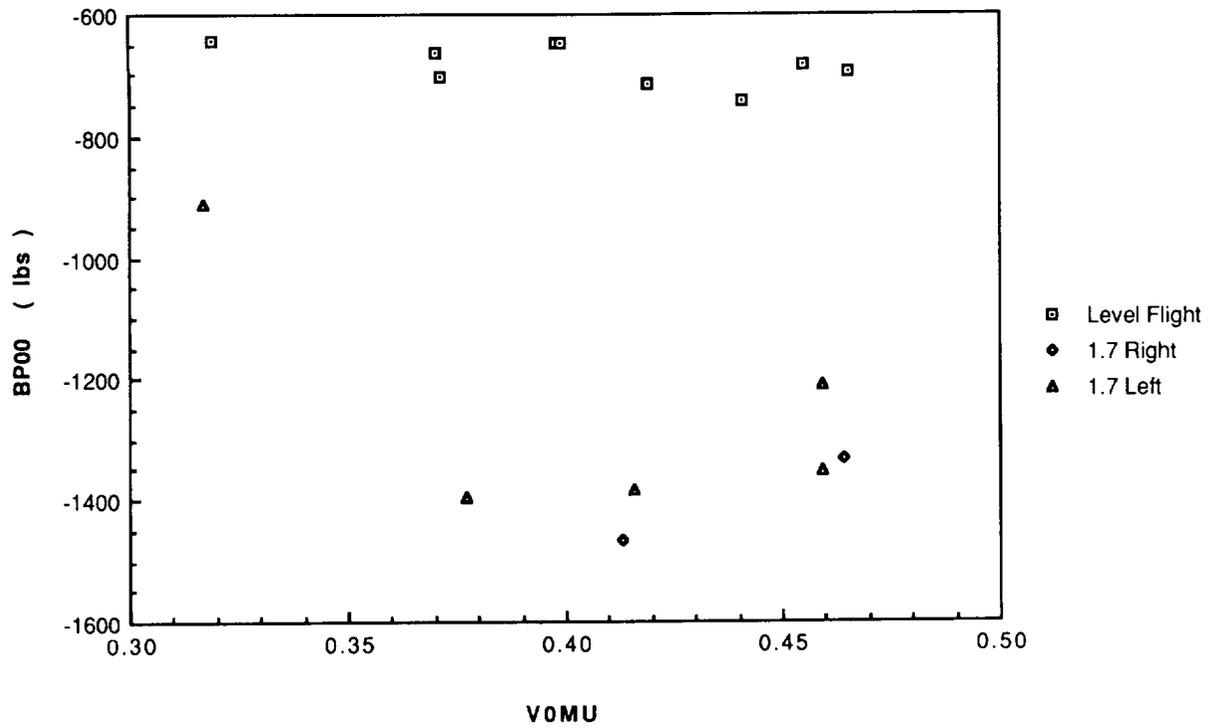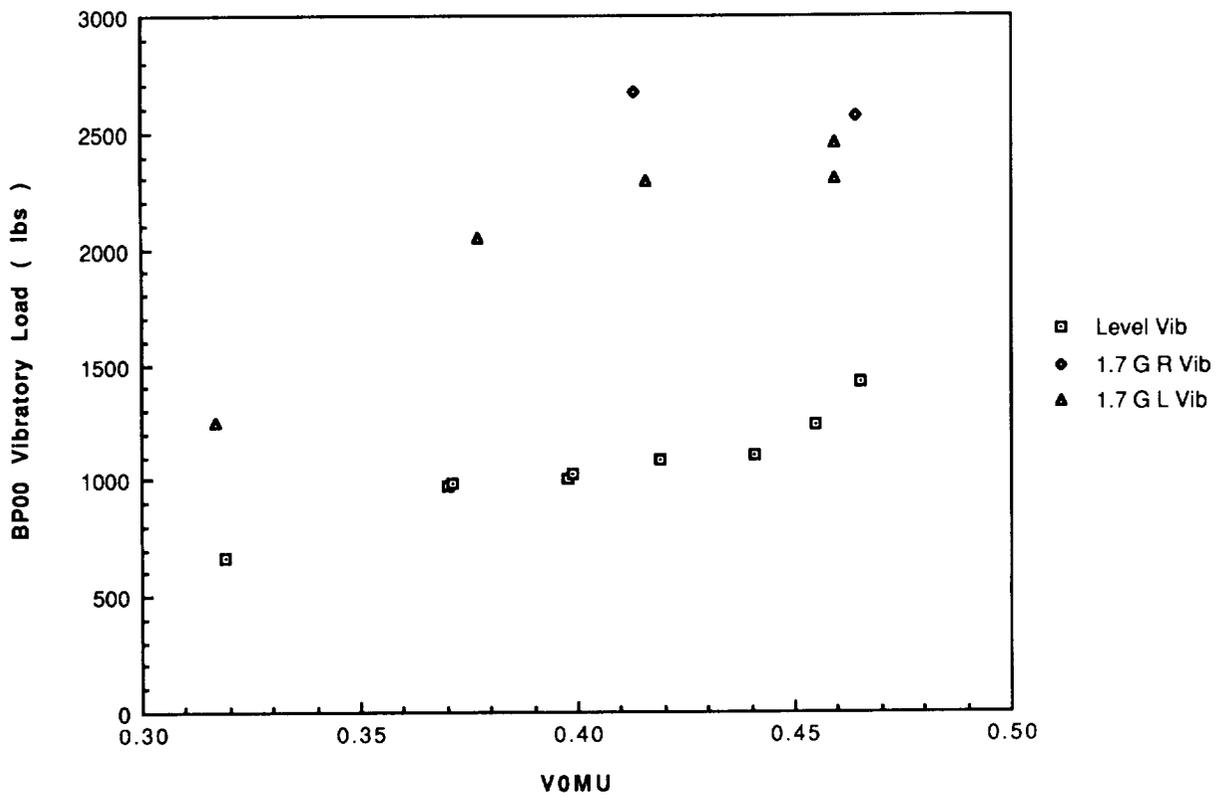
(a) Average.

(b) Vibratory.

Figure 67. Pitch-link load vs μ, left and right banks, 1.7 g.
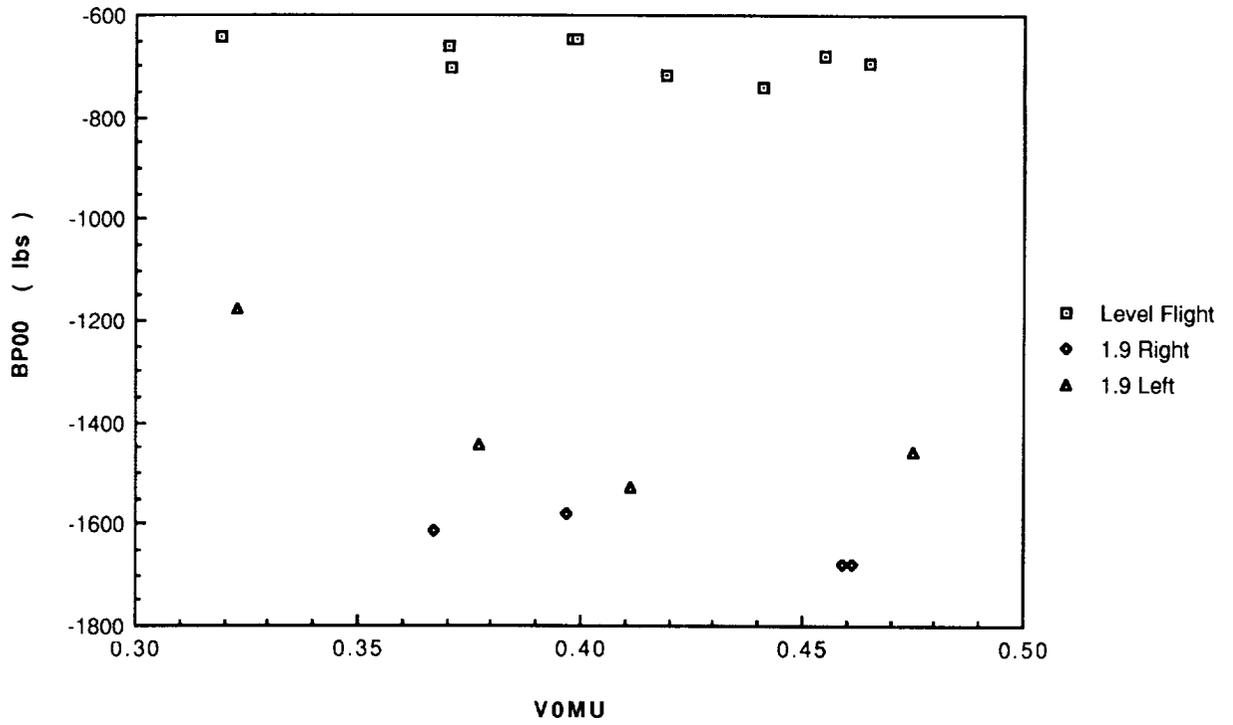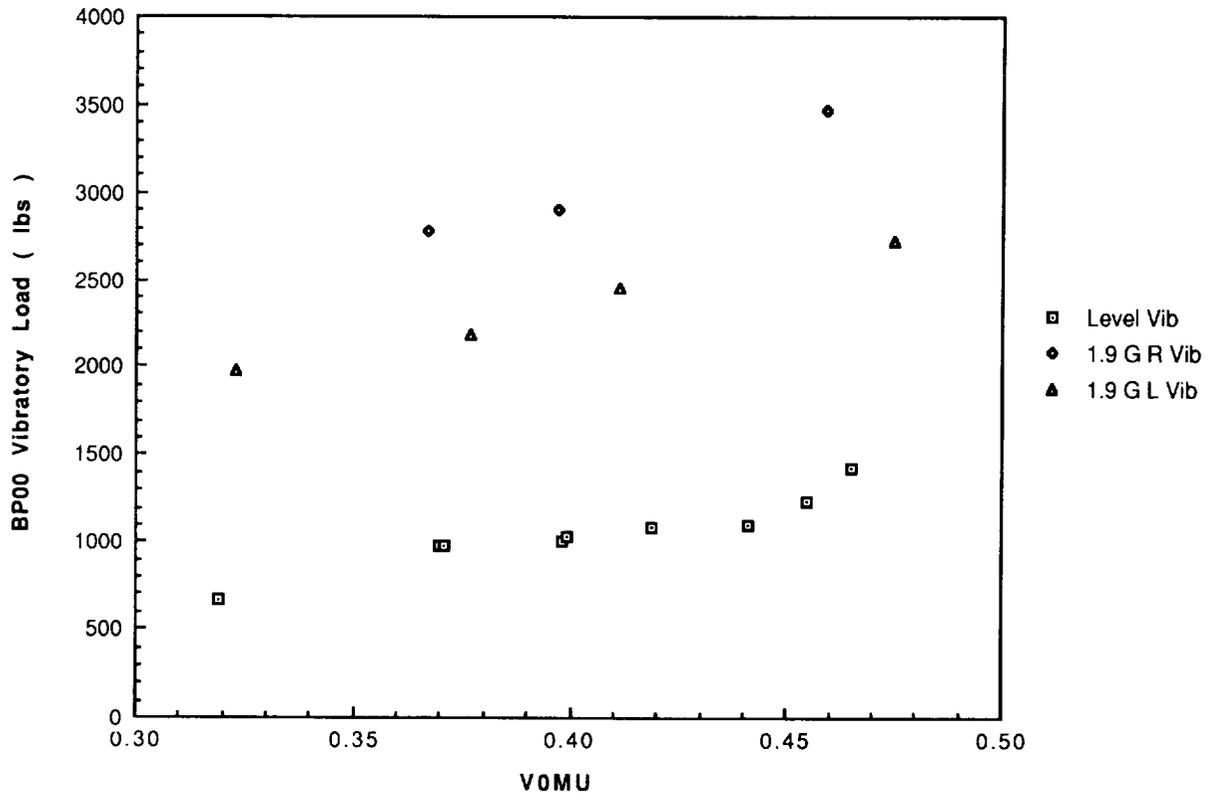
(a) Average.

(b) Vibratory.

Figure 68. Pitch-link load vs μ, left and right banks, 1.9 g.

(a) Average.

(b) Vibratory.

Figure 69. Forward link load vs μ, left and right banks, 1.3 g.
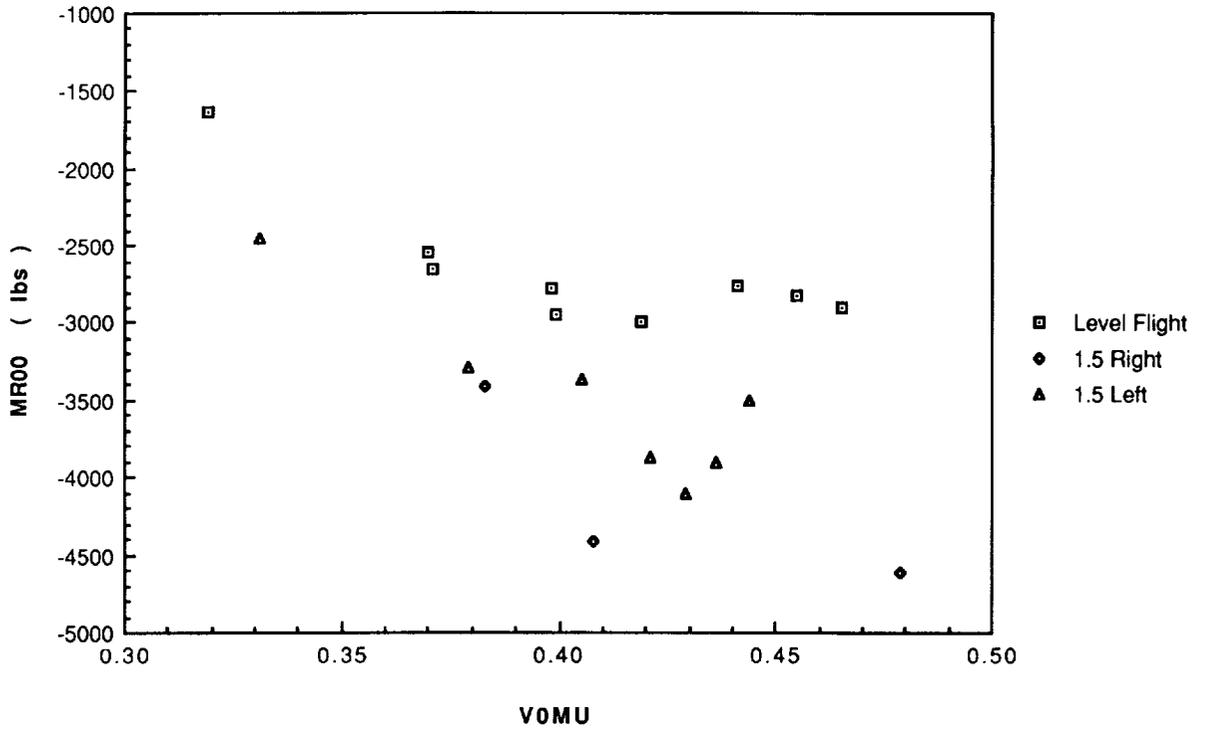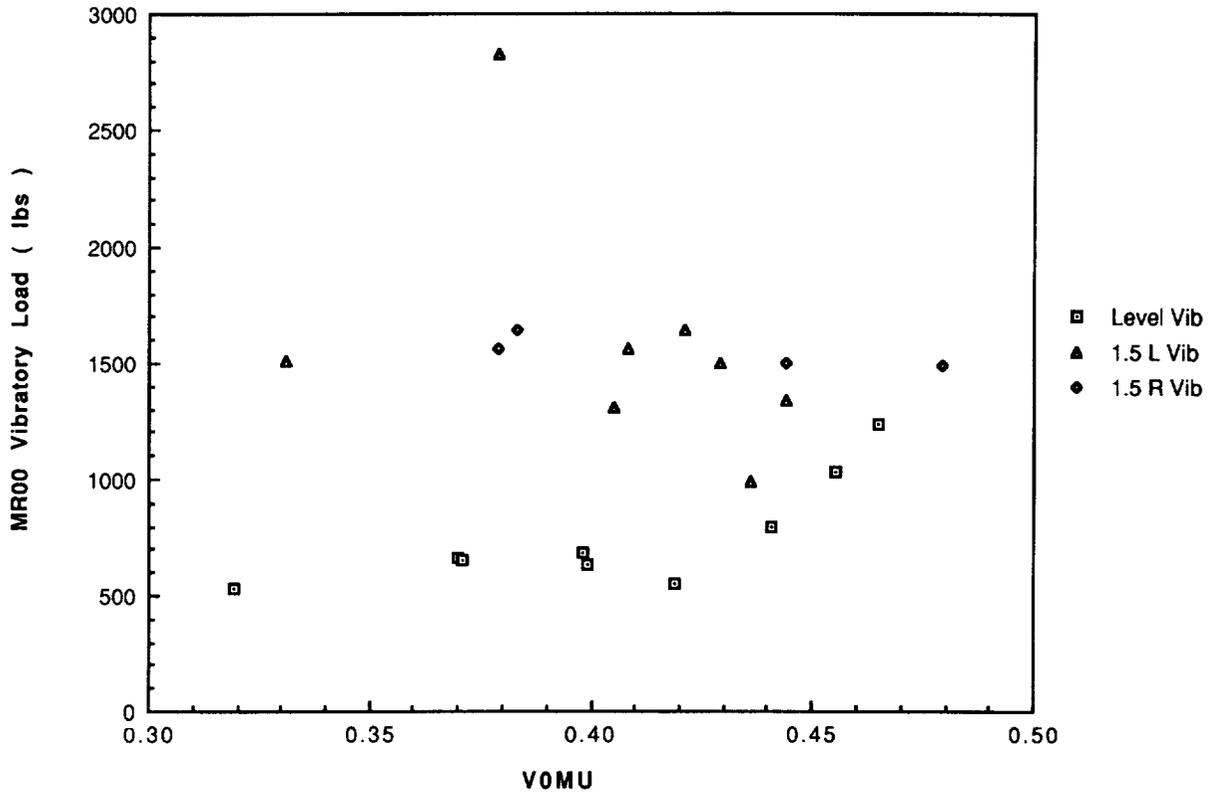
(a) Average.

(b) Vibratory.

Figure 70. Forward link load vs μ, left and right banks, 1.5 g.
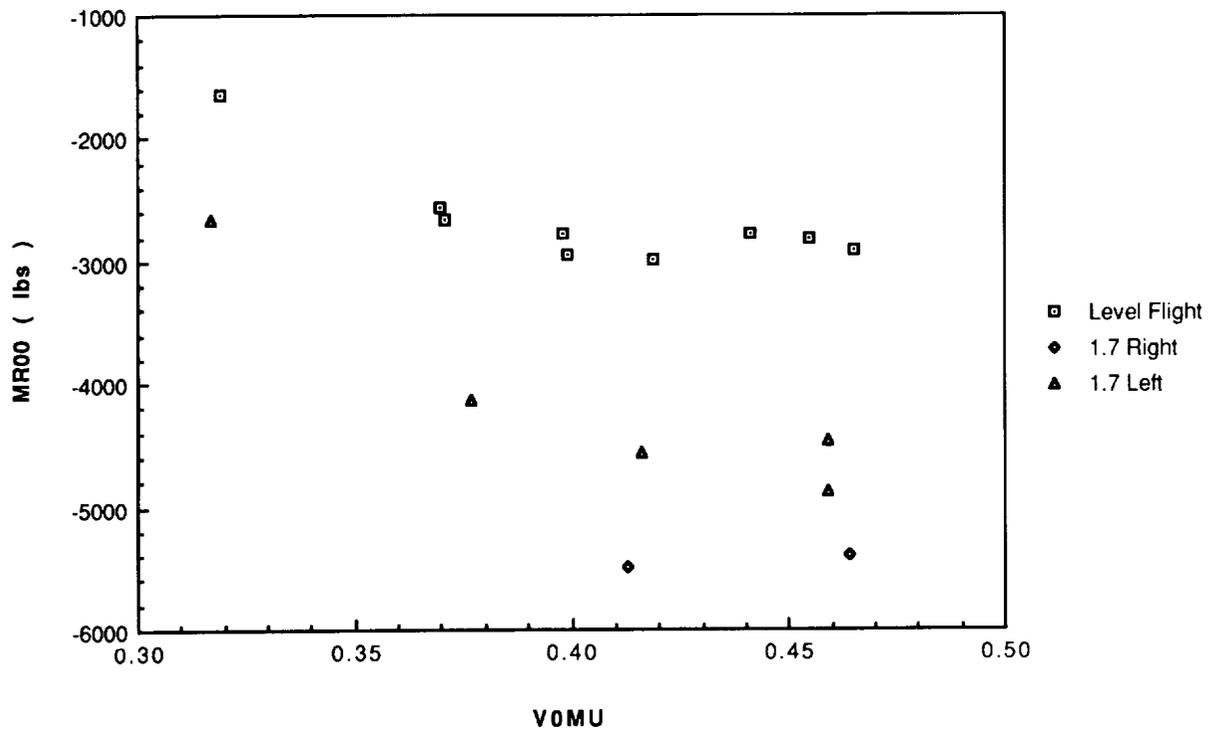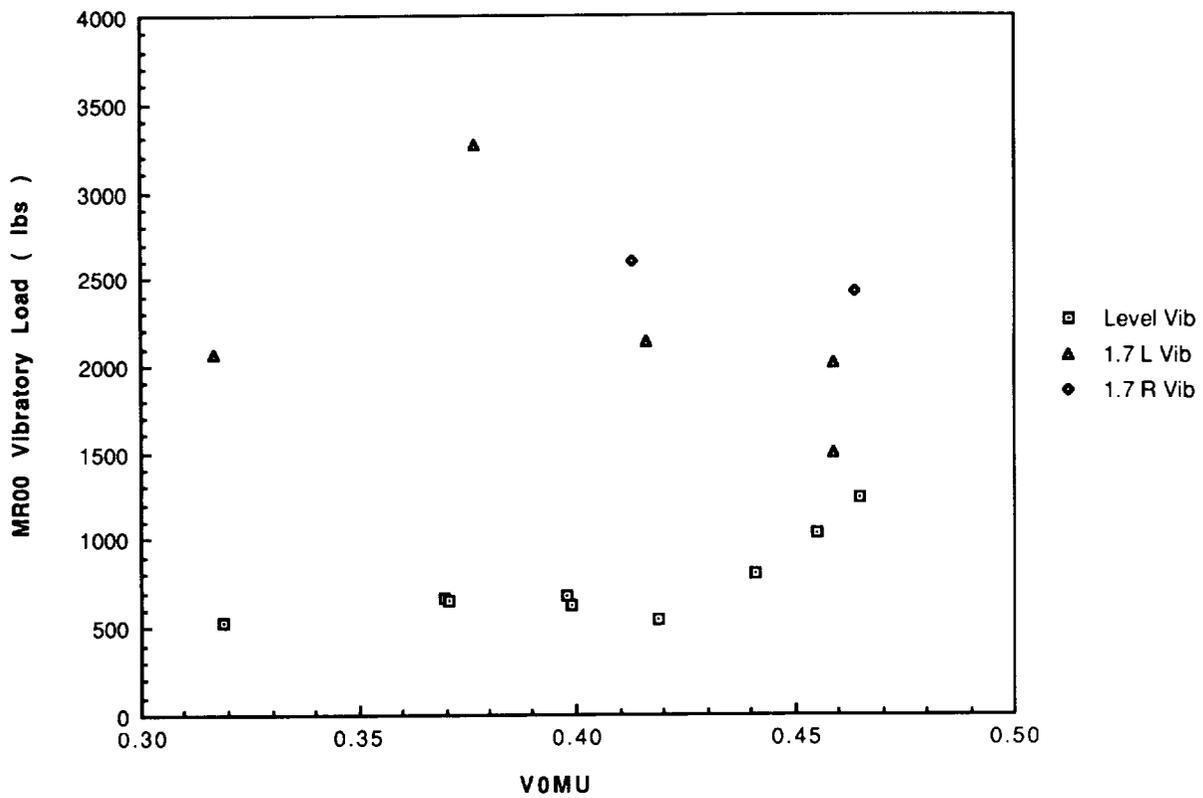
(a) Average.

(b) Vibratory.

Figure 71. Forward link load vs μ, left and right banks, 1.7 g.
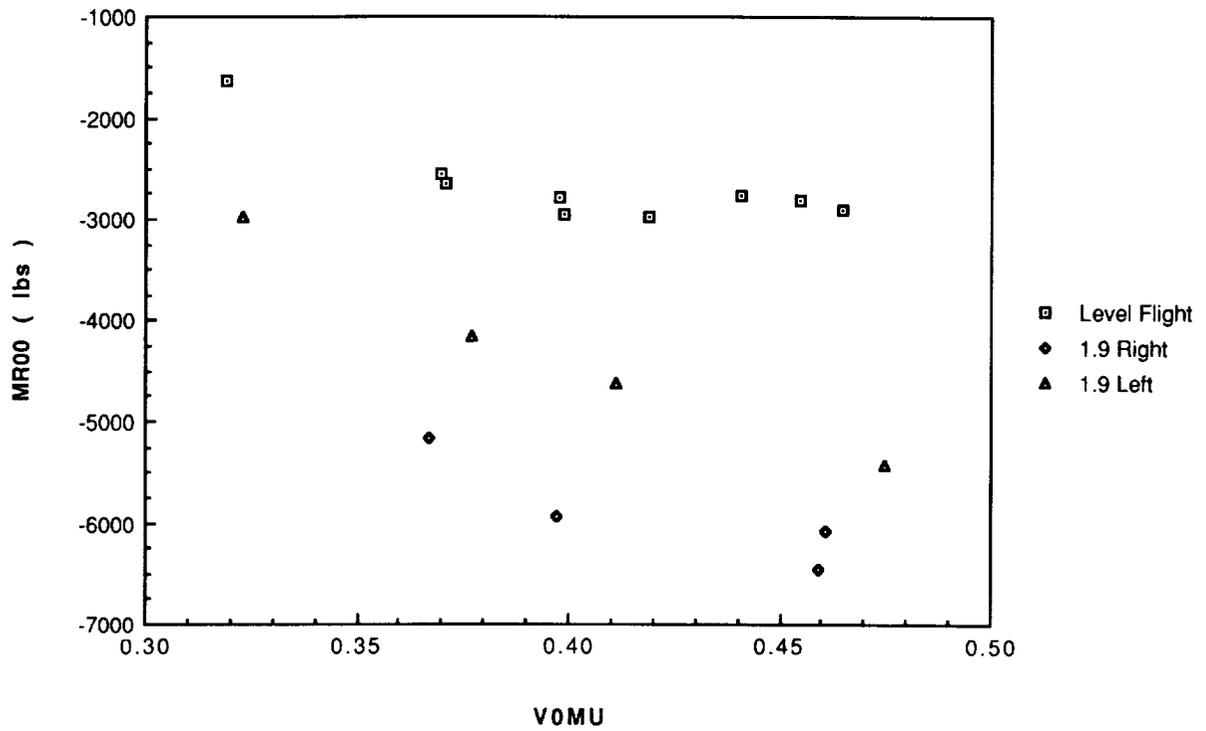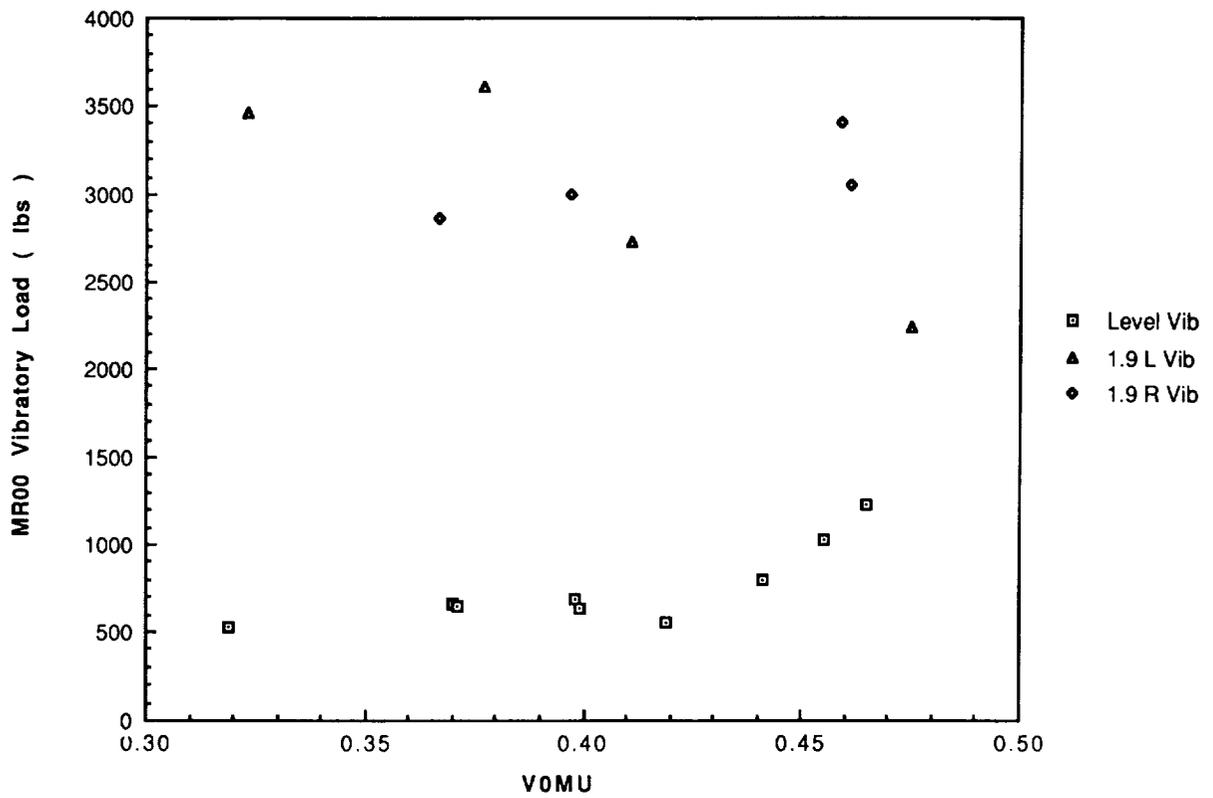
(a) Average.

(b) Vibratory.

Figure 72. Forward link load vs μ, left and right banks, 1.9 g.
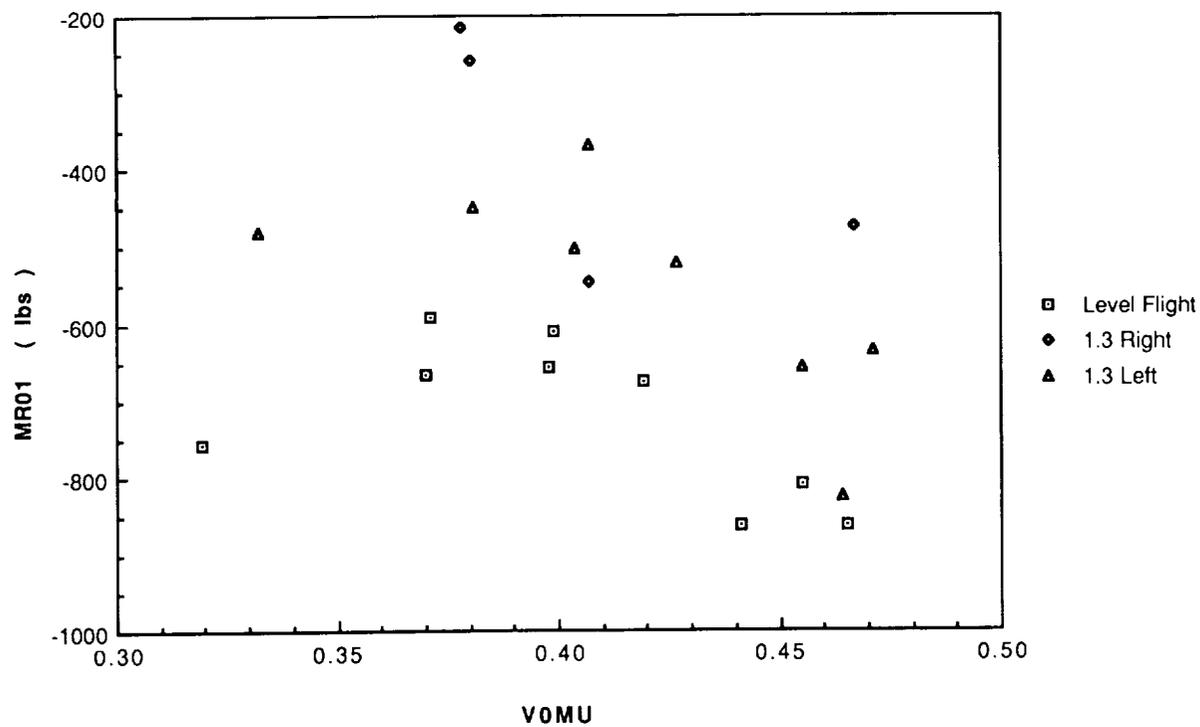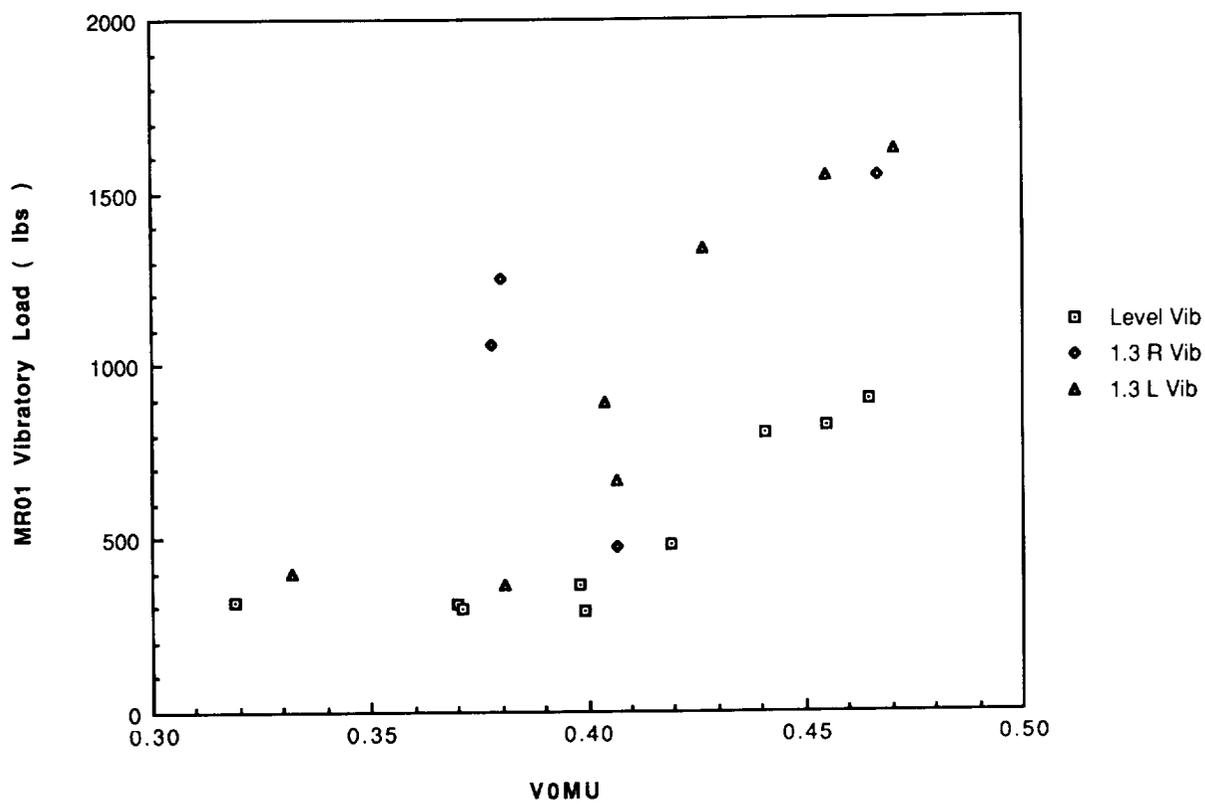
(a) Average.

(b) Vibratory.

Figure 73. Lateral link load vs μ, left and right banks, 1.3 g.
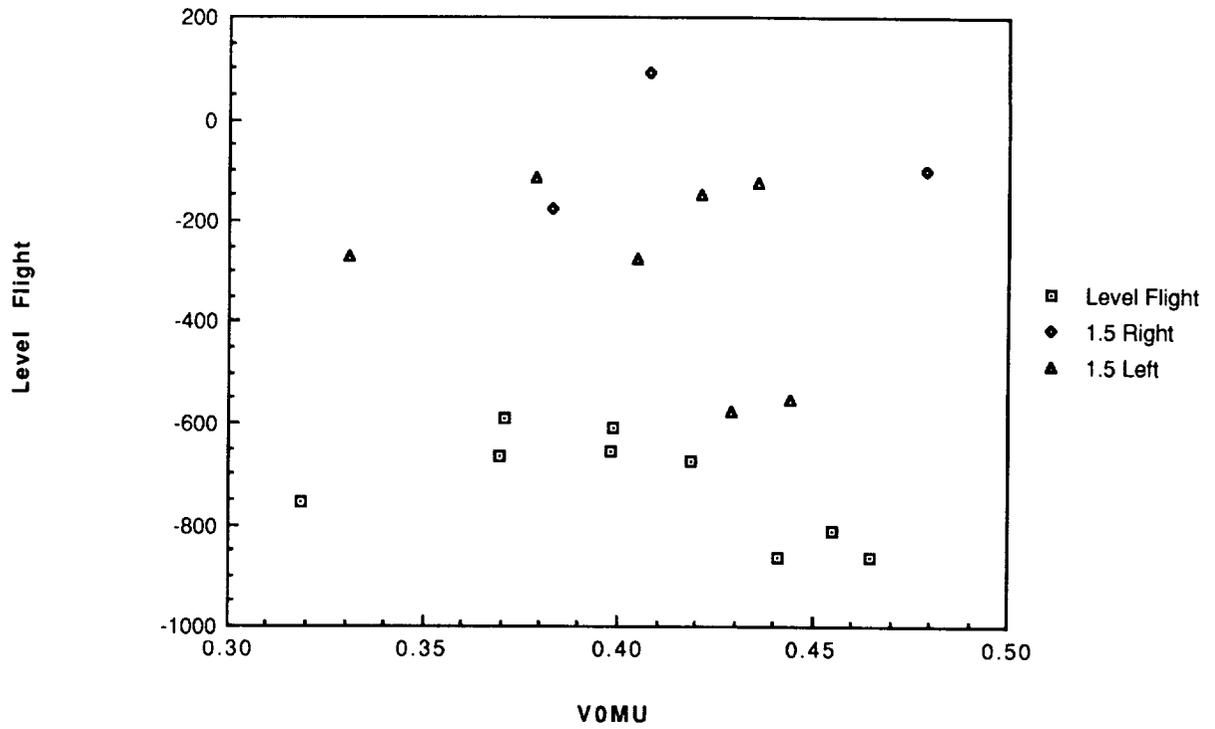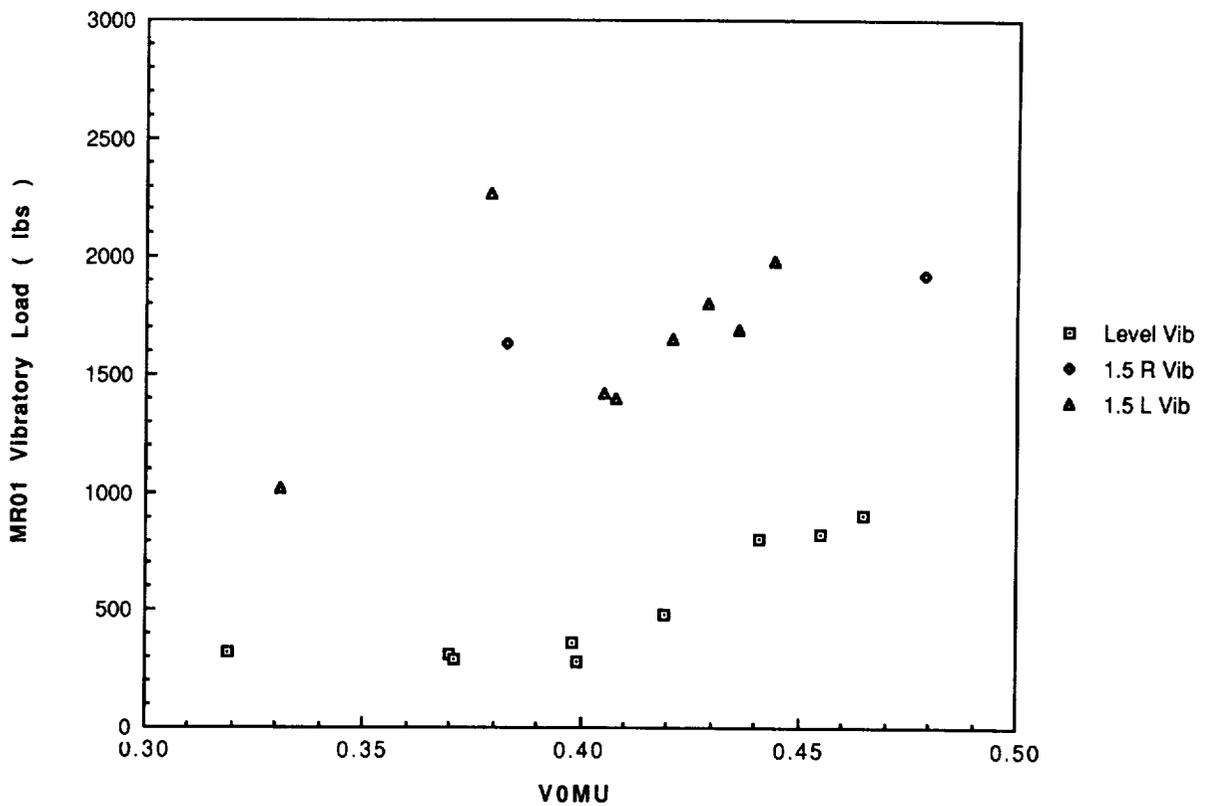
(a) Average.

(b) Vibratory.

Figure 74. Lateral link load vs μ, left and right banks, 1.5 g.
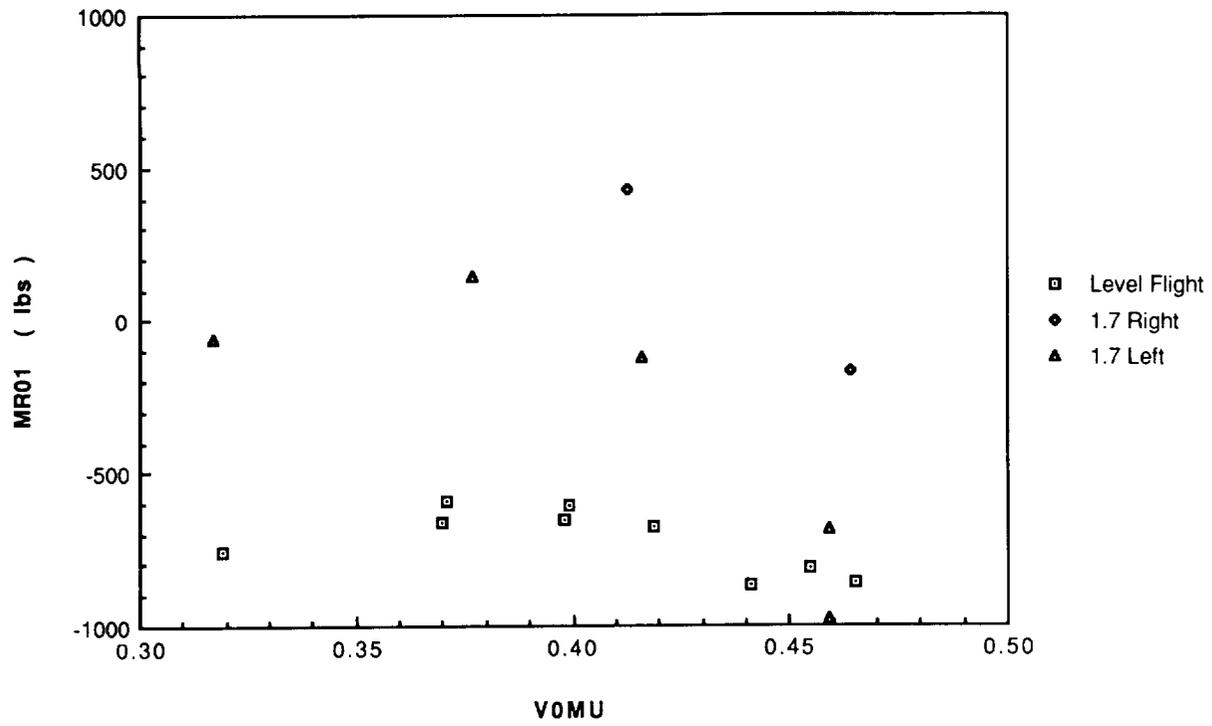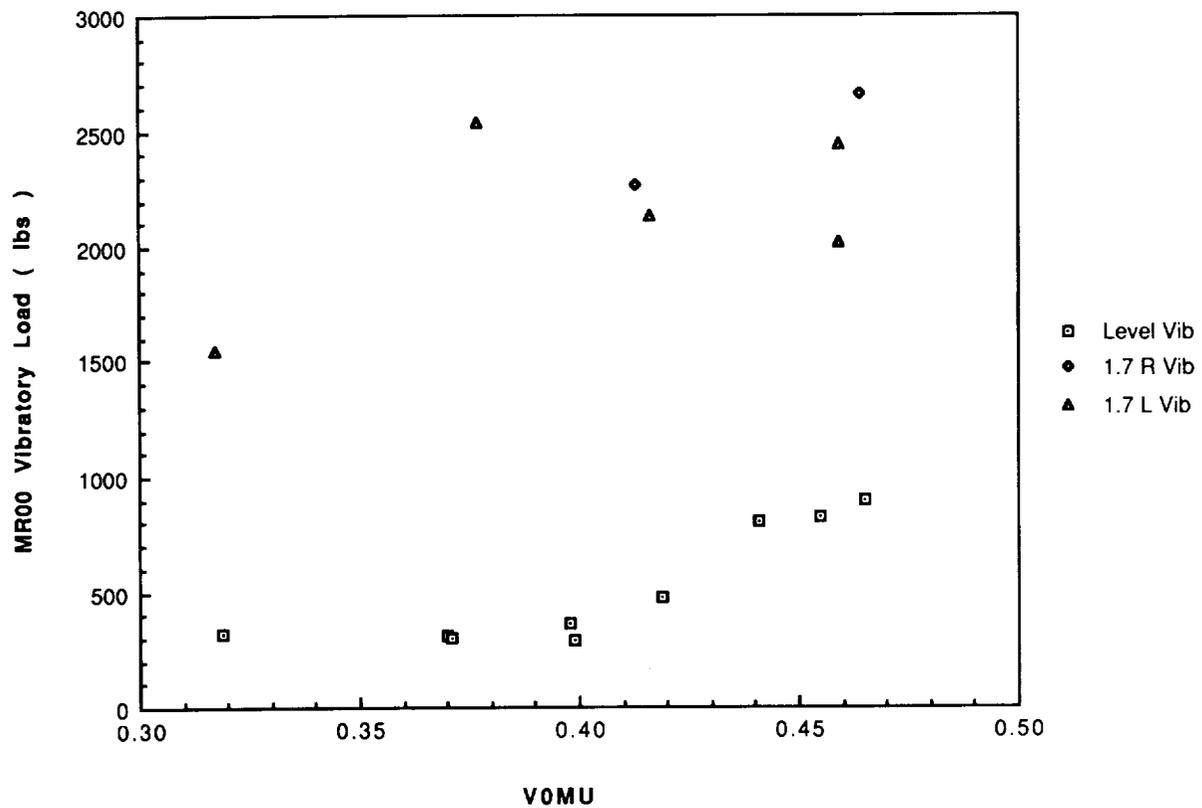
(a) Average.

(b) Vibratory.

Figure 75. Lateral link load vs μ, left and right banks, 1.7 g.
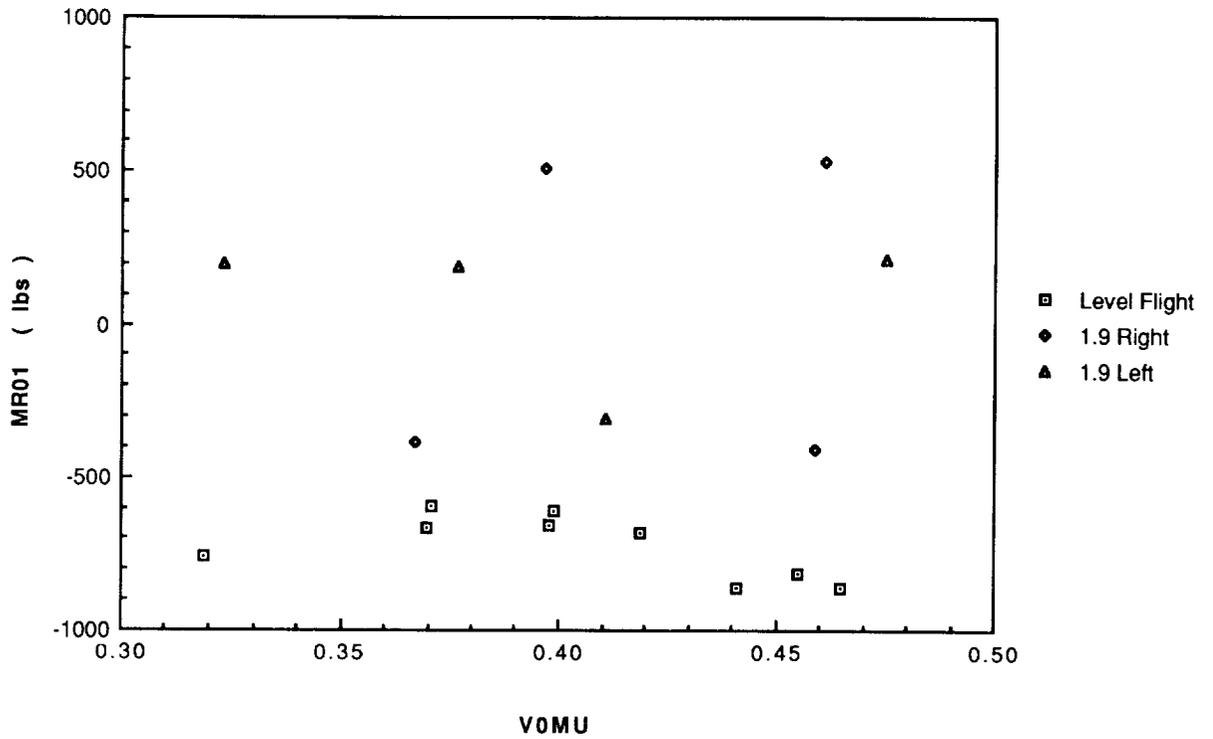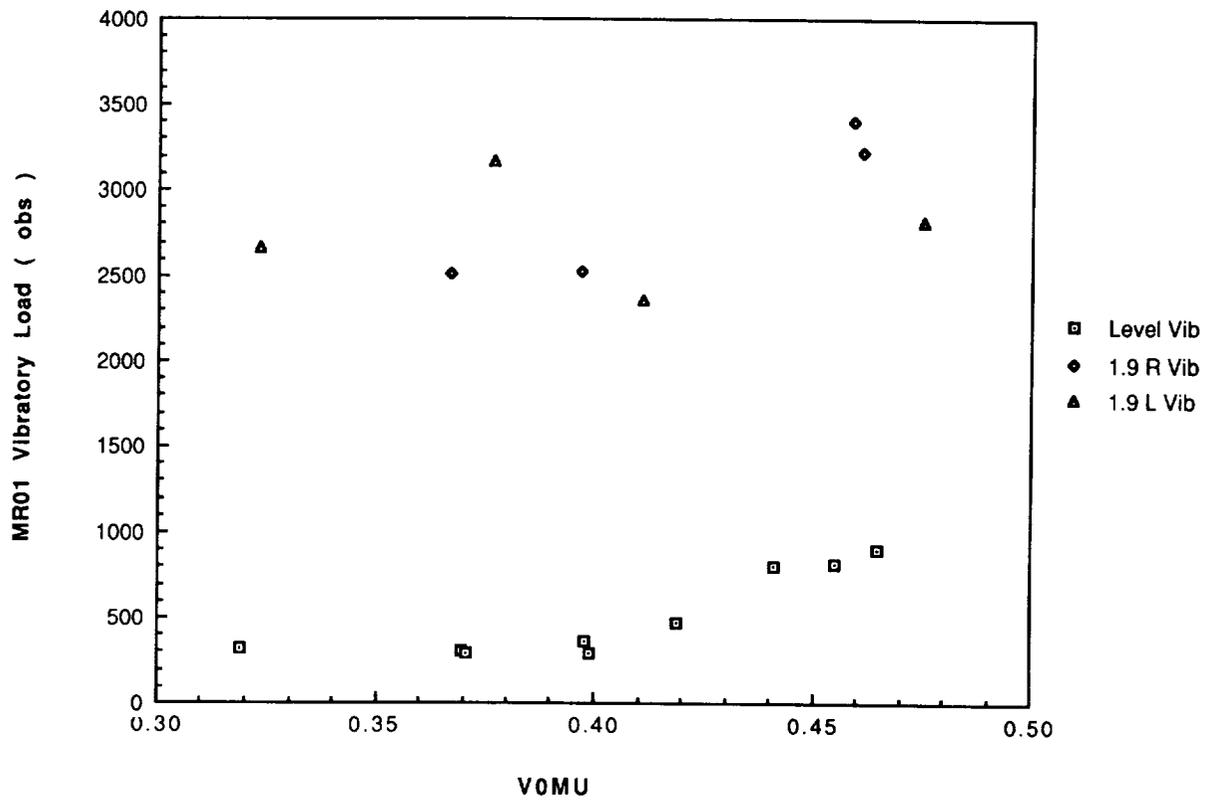
(a) Average.

(b) Vibratory.

Figure 76. Lateral link load vs μ, left and right banks, 1.9 g.
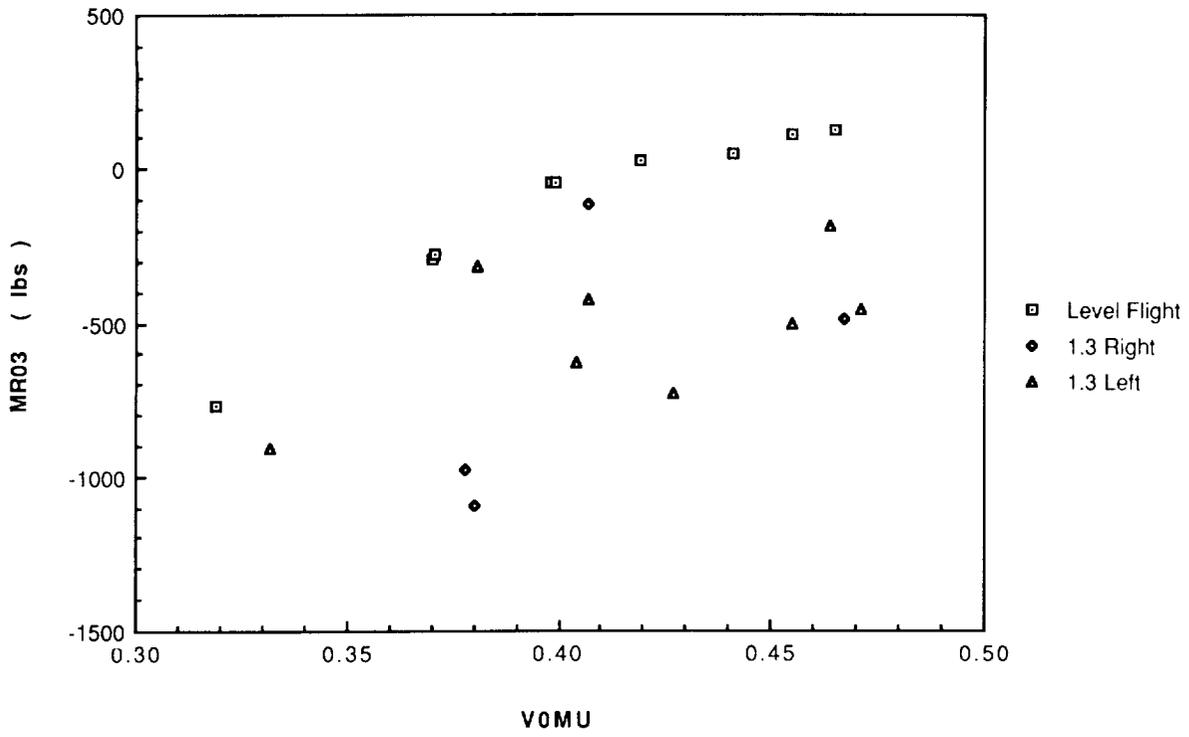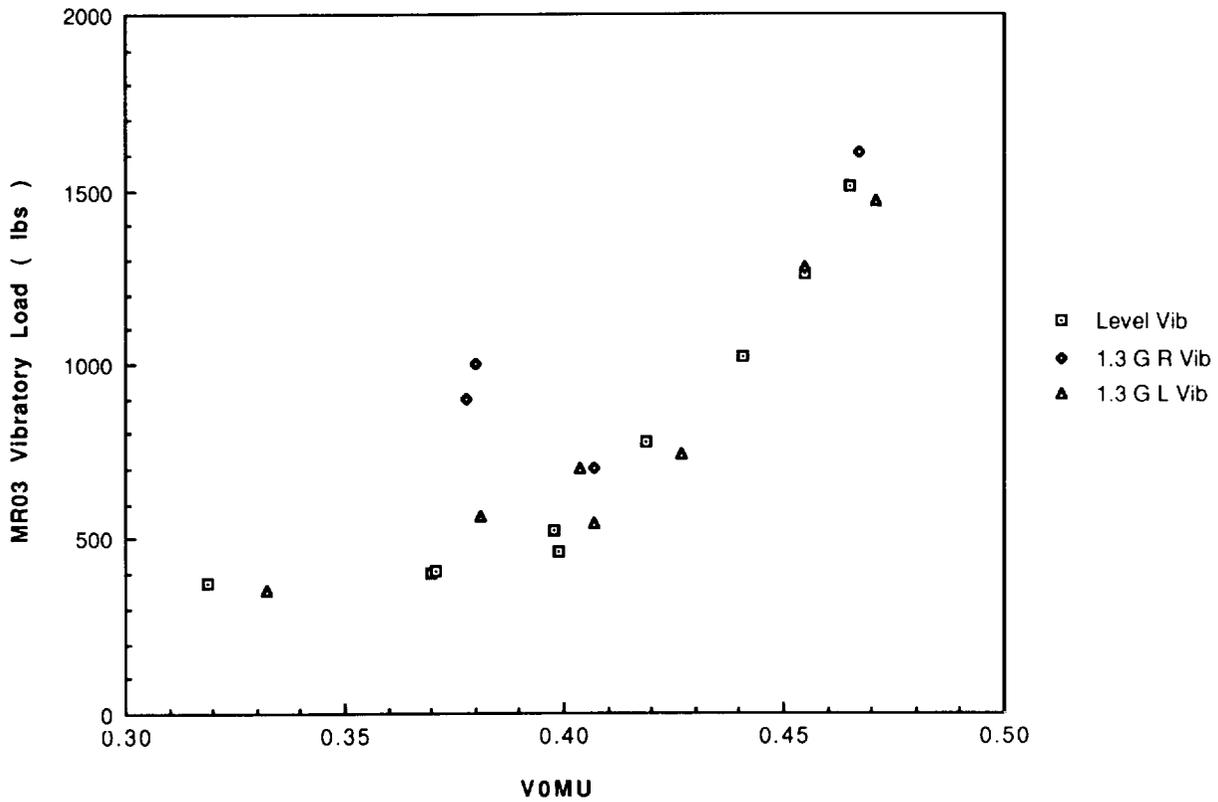
(a) Average.

(b) Vibratory.

Figure 77. Aft link load vs μ, left and right banks, 1.3 g.
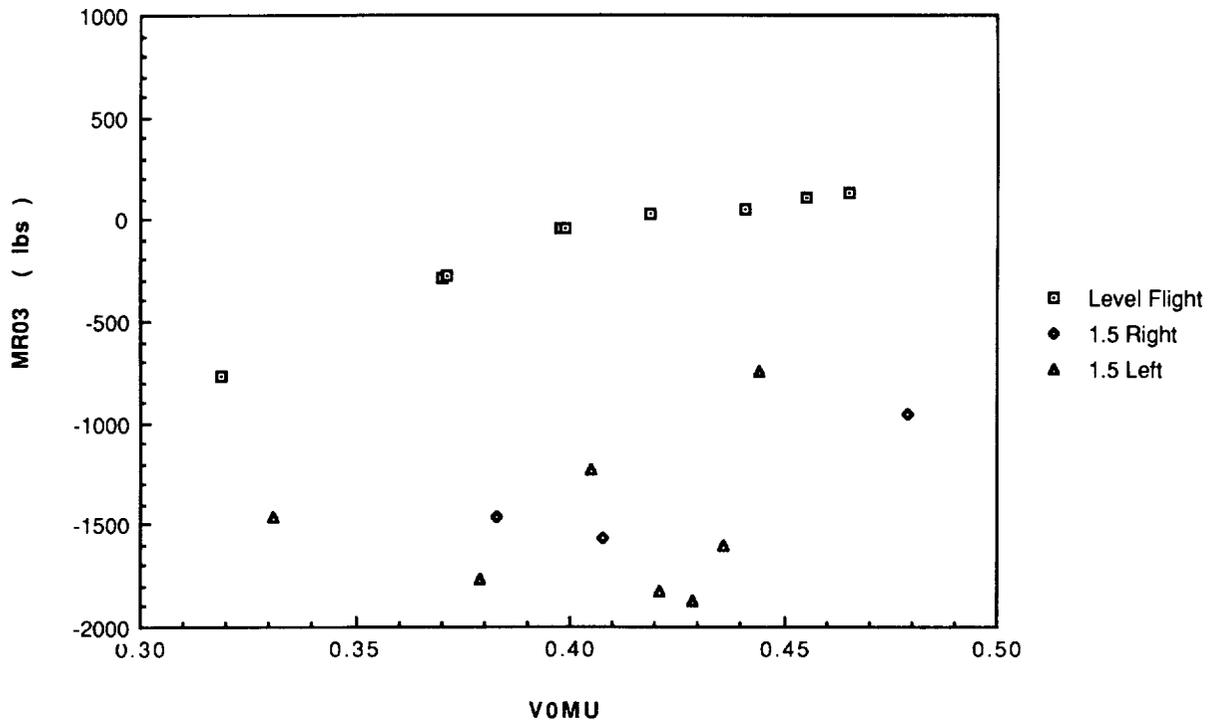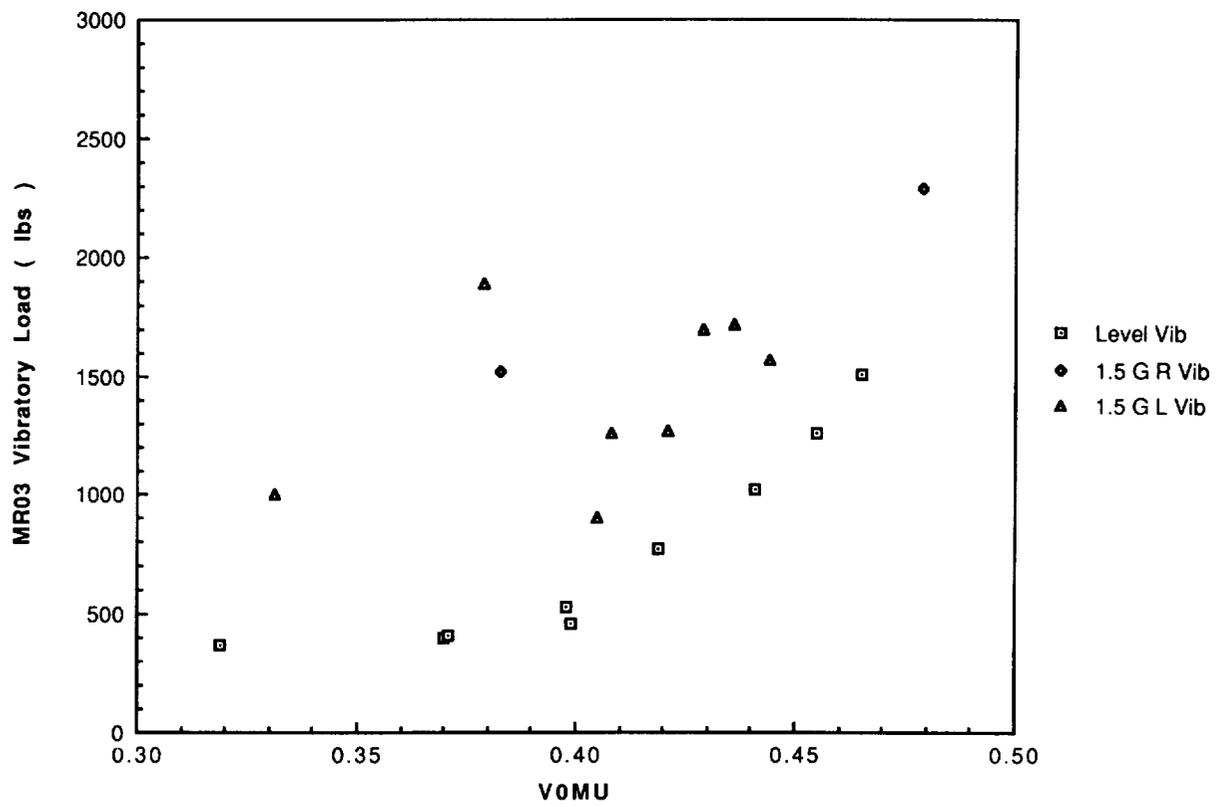
(a) Average.

(b) Vibratory.

Figure 78. Aft link load vs μ, left and right banks, 1.5 g.
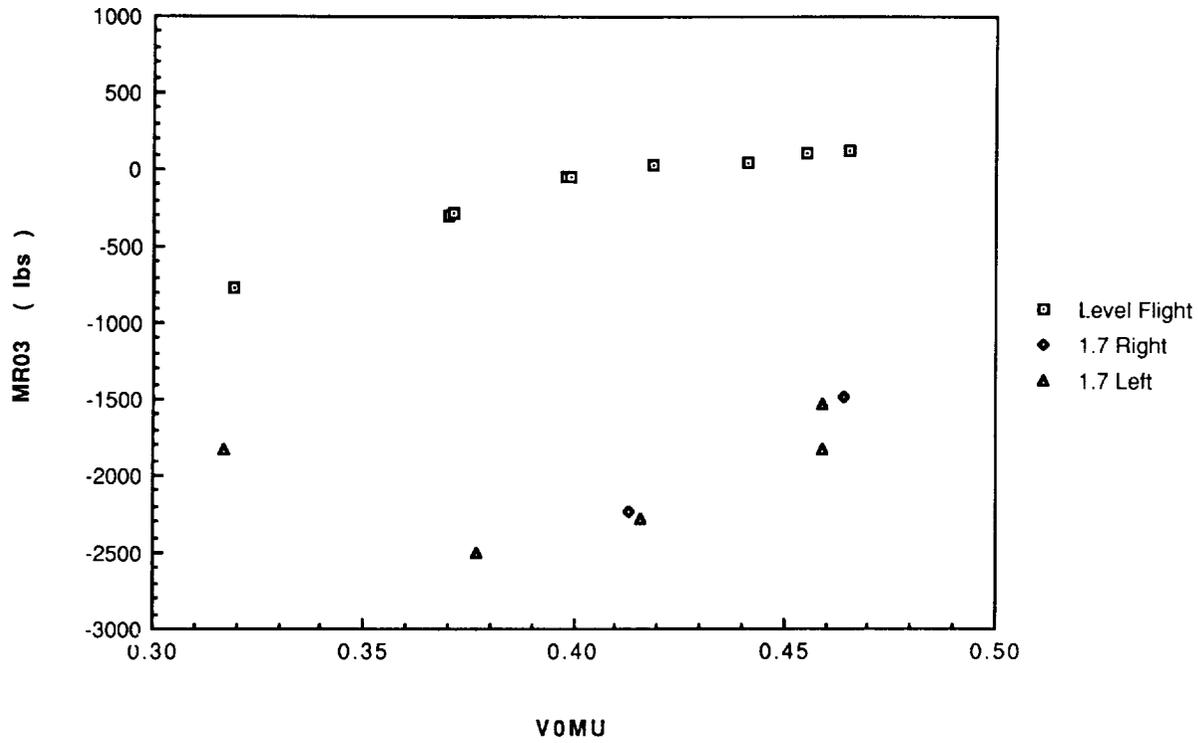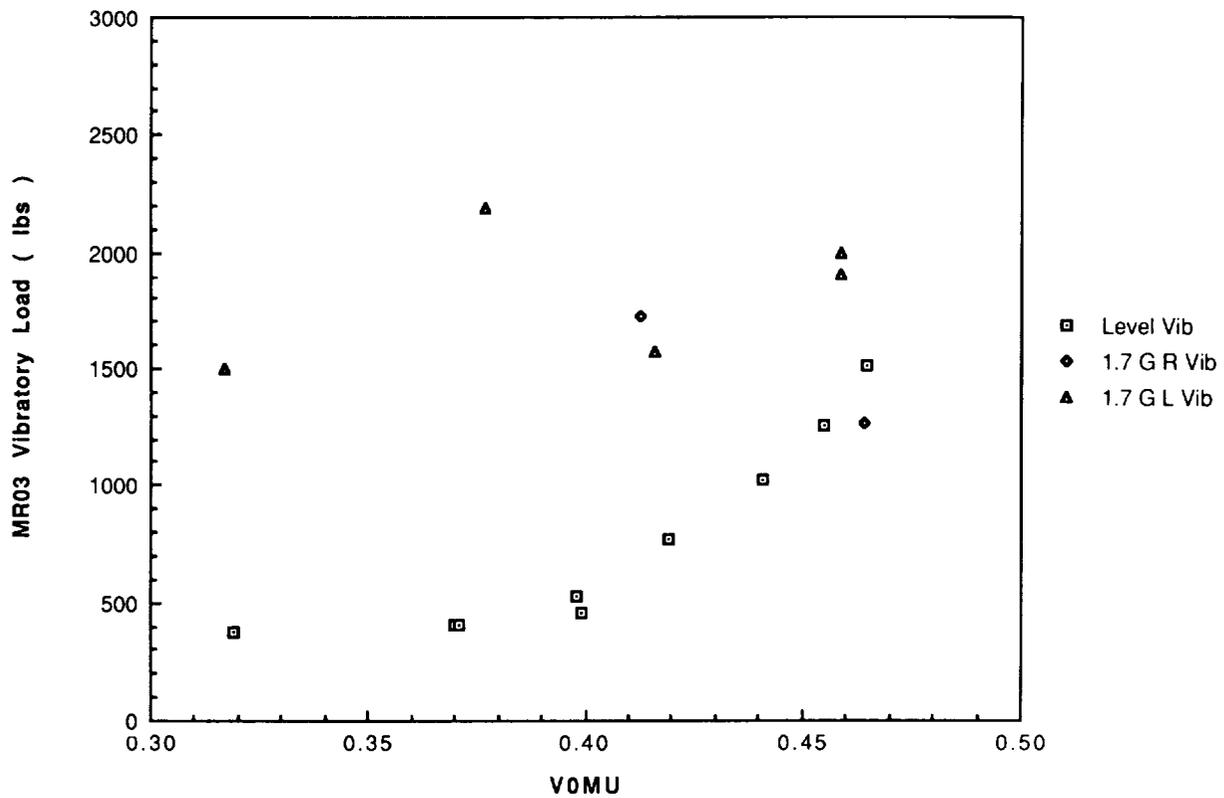
(a) Average.

(b) Vibratory.

Figure 79. Aft link load vs μ, left and right banks, 1.7 g.
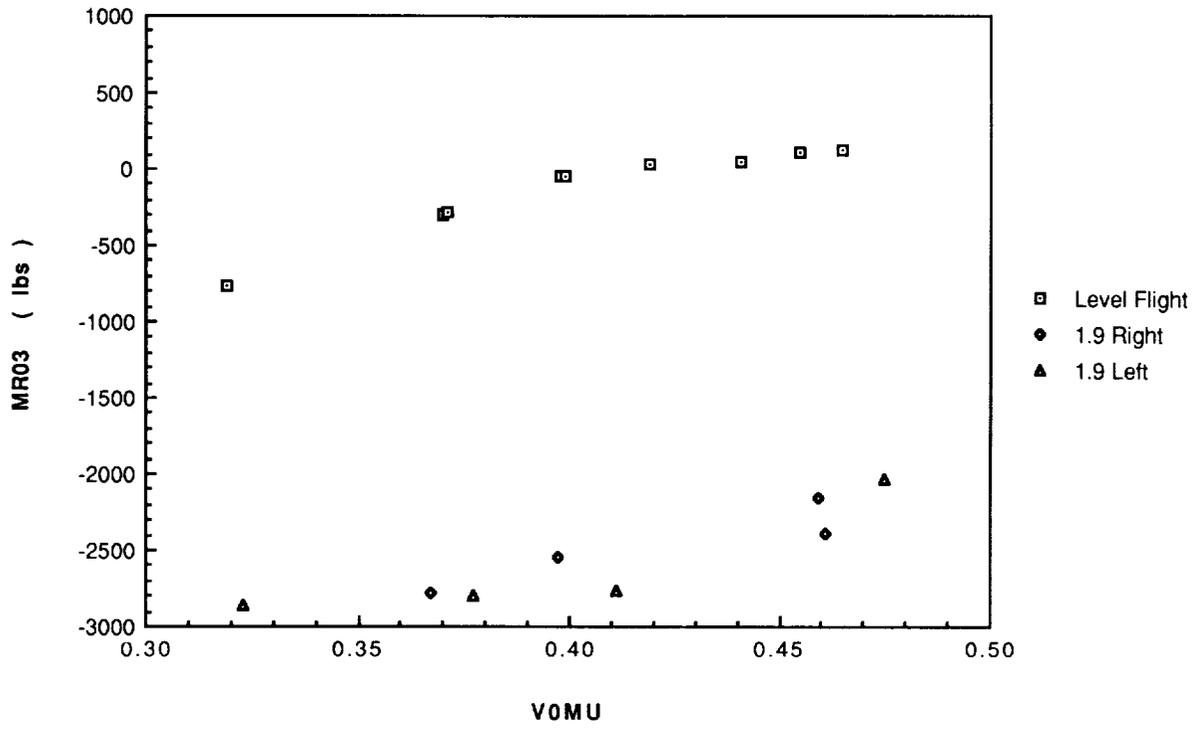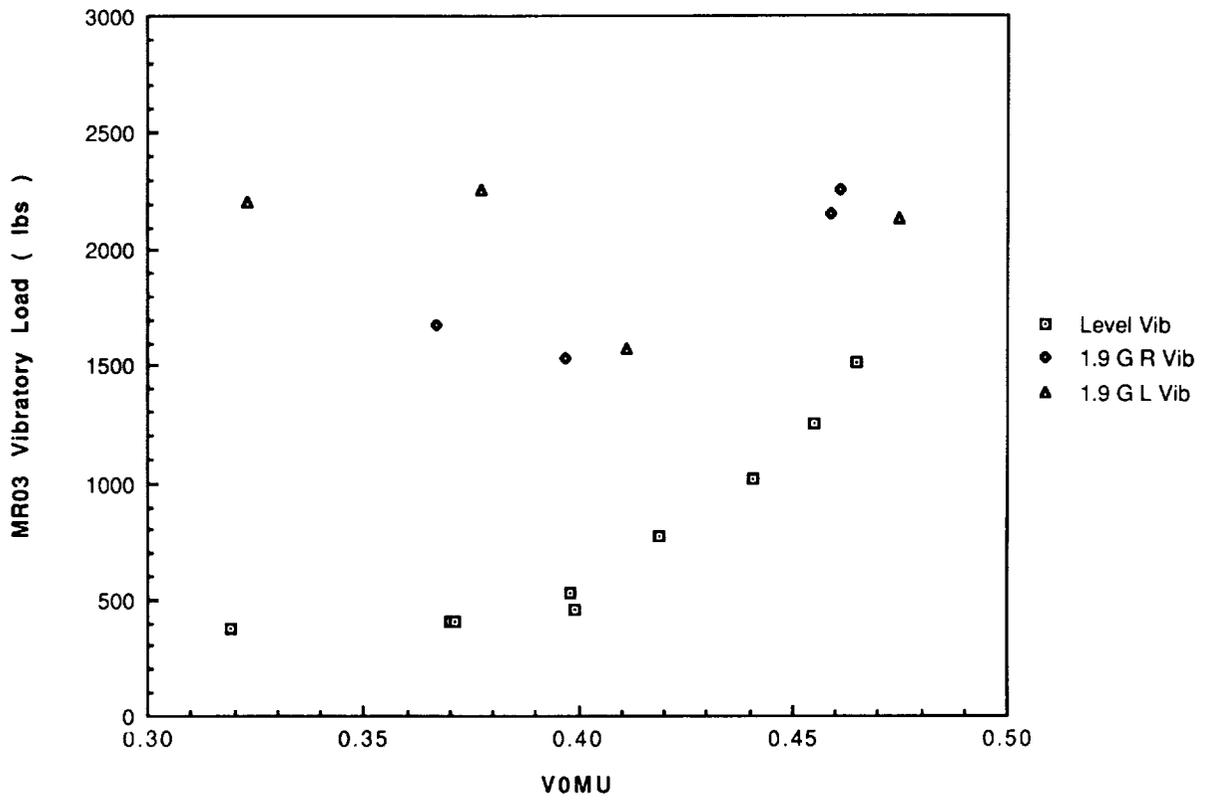
(a) Average.

(b) Vibratory.

Figure 80. Aft link load vs μ, left and right banks, 1.9 g.

Figure 81. Aft link load vs azimuth at four g-loadings.

Figure 82. Lateral link load vs azimuth at four g-loadings.

Figure 83. Forward link load vs azimuth at four g-loadings.

Figure 84. Pitch-link load vs azimuth at four g-loadings.
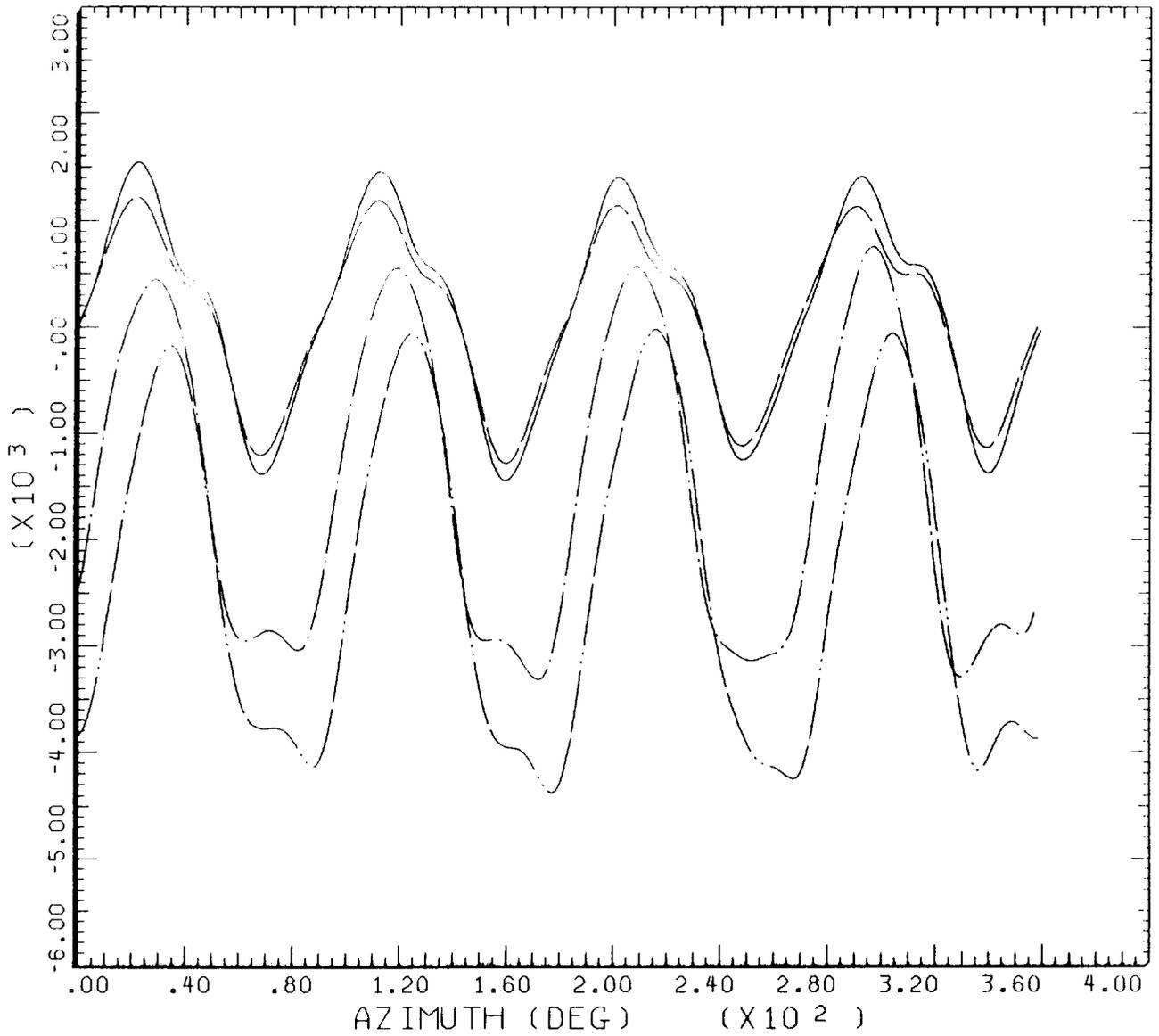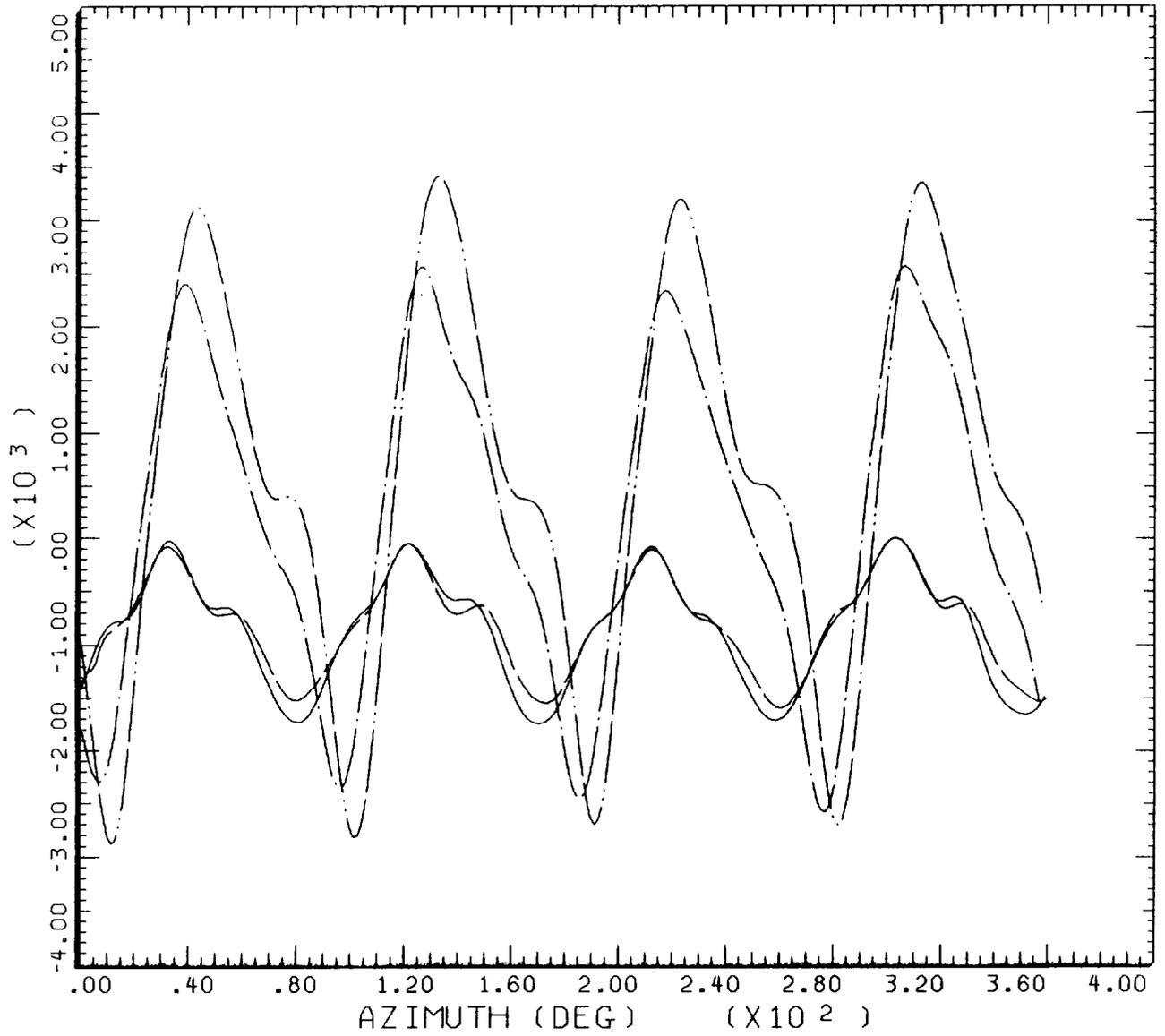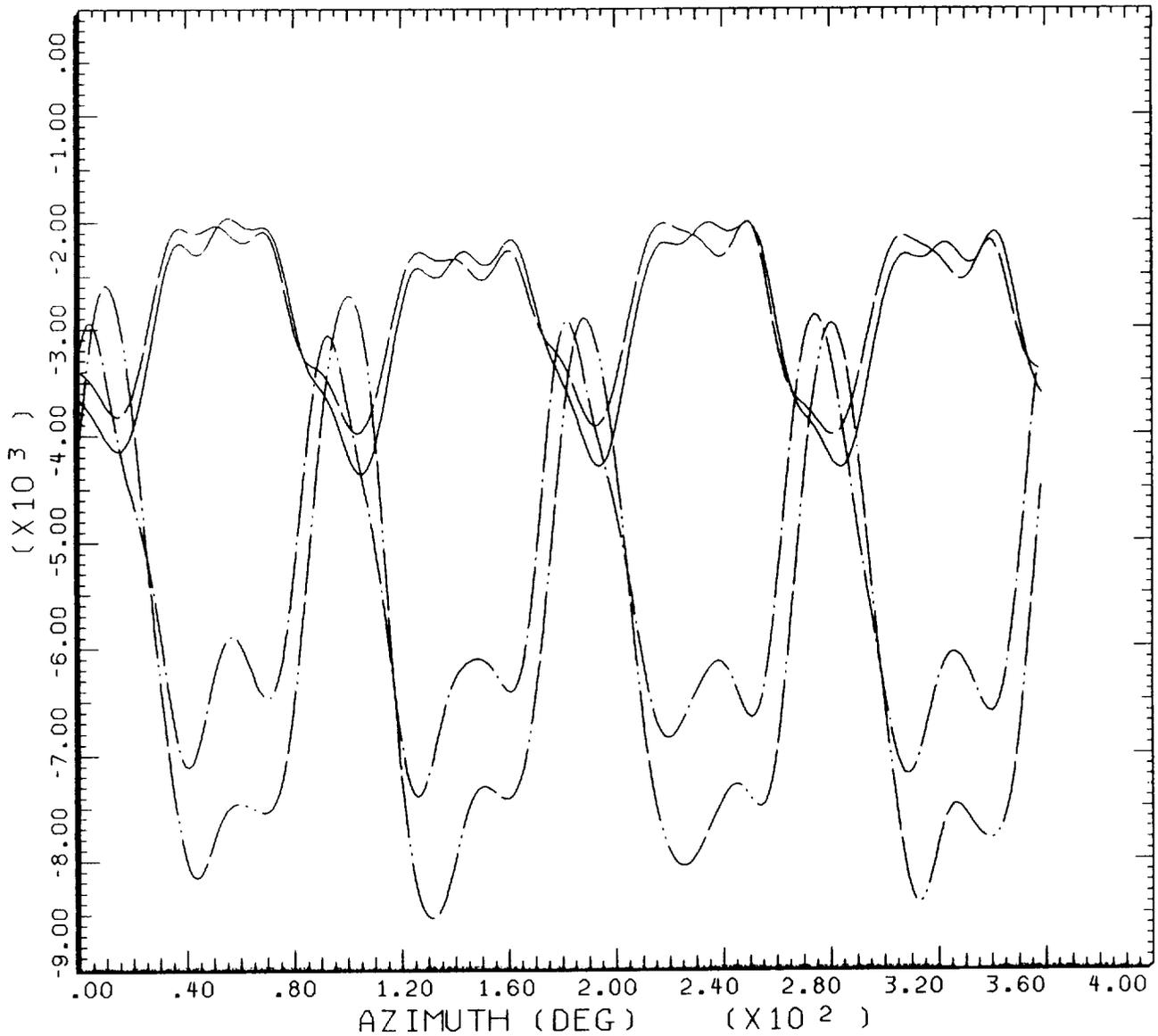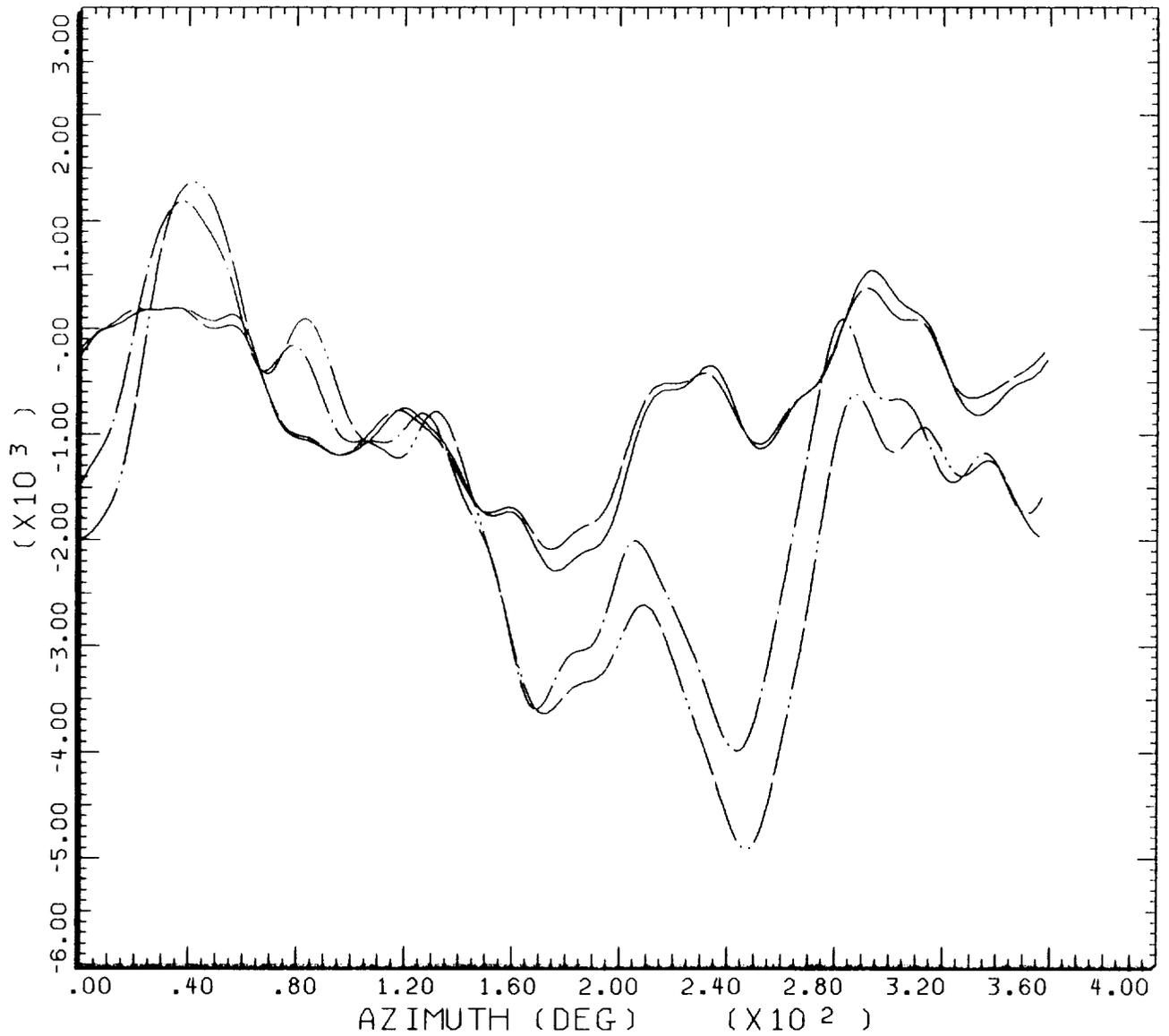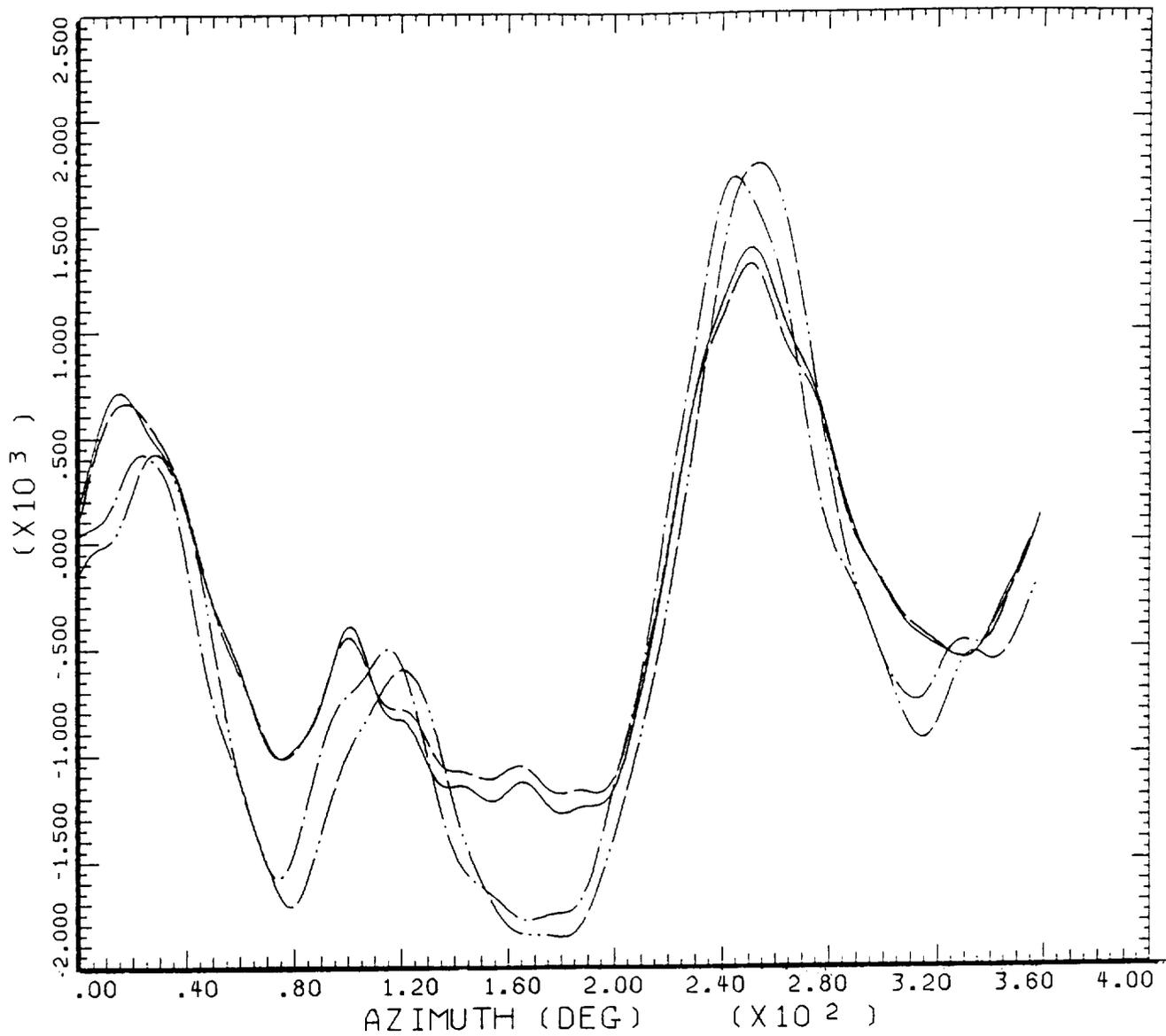
G LOADING SWEEP AT .46 MU

CYCLE AVERAGE: MR NORMAL BENDING 70% RADIUS

COUNTER   MULTIPLE   GROSS WT 16172.   SHIP MODEL   UH-60
                          LONG CG   361.   SHIP ID   748

———————————————   3619/BN70
— —— —— ——   3615/BN70
—·——·——·——   3618/BN70
—··——·——··——   3621/BN70

Figure 85. Normal bending 70% R vs azimuth at four g-loadings.

UH-60A A/C 748 PHASE I TESTS
FLT   20:DYNAMIC STABILITY
CTR   2006: 57KIASB,1 AFT LONG,DOUBLET
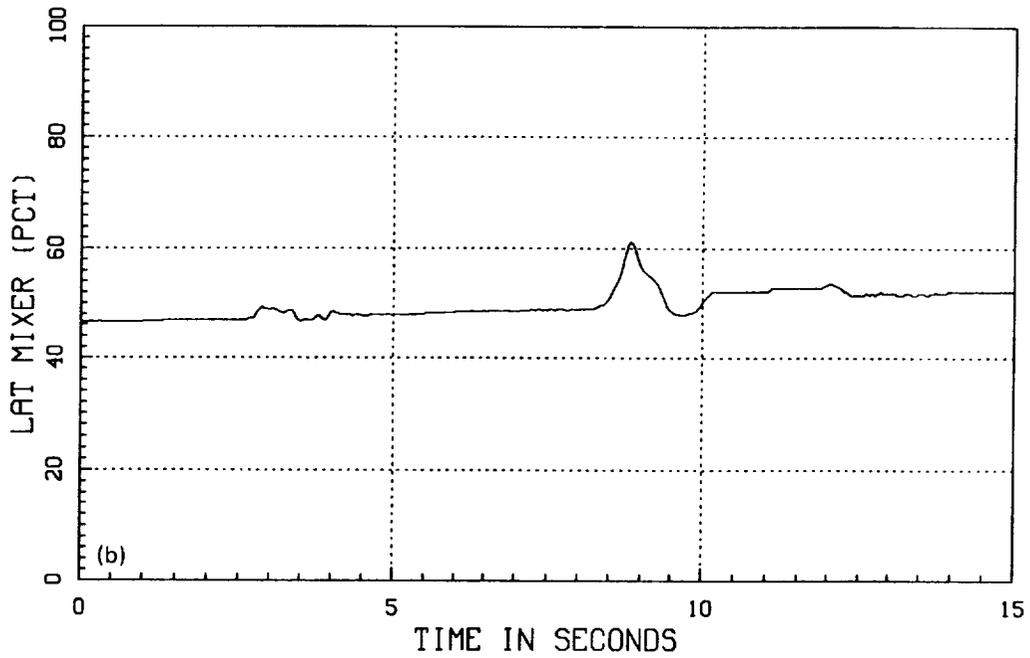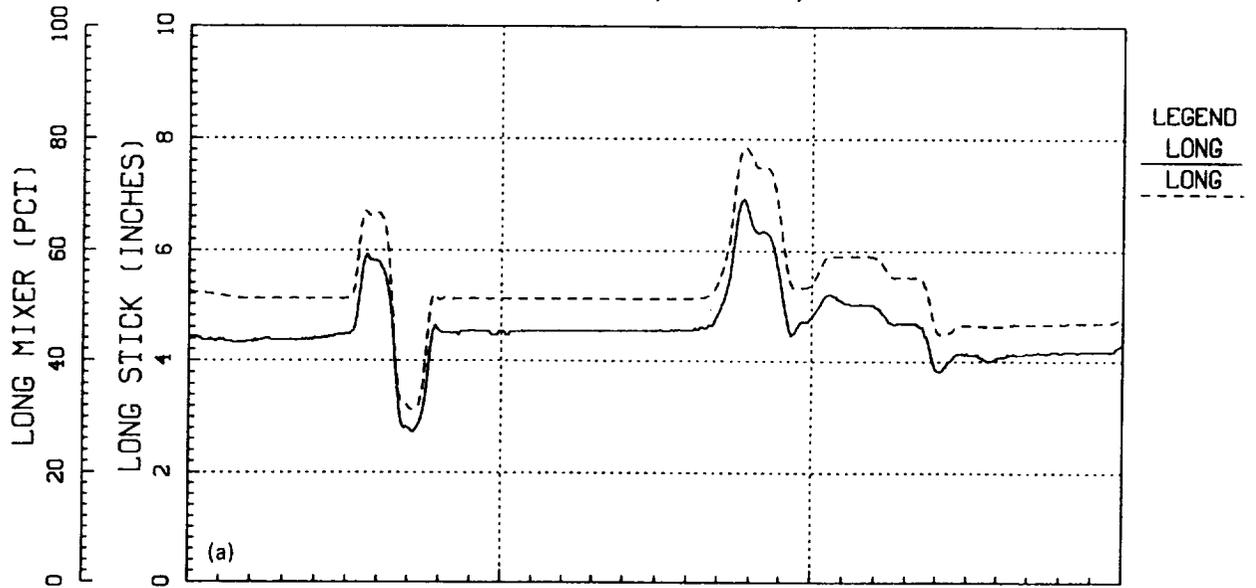
Figure 86. Control positions of longitudinal doublet at 60 knots. (a) Longitudinal cyclic, stick and mixer, (b) lateral cyclic mixer.

224

UH-60A A/C 748 PHASE I TESTS
FLT   20:DYNAMIC STABILITY
CTR   2006: 57KIASB,1 AFT LONG,DOUBLET
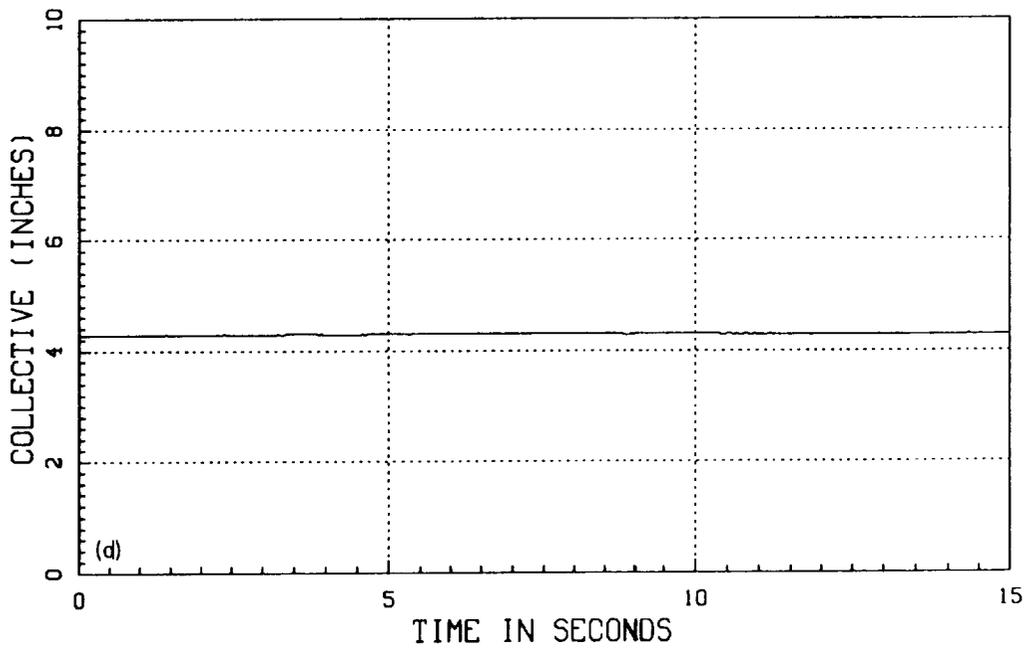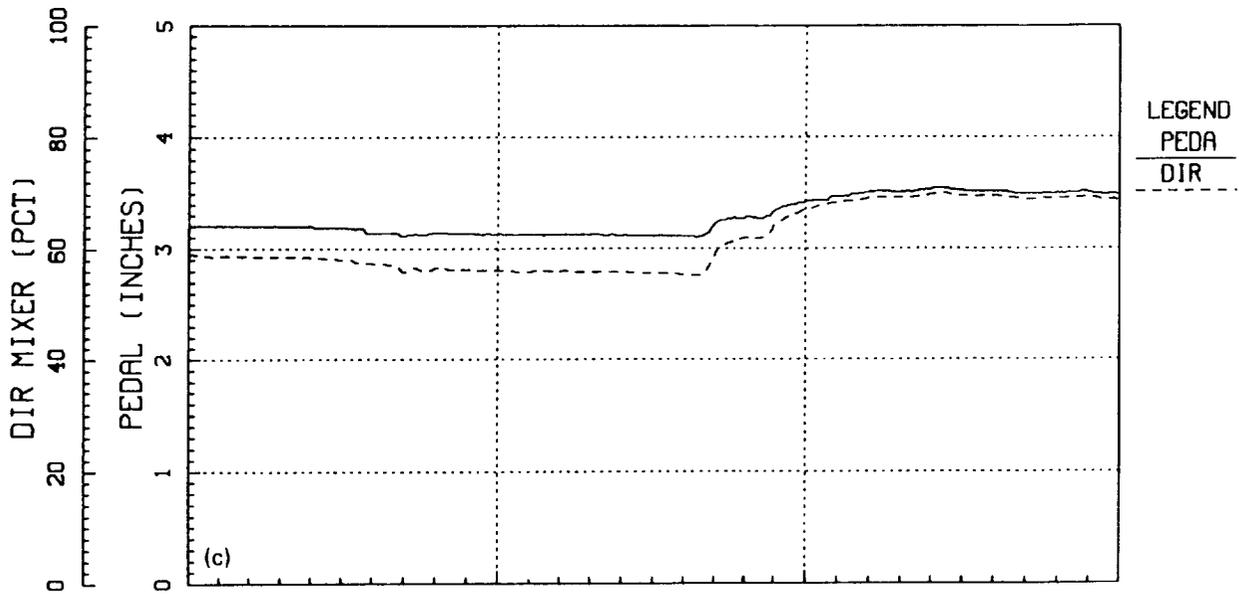
Figure 86. Concluded. (c) Directional control, pedal and mixer, (d) collective position.
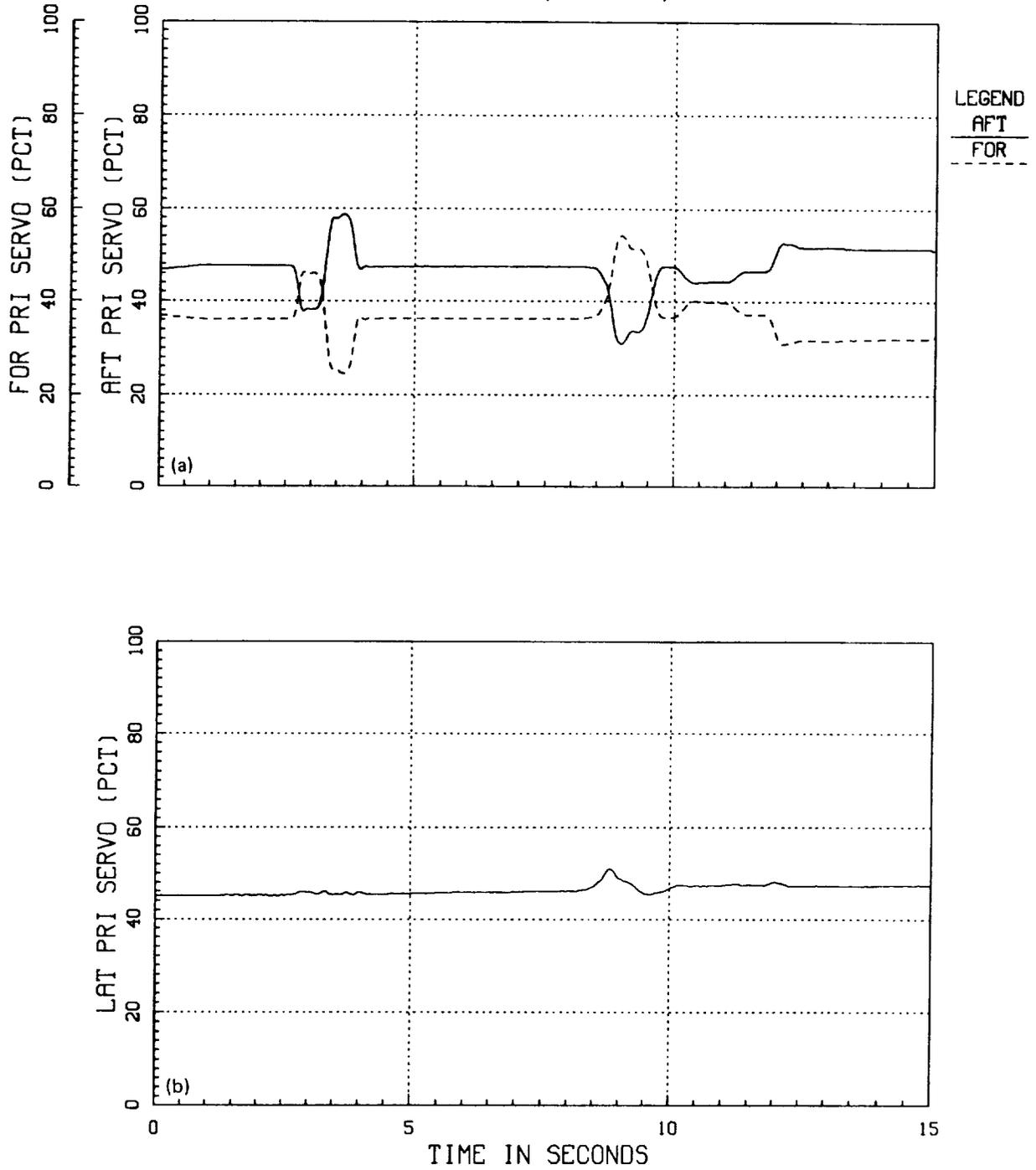
Figure 87. Primary servo positions of longitudinal doublet at 60 knots. (a) Forward and aft primary servo, (b) lateral primary servo.
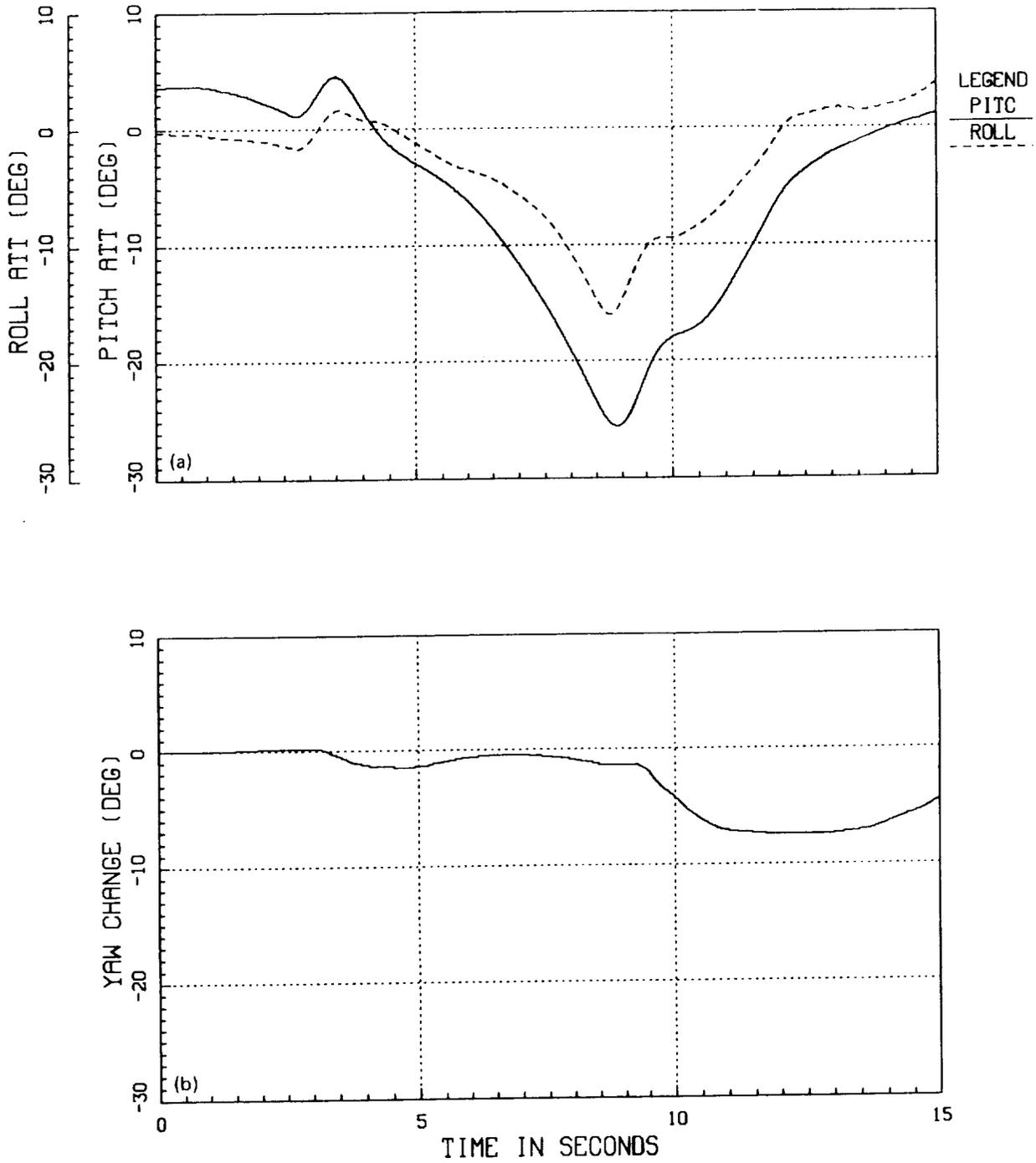
Figure 88. Aircraft attitude of longitudinal doublet at 60 knots. (a) Pitch and roll attitude, (b) yaw change.

UH-60A A/C 748 PHASE I TESTS
FLT 20:DYNAMIC STABILITY
CTR 2006: 57KIASB,1'AFT LONG,DOUBLET
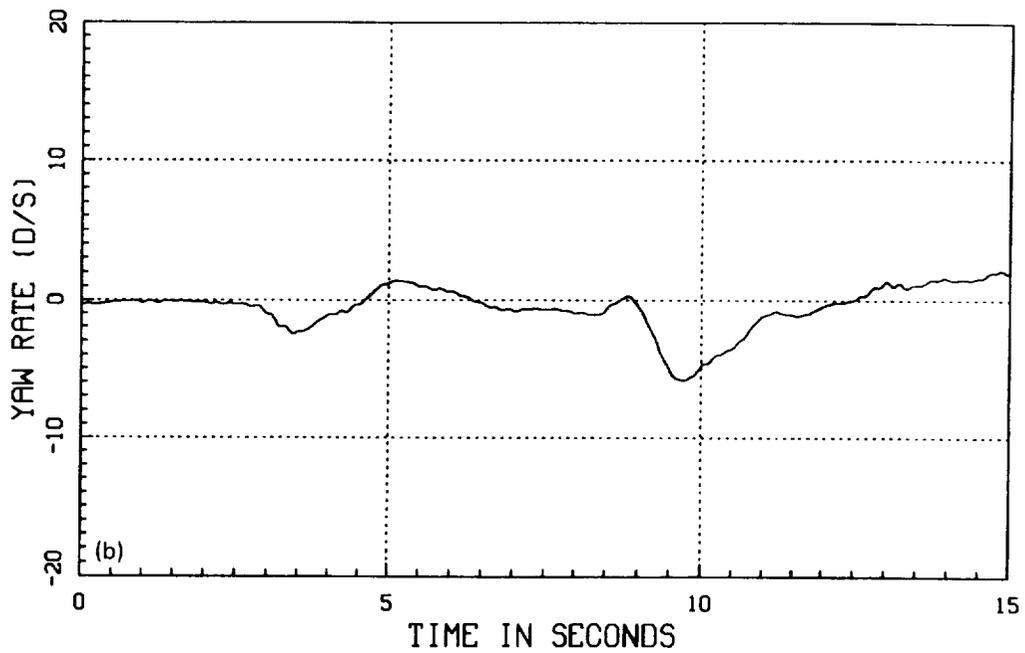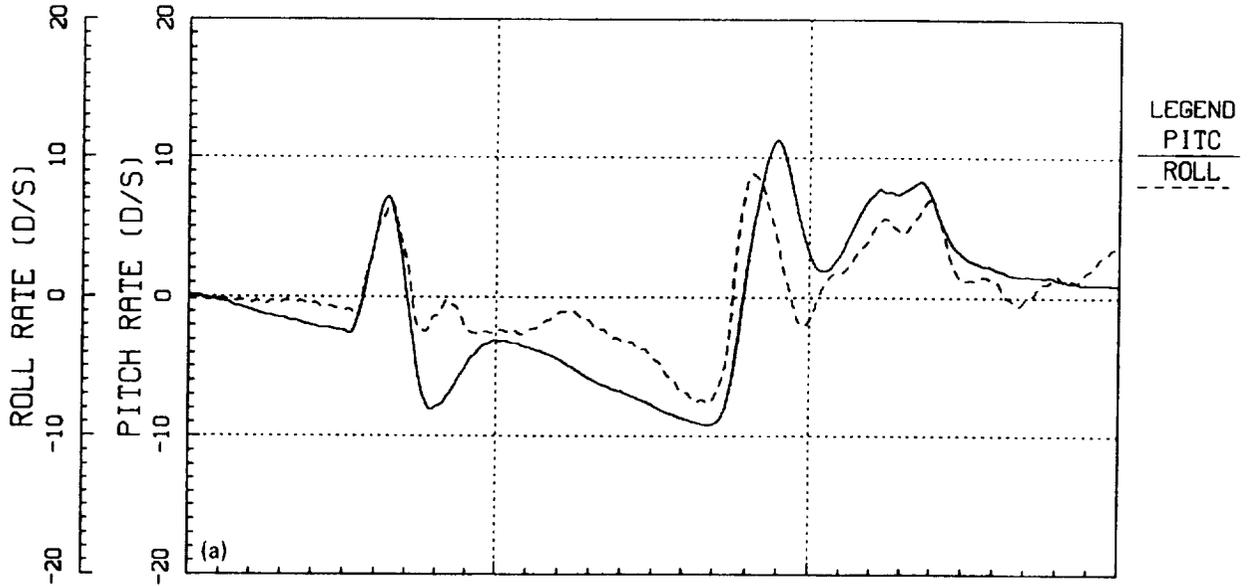
Figure 89. Aircraft angular rates of longitudinal doublet at 60 knots. (a) Pitch and roll rate, (b) yaw rate.

228
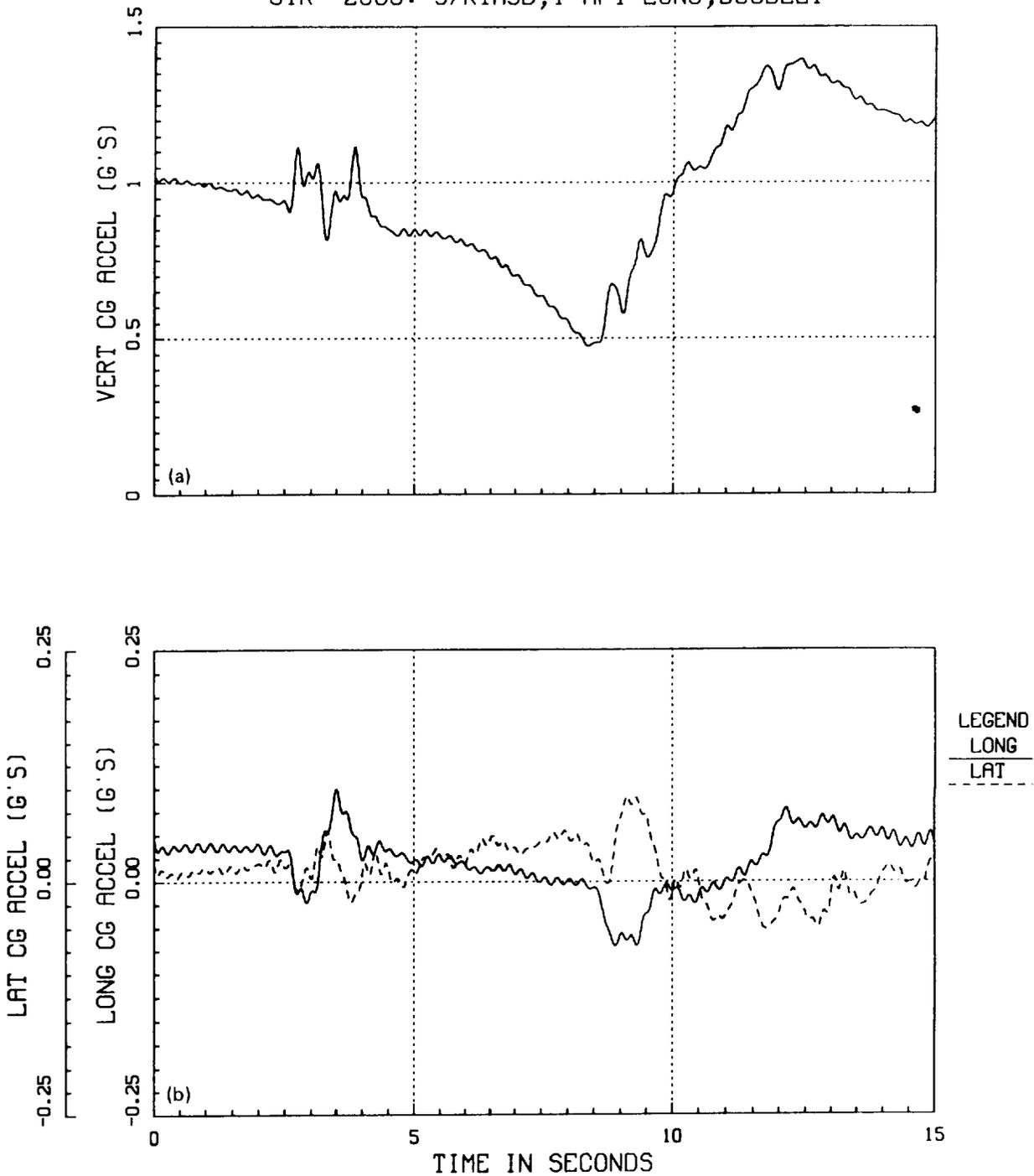
Figure 90. Acceleration at aircraft c.g. of longitudinal doublet at 60 knots. (a) Vertical c.g. acceleration, (b) lateral and longitudinal c.g. acceleration.
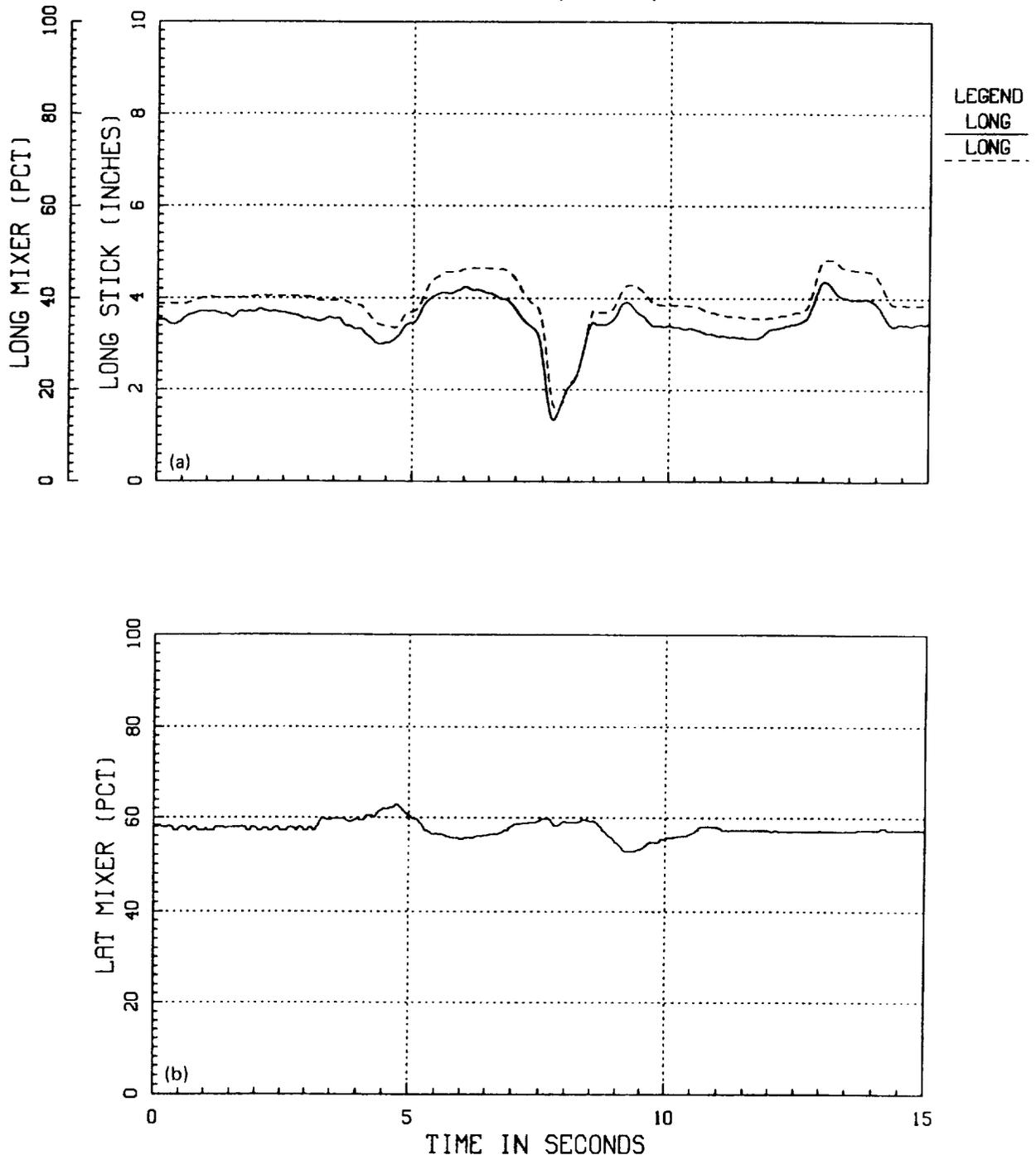
Figure 91. Control positions of directional doublet at 140 knots. (a) Longitudinal cyclic, stick and mixer, (b) lateral cyclic mixer.

230

UH-60A A/C 748 PHASE I TESTS
FLT   20:DYNAMIC STABILITY
CTR   2017: 127KIASB,1 LT PED,DOUBLET

LEGEND
PEDA
DIR

(c)

(d)

TIME IN SECONDS
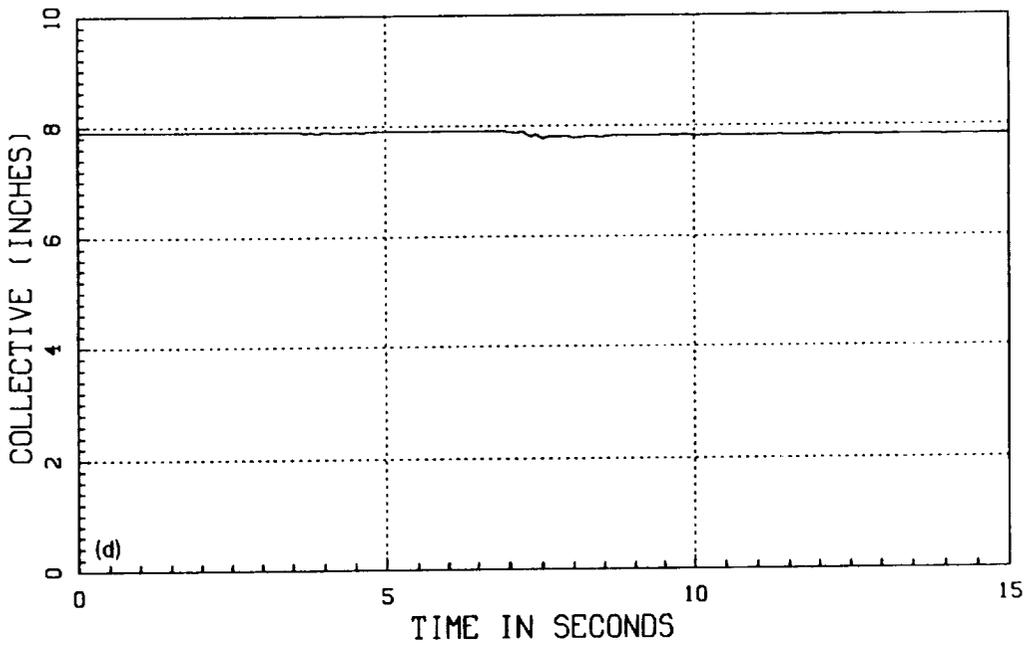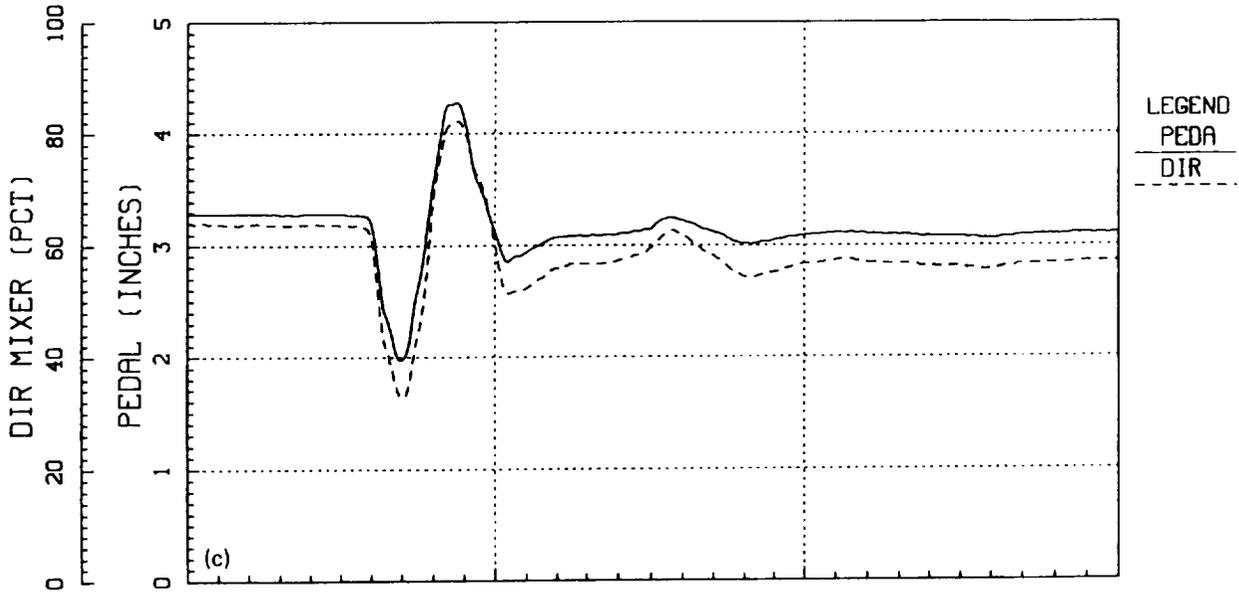
Figure 91. Concluded. (c) Directional control, pedal and mixer, (d) collective position.

231

UH-60A A/C 748 PHASE I TESTS
FLT   20:DYNAMIC STABILITY
CTR   2017: 127KIASB,1 LT PED,DOUBLET
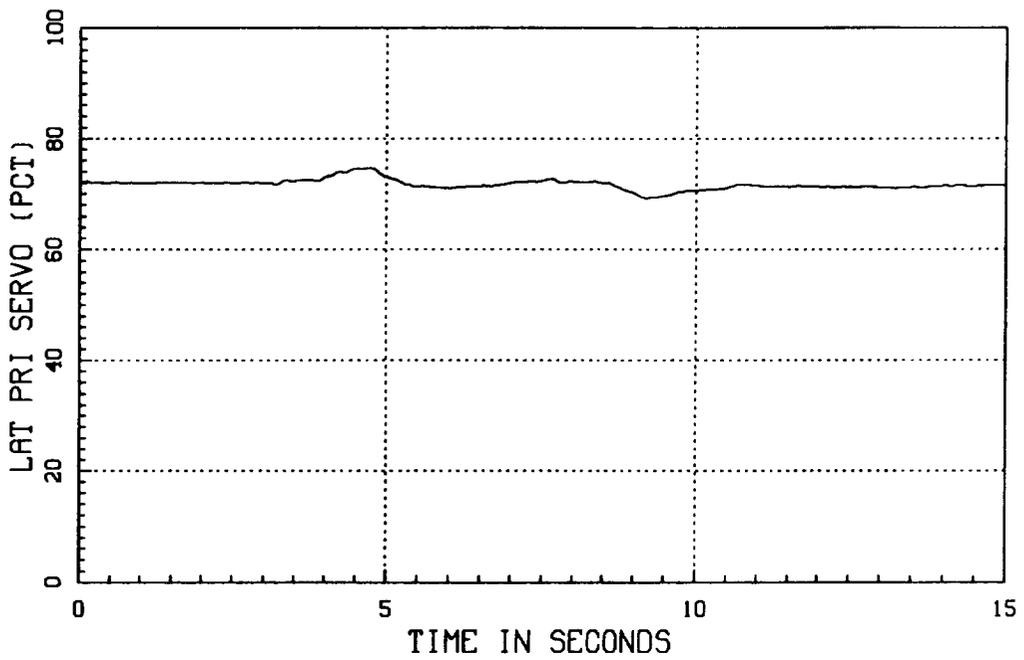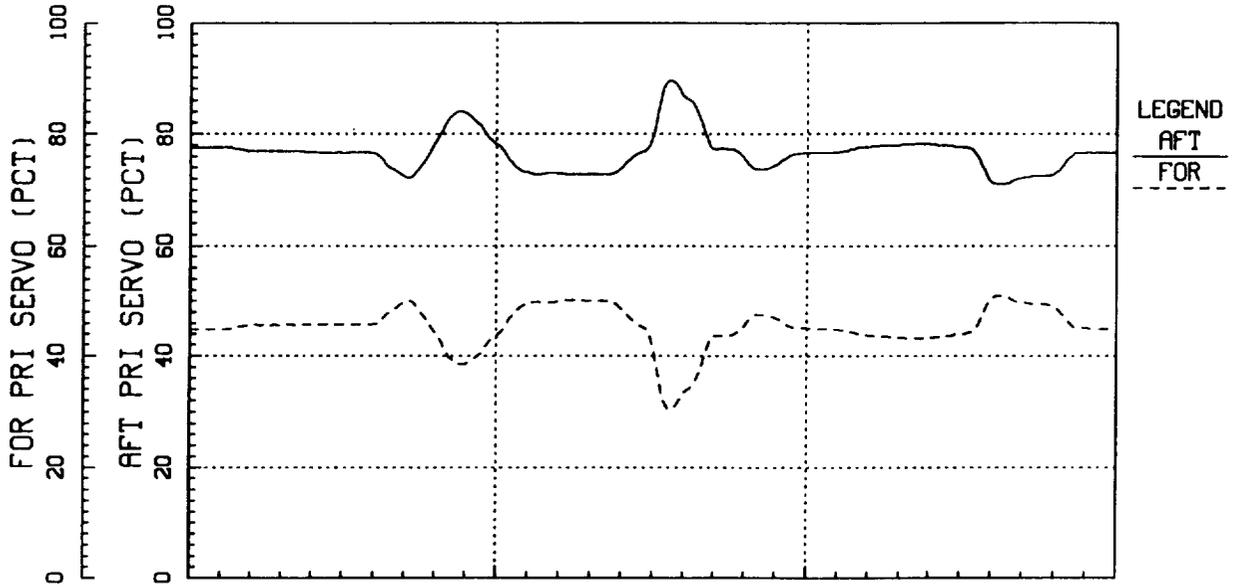
Figure 92. Primary servo positions of pedal doublet at 140 knots.

UH-60A A/C 748 PHASE I TESTS
FLT   20:DYNAMIC STABILITY
CTR   2017: 127KIASB,1 LT PED,DOUBLET

LEGEND
PITC
ROLL
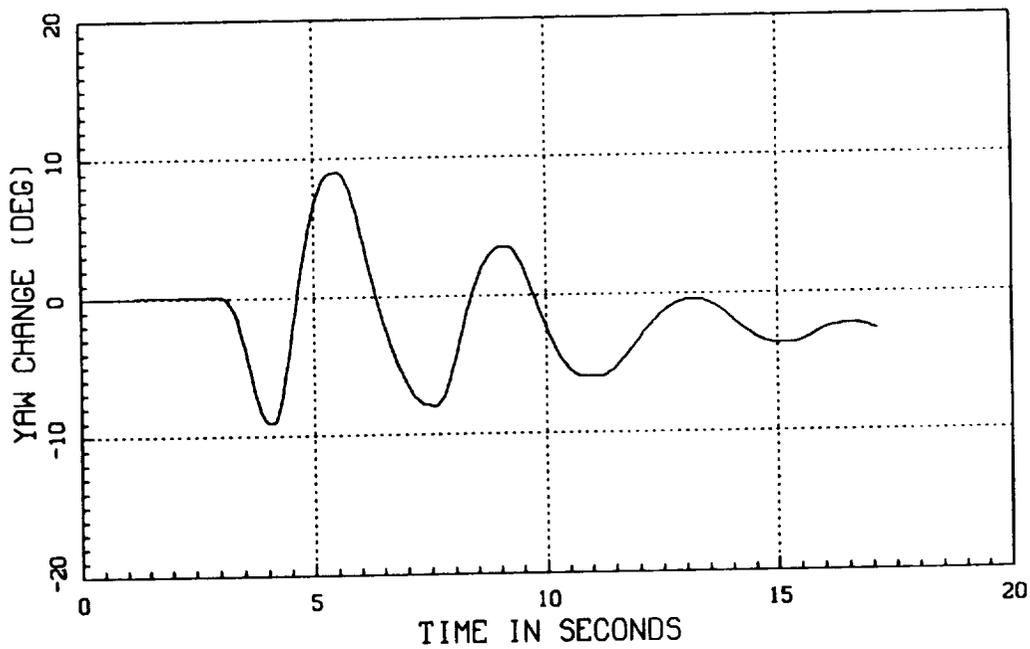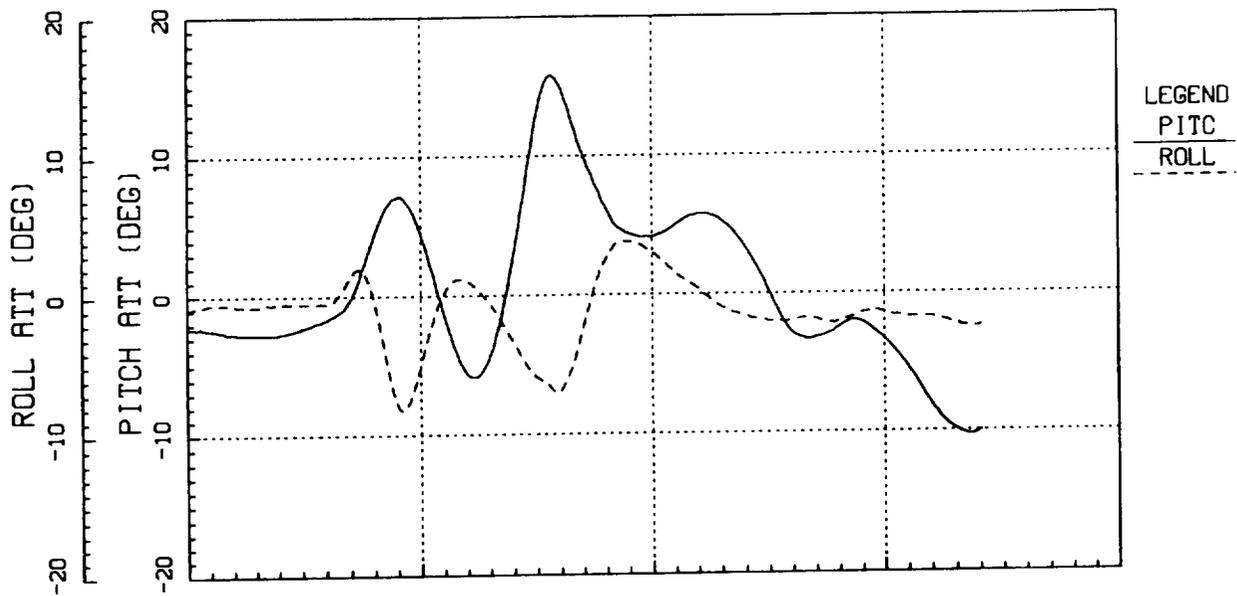
Figure 93.   Aircraft attitude of pedal doublet at 140 knots.

UH-60A A/C 748 PHASE I TESTS
FLT   20:DYNAMIC STABILITY
CTR   2017: 127KIASB,1'LT PED,DOUBLET

LEGEND
PITC
ROLL

TIME IN SECONDS
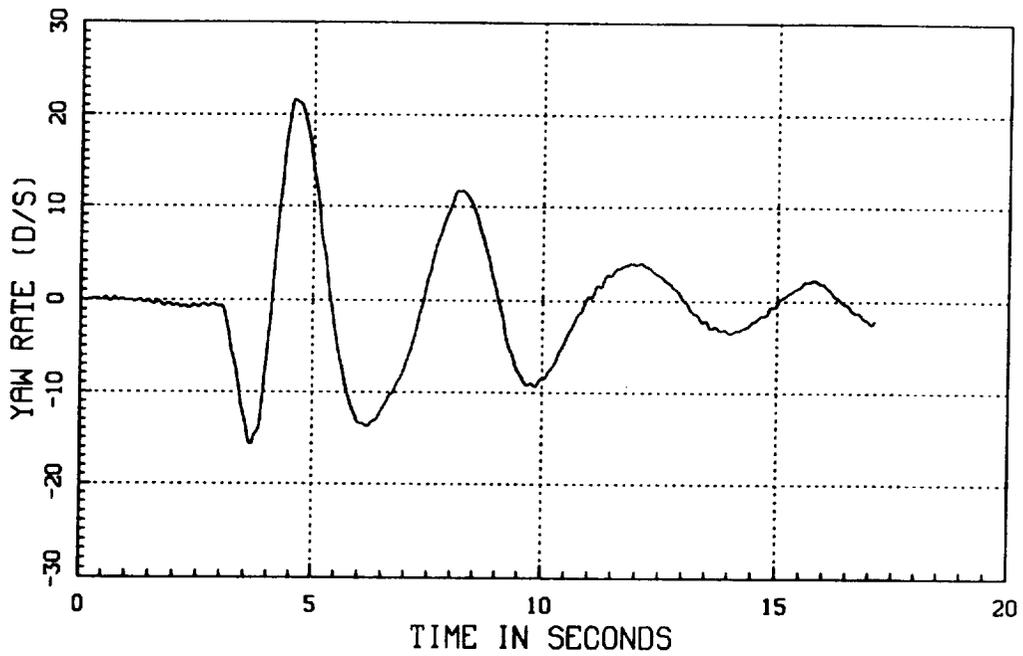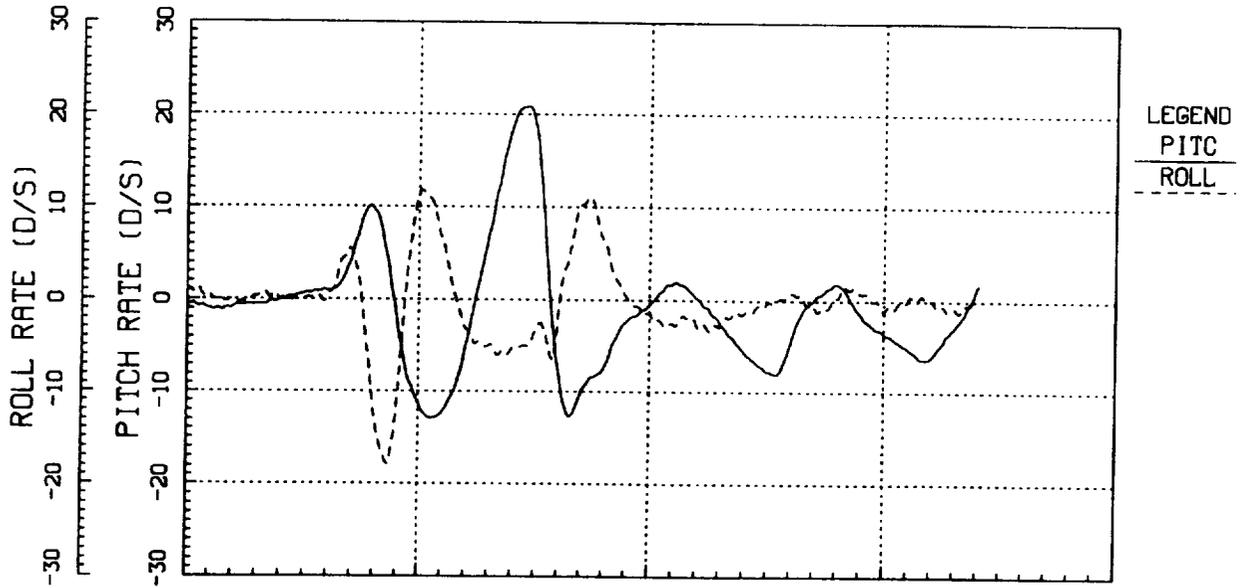
Figure 94. Aircraft angular rates of pedal doublet at 140 knots.

234

UH-60A A/C 748 PHASE I TESTS
FLT   20:DYNAMIC STABILITY
CTR   2017: 127KIASB,1'LT PED,DOUBLET
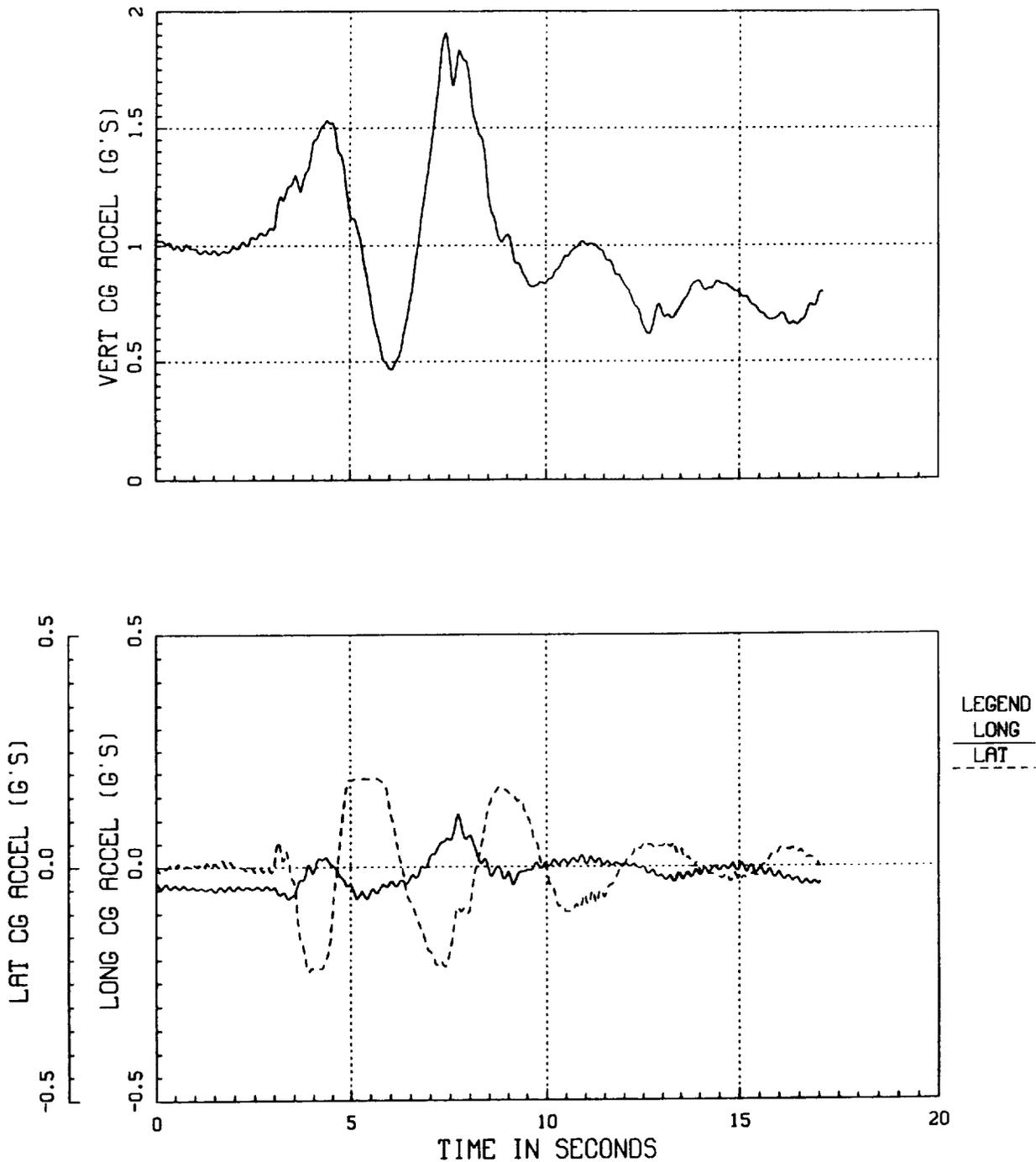
Figure 95. Acceleration at aircraft c.g. of pedal doublet at 140 knots.
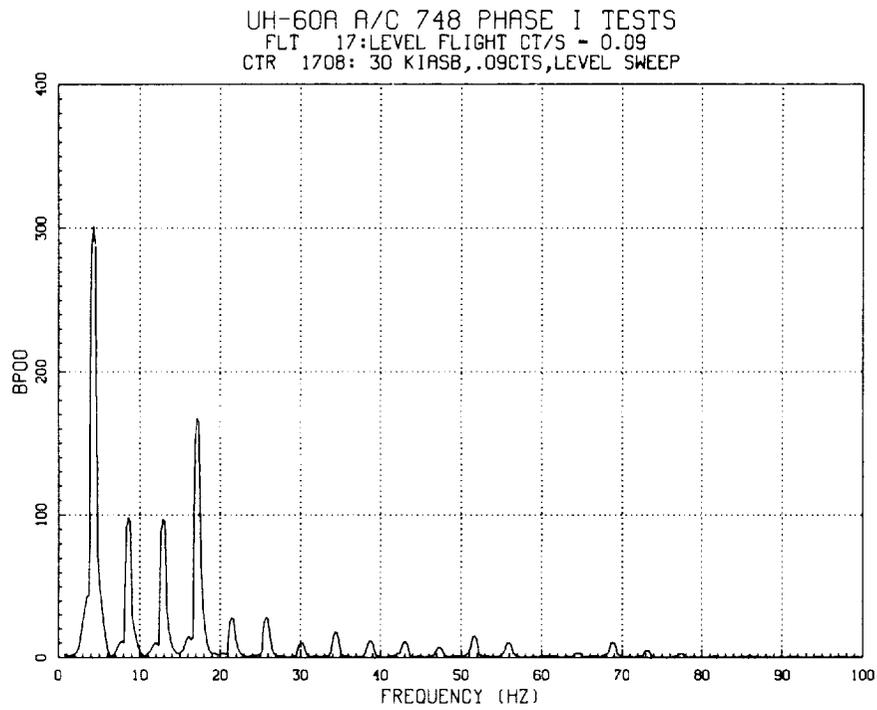
Figure 96. Pitch-link load vs frequency at 30 KIASB; $C_T/\sigma = 0.09$.
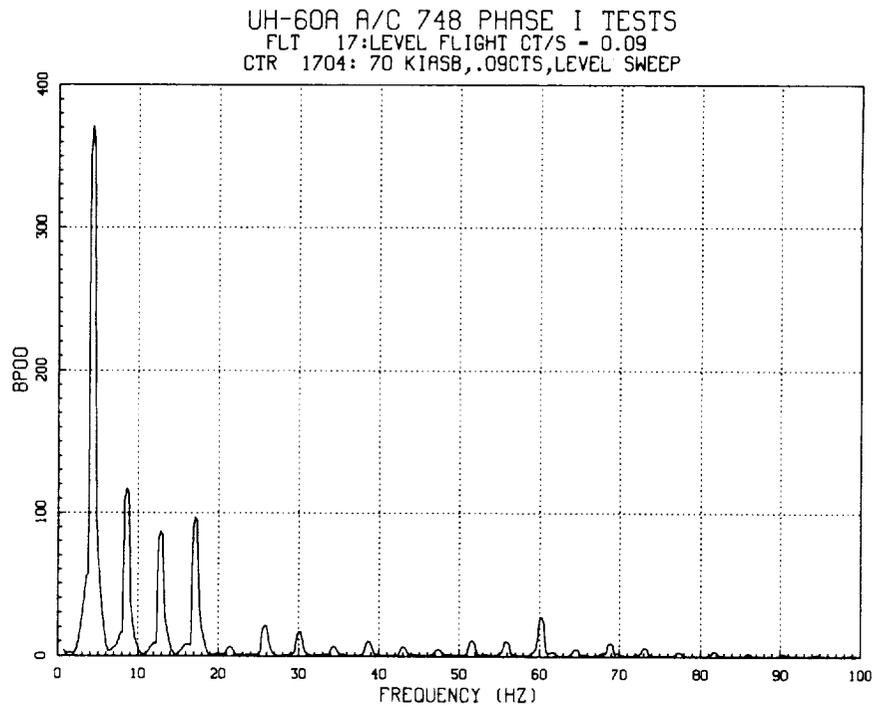
Figure 97. Pitch-link load vs frequency at 70 KIASB; $C_T/\sigma = 0.09$.

UH-60A A/C 748 PHASE I TESTS
FLT   17:LEVEL FLIGHT CT/S - 0.09
CTR   1717: 110 KIASB,.09CTS LEVEL SWEEP
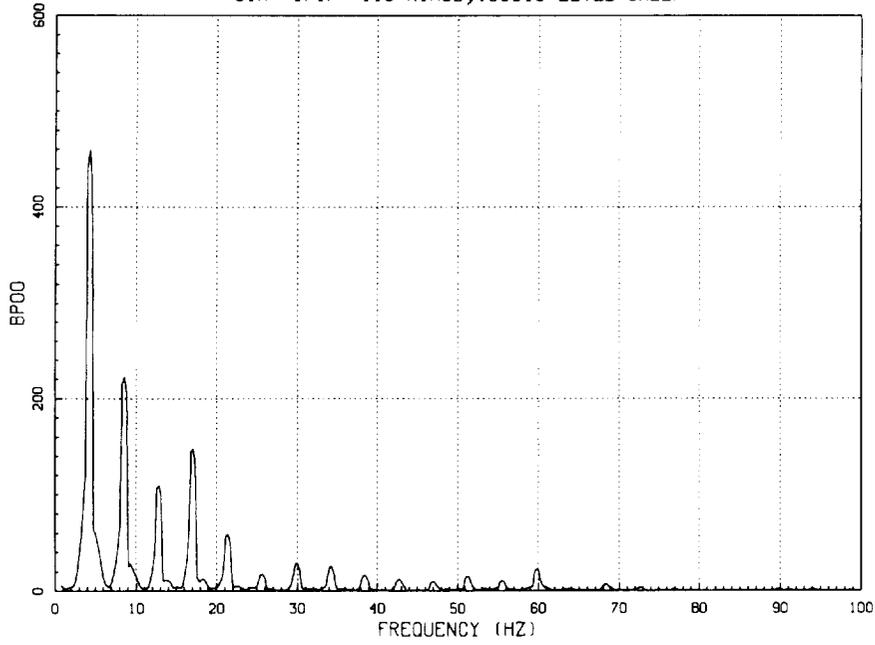
Figure 98. Pitch-link load vs frequency at 110 KIASB; $C_T/\sigma = 0.09$.

UH-60A A/C 748 PHASE I TESTS
FLT   30:POWERED DESCENTS   0.09
CTR   3016: 142KIASB.09CTS,400R/S,SWEEP
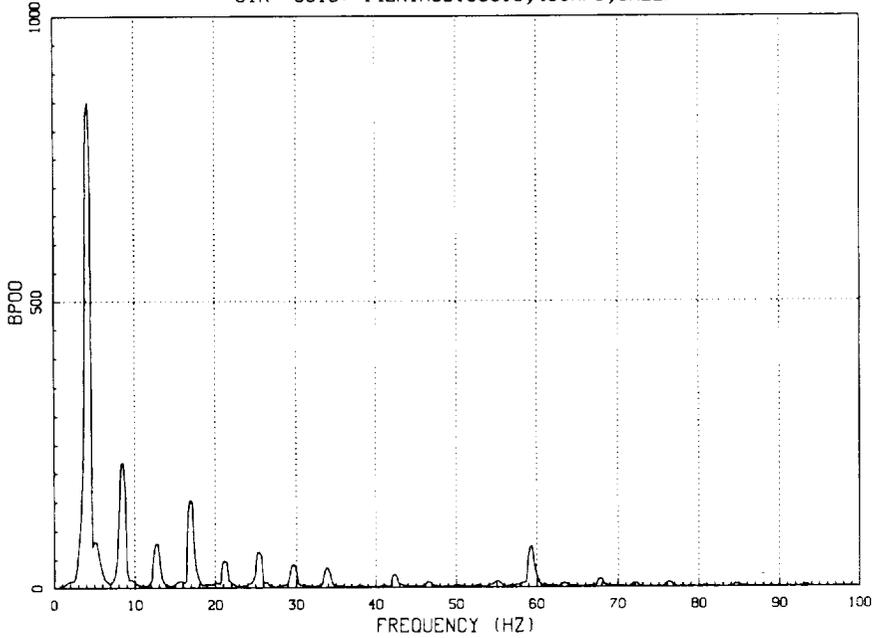
Figure 99. Pitch-link load vs frequency at 142 KIASB; $C_T/\sigma = 0.09$.

237

UH-60A A/C 748 PHASE I TESTS
FLT   30:POWERED DESCENTS   0.09
CTR 3011: 169KIASB.09CTS,3200R/S,SWEEP
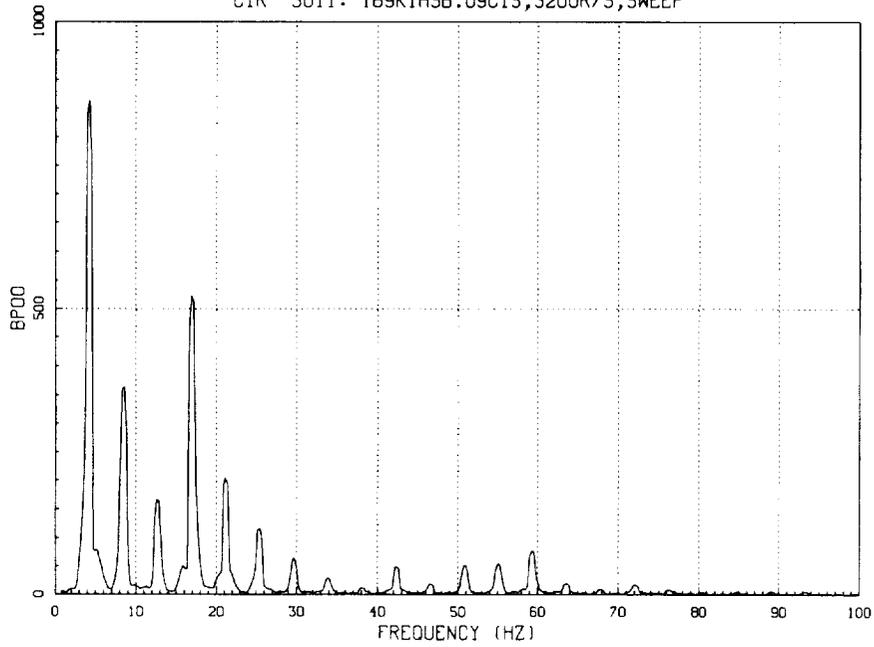
Figure 100. Pitch-link load vs frequency at 169 KIASB; $C_T/\sigma = 0.09$.

Peak to Peak Phase Shift

Quad 1-2
Quad 2-3
Quad 3-4
Quad 4-1
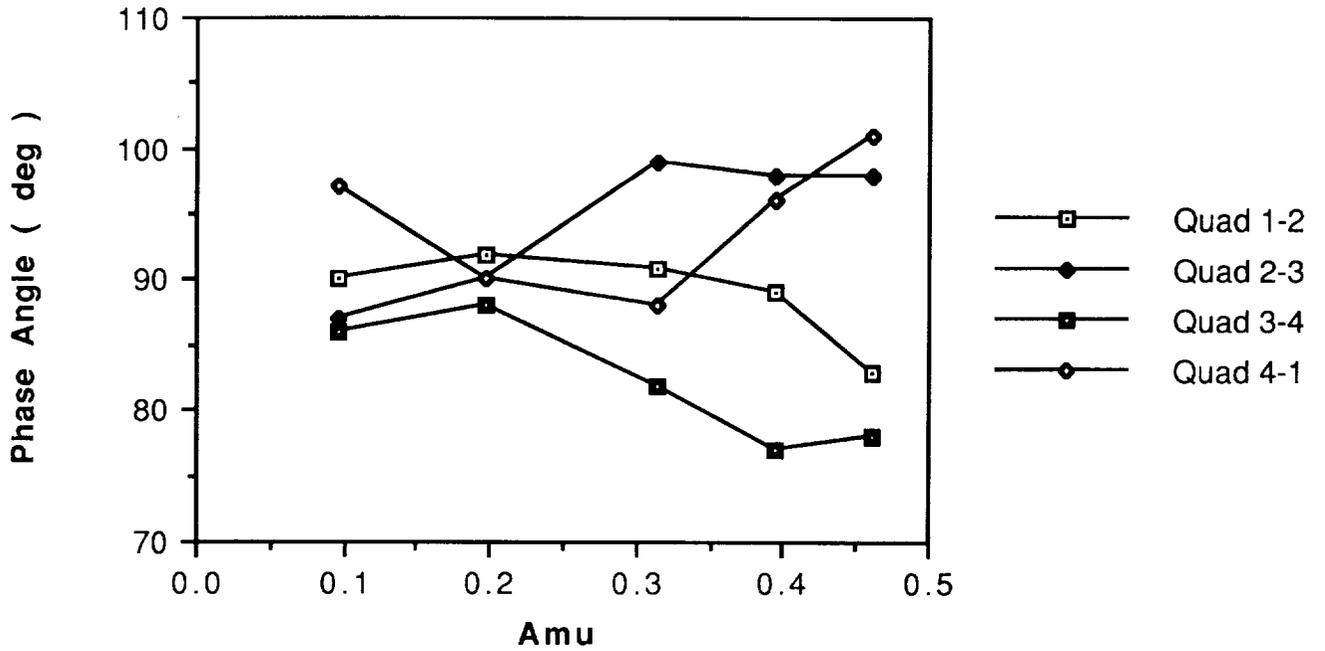
Figure 101. Pitch-link load phase angle vs advance ratio.
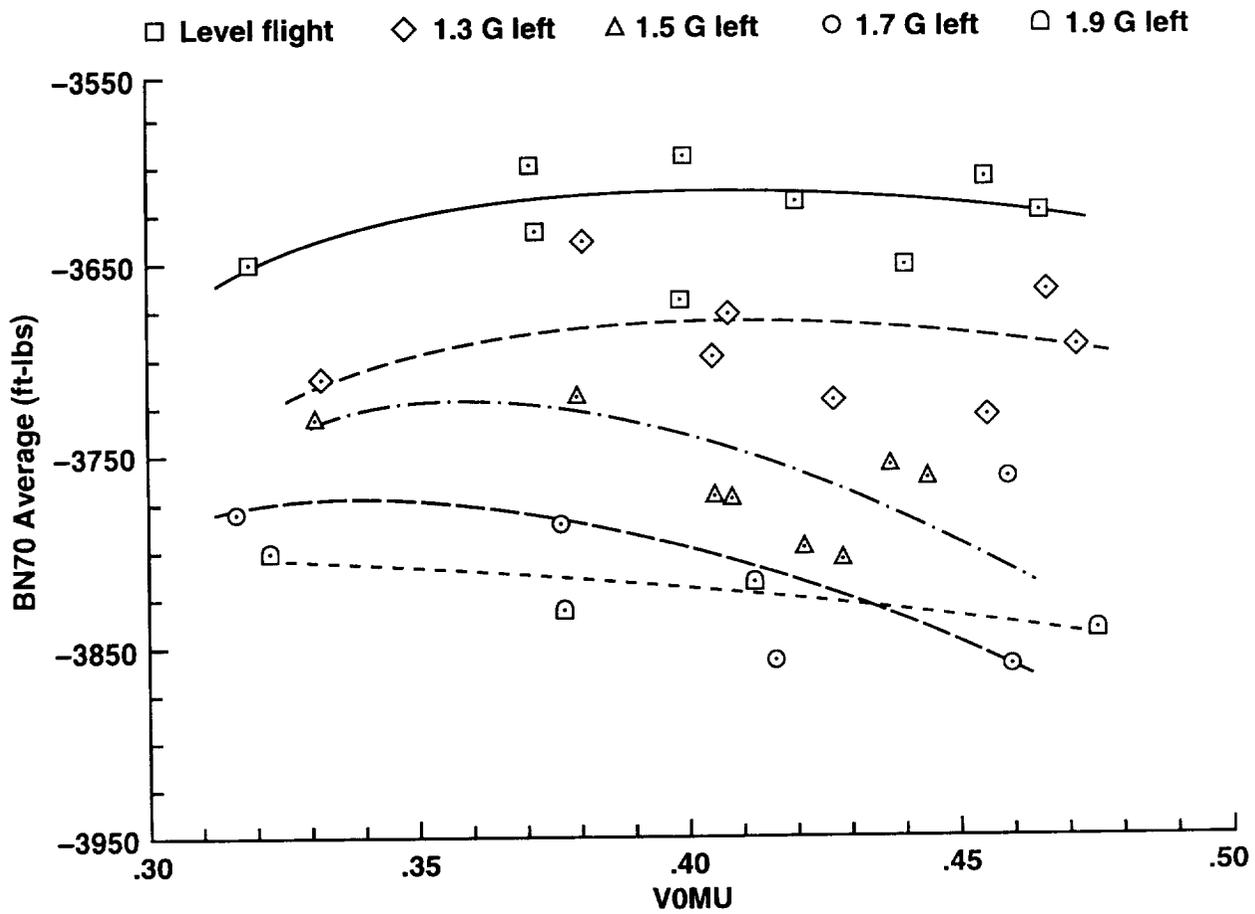
(a) Average.

Figure 102. Normal bending 70% R vs advance ratio over g-loading sweep.
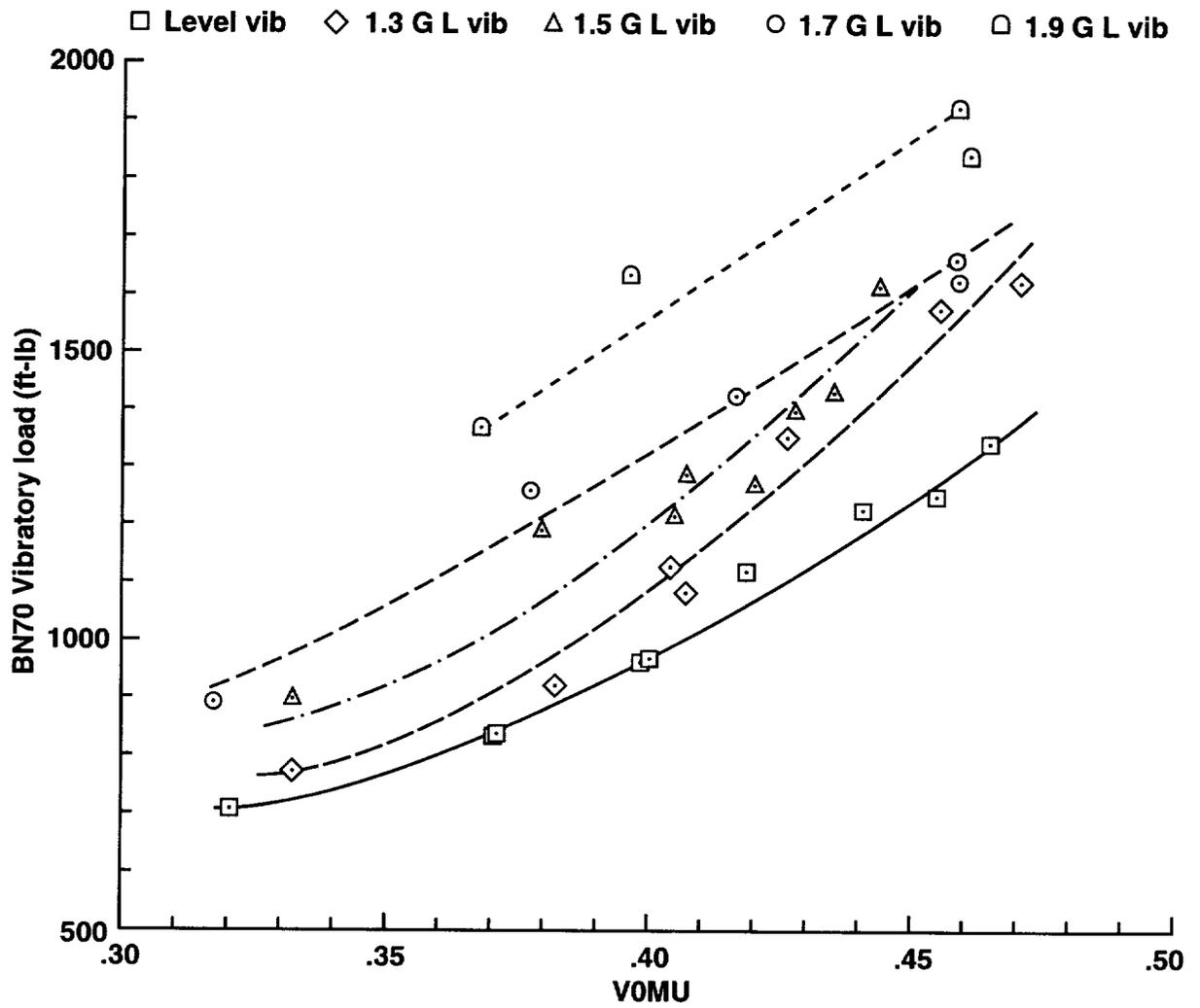
(b) Vibratory.

Figure 102. Concluded.
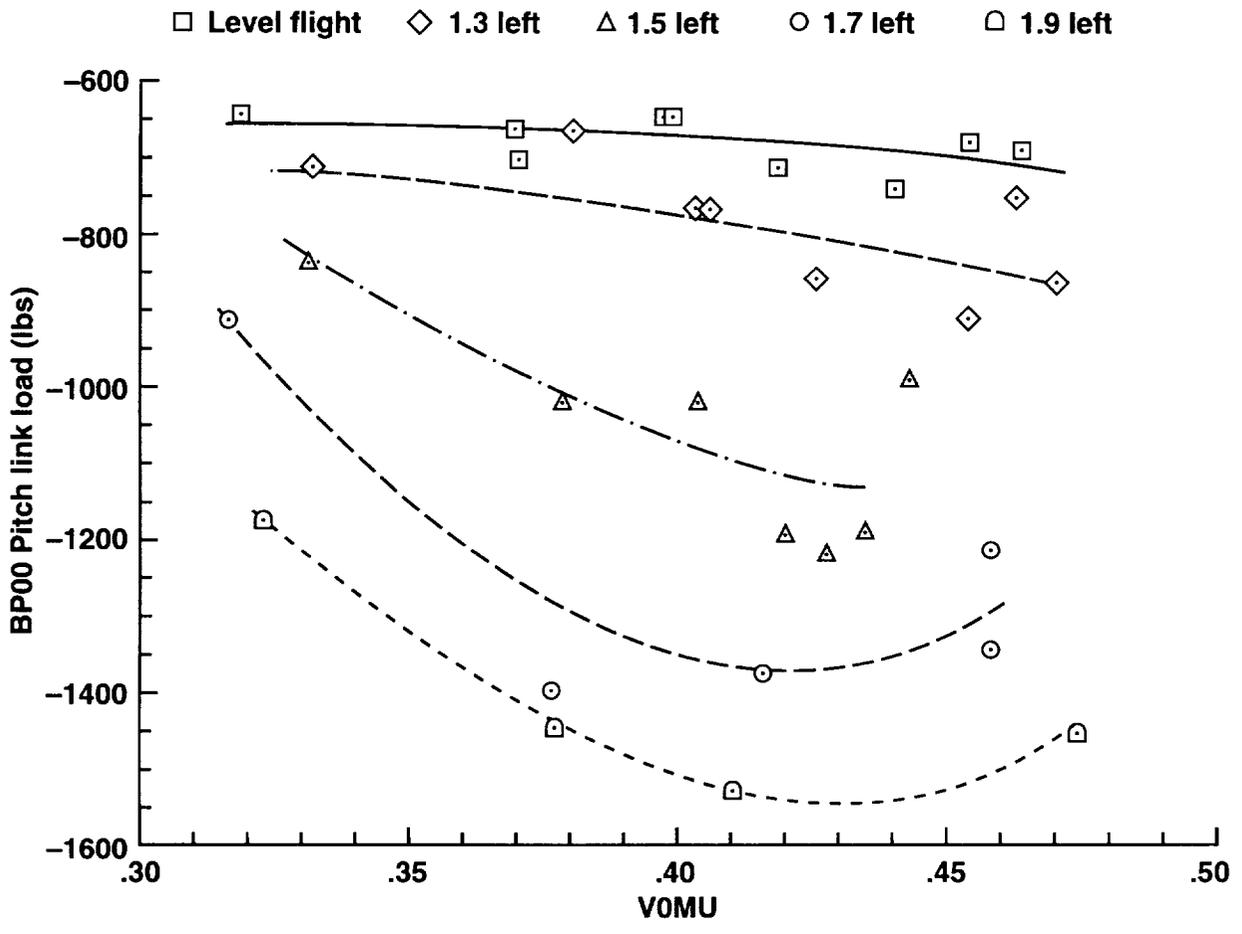
(a) Average.

Figure 103. Pitch-link vs advance ratio over g-loading sweep.
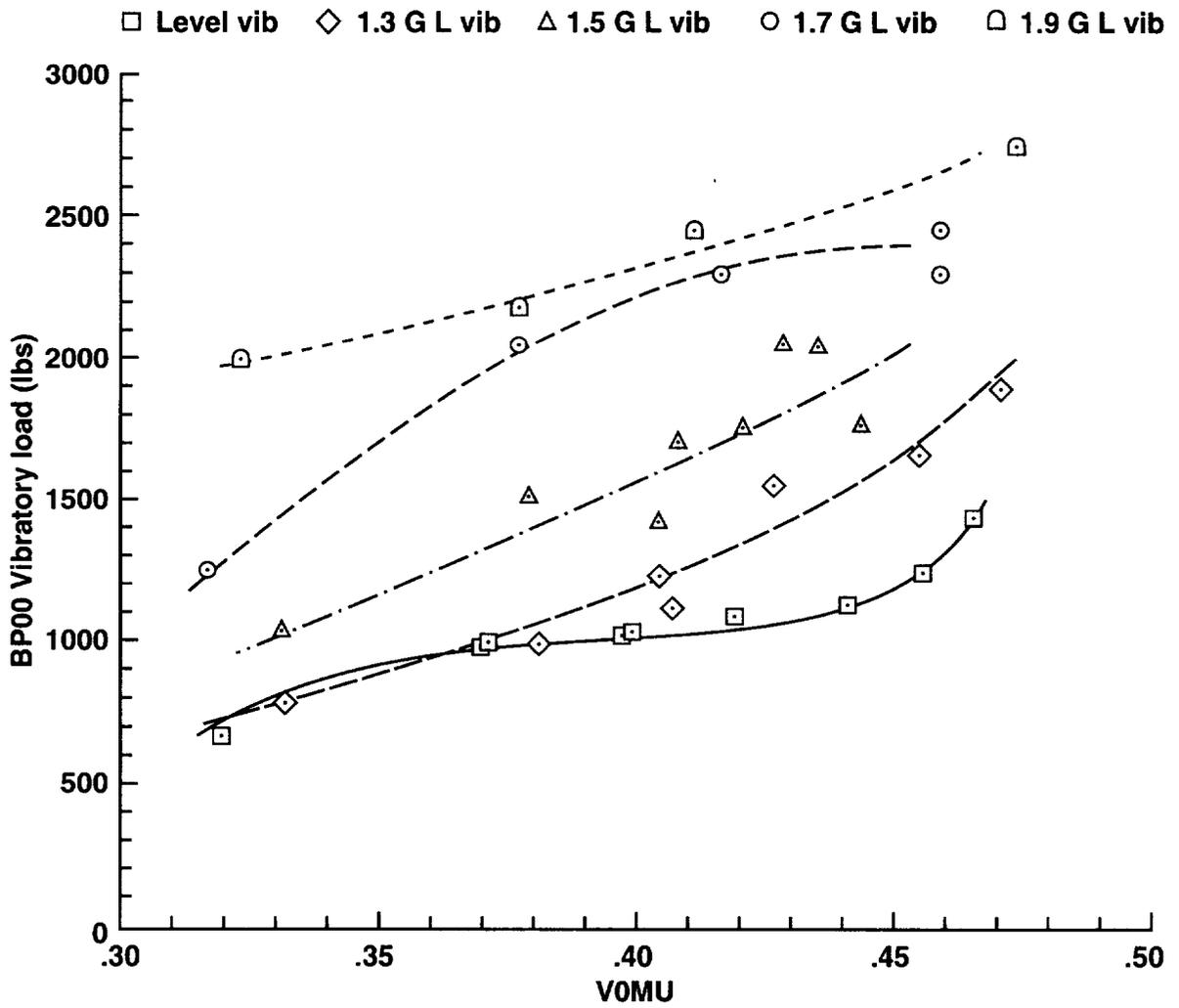
(b) Vibratory.

Figure 103. Concluded.

242
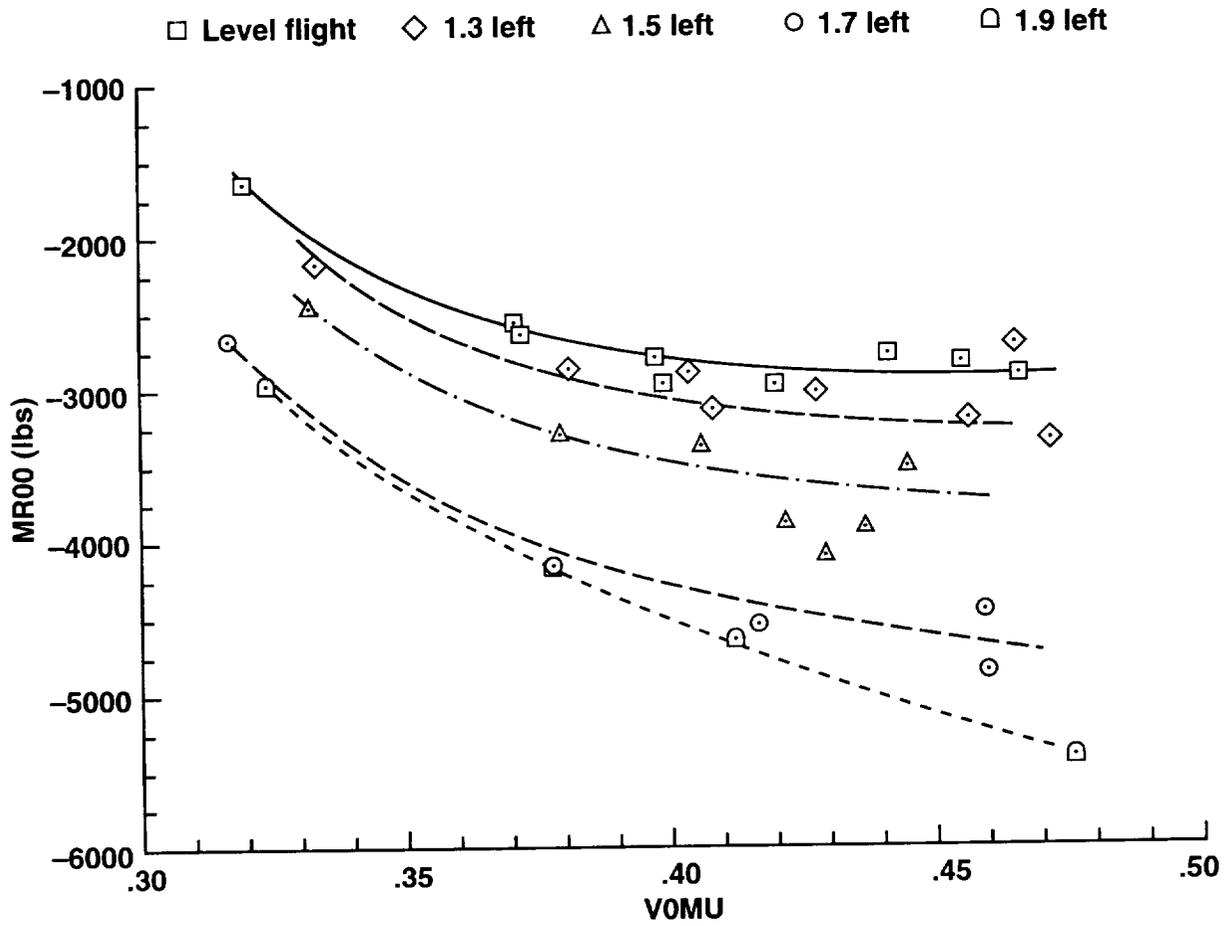
(a) Average.

Figure 104. Forward link load vs advance ratio over g-loading sweep.
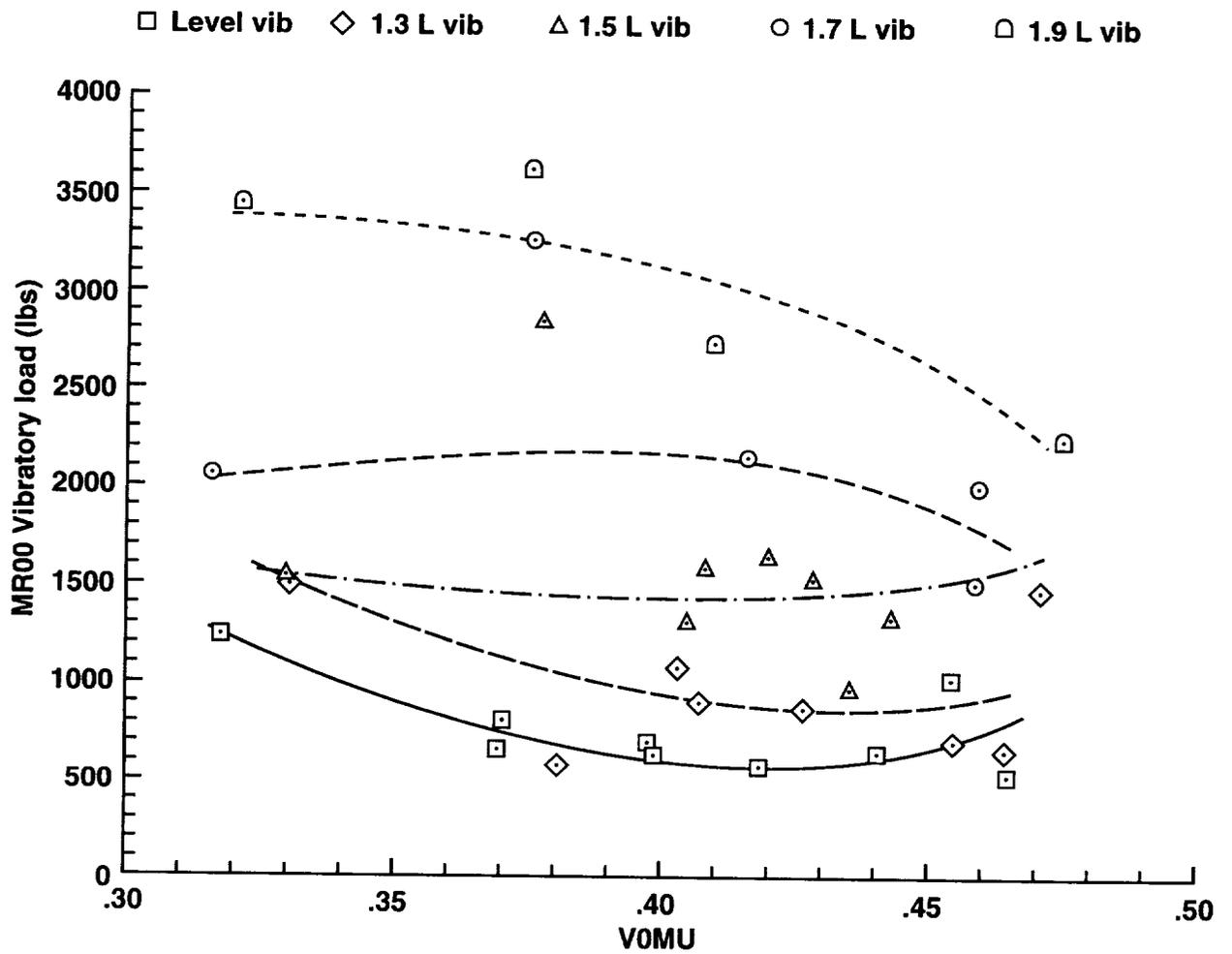
(b) Vibratory.

Figure 104. Concluded.
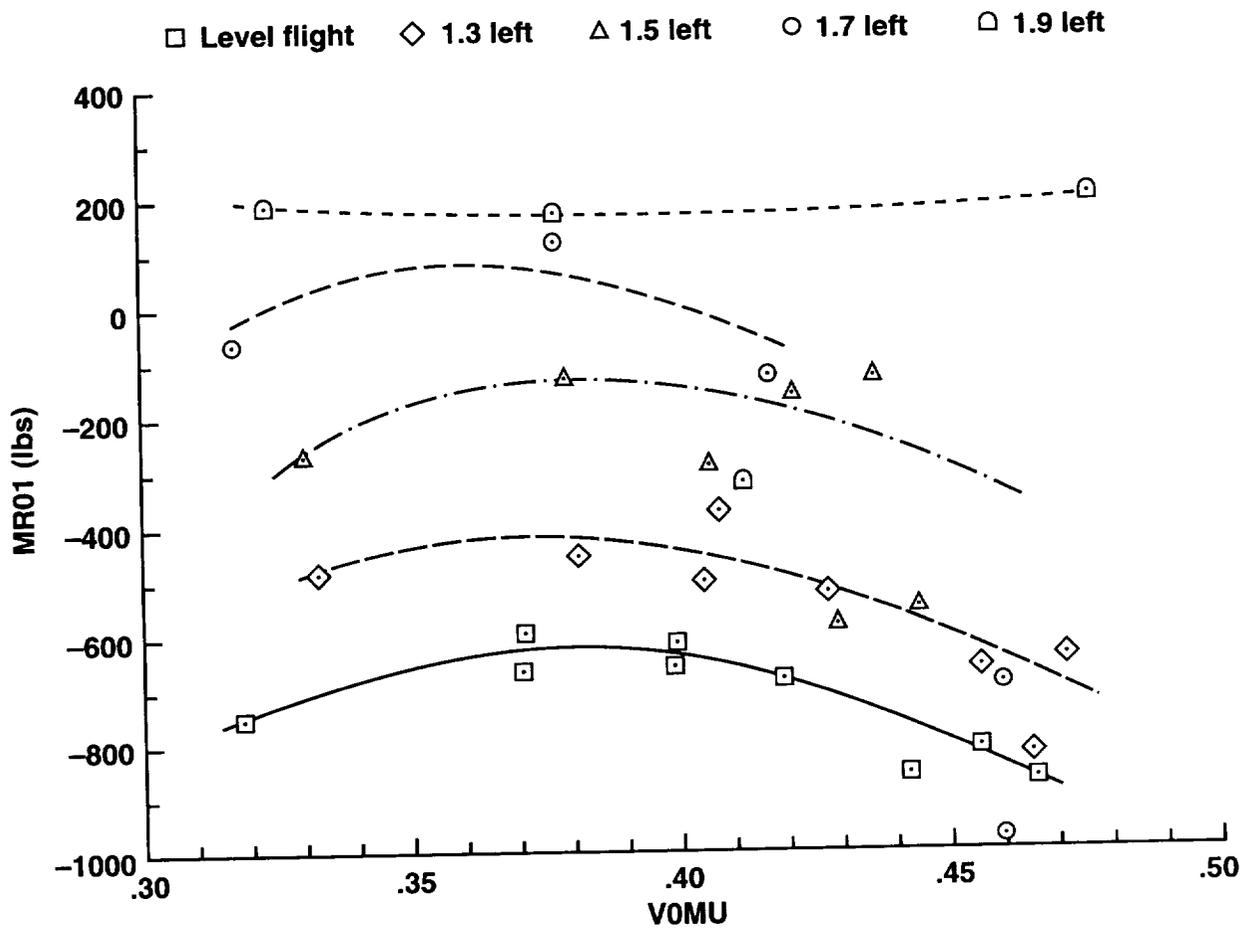
(a) Average.

Figure 105. Lateral link load vs advance ratio over g-loading sweep.
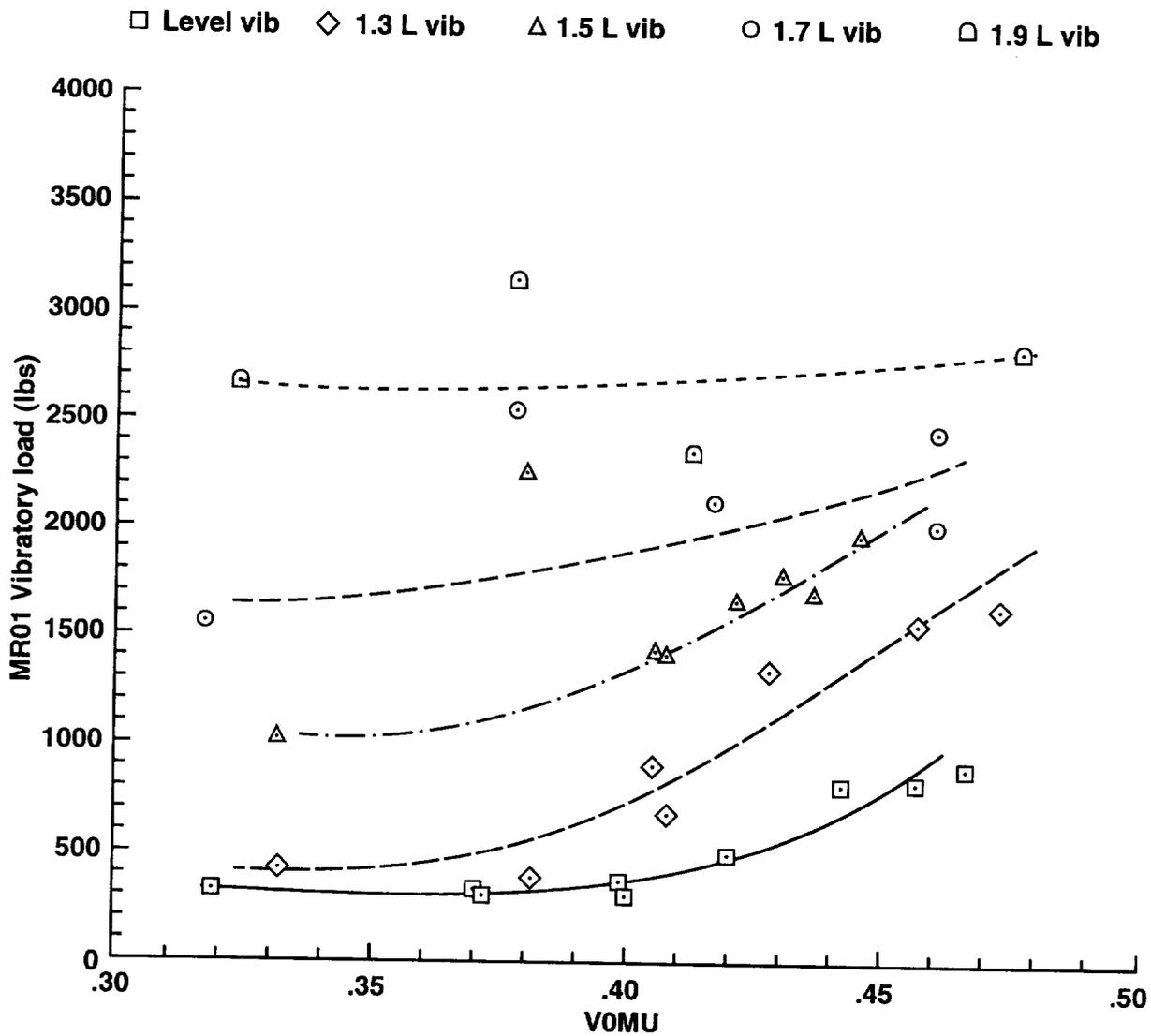
(b) Vibratory.

Figure 105. Concluded.
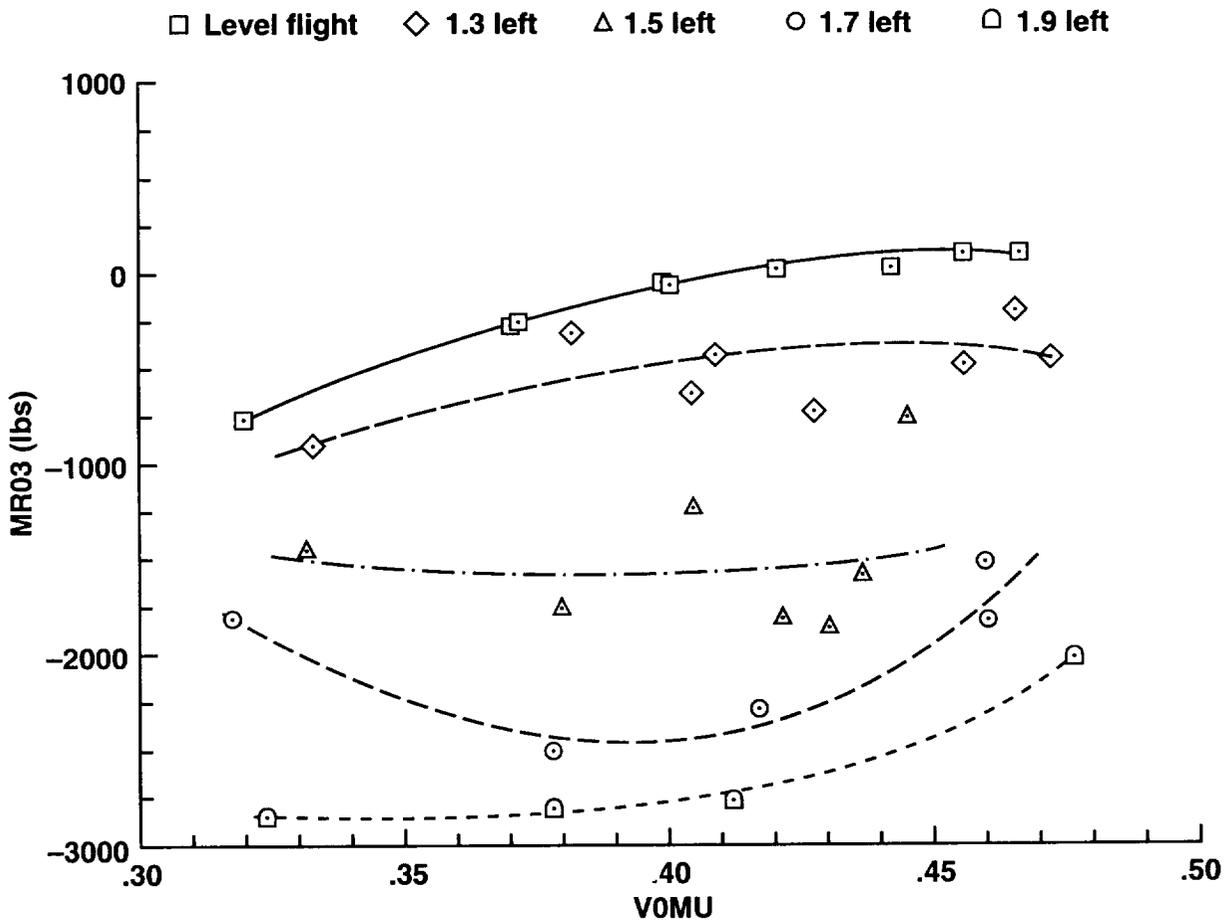
(a) Average.

Figure 106. Aft link load vs advance ratio over g-loading sweep.
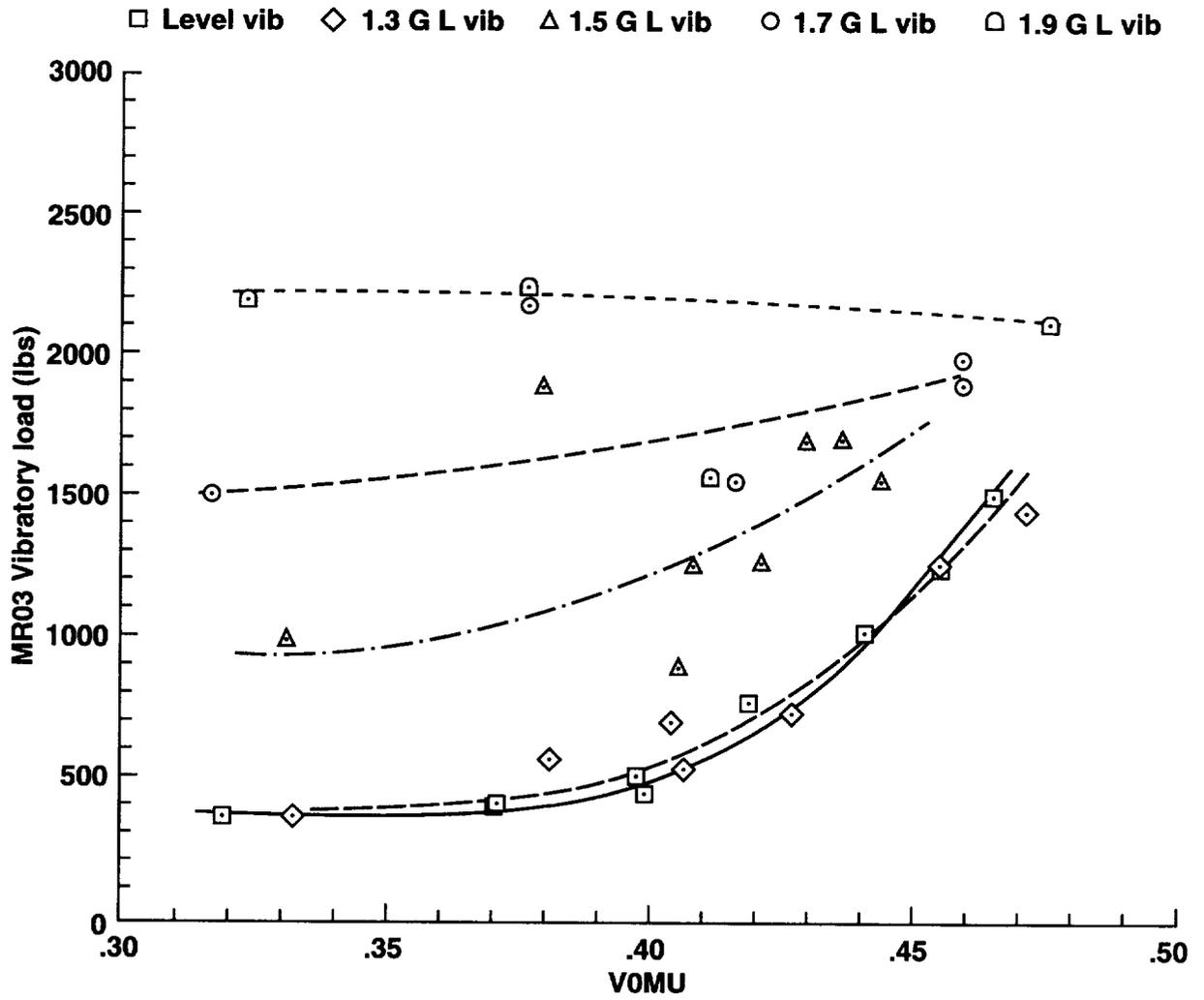
(b) Vibratory.

Figure 106. Concluded.
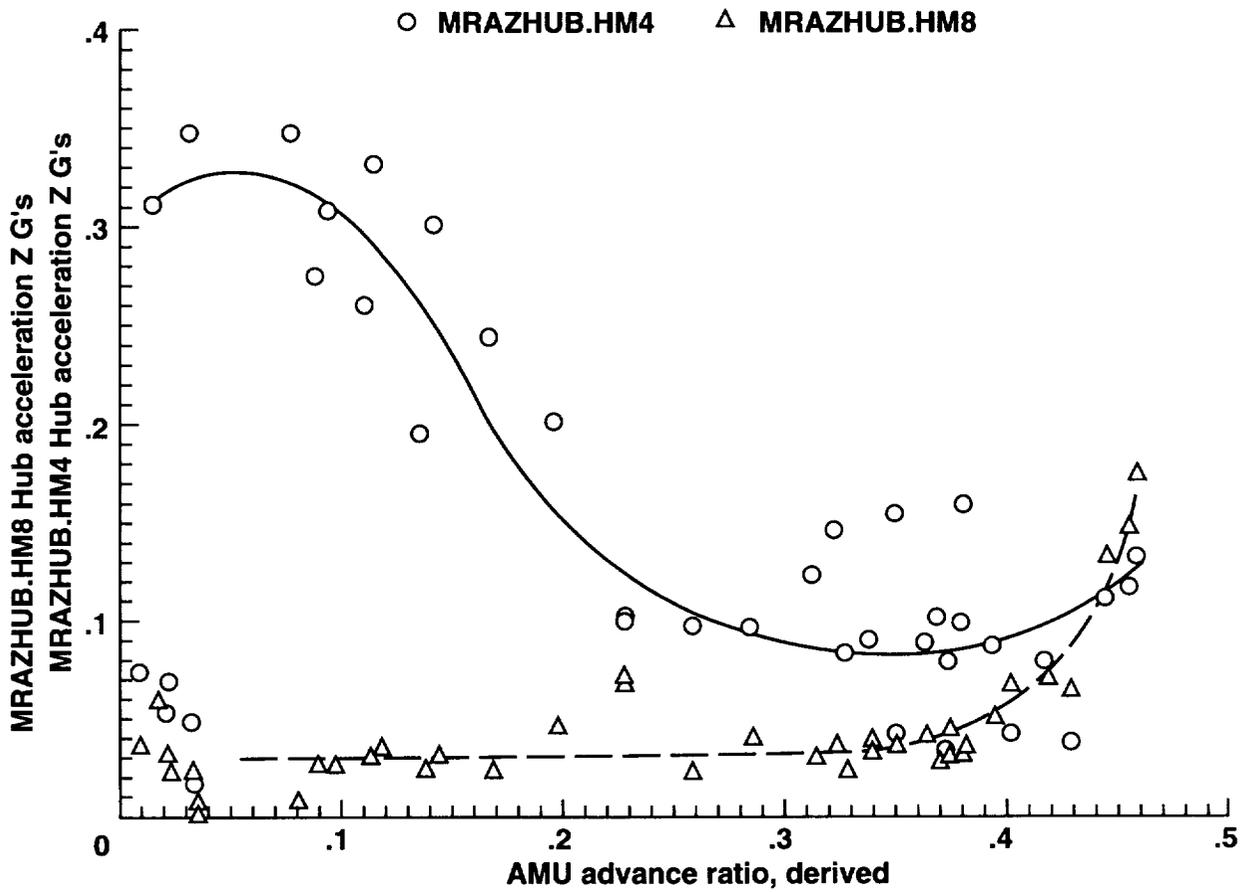
Figure 107. Hub vertical vibration 4/rev and 8/rev harmonics vs advance ratio.
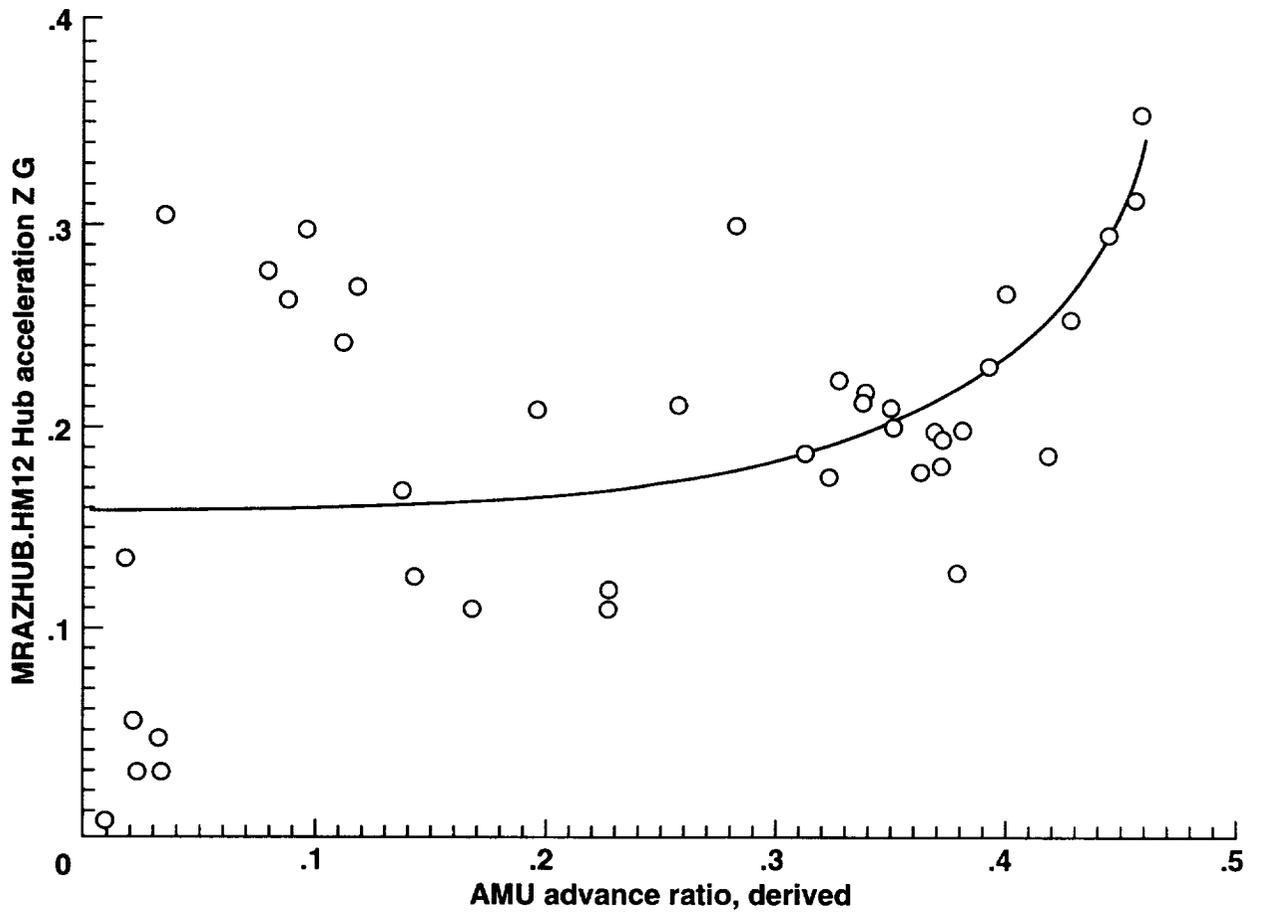
Figure 108. Hub vertical vibration 12/rev harmonics vs advance ratio.
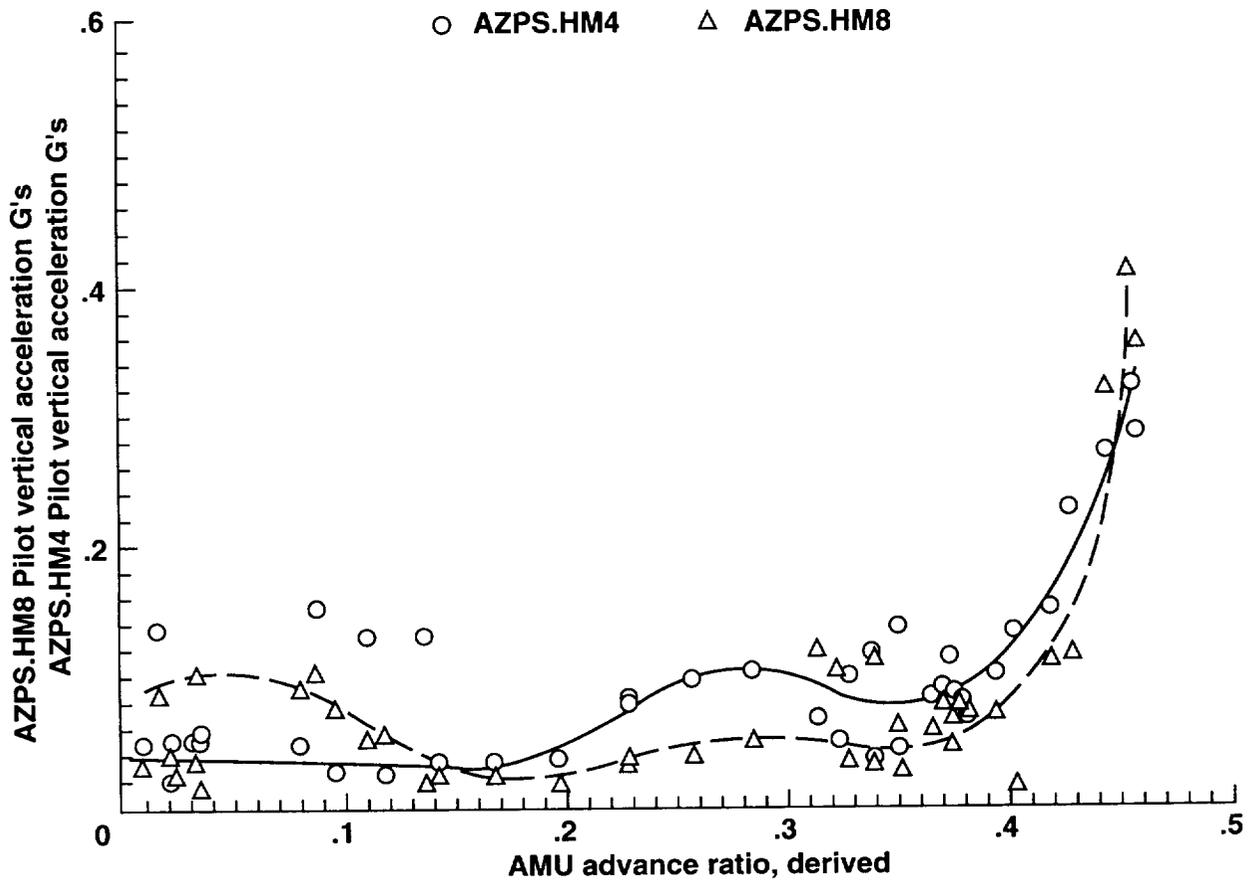
Figure 109. Pilots seat vertical 4/rev and 8/rev harmonics vs advance ratio.
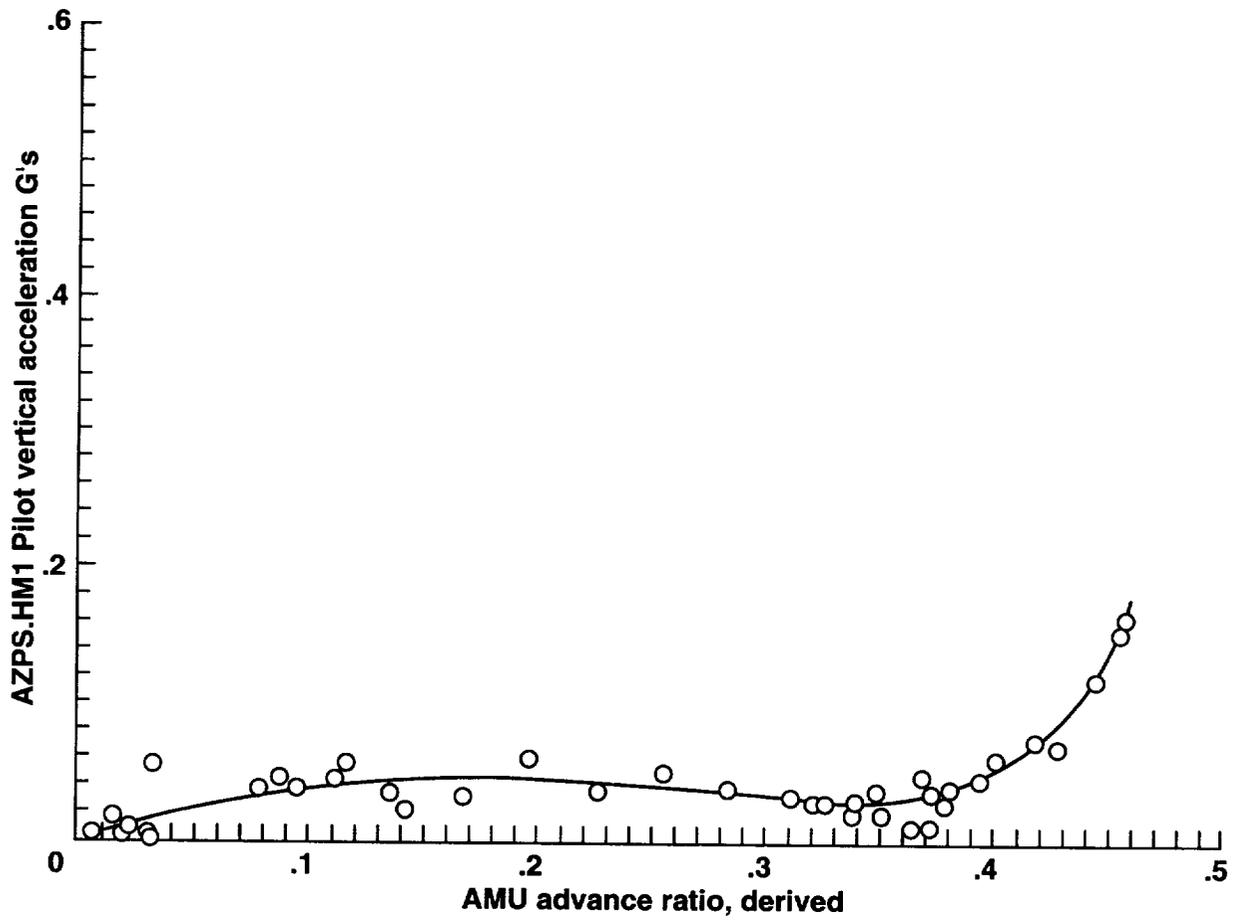
Figure 110. Pilots seat vertical 12/rev harmonics vs advance ratio.
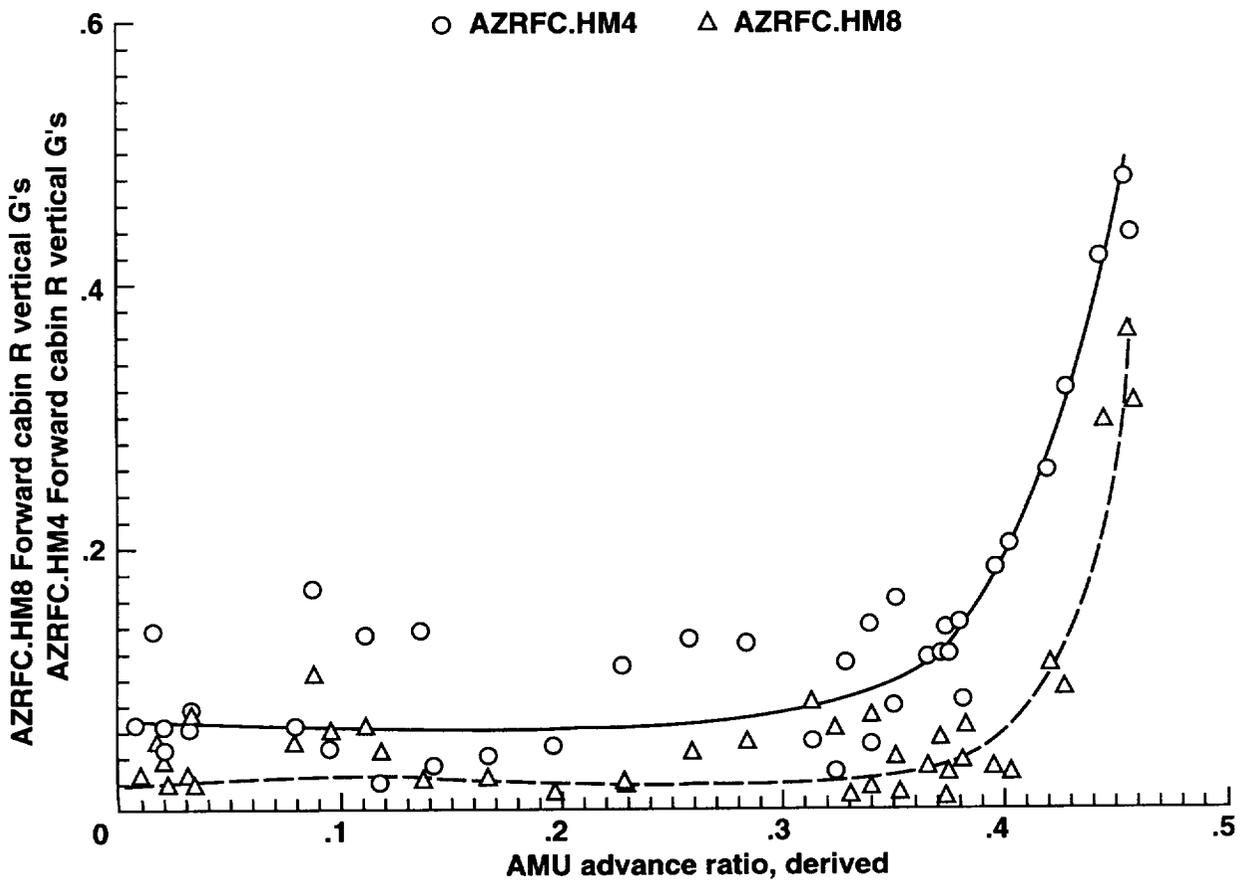
Figure 111. Right forward cabin vertical 4/rev and 8/rev harmonics vs advance ratio.
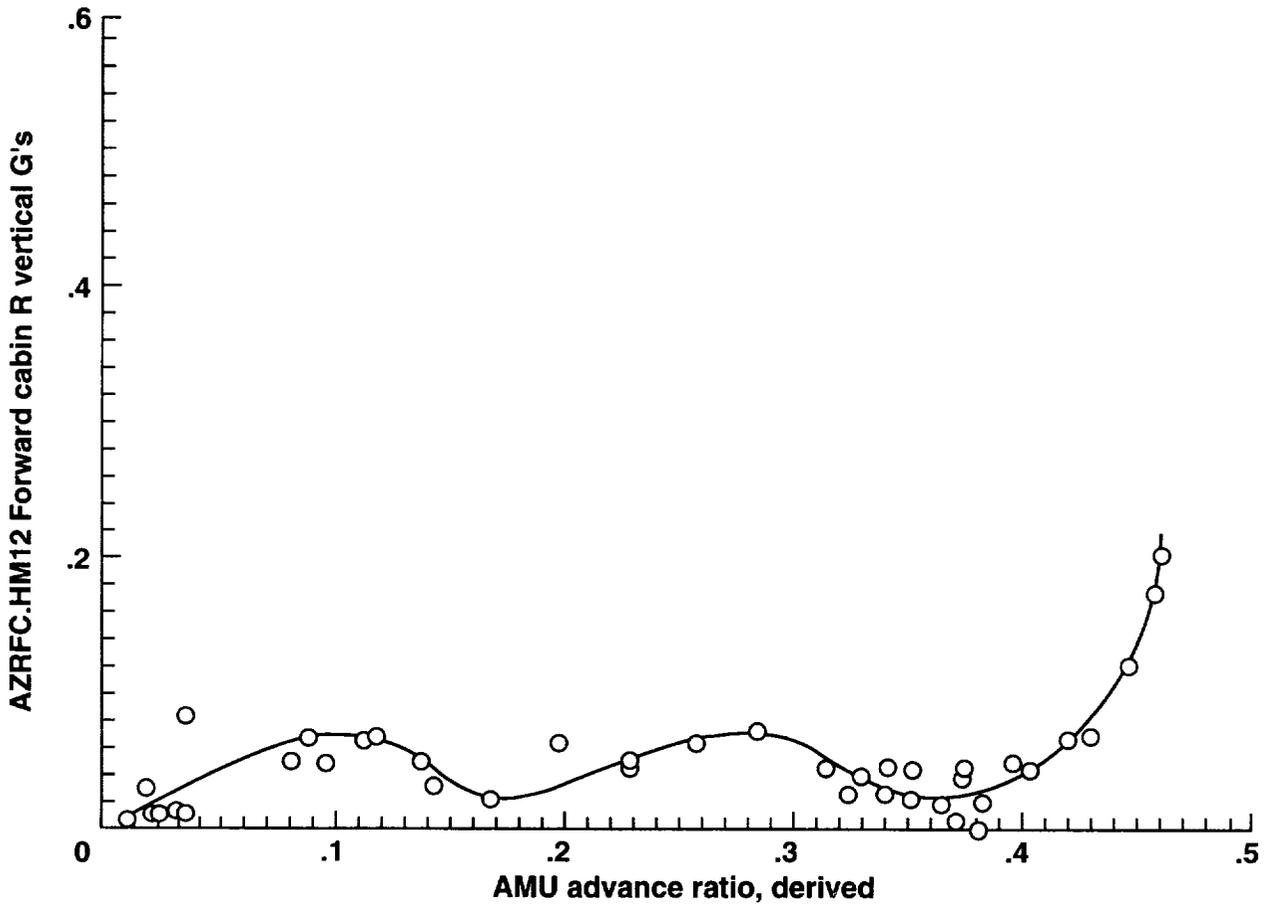
Figure 112. Right forward cabin vertical 12/rev harmonics vs advance ratio.
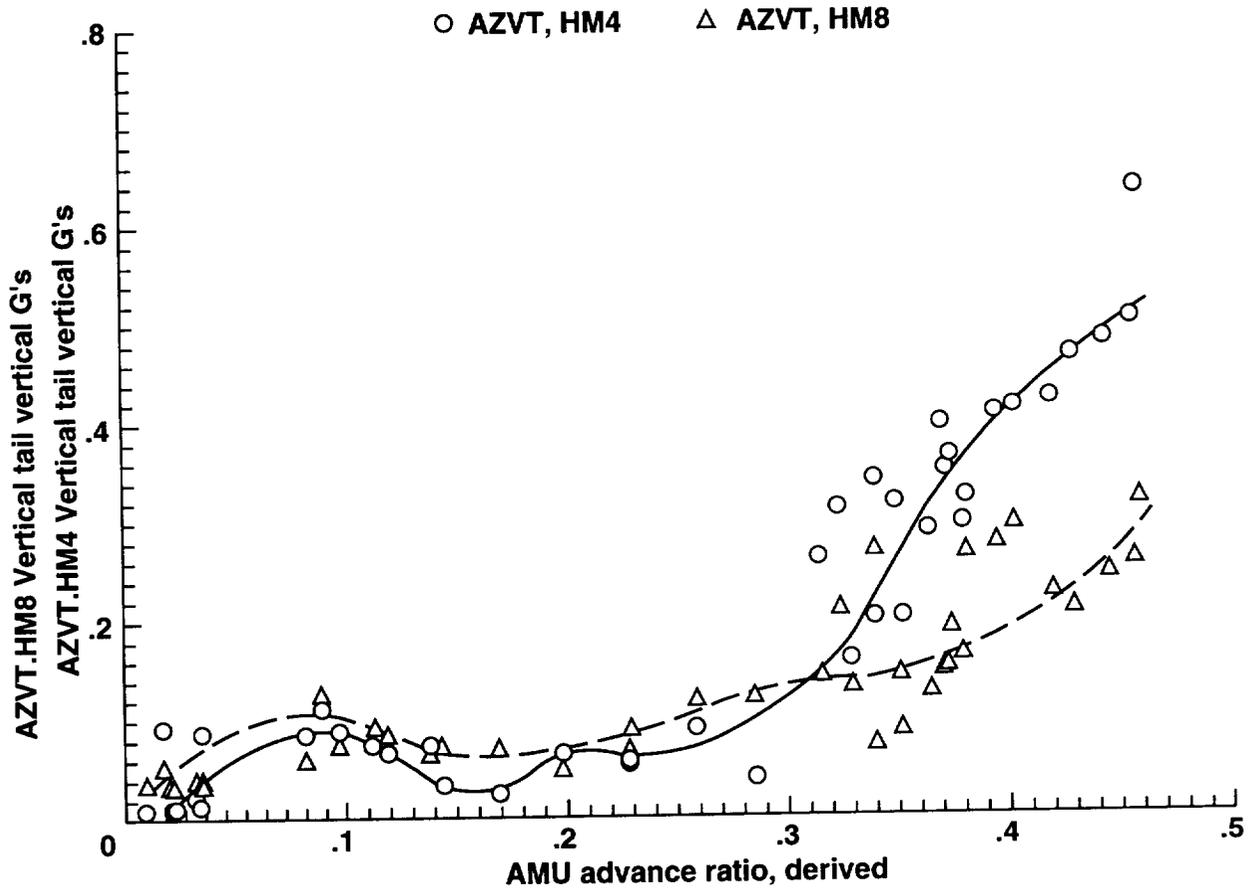
Figure 113. *Vertical tail vertical 4/rev and 8/rev harmonics vs advance ratio.*
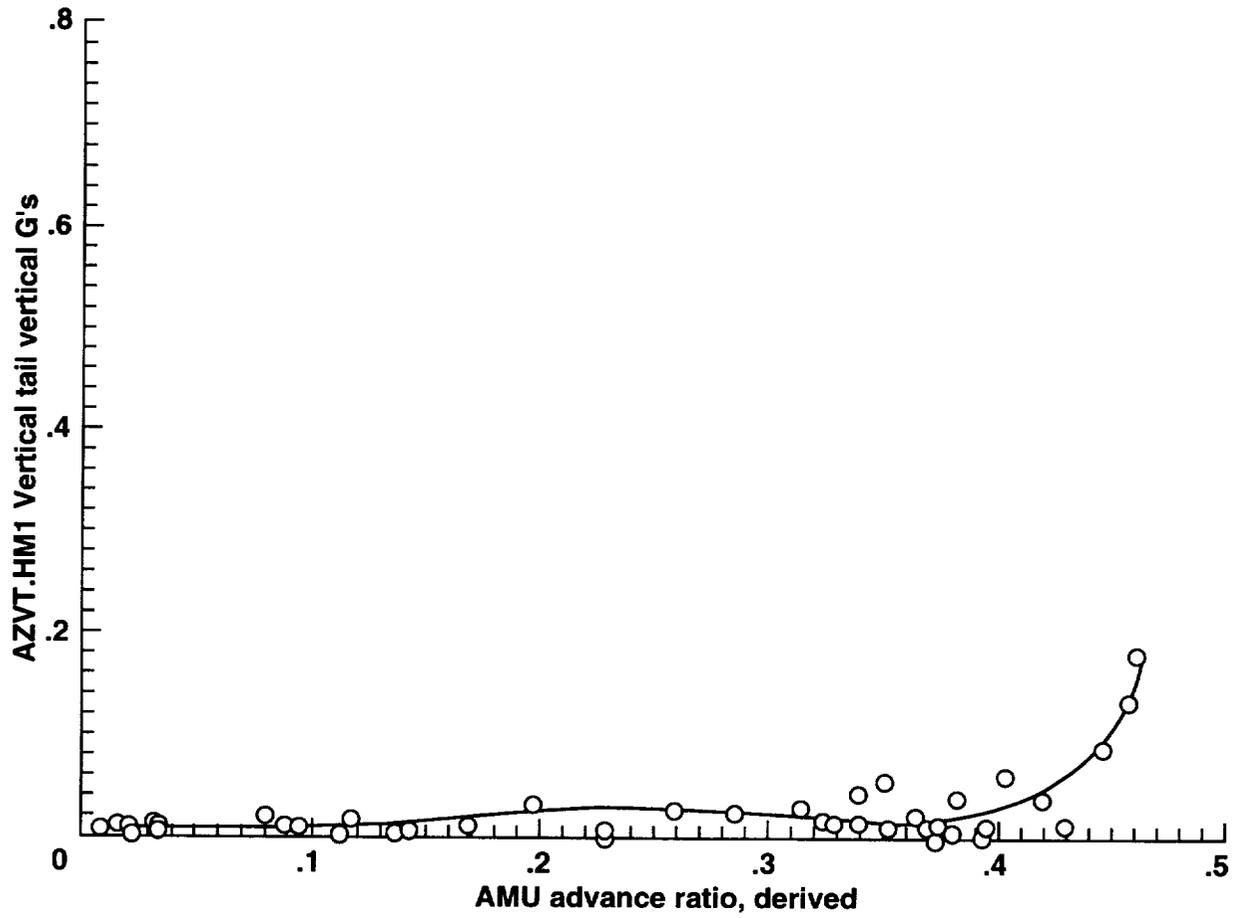
Figure 114. Vertical tail vertical 12/rev harmonics vs advance ratio.
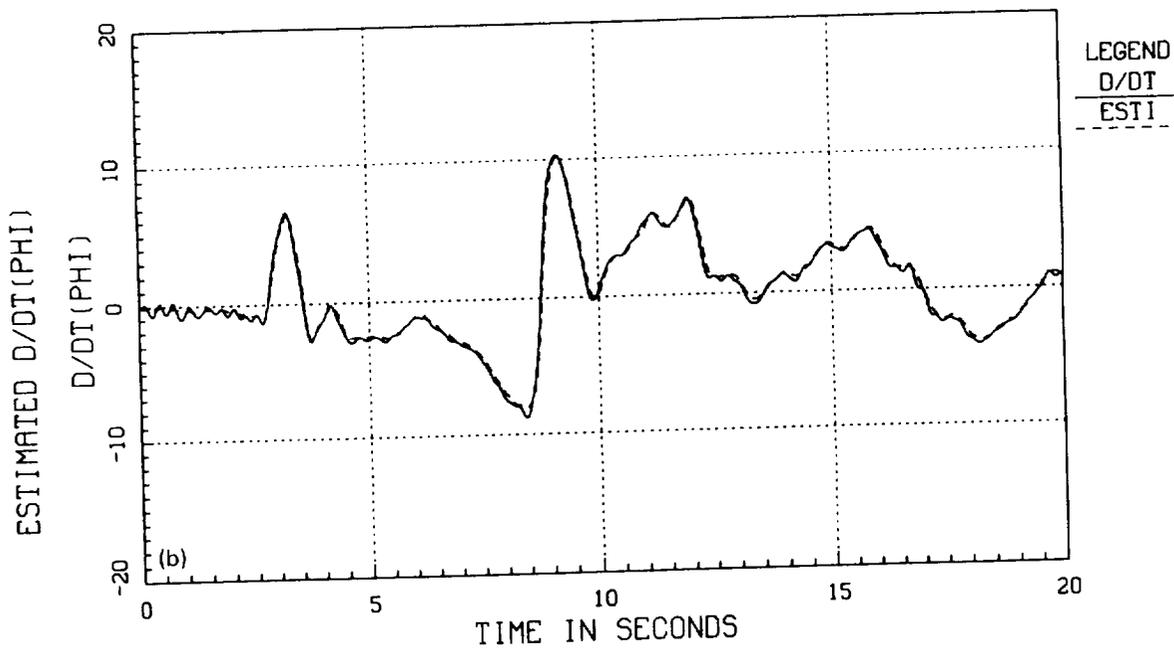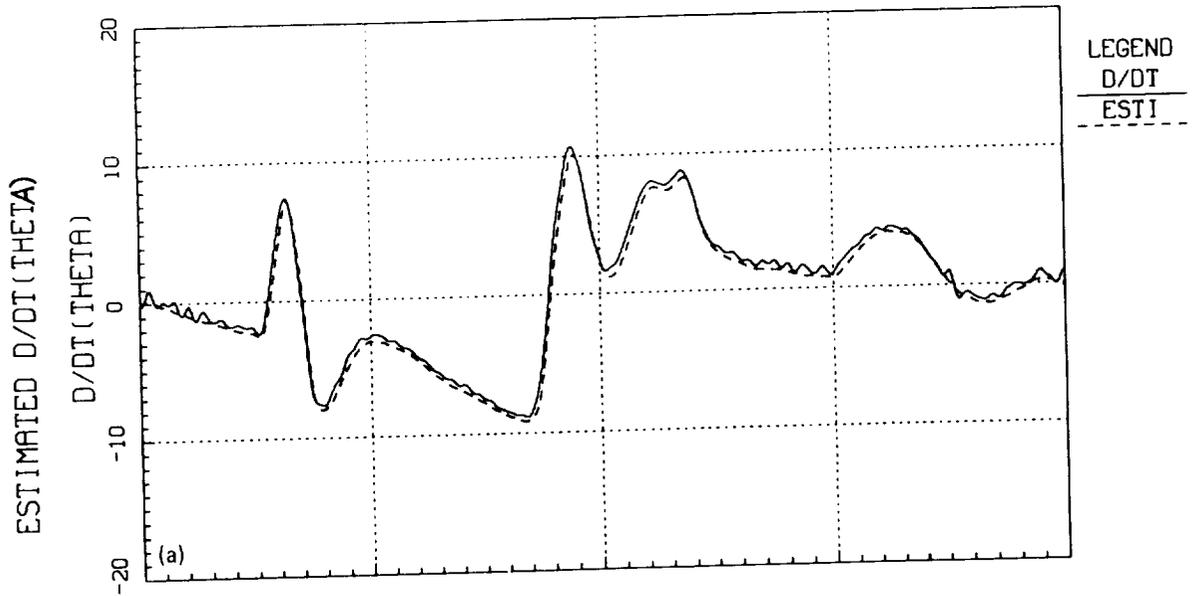
Figure 115. Comparison of Euler rates for longitudinal doublet at 60 knots. (a) Measured and estimated $d\theta/dt$, (b) measured and estimated $d\phi/dt$.
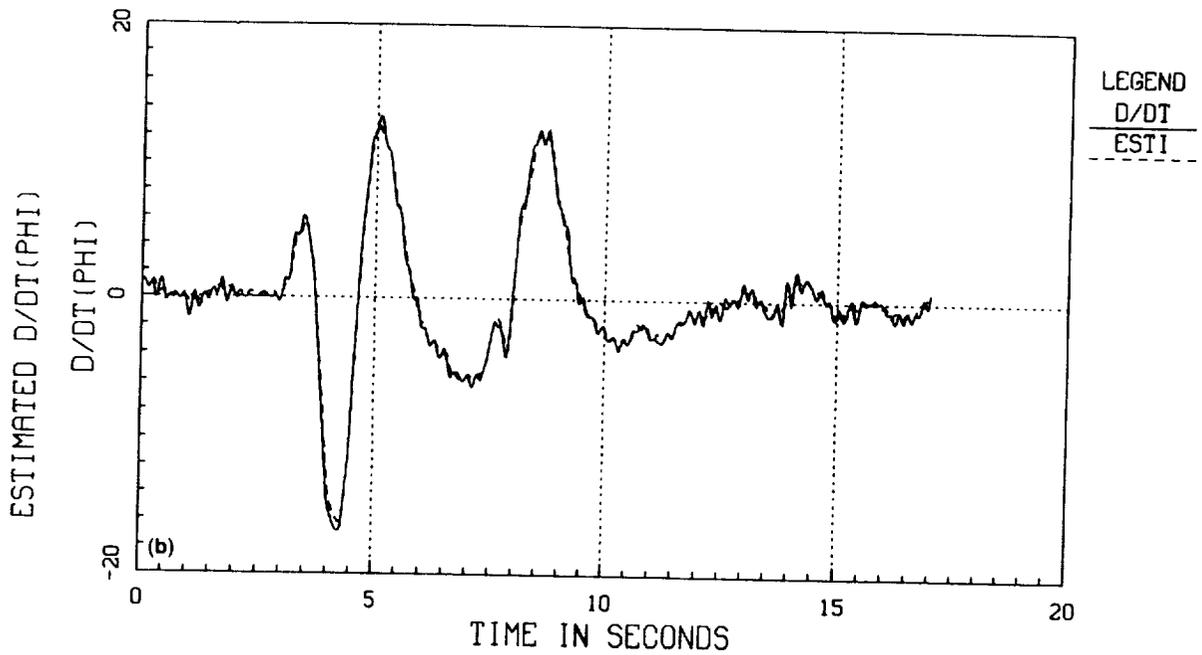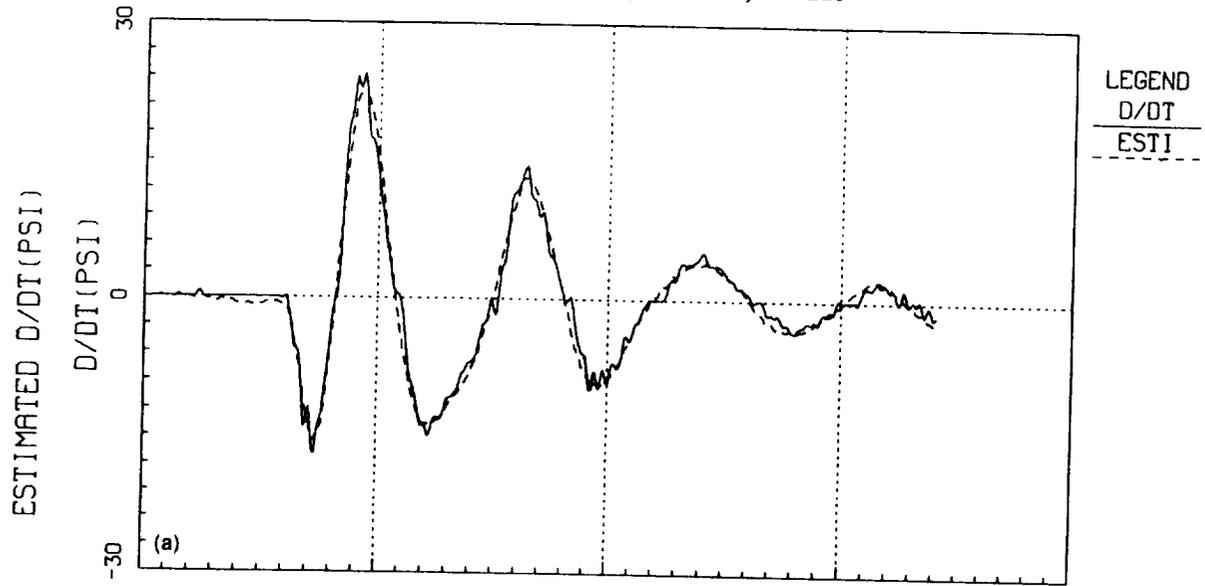
Figure 116. Comparison of Euler rates for pedal doublet at 140 knots. (a) Measured and estimated $d\psi/dt$, (b) measured and estimated $d\phi/dt$.
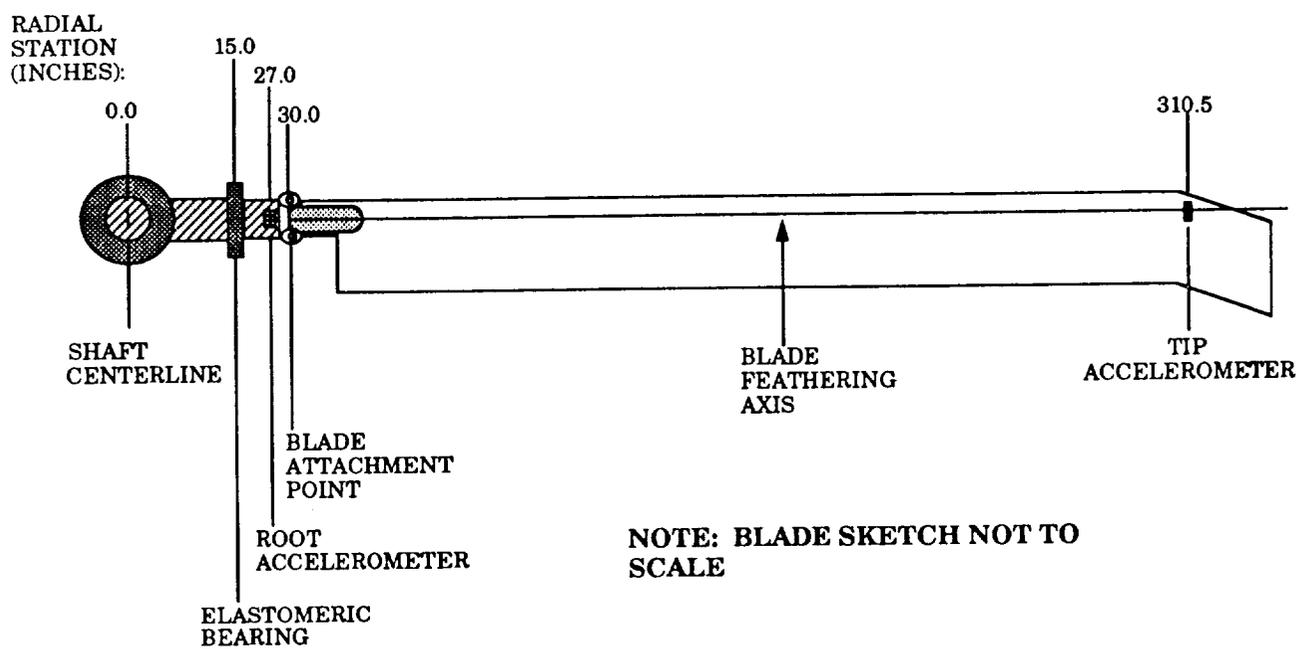
Figure 117. Radial locations of blade accelerometers.

Figure 118. Time and frequency plots of root acceleration at 80 knots.

UH-60A A/C 748 PHASE I TESTS
FLT   17:LEVEL FLIGHT CT/S - 0.09
CTR 1713: 80 KIASB,.09CTS,LEVEL SWEEP
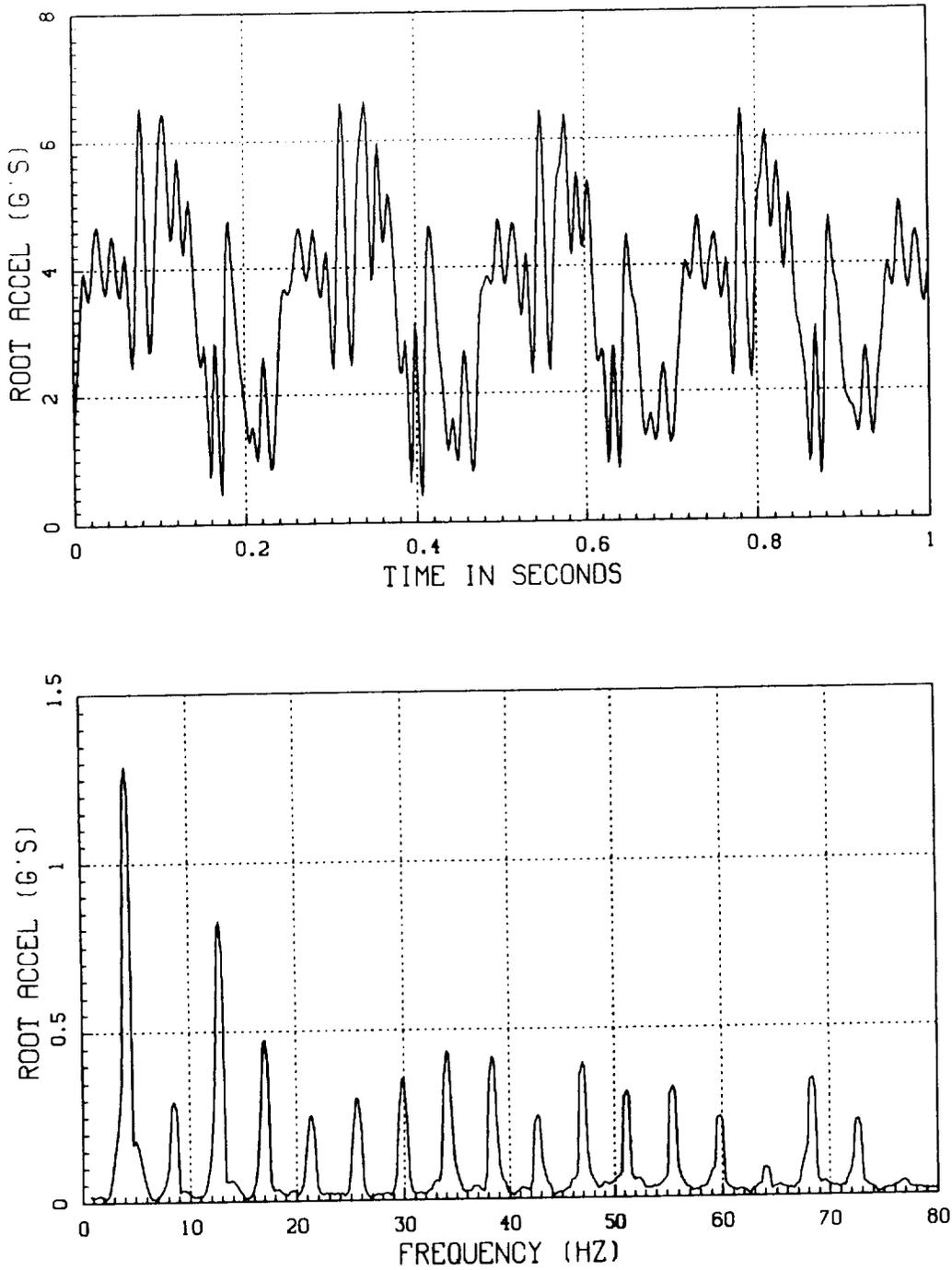
Figure 119. Time and frequency plots of tip acceleration at 80 knots.
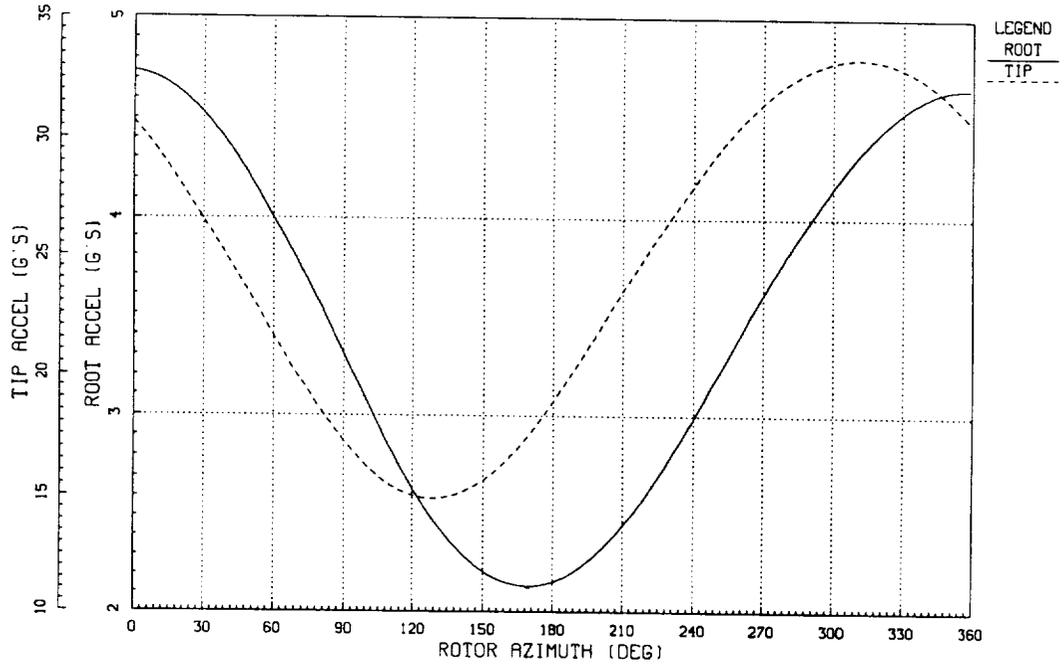
Figure 120. Root and tip accelerometer response at 80 knots.
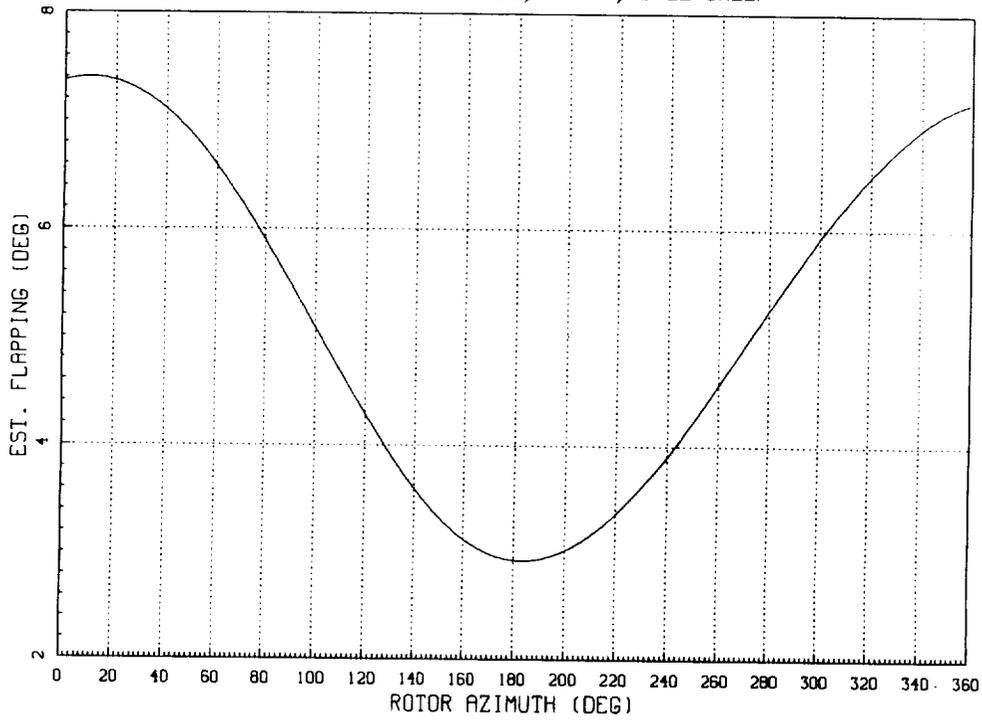
Figure 121. Calculated blade flapping from accelerometers.

262

*Figure 122. First and second flapwise mode shapes.*

Figure 123. Pitch-link load vs azimuth of low-speed data scatter.
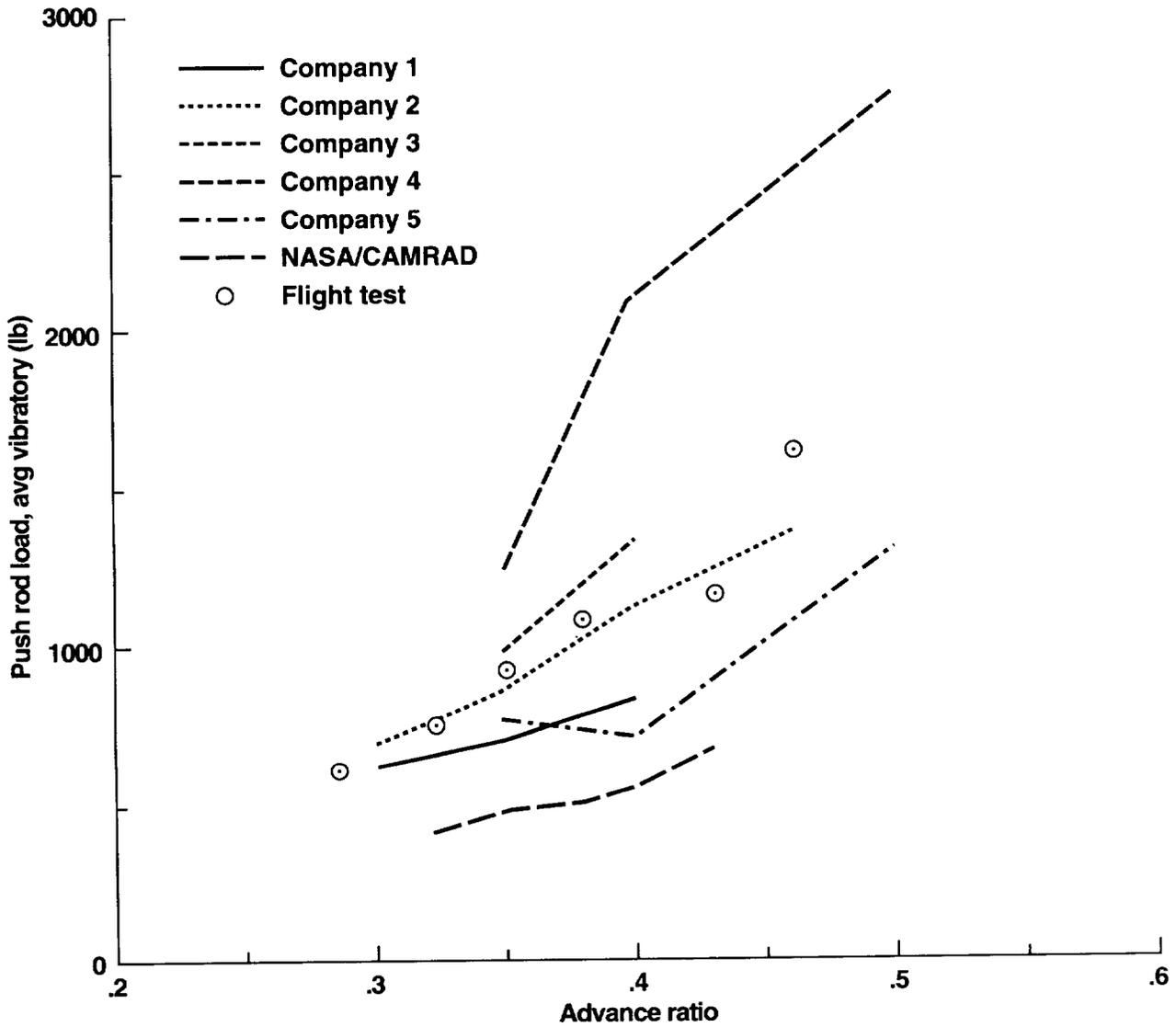
Figure 124. Pitch-link load vs advance ratio, flight vs industry predictions.
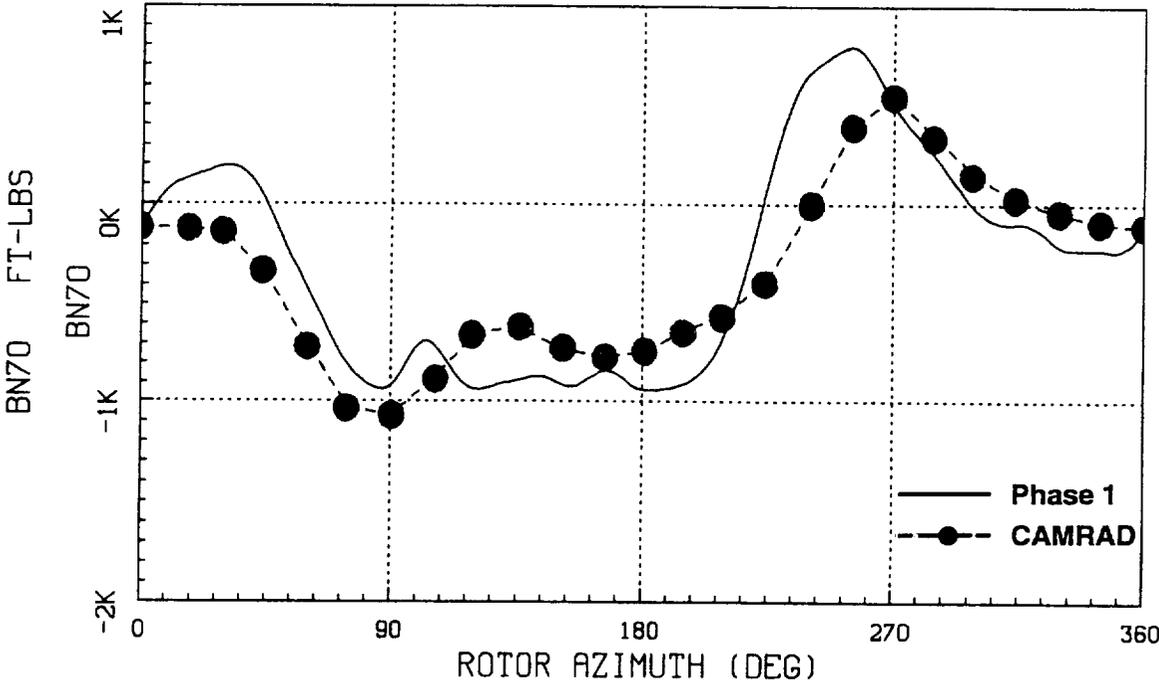
Figure 125. CAMRAD/MRALS correlation of blade-normal bending.

266

REPORT DOCUMENTATION PAGE

Public reporting burden for this collection of information is estimated to average 1 hour per response, including the time for reviewing instructions, searching existing data sources, gathering and maintaining the data needed, and completing and reviewing the collection of information. Send comments regarding this burden estimate or any other aspect of this collection of information, including suggestions for reducing this burden, to Washington Headquarters Services, Directorate for information Operations and Reports, 1215 Jefferson Davis Highway, Suite 1204, Arlington, VA 22202-4302, and to the Office of Management and Budget, Paperwork Reduction Project (0704-0188), Washington, DC 20503.

1. AGENCY USE ONLY (Leave blank)	2. REPORT DATE October 1993	3. REPORT TYPE AND DATES COVERED Technical Memorandum

4. TITLE AND SUBTITLE

The Modern Rotor Aerodynamic Limits Survey:
A Report and Data Survey

5. FUNDING NUMBERS

505-59-36

6. AUTHOR(S)

J. Cross, J. Brilla, R. Kufeld, and D. Balough

7. PERFORMING ORGANIZATION NAME(S) AND ADDRESS(ES)

Ames Research Center
Moffett Field, CA 94035-1000

8. PERFORMING ORGANIZATION REPORT NUMBER

A-91183

9. SPONSORING/MONITORING AGENCY NAME(S) AND ADDRESS(ES)

National Aeronautics and Space Administration
Washington, DC 20546-0001

10. SPONSORING/MONITORING AGENCY REPORT NUMBER

NASA TM-4446

11. SUPPLEMENTARY NOTES

Point of Contact: J. Cross, Ames Research Center, MS 237-5, Moffett Field, CA 94035-1000;
(415) 604-6571

12a. DISTRIBUTION/AVAILABILITY STATEMENT

Unclassified — Unlimited
Subject Category 01

12b. DISTRIBUTION CODE

13. ABSTRACT (Maximum 200 words)

The first phase of the Modern Technology Rotor program, the Modern Rotor Aerodynamic Limits Survey, was a flight test conducted by the United States Army Aviation Engineering Flight Activity for NASA Ames Research Center. The test was performed using a United States Army UH-60A Black Hawk aircraft and the United States Air Force HH-60A Night Hawk instrumented main-rotor blade. The primary purpose of this test was to gather high-speed, steady-state, and maneuvering data suitable for correlation purposes with analytical prediction tools. All aspects of the data base, flight-test instrumentation, and test procedures are presented and analyzed. Because of the high volume of data, only select data points are presented here. However, access to the entire data set is available upon request.

14. SUBJECT TERMS

UH-60, Rotor loads, Fuselage vibration

15. NUMBER OF PAGES

270

16. PRICE CODE

A12

17. SECURITY CLASSIFICATION OF REPORT Unclassified	18. SECURITY CLASSIFICATION OF THIS PAGE Unclassified	19. SECURITY CLASSIFICATION OF ABSTRACT	20. LIMITATION OF ABSTRACT

NSN 7540-01-280-5500

GPO 583-676/19027

Standard Form 298 (Rev. 2-89)
Prescribed by ANSI Std. Z39-18
298-102